Journal of Fluids Engineering

Published Monthly by ASME

VOLUME 132 • NUMBER 1 • JANUARY 2010

RESEARCH PAPERS

Flows in Complex Systems

Fundamental Issues and Canonical Flows

Multiphase Flows

Techniques and Procedures

TECHNICAL BRIEFS

(Contents continued on inside back cover)

(**Contents continued**)

Journal of Fluids Engineering **Volume 132, Number 1** **JANUARY 2010**

The ASME Journal of Fluids Engineering is abstracted and indexed in the following:

Applied Science & Technology Index, Chemical Abstracts, Chemical Engineering and Biotechnology Abstracts (Electronic equivalent of Process and Chemical Engineering), Civil Engineering Abstracts, Computer & Information Systems Abstracts, Corrosion Abstracts, Current Contents, Ei EncompassLit, Electronics & Communications Abstracts, Engineered Materials Abstracts, Engineering Index, Environmental Engineering Abstracts, Environmental Science and Pollution Management, Excerpta Medica, Fluidex, Index to Scientific Reviews, INSPEC, International Building Services Abstracts, Mechanical & Transportation Engineering Abstracts, Mechanical Engineering Abstracts, METADEX (The electronic equivalent of Metals Abstracts and Alloys Index), Petroleum Abstracts, Process and Chemical Engineering, Referativnyi Zhurnal, Science Citation Index, SciSearch (The electronic equivalent of Science Citation Index), Shock and Vibration Digest, Solid State and Superconductivity Abstracts, Theoretical Chemical Engineering

Sintu Singha

K. P. Sinhamahapatra

Department of Aerospace Engineering,
IIT Kharagpur,
Kharagpur, 721302 India

High-Resolution Numerical Simulation of Low Reynolds Number Incompressible Flow About Two Cylinders in Tandem

Low Reynolds number steady and unsteady incompressible flows over two circular cylinders in tandem are numerically simulated for a range of Reynolds numbers with varying gap size. The governing equations are solved on an unstructured collocated mesh using a second-order implicit finite volume method. The effects of the gap and Reynolds number on the vortex structure of the wake and on the fluid dynamic forces acting on the cylinders are reported and discussed. Both the parameters have significant influence on the flow field. An attempt is made to unify their influence on some global parameters. [DOI: 10.1115/1.4000649]

Keywords: tandem cylinders, wake structure, interacting shear layers, vortex impingement, vortex enveloping, unsteady fluid forces, collocated grid

1 Introduction

Flow past a system of two or more circular cylinders is a generic flow-structure interaction having important applications that include heat exchanger tubes, bundled transmission lines, buildings, and offshore risers. The two-cylinder system represents an idealization of certain features of unsteady flow occurring in an array of cylinders. Two cylinders can be arranged in infinite number of ways, each arrangement having its own flow features. The dominant characteristics of the flow over a tandem arrangement of two cylinders are the complex interaction between the shear layers from the cylinders and vortex impingement and enveloping. In addition to the Reynolds number, the gap size (g), i.e., the shortest distance between the surfaces of the two cylinders, strongly influences the flow. If the gap is greater than a critical value, the upstream cylinder sheds vortices onto the downstream cylinder, but no shedding occurs from the upstream cylinder if the gap space is less than the critical value. When the upstream cylinder sheds vortices, the downstream cylinder lies in the unsteady vortex wake of the upstream cylinder. The vortex impingement influences the fluid dynamic forces, vortex-shedding frequencies, and the overall flow features significantly. The unsteady wake of the front cylinder causes large fluctuating fluid forces on the downstream cylinder. However, the mean drag force decreases considerably. The interaction also affects the flow considerably when the upstream cylinder does not shed vortices in the gap. A particular point of interest is the negative drag force experienced by the downstream cylinder at lower spacings.

Due to the importance of the problem in many engineering applications and because of the complex flow physics involved, considerable amount of research work, largely experimental [1–5], has gone into the understanding of the flow dynamics of cylinders in tandem. Numerical investigations of flow past multiple cylinders, including two cylinders in tandem, are relatively less reported in the open literature. Most of the studies are found to be limited to one or two Reynolds numbers with one or two gaps and do not reflect the trends of the flow parameters. Systematic studies of the flow interference over wide ranges of gaps and Reynolds numbers are scarce. Oka et al. [1] and Jendrzejczyk and Chen [2] measured the fluid forces on the cylinders and vortex-shedding frequencies behind the two cylinders for different gap sizes. Zdravkovich [3] presented an extensive review of flow interference between two circular cylinders in various arrangements. Subsequently, Zdravkovich [4] classified the flow pattern behind two circular cylinders in tandem. According to the observations, for pitch ratios $1 < L/D < 1.3-1.8$, where L is the center-to-center distance between the two cylinders and D is the diameter of each cylinder, the cylinders behave as a single bluff body and the shear layers that shed from the upstream cylinder do not reattach on the downstream cylinder. As the pitch ratio increases to the range $1.2-1.8 < L/D < 3.4-3.8$, the shear layer that shed from the upstream cylinder reattaches the downstream cylinder and the vortices are shed off the downstream cylinder only. With further increase in pitch ratio, the vortex shedding occurred in the gap and in the downstream side of the rear cylinder. Carrying out experiments at high Reynolds numbers, Kiya et al. [5] observed flip-flopping flow about two cylinders in tandem. It was shown that when the distance between the cylinders was in an appropriate range, the flow randomly switched between two patterns in one of which the flow reattached on the downstream cylinder and in the other vortex shedding occurred in the gap. An elegant overview of the flow problem is given in Ref. [6].

Li et al. [7] studied the flow about two cylinders in tandem at a Reynolds number of 100 using a Galerkin velocity-pressure finite element formulation implemented on a coarse mesh. Four different gap spacings were simulated and were compared with experiments that were performed at much higher Reynolds numbers where turbulence and three dimensionality are important factors. However, the comparison showed similarities between the numerical and experimental findings. Johnson et al. [8] studied the low Reynolds number flow around periodic arrays of cylinders using vorticity-stream function based Petrov–Galerkin finite element method. Mittal et al. [9] investigated the flow phenomena over a pair of circular cylinder at $\mathrm{Re}=100$ and 1000 with tandem and staggered arrangement using a stabilized finite element method. Only two pitch ratios (L/D), namely, 2.5 and 5.5, were selected for the tandem arrangement. Farrant et al. [10] studied the laminar wake structures behind two cylinders arranged in either side-by-side or in tandem arrangement using a cell boundary element numerical technique. Only a single tandem configuration

---

Contributed by the Fluids Engineering Division of ASME for publication in the JOURNAL OF FLUIDS ENGINEERING. Manuscript received March 13, 2009; final manuscript received: November 6, 2009; published online December 15, 2009. Assoc. Editor: Rajat Mittal.

with normalized gap (g/D) of 4.0 at Re=200 was considered in the study and the synchronized mode of vortex shedding was observed for the case. Hall et al. [11] found an acoustic standing wave to have significant effects on the wake structures behind an isolated cylinder and two cylinders arranged in tandem with low to moderate spacing $(1.75 \leq L/D \leq 2.5)$. It was found that the applied acoustic filed induces vortex shedding in the gap for pitch ratio (L/D) of 2.5. Meneghini et al. [12] reported a systematic finite element simulation of the problem over a range of gaps at Reynolds numbers of 100 and 200. Numerical studies using unstructured collocated grid have been conducted at a Reynolds number of 100 over a very wide range of gaps by Sharman et al. [13]. Ding et al. [14] carried out an explicit mesh-free least squares finite difference solution of the vorticity-stream function formulation at Reynolds numbers of 100 and 200 for normalized gap sizes of 1.5 and 4.5.

The present study attempts to investigate the flow past two circular cylinders arranged in tandem over wide ranges of Reynolds numbers (Re) and gaps (g/D). The governing equations for two-dimensional incompressible flow in the primitive-variable form are solved using an implicit collocated grid finite volume method implemented on a triangular mesh. Appropriate interpolations [15] are incorporated to suppress the spurious oscillations associated with collocated grid incompressible solution. Sequential changes in the flow pattern for a particular Reynolds number with varying g/D are presented here. High-resolution meshes are used to capture the vortical structure of the wakes. Simulations are carried out for sufficiently long duration to capture the changes in the flow field adequately. Significant effects of the gap on the flow patterns at a particular Reynolds number have been observed in both steady and unsteady flow cases. The effects of Reynolds number and gap on drag coefficient and Strouhal number are unified through approximate correlations.

2 Numerical Method

The governing equations for an incompressible flow are the conservation equations for mass and momentum, respectively. These are written in integral form as follows:

$$\oint_S \mathbf{V} \cdot \hat{\mathbf{n}} dS = 0 \tag{1}$$

$$\frac{\partial}{\partial t}\int_\Omega u_i d\Omega + \oint_S u_i \mathbf{V} \cdot \hat{\mathbf{n}} dS = -\frac{1}{\rho}\oint_S p n_i dS + \upsilon \oint_S \nabla u_i \cdot \hat{\mathbf{n}} dS \tag{2}$$

where $\mathbf{V}$ is the velocity vector of a fluid element, u_i are the Cartesian components of the velocity, υ is the kinematic viscosity, and Ω and S denote the control volume and the bounding surface of the control volume, respectively. The unit vector normal to the surface S is $\hat{\mathbf{n}}$, and n_i denotes the Cartesian components of the vector.

The fluid flow equations are discretized and solved as follows. The convective terms in the momentum equations for a cell are computed as the sum of fluxes across the three faces where the flux across each face is computed as a product of the outward mass flux and the appropriate cell face velocity component. The velocity on a face is obtained using a quadratic upwind interpolation [16] from the velocity at three points. Two of these three points are the cell centers on either side of the face. The projection of the distant vertex of the triangle that is in the upstream side of the face on the line joining the two cell centers provides the third point. The stencil used for the quadratic upwind approximation is shown in Fig. 1. Considering the points R, S, and P in Fig. 1, the quadratic polynomial $P_n(s)$ can be obtained as

$$P_n(s) = as^2 + bs + c \tag{3}$$

In Eq. (3), s is the distance from a reference point, and the coefficients a, b, and c are given by

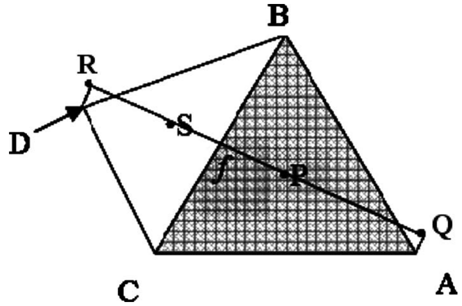

Fig. 1 Stencil (made up of *P*, *S*, and *Q* or *R*) for quadratic interpolation at face *BC*

$$a = -\left[\frac{1}{(d_P - d_R)(d_R - d_S)}u_{iR} + \frac{1}{(d_R - d_S)(d_S - d_P)}u_{iS} + \frac{1}{(d_S - d_P)(d_P - d_R)}u_{iP}\right]$$

$$b = \frac{(d_S + d_P)}{(d_P - d_R)(d_R - d_S)}u_{iR} + \frac{(d_R + d_P)}{(d_R - d_S)(d_S - d_P)}u_{iS} + \frac{(d_S + d_R)}{(d_S - d_P)(d_P - d_R)}u_{iP}$$

$$c = -\left[\frac{(d_S d_P)}{(d_P - d_R)(d_R - d_S)}u_{iR} + \frac{(d_R d_P)}{(d_R - d_S)(d_S - d_P)}u_{iS} + \frac{(d_S d_R)}{(d_S - d_P)(d_P - d_R)}u_{iP}\right]$$

where d_R, d_S, and d_P are the distance of the points R, S, and P from a reference point and u_{iR}, u_{iS}, and u_{iP} are the velocity components at these points.

Integrated over a triangular control volume, the diffusive terms in the momentum equations can be expressed in the following generic form:

$$\oint_S \nabla u_i \cdot \hat{n} dS \approx \sum_{k=1}^{3} \frac{\partial u_i}{\partial x_{jk}} n_{jk} dS_k \quad i,j = 1,2 \tag{4}$$

The gradients along the face of a control volume are computed using the values of the variable at the two adjacent cell centers and at the two terminating vertices of the face, as shown in Fig. 2(*a*). The value of the variable u_i at a vertex of the face is obtained by an interpolation from the cell-centered values of the surrounding cells using the linearity-preserving Laplacian due to Holmes and Connel [17]. The stencil is shown in Fig. 2(*b*). The procedure is based on perturbing the weights of the cells and minimizing the sum of the square of the perturbations. The perturbations are found by applying Lagrange multipliers with the constraint that the constructed Laplacian is zero for all linear data. Finally, the diffusive flux terms (F_{di}) for a cell with center P are obtained in terms of the variable at P and at the center of all the neighboring cells shared by the vertices of the triangular cell P. This is given by

$$F_{di} = \oint_S \nabla u_i \cdot \hat{n} dS = a_P u_{iP} + \sum_{m \neq P}^{N_1} c_m u_{im} + \sum_{m \neq P}^{N_2} d_m u_{im} + \sum_{m \neq P}^{N_3} e_m u_{im} \tag{5}$$

where N_1, N_2, and N_3 are the number of triangular cells connected, respectively, to each of the three vertices of the triangular cell P.

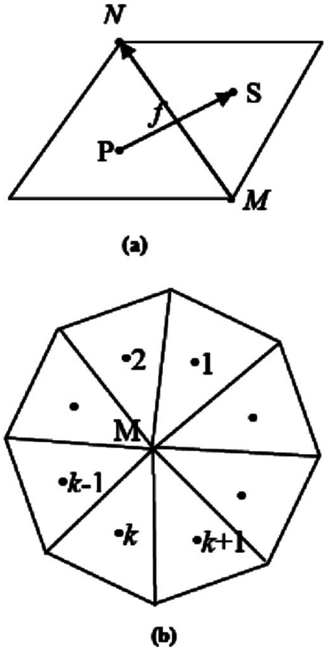

Fig. 2 (*a*) **Stencil and notations for the gradients in diffusive flux across face** ***MN***. (*b*) **Stencil for the Laplacian interpolation for the vertex** ***M***

The solution is advanced in time using a fractional step method based on the implicit Crank–Nicolson scheme. A provisional velocity field ($\mathbf{V}^*$) is first computed from the latest available mass flux and velocity field using

$$\frac{u_{iP}^{*}-u_{iP}^{n}}{\Delta t}+\frac{1}{2}\left(\sum_{f} m_{f}^{*,l}u_{if}^{*}+\sum_{f} m_{f}^{n}u_{if}^{n}\right)=\frac{1}{2}\left(\sum_{f} F_{\text{dif}}^{*}+\sum_{f} F_{\text{dif}}^{n}\right) \tag{6}$$

where P and f denote the cell center and a cell face, respectively. F_d is the diffusive flux term and m is mass flux. The index $i=1,2$ denotes the streamwise (x) and cross-stream (y) directions, respectively. The superscript $*$ indicates provisional or intermediate values during a time step and l denotes the iteration count. The iteration procedure is described below. The above equations are solved using a Gauss–Seidel iterative solver along with the discretized continuity equation written as

$$\sum_{f} m_{f}^{n+1}=0 \tag{7}$$

The provisional velocity field is used to compute the cell face velocities from Eq. (8) using the Rhie and Chow [15] interpolation. The interpolation suppresses the spurious numerical oscillations usually associated with collocated grid incompressible Navier–Stokes solver:

$$u_{if}=\Gamma(u_i^{*})-\Delta t\nabla_{i}p \tag{8}$$

where Γ denotes the interpolation operator. The mass flux through a face of the control volume is written as

$$m_{f}=m_{f}^{*}-\Delta t(\nabla p\cdot\hat{n}dS)_{f} \tag{9}$$

Thus the sum of the mass flux across all the faces of the control volume is given by

$$\sum_{f} m_{f}=\sum_{f} m_{f}^{*}-\Delta t\sum_{f}\nabla p\cdot\hat{n}dS \tag{10}$$

Imposing the continuity equation (7) on equation (10), the following equation for intermediate pressure is obtained:

$$\sum_{f}\nabla p\cdot\hat{n}dS=\frac{\sum_{f} m_{f}^{*}}{\Delta t} \tag{11}$$

The computed pressure field is used to update the mass flux from Eq. (9). The updated mass flux does not generally satisfy the continuity equation (7) at this stage. Thus an iterative procedure is needed to correct the mass flux (m_f) up to a tolerance limit. The iterative procedure is summarized as follows.

Starting with the velocity and pressure fields at the nth time step (u_i^n,p^n), the iterative loop starts with setting $u_i^{*,l}=u_i^n$ and $m_f^{*,l}=m_f^n$, where l is the iteration counter.

(1) The provisional velocity field (u_i^*) is updated using Eq. (6).
(2) An intermediate pressure field is computed from Eq. (11).
(3) The newly obtained pressure field is used to update the mass flux $(m_f^{*,l+1})$ using Eq. (9).
(4) If the updated mass flux satisfies $|m_f^{*,l+1}-m_f^{*,l}|<\varepsilon$, the discretized momentum equation given below as Eq. (12) is solved using the converged mass flux and the corresponding pressure field to get (u_i^{n+1}). Otherwise steps 1–3 are repeated. The tolerance limit ε is set to 10^{-5}.

$$\frac{u_{iP}^{n+1}-u_{iP}^{n}}{\Delta t}+\frac{1}{2}\left(\sum_{f} m_{f}^{n+1}u_{if}^{n+1}+\sum_{f} m_{f}^{n}u_{if}^{n}\right)=-\sum_{f} p_{f}^{n+1}n_{if}dS_{f}+\frac{1}{2}\left(\sum_{f} F_{\text{dif}}^{n+1}+\sum_{f} F_{\text{dif}}^{n}\right) \tag{12}$$

The boundary conditions used are as follows. A uniform freestream is specified in the inflow boundary. A convective boundary condition is used in the exit plane so that the vortices pass out smoothly. The convective boundary condition [13,18] is taken in the form

$$\frac{\partial u_i}{\partial n}+U_c\frac{\partial u_i}{\partial n}=0 \tag{13}$$

The convection velocity U_c is taken as the average of the velocity distribution at the exit plane. On a far field boundary, both the velocity and pressure satisfy the Neumann condition. The no-slip boundary condition for velocity and the Neumann condition for pressure are satisfied on all solid boundaries.

A schematic diagram defining the flow problem and the computational domain is shown in Fig. 3(*a*). The upstream and downstream cylinders are also referred to as cylinder 1 and cylinder 2, respectively. Both the cylinders are of equal diameter. The Reynolds numbers (Re), based on the velocity of incoming freestream (V_∞) and diameter (D) of the cylinders, are varied in the range $40\leq \text{Re}\leq 150$. For flow past an isolated cylinder, the transition to turbulence and three dimensionality occur at a Reynolds number between 190 and 200. Consequently, it is assumed that the flow about two cylinders in tandem is likely to be laminar and two dimensional for $\text{Re}\leq 150$. The normalized gap (g/D) between the cylinders is chosen to lie in the range $0.2\leq g/D\leq 4.0$.

The computational domain is discretized using 53,161 triangular cells with 26,931 nodes for $g/D=1.5$. The total numbers of cells and nodes increase slightly with gap between the cylinders. Each of the cylinders is described by 180 points. A portion of a computational grid around the cylinders is shown in Fig. 3(*b*). The computational mesh in all the cases satisfies the grid independency checks. A sample test case is presented in Fig. 4 where the pressure distribution on the cylinders at $\text{Re}=150$, $g/D=1.0$ computed on three different meshes is shown. The angle θ is measured counterclockwise from the positive x-axis. The pressure distribution shown in the figure is at the instant of peak lift coefficient on cylinder 2. The figure shows that there is no difference between

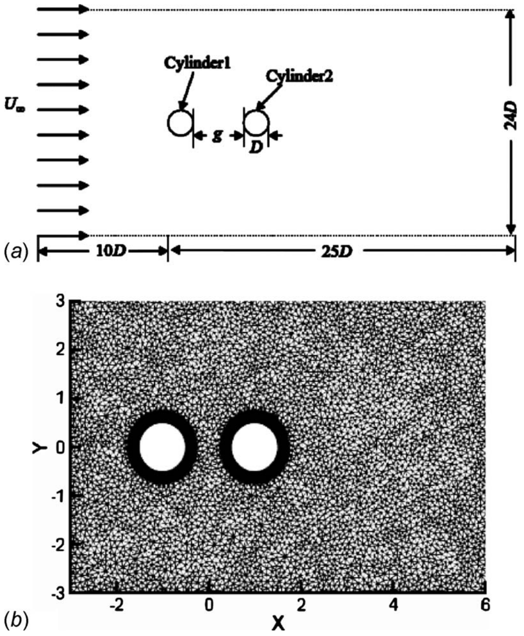

Fig. 3 (*a*) **Schematic diagram showing the flow configuration and computational domain. (*b*) Part of the computational mesh at $g/D=1.5$.**

the results computed on two meshes with 42,462 and 50,000 elements. The mesh with 50,000 elements is used for this case in order to achieve improved resolution of the vortical structure of the downstream wake.

3 Results and Discussions

The developed incompressible flow solver (IFSOL) is extensively tested for flow over an isolated cylinder before using it for two-cylinder arrangements. Typical comparisons with earlier numerical works [14,19,20] and compilation of experimental data and correlation [21] are shown in Table 1. These results are computed on a mesh consisting of 50,000 triangular cells in a rectangular domain of $35D \times 20D$. The simulations are carried out for a long time so that appropriate evolution of the flow characteristics is obtained. Long time simulations are carried out for two-cylinder cases as well.

3.1 Flow Characteristics at Re=40. The flow about two tandem cylinders at Reynolds number of 40 remains steady irrespective of the gap space. A closed wake attached to the rear face of the downstream cylinder is observed for all the gap ratios considered in the present study, namely, $g/D=0.2$, 0.7, 1.0, 1.5, 2.0, 3.0, and 4.0. The streamlines of the flow for several gap spaces are shown in Figs. 5(*a*)–5(*e*). Similar to an isolated cylinder in the steady flow regime, the shear layers of both cylinders separate and tend to merge at a downstream point on the centerline. However, Figs. 5(*a*)–5(*d*) show that closed wakes cannot form behind the upstream cylinder for $g/D \leq 3.0$ due to insufficient space in the gap. The separated shear layers of the upstream cylinder in these cases form two counter-rotating vortices above and below the centerline between the cylinders. As the gap increases to $g/D=4.0$, the space is sufficient to allow the shear layers of the upstream cylinder to merge on the centerline and a closed wake forms behind the upstream cylinder. The streamlines in Fig. 5(*e*) clearly show the wakes behind both cylinders at $g/D=4.0$. Figure 6 shows the close up views of the streamlines for two of the smaller gaps with $g/D=0.2$ and 1.5. The figure shows the characteristics of the gap flows for small gap sizes. The upper shear layer of the upstream cylinder divides on striking the front face of the downstream cylinder and a part of it turns toward the lower surface of the upstream cylinder and merges with the lower shear layer of the upstream cylinder. Thus, two counter-rotating vortices are formed in the gap. The upper and lower rotational zones in the gap are attached to the upstream and downstream cylinders, respectively. However, the opposite may also occur as the flow is symmetric about the centerline and should have no bias. It is also observed that the separation points on the rear cylinder shift downstream

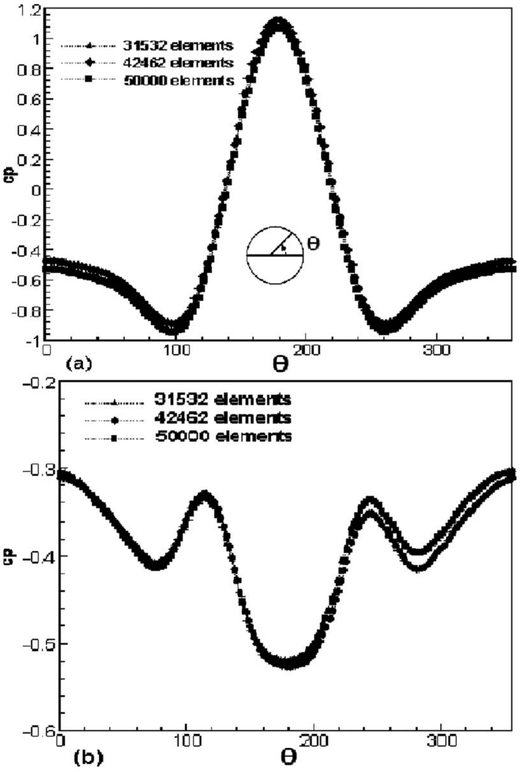

Fig. 4 Pressure distribution on the surface of the cylinders at Re=100, $g/D=1.0$ during peak C_l on cylinder 2; (*a*) cylinder 1 and (*b*) cylinder 2

Table 1 Comparison of force coefficients and Strouhal number at Re=100 and 200 for an isolated cylinder

	$C_{d_{\text{mean}}}$		$C_{l_{\text{rms}}}$		St	
	Re=100	Re=200	Re=100	Re=200	Re=100	Re=200
Zhou et al. [18]	1.474	1.320	0.219	-	0.163	0.192
Liu et al. [19]	1.350	1.31	0.235	0.487	0.164	0.192
Ding et al. [14]	1.356	1.348	0.202	0.467	0.166	0.196
Compilation in Ref. [21]	1.4	1.3			0.167	0.189
Present	1.431	1.337	0.226	0.474	0.165	0.195

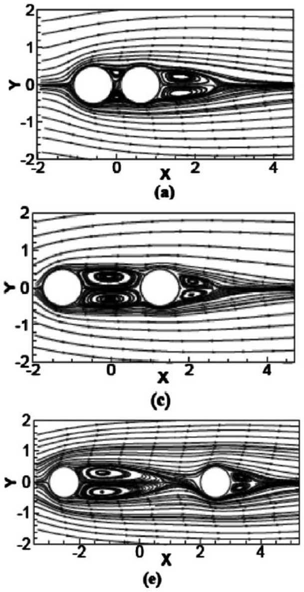

Fig. 5 Streamlines at Re=40 for different gap sizes: (*a*) *g*/*D* =0.2, (*b*) *g*/*D*=0.7, (*c*) *g*/*D*=1.5, (*d*) *g*/*D*=3.0, and (*e*) *g*/*D*=4.0

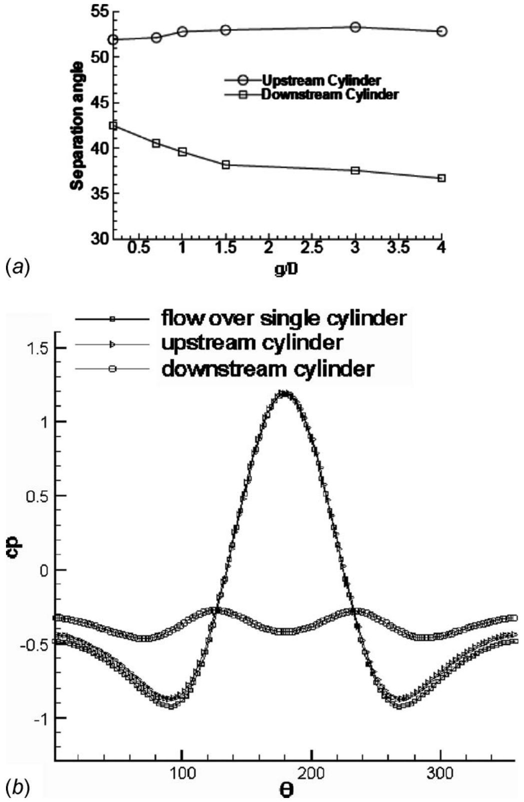

Fig. 7 (*a*) Variation in the separation point with normalized gap at Re=40. (*b*) Comparison of pressure distribution on a pair of cylinders in tandem (*g*/*D*=1.0) and on an isolated cylinder at Re=40

with increasing gap, while they remain more or less fixed on the upstream cylinder. Hence, the wake region of the rear cylinder reduces as the gap increases.

Figure 7(*a*) shows the locations of the separation points on the cylinders for different gap sizes. The location is specified in terms of the angle measured counterclockwise from the positive *x*-axis. The separation points on the front cylinder remain fixed around ±52 deg indicating a marginal downstream shift compared with an isolated cylinder where the points are at about ±53.5 deg [21]. The separation point on an isolated cylinder computed by the present method (±53.3 deg) agrees well with the experimental value. Thus the recirculating zone behind the upstream cylinder is nearly identical to an isolated cylinder. However, the separation points move downstream on the rear cylinder with increasing gap. The shift is faster at small gaps ($g/D \leq 1.5$). The pressure distribution on the upstream cylinder at $g/D=1.0$, presented in Fig. 7(*b*), reveals that the pressure on the upstream cylinder is almost identical to that on an isolated cylinder with marginal difference in the base pressure. The stagnation and base pressure values for an isolated cylinder, about 1.18 and −0.52 respectively, agree well with compilation of experimental data [21]. The vorticity contours are symmetric about the centerline and the lift coefficient of both cylinders is zero irrespective of the gap as expected for flows in the symmetric steady state regime.

The drag coefficients also show the steady state behavior. The drag coefficient of the upstream cylinder does not change appreciably with gap size and is close to that of an isolated cylinder (about 1.5). The drag coefficient of the rear cylinder is considerably smaller in all the cases. Figure 8 shows negligible decrease in the drag coefficient of the upstream cylinder but considerable increase on the downstream cylinder when the gap is increased. The variation in the drag coefficient can be attributed to the nature of the gap flow and movement of the separation points. The vortices in the gap create suction on the forward face of the rear cylinder and on the rear face of the front cylinder. The suction almost nullifies the other contributions to the drag force on the downstream cylinder when the gap is very small. With increasing gap, the forward suction reduces and suction on the rear face increases causing the drag coefficient to increase gradually. However, the upstream cylinder, irrespective of the gap size, experiences a large drag force as it is subjected to positive and negative gauge pressure on the front and the rear face (gap side) as in case of an isolated cylinder. The changes in pressure on the pressure and suction sides with gap size nearly cancel each other, so that the

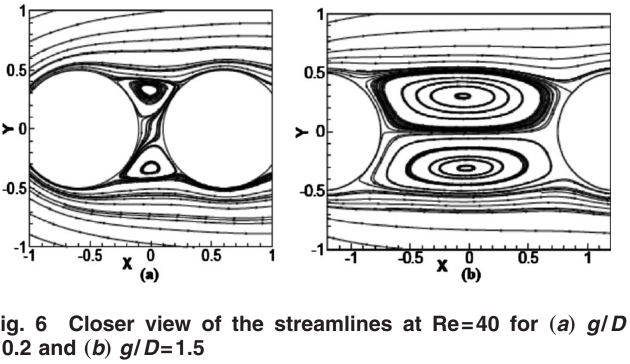

Fig. 6 Closer view of the streamlines at Re=40 for (*a*) *g*/*D* =0.2 and (*b*) *g*/*D*=1.5

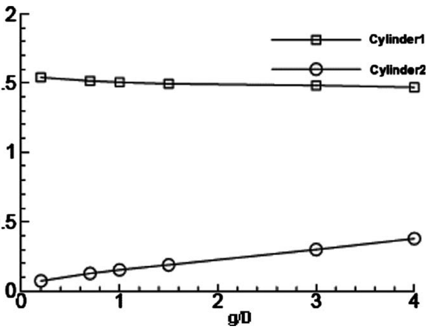

Fig. 8 Variation in drag coefficient with normalized gap at Re =40

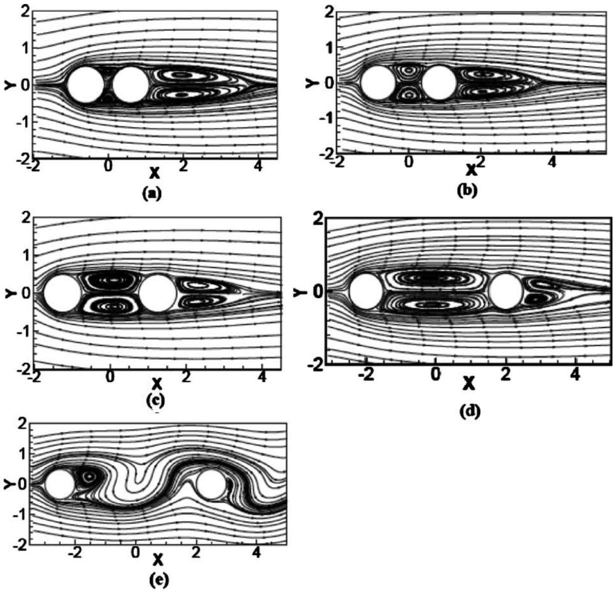

Fig. 9 Streamlines at Re=70 for different gap sizes: (*a*) $g/D=0.2$, (*b*) $g/D=0.7$, (*c*) $g/D=1.5$, (*d*) $g/D=3.0$, and (*e*) $g/D=4.0$

stagnation region pressure as well as base pressure remains almost unchanged. Consequently, the drag coefficient does not change appreciably. The fixed location of the separation points, nearly identical to an isolated cylinder, also supports the observation.

3.2 Flow Characteristics at Re=70. Flow past an isolated cylinder at Reynolds number of 70 is unsteady with a Karman vortex street wake. However, for two cylinders in tandem, the flows at this Reynolds number attain steady state when the gap is small with $g/D \leq 2.0$. The streamline patterns for the cases $g/D=0.2$, 0.7, and 1.5 are shown in Figs. 9(*a*)–9(*c*), respectively. The numerical flow visualization indicates that the flow characteristics in the gap and in the wake of the rear cylinder are similar to those at Reynolds number of 40. As g/D increases to 3.0, the shedding of vortices from the downstream cylinder just initiates, as seen in Fig. 9(*d*). There is no shedding from the upstream cylinder and the gap flow characteristics remain identical to the lower spacing cases. A different type of flow is observed for $g/D=4.0$, as seen in Fig. 9(*e*). Both the cylinders now shed vortices and consequently the wakes of both cylinders are unsteady. It is also seen that the separated region on the rear face of the downstream cylinder is considerably narrow. The vorticity contours are found to be symmetric about the centerline for the flows with $g/D=0.2$, 0.7, and 1.5, i.e., when the flows are steady. These contours are shown in Figs. 10(*a*)–10(*c*). Figure 10(*d*) shows a slightly asymmetric wake pattern for $g/D=3.0$. The asymmetric wake pattern for this case is confirmed from the pressure contours presented in Fig. 11. The constant pressure lines are asymmetric in the downstream for $x/D>6$. It may be concluded that the flow undergoes a transition from the steady to the unsteady regime at this particular spacing, i.e., the critical normalized spacing is about 3.0. The value compares satisfactorily with the experimental findings [3,4,6] at higher Reynolds numbers. The vorticity contours in Fig. 10(*e*), which represents an unsteady flow corresponding to $g/D=4.0$, reveal that the vortices shed from the upstream cylinder impinge on the downstream cylinder.

The time dependent lift and drag coefficients for $g/D=3.0$ and 4.0 are shown in Figs. 12(*a*) and 12(*b*). A very small amplitude periodic lift coefficient is observed on the downstream cylinder for $g/D=3.0$ and periodic lift and drag coefficients on both cylinders are observed for $g/D=4.0$. The amplitude of the lift coefficient on the downstream cylinder is found to be considerably larger than that on the upstream cylinder. Figure 12(*c*), which is a

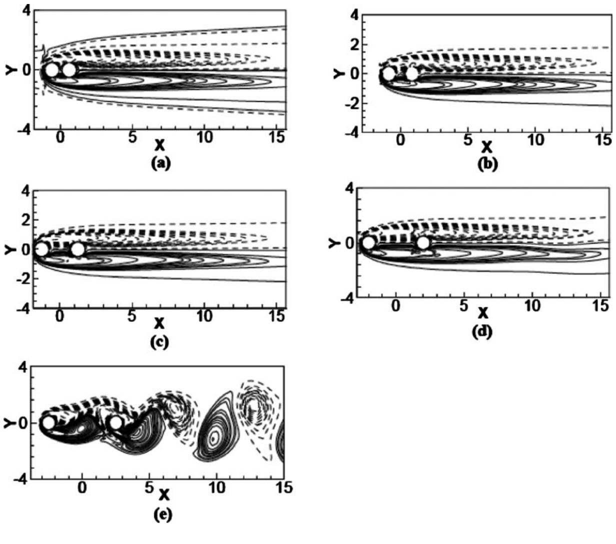

Fig. 10 Vorticity contours at Re=70 for different gap sizes: (*a*) $g/D=0.2$, (*b*) $g/D=0.7$, (*c*) $g/D=1.5$, (*d*) $g/D=3.0$, and (*e*) $g/D=4.0$

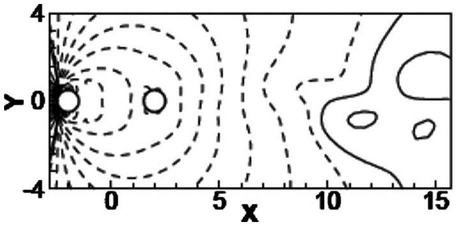

Fig. 11 Pressure contours at Re=70, $g/D=3.0$

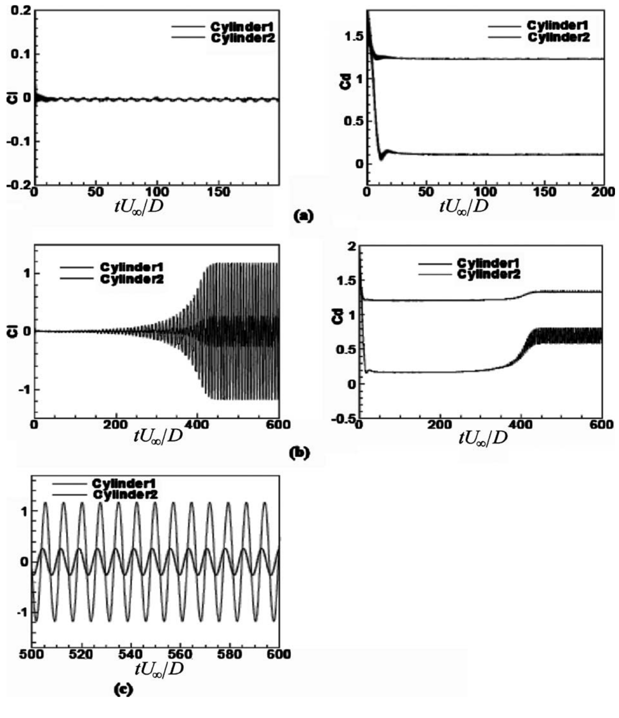

Fig. 12 Time dependent lift (left column) and drag (right column) coefficients at Re=70 for different gaps: (*a*) $g/D=3.0$ and (*b*) $g/D=4.0$; (*c*) close view of the case $g/D=4.0$

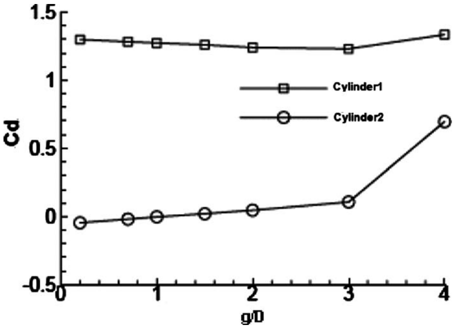

Fig. 13 Variation in mean drag coefficient on the cylinders with normalized gap at Re=70

part of Fig. 12(*b*), presents the variations in lift coefficients for the two cylinders for a shorter duration. The figure shows that vortex-shedding frequencies for the two cylinders are identical and the shedding off the cylinders is synchronized. However, the shedding off the cylinders differs in phase by about $\pi/3$. The mean drag coefficients on the upstream cylinder differ significantly from the drag coefficients on the downstream cylinder, as seen in Fig. 13. The drag coefficient of the upstream cylinder changes nominally with the normalized gap. The downstream cylinder drag coefficient increases marginally with the gap size up to $g/D=3.0$ and subsequently increases very rapidly. Since negative gauge pressure acts on the downstream cylinder from both sides, the mean drag on this cylinder is substantially less. The suction on the downstream cylinder is found to increase with a decrease in gap. Consequently, the negative contribution to the drag of the downstream cylinder increases with a decrease in gap. At the Reynolds number of 70, the negative contribution exceeds the other positive contributions for the smaller gap ratios $g/D=0.2$, 0.7, and 1.0. The corresponding drag coefficients of the rear cylinder are found to be −0.0456, −0.0191, and −0.0021, respectively. A drastic change in the mean drag coefficient of the rear cylinder is observed at $g/D=4.0$ because the suction on the front greatly reduces as the flow undergoes a change from steady to unsteady regime.

3.3 Flow Characteristics at Re=100. With the Reynolds number increased to 100, the downstream cylinder sheds vortices irrespective of the gap size and the wake flow downstream of the second cylinder is unsteady for all the cases. However, there is no distinct shedding from the upstream cylinder for lower values of the gap with $g/D\leq 2.0$. This agrees well with various experimental and numerical predictions [3,4,6,9,13]. The vorticity contours of the flows at $g/D=0.2$, 0.7, 1.5, and 3.0 are presented in Figs. 14(*a*)–14(*d*). The flows at $g/D=0.2$, 0.7, and 1.5, as seen in Figs. 14(*a*)–14(*c*), are characterized by an elongated vortex in the near wake region. The vorticity generated on the downstream cylinder is enveloped by a vortex from the upstream cylinder and a highly elongated vortex is formed before shedding. The length of this vortex is about $15D$ for $g/D=1.5$. As the gap increases in the range $0.2\leq g/D\leq 1.5$, the distance between the downstream vortices increases. As shown in Fig. 14(*d*), at $g/D=3.0$, the upstream cylinder shed vortices onto the downstream cylinder and vortex shedding similar to "Karman vortex street" occur from the downstream cylinder. At $g/D=4.0$ (not shown here), the Karman vortex street is more clearly defined. The shedding off the two cylinders is synchronized nearly in antiphase where one cylinder sheds a vortex from the upper side and the other cylinder sheds a vortex of opposite sense from the bottom side.

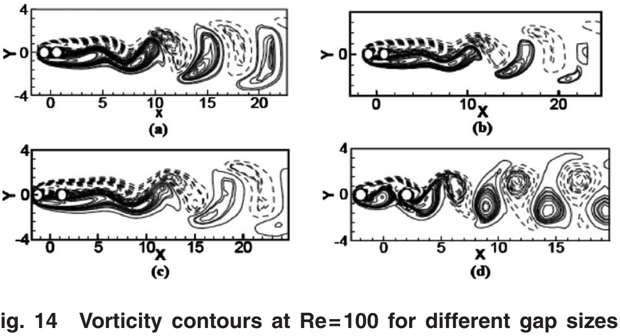

Fig. 14 Vorticity contours at Re=100 for different gap sizes: (*a*) $g/D=0.2$, (*b*) $g/D=0.7$, (*c*) $g/D=1.5$, and (*d*) $g/D=3.0$

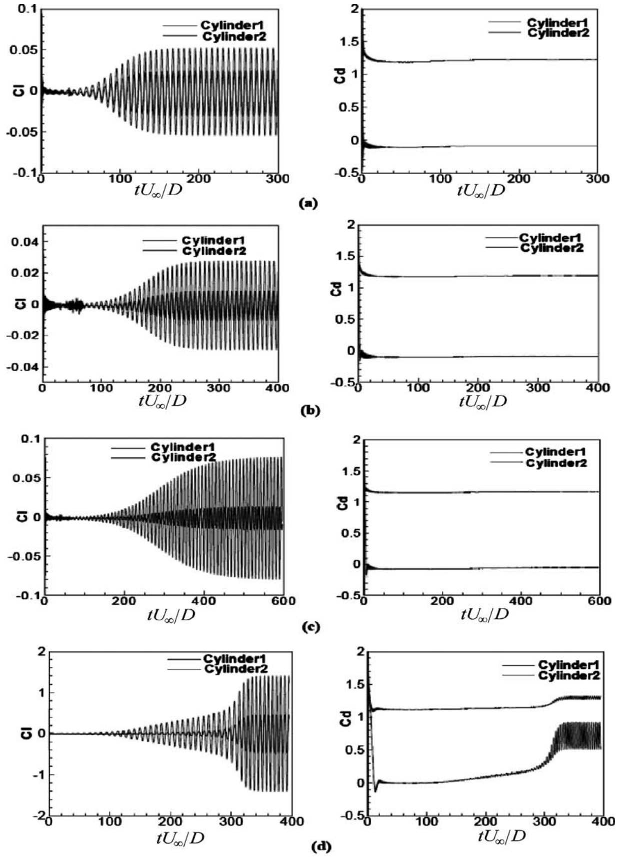

Fig. 15 Time dependent lift (left column) and drag (right column) coefficients at Re=100: (*a*) $g/D=0.2$, (*b*) $g/D=0.7$, (*c*) $g/D=1.5$, and (*d*) $g/D=3.0$

Figure 15 shows the time dependent lift and drag coefficients for different gap sizes. The upstream cylinder experiences considerably larger mean drag but the fluctuation in drag is larger on the downstream cylinder. The root mean squared (rms) lift coefficient is significantly larger on the downstream cylinder. Thus, the rear cylinder experiences larger fluctuating forces in both streamwise and cross flow directions. The lift coefficient of each cylinder consists of a single frequency and the nondimensional frequency (Strouhal number) for the two cylinders is identical. The two lift coefficients are, however, almost out of phase. A small negative drag force acts on the rear cylinder for $g/D\leq 1.5$, but this attraction toward the front cylinder ceases for $g/D\geq 3.0$ when the vortex shedding starts from the front cylinder as well. The magnitudes of the negative drag coefficient for $g/D\leq 1.5$ are significantly smaller than the measured values at higher Reynolds numbers. The numerical simulation due to Ding et al. [14] shows that the amplitude of lift coefficient at $g/D=1.5$ gradually decays with time and the fluctuation becomes extremely small after the nondimensional time of 300. Thus, the vortex shedding off the downstream cylinder ceases after some time. However, a steady

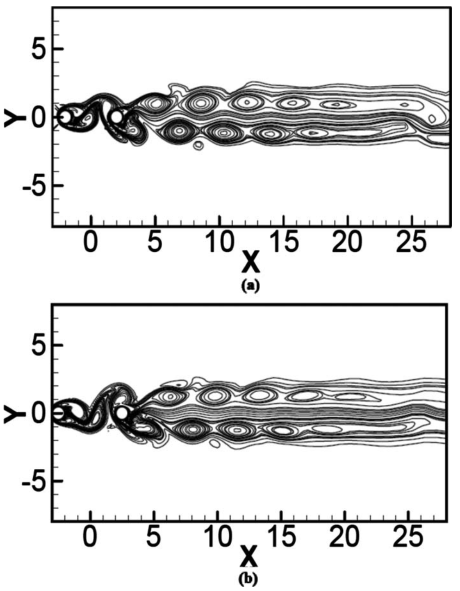

Fig. 16 Vorticity contours at Re=150; (*a*) *g*/*D*=3.0 and (*b*) *g*/*D*=4.0

state fluctuation is observed in the present simulation up to the nondimensional time of 600 indicating a continued vortex shedding. Steady state fluctuations are also observed for smaller values of g/D. This observation agrees with Sharman et al. [13] who have shown distinct vortex shedding from the downstream cylinder at $g/D=1.0$ with a Strouhal number of about 0.122. The Strouhal number predicted here agrees well with this value.

3.4 Flow Characteristics at Re=120 and 150. The flow structures for different gap ratios at Reynolds number 120 are almost identical to the corresponding cases at Re=100 except marginal improvement in the organization of the vortex structure in the unsteady wake regime for $g/D \geq 3.0$. The flow patterns are not presented here for brevity. Similarly, the basic flow patterns at Re=150 remain the same for $g/D \leq 2.0$. However, a different kind of vortex structure is observed when $g/D \geq 3.0$, as shown in Figs. 16(*a*) and 16(*b*). The downstream vortices are arranged in two rows of counter-rotating vortices with decreased longitudinal (streamwise) and increased lateral (cross-stream) separations, due to simultaneous shedding from the two cylinders and merging of similar smaller vortices. The lateral spacing between the two rows of vortices is greatly increased and the ratio of the lateral to longitudinal spacing becomes quite high. The value is about 0.65 for $g/D=3.0$. This is larger than the linear stability limit of two rows of opposite-signed vortices. The Karman limit for linear stability of an inviscid array of point vortices [21,22] is 0.28 and the limit is 0.4 for an array of finite vortices [23]. Thus, this vortex street is inherently unstable. This is indicated in the snapshots of vorticity contours presented in Figs. 16(*a*) and 16(*b*). However, the computational domain (Fig. 3(*a*)) seems to be not long enough to capture the instability process completely.

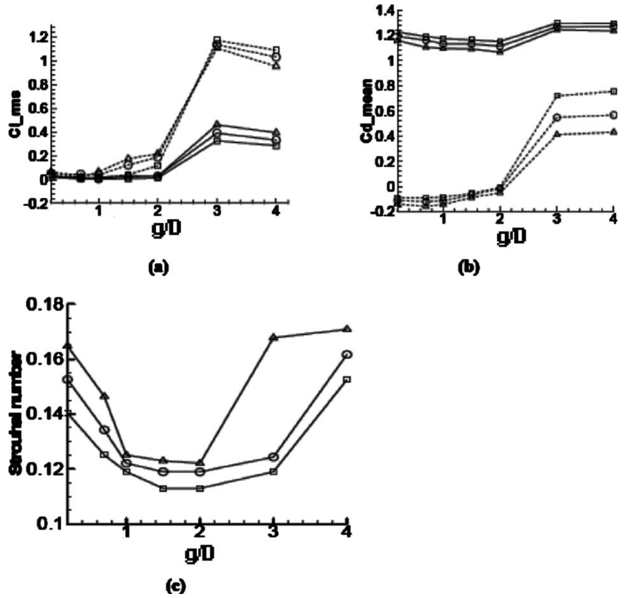

Fig. 17 Variation in flow parameters with nondimensional gap: (*a*) root mean squared lift coefficient; (*b*) mean drag coefficient; the dotted and solid lines represent downstream and upstream cylinders, respectively; and (*c*) Strouhal number for downstream cylinder. The symbols "□," "○," and "△" denotes Re =100, 120, and 150, respectively.

3.5 Variation of the Flow Parameters With Gap at Different Reynolds Numbers. Figures 17(*a*)–17(*c*) shows the variation in rms lift coefficient ($C_{l_{\mathrm{rms}}}$), mean drag coefficient ($C_{d_{\mathrm{mean}}}$), and Strouhal number at Re=100, 120, and 150 with normalized gap spacing. The parameters in each case are computed over all the complete cycles during the last 100 nondimensional time interval. The predicted values agree reasonably with the solutions of Sharman et al. [13] and Ding et al. [14]. A few comparisons are shown in Table 2. It is seen from Fig. 17(*a*) that $C_{l_{\mathrm{rms}}}$ remains fixed at zero on the upstream cylinder (solid line) and marginally increases with gap on the downstream cylinder for $g/D \leq 2.0$. The rms lift coefficients on both cylinders increase greatly as g/D is increased from 2.0 to 3.0. The value increases from nearly 0.1 to about 1.15 on the rear cylinder, while it increases from zero to about 0.3 on the front cylinder at Re=100. The lift coefficients (rms) then decrease slightly as g/D increases to 4.0. It is also observed that the rms lift coefficient on the downstream cylinder is higher than that on the upstream cylinder for $g/D \geq 2.0$. Figure 17(*b*) shows variation in the mean drag coefficient with gap. It is seen that the mean drag coefficient on the downstream cylinder has small negative values, while it has large positive values on the upstream cylinder when $g/D \leq 2.0$. As g/D increases to 3.0, the mean drag coefficient increases on both cylinders. However, the increase is drastic on the downstream cylinder. The mean drag coefficient remains nearly constant on both cylinders for $g/D \geq 3.0$. It is also observed that the mean drag coefficient on the upstream cylinder is

Table 2 Comparison of global parameters for two tandem cylinders at Re=100

			$C_{d_{\mathrm{mean}}}$		$C_{l_{\mathrm{rms}}}$		St
	g/D	Re	Cylinder 1	Cylinder 2	Cylinder 1	Cylinder 2	(Cylinder 2)
Ding et al. [14]	1.5	100	1.163	−0.0895	0	0	-
Present study	1.5	100	1.176	−0.0796	0	0.08	0.113
Sharman et al. [13] (read from graph)	4.0	100	1.3	0.66	0.26	0.97	0.15
Present study	4.0	100	1.288	0.724	0.257	1.053	0.152

much higher in each of the cases considered. Both lift and drag coefficients on the downstream cylinder are highly affected when this cylinder lies directly in the unsteady wake of the upstream cylinder.

When distinct shedding from both cylinders occurs, Strouhal numbers of the cylinders are found to be the same confirming a synchronized vortex shedding from the cylinders. Figure 17(*c*) presents the variation in Strouhal number with nondimensional gap for the downstream cylinder. The variation at each Reynolds number takes approximately the "u" shape in the range $0.2 \leq g/D \leq 4.0$. As g/D increases, the Strouhal number initially decreases to reach the minimum value at $g/D=1.5$ and then remain constant up to $g/D=2.0$. Subsequently, it increases again to approach the value for an isolated cylinder. For $g/D \geq 3.0$, when vortex shedding occurs from both cylinders, the Strouhal number found to be quite close to that of an isolated cylinder. The figure shows that Strouhal number increases very rapidly as the gap ratio changes from 3.0 to 4.0 for Reynolds numbers of 100 and 120, and from 2.0 to 3.0 for Reynolds number of 150. This suggests that the critical spacing for Re=150 is little less than 3.0, while it is about 3.0 for Re=100 and 120.

It is shown in Fig. 18 that the computed Strouhal number data in the chosen parameter space collapses reasonably when plotted against the parameter $\mathrm{Re}^{1/2}\,\bar{g}^{4/5}$ about the curve $\mathrm{St}=1.6 \times 10^{-4}(\mathrm{Re}^{1/2}\ \bar{g}^{4/5})^2-5.5\times10^{-3}(\mathrm{Re}^{1/2}\ \bar{g}^{4/5})+0.16$, where $\bar{g}=g/D$. It should also be noted that there is no vortex shedding off the upstream cylinder for small values of gap and the Strouhal number applies to the downstream cylinder only. The Strouhal number applies to both cylinders for larger gaps. Similarly, the mean drag coefficient on the upstream cylinder can be approximated by the linear relation $(C_{d_{\mathrm{mean}}})^{1/3}=1.82\times10^{-4}\ \mathrm{Re}^{2/3}\ \bar{g}^{3/2}+1.043$. The matching is shown in Fig. 19. The drag coefficient on the downstream cylinder for the range of Reynolds numbers and gaps could not be approximated satisfactorily by a simple relation that reflects the trends. However, a reasonable approximation is shown in Fig. 19 where two different linear relations are used over two different ranges of the parameter $\mathrm{Re}^{2/3}\ \bar{g}^{3/2}$. The approximation is given by $(C_{d_{\mathrm{mean}}})^{1/3}=2.9\times10^{-3}\ \mathrm{Re}^{2/3}\ \bar{g}^{3/2}-0.518$ for $0 < \mathrm{Re}^{2/3}\ \bar{g}^{3/2} \leq 90$ and $(C_{d_{\mathrm{mean}}})^{1/3}=-6.0\times10^{-4}\ \mathrm{Re}^{2/3}\ \bar{g}^{3/2}+0.923$ for $\mathrm{Re}^{2/3}\ \bar{g}^{3/2} \geq 100$. A reasonable approximation that reflects the important trends over the ranges of selected Reynolds numbers and gaps can also be achieved through the following cubic relation (not shown in figure):

$$(C_{d_{\mathrm{mean}}})^{1/3} = -\,7.0\times10^{-7}(\mathrm{Re}^{2/3}\ \bar{g}^{3/2})^3 + 2\times10^{-4}(\mathrm{Re}^{2/3}\ \bar{g}^{3/2})^2 - 0.006\ \mathrm{Re}^{2/3}\ \bar{g}^{3/2} - 0.46$$

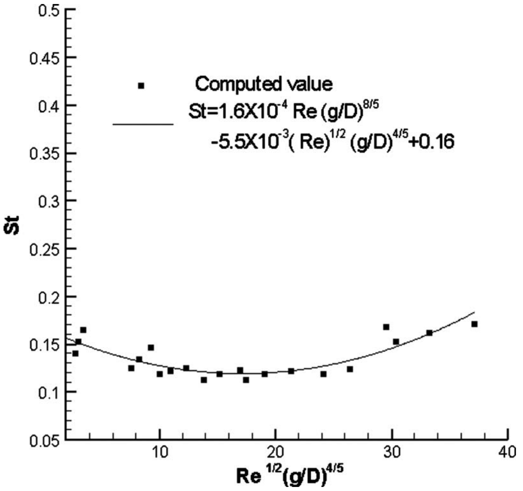

Fig. 18 Strouhal number versus $\mathrm{Re}^{1/2}(g/D)^{4/5}$ plot

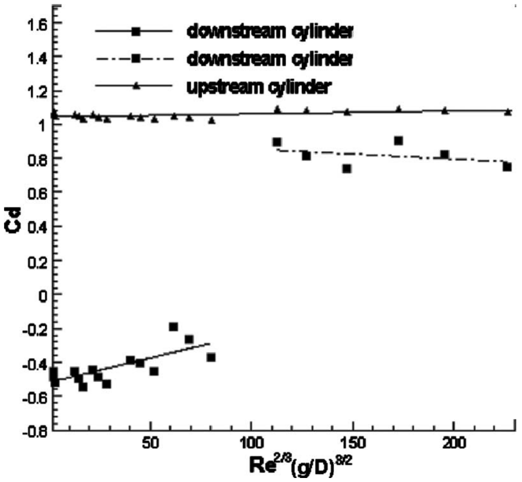

Fig. 19 Mean drag coefficient of the cylinders versus $\mathrm{Re}^{2/3}(g/D)^{3/2}$ plot

To see the effect of larger gap on the flow field, simulation was carried out for a case at Re=100, $g/D=8.0$. Similar to $g/D=3.0$ and 4.0, shedding off both the cylinders in this case is synchronized. The Strouhal number reaches a value of 0.164, identical to an isolated cylinder. The unsteady wake of the upstream cylinder gets more space to develop at this larger gap and the flow about the upstream cylinder is similar to flow past an isolated cylinder. The mean drag coefficient and rms lift coefficient for the upstream cylinder become 1.374 and 0.24, respectively. The values are very close to the isolated cylinder values. On the downstream cylinder, the fluctuations and, hence, rms lift coefficient reduce considerably compared with $g/D=3.0$ and 4.0. The mean drag coefficient increases marginally. The corresponding values are $C_{d_{\mathrm{mean}}}=0.78$ and $C_{l_{\mathrm{rms}}}=0.74$. This shows that even at a large separation between the cylinders, the downstream cylinder experiences large fluctuating lift force.

4 Conclusions

Numerical studies on flow past two tandem cylinders have been carried out over a range of Reynolds numbers $40 \leq \mathrm{Re} \leq 150$. The Reynolds numbers are chosen so that the wake flows can be assumed two dimensional and laminar. The nondimensional gap (g/D) between the cylinders is varied over a wide range $0.2 \leq g/D \leq 4.0$ for each Reynolds number. The flow characteristics depend strongly on both Re and g/D. At Re=40, the flows remain steady with closed wakes irrespective of the gap. At Re=70, the wake flows remain steady for $g/D \leq 2.0$ but become unsteady for $g/D \geq 3.0$. The wake flows are found to be unsteady for all g/D considered at $\mathrm{Re} \geq 100$ but without distinct shedding from the upstream cylinder when $g/D \leq 2.0$. The unsteady flows at lower gaps $(g/D \leq 2.0)$ are characterized by formation of long vortices behind the downstream cylinder due to vortex enveloping. At higher g/D, the shed vortices from the upstream cylinder impinge on the downstream cylinder and vortex streets similar to the Karman vortex street develop behind the downstream cylinder.

It is observed that the mean drag coefficient is much higher on the upstream cylinder in steady and in unsteady flow cases. However, fluctuations in both lift and drag coefficients are significantly higher on the downstream cylinder. The mean drag coefficients and root mean squared lift coefficients for $\mathrm{Re} \geq 100$ experience a large increase as g/D increases from 2.0 to 3.0. For the closely spaced cylinders with $g/D \leq 2.0$, a small negative drag force acts on the downstream cylinder, i.e., the rear cylinder feels a force of attraction toward the front cylinder. The magnitude of the negative drag coefficient increases with Reynolds number. The negative force changes to large positive drag force as the spacing becomes sufficient to allow distinct vortex shedding from the front cylinder. Strouhal number (St) initially decreases when g/D increases up to 1.0, remains approximately constant up to $g/D=2.0$, and increases subsequently. Strouhal numbers of both cylinders are almost equal suggesting a synchronized vortex shedding from the cylinders. For larger gaps with $g/D \geq 4.0$, Strouhal numbers of the two cylinders are very close to the Strouhal number of an isolated cylinder.

All the flow parameters change drastically at $g/D=3.0$. It is also observed that vortices from the upstream cylinder envelop the vortices of the downstream cylinder to form highly elongated vortices prior to their shedding off the downstream cylinder for $g/D \leq 2.0$. The wake changes to a nearly Karman vortex street type wake at $g/D=3.0$. The drastic changes in the flow parameters may be attributed to transition from steady to unsteady wake flow at about $g/D=3.0$.

In the unsteady flow regime, the mean drag coefficients and Strouhal number are found to correlate with $\mathrm{Re}^{2/3}(g/D)^{3/2}$ and $\mathrm{Re}^{1/2}(g/D)^{4/5}$, respectively. At large separating distance, there are practically no interference effects on the upstream cylinder. The fluctuations on the downstream cylinder decrease considerably but still remain quite significant.

References

[1] Oka, S., Kostic, Z. G., and Sikmanovic, S., 1972, “Investigation of the Heat Transfer Processes in Tube Banks in Cross Flow,” International Seminar on Recent Developments in Heat Exchangers, Trogir, Yugoslavia.

[2] Jendrzejczyk J. A., and Chen, S. S., 1986, “Fluid Forces on Two Circular Cylinders in Cross Flow,” PVP (Am. Soc. Mech. Eng.), **104**, pp. 1–13.

[3] Zdravkovich M. M., 1977, “Review of Flow Interference Between Two Circular Cylinders in Various Arrangements,” ASME J. Fluids Eng., **99**(4), pp. 618–633.

[4] Zdravkovich, M. M., 1987, “The Effects of Interference Between Circular Cylinders in a Cross Flow,” J. Fluids Structures, **1**, pp. 239–261.

[5] Kiya, M., Mochizuki, O., Ido, Y., Suzuki, T., and Arai, T., 1993, “Flip-Flopping Flow Around Two Bluff Bodies in Tandem Arrangement,” *Bluff-body Wakes, Dynamics and Instabilities*, IUTAM Symposium 1992, Springer-Verlag, Berlin, pp. 15–18.

[6] Chen, S. S., 1987, *Flow Induced Vibrations of Circular Cylindrical Structures*, Hemisphere, New York.

[7] Li, J., Chambarel, A., Donneaud, M., and Martin, R., 1991, “Numerical Study of Laminar Flow Past One and Two Cylinders,” Comput. Fluids, **19**(2), pp. 155–170.

[8] Johnson, A. A., Tezduyar, T. E., and Liou, J., 1993, “Numerical Simulation of Flows Past Periodic Arrays of Cylinders,” Comput. Mech., **11**, pp. 371–383.

[9] Mittal, S., Kumar, V., and Raghuvashi, A., 1997, “Unsteady Incompressible Flows Past Two Cylinders in Tandem and Staggered Arrangement,” Int. J. Numer. Methods Fluids, **25**, pp. 1315–1344.

[10] Farrant, T., Tan, M., and Price, W. G., 2001, “A Cell Boundary Element Method Applied to Laminar Vortex Shedding From Circular Cylinders,” Comput. Fluids, **30**, pp. 211–236.

[11] Hall, J. W., Ziada, S., and Weaver, D. S., 2003, “Vortex Shedding From Single and Tandem Cylinders in the Presence of Applied Sound,” J. Fluids Struct., **18**, pp. 741–758.

[12] Meneghini, J. R., Saltara, F., Siqueira, C. L. R., and Ferrari, J. A., Jr., 2001, “Numerical Simulation of Flow Interference Between Two Circular Cylinders in Tandem and Side-by-Side Arrangements,” J. Fluids Struct., **15**, pp. 327–350.

[13] Sharman, B., Lien, F. S., Davidson, L., and Norberg, C., 2005, “Numerical Predictions of Low Reynolds Number Flows Over Two Tandem Circular Cylinders,” Int. J. Numer. Methods Fluids, **47**, pp. 423–447.

[14] Ding, H., Shu, C., Yeo, K. S., and Xu, D., 2007, “Numerical Simulation of Flows Around Two Circular Cylinders by Mesh-Free Least Square Based Finite Difference Methods,” Int. J. Numer. Methods Fluids, **53**, pp. 305–332.

[15] Rhie, C. M., and Chow, W. L., 1983, “A Numerical Study of the Turbulent Flow Past an Isolated Airfoil With Trailing Edge Separation,” AIAA J., **21**, pp. 1525–1532.

[16] Leonard, B. P., 1979, “A Stable and Accurate Convective Modeling Procedure Based on Quadratic Upstream Interpolation,” Comput. Methods Appl. Mech. Eng., **19**, pp. 59–98.

[17] Holmes D. G., and Connel S. D., 1989, “Solution of 2D Navier-Stokes Equations on Unstructured Adaptive Grids,” AIAA Paper No. 89-1932-CP.

[18] Kang, S., 2003, “Characteristics of Flow Over Two Circular Cylinders in a Side-by-Side Arrangement at Low Reynolds Numbers,” Phys. Fluids, **15**, pp. 2486–2498.

[19] Zhou, C. Y., So, R. M. C., and Lam, K., 1999, “Vortex-Induced Vibration of an Elastic Circular Cylinder,” J. Fluids Struct., **13**, pp. 165–189.

[20] Liu, C., Zheng, X., and Sung, C. H., 1998, “Preconditioned Multigrid Methods for Unsteady Incompressible Flows,” J. Comput. Phys., **139**, pp. 35–49.

[21] Zdravkovich, M. M., 1997, *Flow Around Circular Cylinders, Volume 1: Fundamentals*, Oxford University Press, New York.

[22] Newman, D. J., and Karniadakis, G. E., 1997, “A Direct Numerical Simulation Study of Flow Past a Freely Vibrating Cable,” J. Fluid Mech., **344**, pp. 95–136.

[23] Saffman, P. G., and Schatzman, J. C., 1982, “Stability of a Vortex Street of Finite Vortices,” J. Fluid Mech., **117**, pp. 171–185.

Vorticity Dynamics in Axial Compressor Flow Diagnosis and Design—Part II: Methodology and Application of Boundary Vorticity Flux

Qiushi Li

Hong Wu

Ming Guo

National Key Laboratory on Aero-Engines,
School of Jet Propulsion,
Beihang University,
Beijing 100083, China

Jie-Zhi Wu
State Key Laboratory for Turbulence and Complex Systems,
College of Engineering,
Peking University,
Beijing 100871, China;
University of Tennessee Space Institute,
Tullahoma, TN 37388

*In a companion paper (2008, "Vorticity Dynamics in Axial Compressor Flow Diagnosis and Design," ASME J. Fluids Eng., **130**, p. 041102), a study has been made on the critical role of circumferential vorticity (CV) in the performance of axial compressor in through-flow design (TFD). It has been shown there that to enhance the pressure ratio, the positive and negative CV peaks should be pushed to the casing and hub, respectively. This criterion has led to an optimal TFD that indeed improves the pressure ratio and efficiency. The CV also has great impact on the stall margin as it reflects the end wall blockage, especially at the tip region of the compressor. While that work was based on inviscid and axisymmetric theory, in this paper, we move on to the diagnosis and optimal design of fully three-dimensional (3D) viscous flow in axial compressors, focusing on the boundary vorticity flux (BVF), which captures the highly localized peaks of pressure gradient on the surface of the compressor blade, and thereby signifies the boundary layer separation and dominates the work rate done to the fluid by the compressor. For the 2D cascade flow we show that the BVF is directly related to the blade geometry. BVF-based 2D and 3D optimal blade design methodologies are developed to control the velocity diffusion, of which the results are confirmed by Reynolds-averaged Navier–Stokes simulations to more significantly improve the compressor performance than that of CV-based TFD. The methodology enriches the current aerodynamic design system of compressors.* [DOI: 10.1115/1.4000650]

1 Introduction

The theory of boundary vorticity dynamics was developed by the one of the present authors Wu and co-workers [1–4]. A key concept of the theory is the boundary vorticity flux (BVF), which was first introduced by Lighthill [5] as the measure of vorticity creation rate at a solid boundary, which is, in turn (viewed in a frame of reference fixed to the solid surface), dominated by the tangential pressure gradient. Thus, the BVF is both an on-wall signature of the global flow field and a major root of the vortical structures of the flow. At large Reynolds numbers, its distribution is highly localized. The boundary vorticity dynamics theory further reveals that the BVF provides a convenient criterion for two- or three-dimensional boundary-layer separation; and at arbitrary Re, the integrals of BVF moments over any closed or open surface precisely yield the total force and moment acting on the surface by the surrounding viscous and compressible flow. Because of the highly localized nature and the fact that the most effective management of a vortical flow is to control its generation [1], the boundary vorticity dynamics may find wide applications in various complex flow diagnosis, optimal configuration design, and flow control. The early applications were focused on external flow problems [2,6].

The first successful application to internal flow was due to Li and Guo [7]. Their compressor flow data obtained by Reynolds-averaged Navier–Stokes (RANS) simulation indicated a strong correlation of the circumferential vorticity distribution on he compressor's exit cross-sectional plane and its pressure ratio, efficiency, and stall margin. Thus, Li and Guo traced the observed vortical structures back to the BVF distribution on the surfaces of blades, hub, and casing, which guided them to reform the blade to increase its loading capability and suppress flow separation, especially at off-design points. The stall margin of the compressor was thereby significantly expanded. But in this work, no theoretical interpretation regarding the strong correlation of the circumferential vorticity and compressor performance was given, nor numerical scheme on BVF-based optimal design was developed.

In a companion paper of the present one (referred to as Part I hereafter), Yang et al. [8] investigated on how to apply vorticity dynamics in the through-flow design (TFD) of axial compressor to improve its performance, and showed analytically that the circumferential vorticity does play an important role. For better performance, the positive and negative circumferential vorticities should be pressed to the casing and hub, respectively, i.e., it should be minimized in the effectively inviscid core-flow region on the hub-casing surface ($S2$ stream surface). RANS computations of Part I demonstrated that embedding the above principle into an optimal TFD scheme for a rotor blade can indeed enhance the pressure ratio and efficiency.

In the theoretical analysis of Part I, however, the flow was assumed inviscid and axisymmetric as a simplified model of the core flow away from the boundary layers. This simplification is suitable to TFD but makes it impossible to trace the physical root of the circumferential vorticity to its physical root, since the BVF involves inherently a viscous process. To make an in-depth diagnosis of the BVF behavior on blade surfaces and to use the result to RANS simulation based optimal design, therefore, in this paper we return to the general viscous and compressible flow as the

---

Contributed by the Fluids Engineering Division of ASME for publication in the JOURNAL OF FLUIDS ENGINEERING. Manuscript received October 8, 2008; final manuscript received October 30, 2009; published online December 18, 2009. Assoc. Editor: Chunill Hah.

continuation of Part I. It will be seen that this viscous and 3D study can lead to a much more significant compressor performance enhancement than that obtained in Part I.

2 The Physical Basis of BVF-Based Flow Diagnosis

2.1 Boundary Vorticity Flux. The BVF is defined as

$$\boldsymbol{\sigma} \equiv \nu \mathbf{n}\cdot\nabla\boldsymbol{\omega} = \nu\,\partial\,\boldsymbol{\omega}/\partial\mathbf{n} \tag{1}$$

where ν is the kinematic viscosity and $\mathbf{n}$ is the unit normal vector of the boundary pointing out of the fluid. Since the BVF measures the vorticity creation rate at solid surfaces, it also controls the development of boundary layers and their separation, including that induced by a shock wave. In general, on an accelerating body surface, applying the tangential components of Navier–Stokes (N–S) equation to the surface indicates that the BVF consists of the contributions of the wall acceleration $\mathbf{a}$, on-wall tangent pressure gradient, and a three-dimensional viscous correction

$$\boldsymbol{\sigma} = \boldsymbol{\sigma}_a + \boldsymbol{\sigma}_p + \boldsymbol{\sigma}_{\text{vis}} \tag{2}$$

where

$$\boldsymbol{\sigma}_a \equiv \mathbf{n}\times\mathbf{a}_B, \quad \boldsymbol{\sigma}_p \equiv \frac{1}{\rho}\mathbf{n}\times\nabla p, \quad \boldsymbol{\sigma}_{\text{vis}} = \nu(\boldsymbol{n}\times\nabla)\times\boldsymbol{\omega} \tag{3}$$

To illustrate the properties of BVF, consider two-dimensional flow on the (x,y)-plane over a 2D cascade, with $\boldsymbol{e}_z=\boldsymbol{e}_x\times\boldsymbol{e}_y$ being the unit normal vector of the plane. The boundary of the blade is represented by a fixed closed curve C. Let $\boldsymbol{n}$ and $\boldsymbol{t}$ be the unit vectors normal and tangential to C, pointing out of the fluid and along the counterclockwise direction viewed from the fluid side, respectively. Also, we set $d\boldsymbol{l}=\boldsymbol{t}dl$ such that dl is the arclength of a line element along C, and $dl>0$ along the $\boldsymbol{t}$-direction. In this case, Eq. (2) is reduced to $\boldsymbol{\sigma}=\boldsymbol{\sigma}_p=\sigma_p\mathbf{e}_z$ with

$$\sigma_p = \frac{1}{\rho}\frac{dp}{dl} \tag{4}$$

Note that because along the normal of an attached boundary layer the pressure does not change, the tangential pressure gradient in Eq. (4) can be viewed as that of inviscid flow at the outer edge of the boundary layer, and hence, equals the kinetic energy decrease or velocity diffusion via the Bernoulli equation. This observation implies that controlling the BVF is essentially the same as controlling the diffusion factor of a cascade as one conventionally does.

2.2 BVF and Boundary-Layer Separation. In a 2D flow, the role of BVF appears mainly in two aspects. First, since the newly created vorticity measured by the BVF is diffused into the fluid to enhance or weaken the already existed boundary vorticity (depending on the sign relation of the BVF and boundary vorticity), the BVF may serve to warn the flow separation from blade surface. This is sketched in Fig. 1 for a 2D boundary-layer flow, where it shows the profiles of velocity and vorticity, and the BVF variation on a flat plate, as dp/dl changes from negative (favorable) to zero to positive (adverse). For attached flow in adverse pressure gradient $(dp/dl>0)$, the sign of BVF is opposite to that of the near-wall vorticity, so the newly created vorticity by BVF will offset the existing one, and reaching the Prandtl's separation point with $(\partial V/\partial n)=0$, which is equivalent to $\omega=0$ on the wall. Thus, the appearance of positive peak BVF warns that the separation may soon happen.

Note that the above discussion on flow separation is of merely qualitative value, because the Prandtl's separation criterion is only necessary but an insufficient condition for a boundary layer to break away from the wall and thereby affect the global flow performance, which is, however, precisely one's main concern in engineering applications. Thus, a more powerful criterion for capturing the strong boundary-layer separation is needed, which is again expressible by the BVF, as derived by Wu et al. [6] from the triple-deck theory: at a boundary-layer separation point in a 2D laminar flow, there must be a very strong BVF peak

$$\boldsymbol{\sigma}_p = O(\text{Re}^{1/8}) \gg 1 \tag{5}$$

(a) Velocity Profile

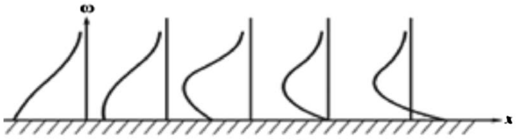

(b) Vorticity Profile

(c) Boundary vorticity flux

Fig. 1 Sketch of the profiles of (*a*) velocity and (*b*) vorticity, and (*c*) the BVF variation for a flat-plate flow in a pressure gradient changing from favorable to adverse [5]

The most important on-wall local process at large Re is the boundary-layer separation that often considerably alters the global flow performance. For steady 2D and 3D flows, this local process has been well explained by the triple-deck theory that also leads to a convenient BVF-based diagnosis criterion [4,6]. Figure 2(*a*) shows an example of a primary 3D boundary-layer separation from a prolate spheroid at an angle of attack, and its induced secondary separation. The triple-deck theory asserts that an interactive pressure $\Delta p=O(\text{Re}^{-1/4})$ must appear in the narrow separation zone of width of only $O(\text{Re}^{-3/8})$, which should be added to the pressure at the outer edge of the attached boundary layer. Thus, although Δp is small and can hardly be detected from numerical data, its tangential gradient or associated BVF peak must be strong and is easily identified in separation zone.

This fact makes strong local BVF peaks a very effective marker to signify boundary-layer separation, which must be in the direction perpendicular to the interactive pressure gradient. In a 3D flow, then, since the boundary-layer separation line is a skin-friction line (a $\boldsymbol{\tau}_w$-line), it can be shown that the interactive $\boldsymbol{\sigma}_p=O(\text{Re}^{1/8})$ must be basically aligned to the $\boldsymbol{\tau}_w$-line direction [4,6]. This feature occurs only in the narrow separation zone. Figure 2(*b*) exemplifies this situation on a prolate spheroid, which shows some vector lines of both the $\boldsymbol{\tau}_w$- and $\boldsymbol{\sigma}$-field. The convergence of the former was the separation criterion proposed by Lighthill [5], which is insufficient to identify whether the boundary-layer separation indeed occurs; but the $(\boldsymbol{\sigma}_p,\boldsymbol{\tau}_w)$ alignment criterion does, including the initial and terminal locations of the boundary-layer separation zones.

2.3 Total Aerodynamic Force and Moment in Terms of BVF. The aerodynamic forces exerted on 2D cascade (Fig. 3) by the fluid can be expressed by the integral of the first moment of BVF [1–3]. At $\text{Re}\gg 1$ the contribution of skin friction can be neglected, and there is an axial force

$$F_x = -\rho\oint_C y\sigma_p dl \tag{6}$$

and pitchwise force

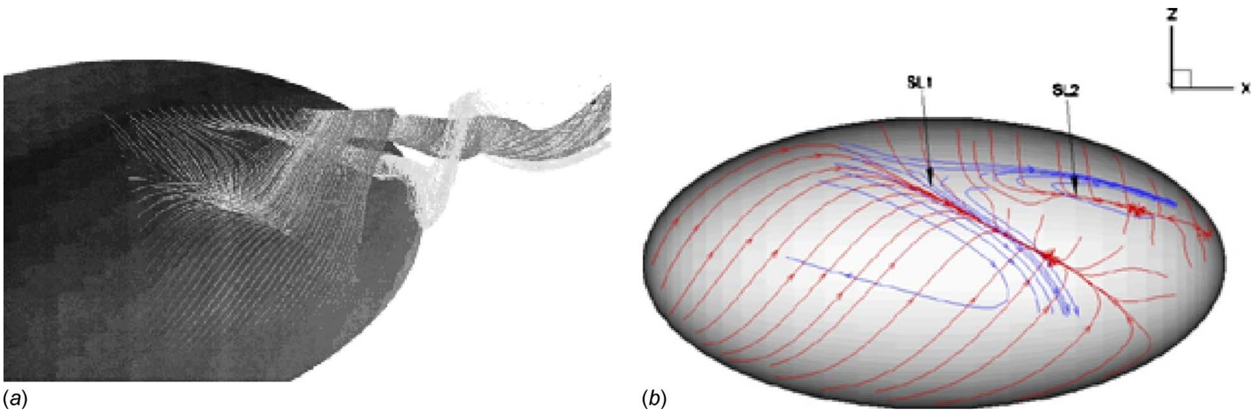

(*a*) (*b*)

Fig. 2 Three-dimensional boundary layer separation and separated flow from a prolate spheroid at incidence [6]: (*a*) flow pattern, and (*b*) skin-friction (red, mainly upward) and BVF-lines (blue, mainly to the right) on the spheroid surface. SL1 and SL2 are the primary and secondary separation lines, respectively

$$F_y = \rho \oint_C x \sigma_p dl \tag{7}$$

The underlying mathematical approach of these formulas is the derivative-moment transformation (DMT) that casts the boundary integral of pressure to that of the moments of the tangential pressure gradients [4]. Here, the origin of the coordinates (x, y) can be arbitrarily chosen, and a convenient choice is to locate it at the midpoint of the chord. Thus, the axial and pitch forces will be positive if sign $y = -\text{sign}\ \sigma_p$, sign $x = \text{sign}\ \sigma_p$, and vise versa.

As to a blade in 3D flow, by an application of DMT to the surface integrals, the total force and moment can be expressed by the first and second integrated moments of σ_p and σ_{vis}, respectively, where σ_{vis} can be neglected at large Reynolds numbers for design purposes. Specifically, on the blade surface S_b (which is open at the blade-hub juncture and has a closed boundary line ∂S_b) the total moment due to pressure is

$$\mathbf{M} = -\int_{S_b} (\mathbf{r} \times p\mathbf{n}) dS = -\frac{1}{2}\int_{S_b} r^2 (n \times \nabla p) dS + \frac{1}{2}\oint_{\partial S_b} (pr^2) dl \tag{8}$$

where $\boldsymbol{n}$ is the unit normal vector pointing out of fluid. Thus, let the angular velocity of the rotor be Ω and the net power L_u acting to the fluid by the rotor is

$$L_u = \Omega M_z = \Omega \left[-\frac{1}{2}\int_{S_b} \rho r^2 \sigma_{pz} dr dz + \frac{1}{2}\oint_{\partial S_b} p r^2 dz \right] \tag{9}$$

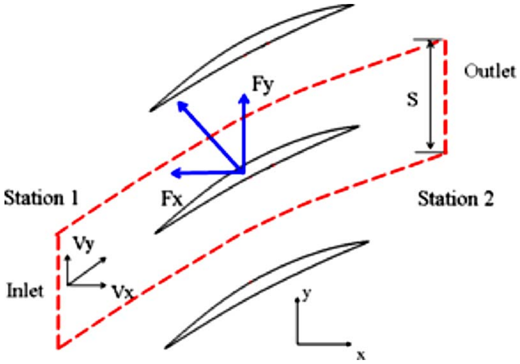

Fig. 3 Control volume of the flow in the 2D compressor cascade

where σ_{pz} is the axial BVF component on the blade surface.

What matters in our flow diagnosis, therefore, is not only the sign of the BVF but also the location of its peaks. For example, a positive BVF peak that lie not far from the trailing edge may have large $x > 0$ and hence, considerably enhance the pitch force and loading; but meanwhile it may also cause the boundary layer to separate before reaching the trailing edge. This twofold consideration will guide our following applications of the BVF-based diagnosis and design.

3 Methodology of 2D Inverse Design by Optimal BVF Distribution

It is possible to control the BVF distribution to get a higher cascade loading with possible reduced loss. In this section, we apply the BVF to the reverse design of the cascade profile through constructing a mathematic relationship between the BVF and the curvature of the camber line.

Consider a 2D incompressible flow past a compressor cascade, as shown in Fig. 3. Define the circumferentially (along y) averaged axial velocity as

$$\bar{V}_x = \frac{\dot{m}}{\rho s} = \frac{1}{\rho s}\int_0^s \rho V_x dy = \frac{1}{s}\int_0^s V_x dy \tag{10}$$

where $\dot{m}$ is the mass flow through the passage. Then the mass-averaged y-component velocity is

$$\bar{V}_y = \frac{1}{\dot{m}}\int_0^s V_y (\rho V_x dy) \tag{11}$$

The mass continuity from inlet station1 to outlet station 2 yields

$$\bar{V}_{x_1} s = \bar{V}_{x_2} s \tag{12}$$

and the momentum theorem gives [9]

$$F_x = s(p_2 - p_1) \tag{13}$$

$$F_y = \rho \bar{V}_x s (\bar{V}_{y_1} - \bar{V}_{y_2}) \tag{14}$$

For the partial part of fluid shown in the shadowed region of Fig. 4, the local force in the y-direction exerting on the fluid is

$$\Delta F_y = p^+ - p^- = \dot{m}\frac{d\bar{V}_y}{dx} \tag{15}$$

where the superscripts "+"and "−" represent the suction and pressure sides, respectively. Approximately, the circumferential velocity is related to the axial velocity by

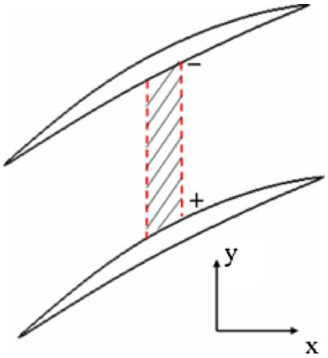

Fig. 4 Partial part of the fluid in the 2D compressor cascade field

$$\bar{V}_y = \bar{V}_x tg\beta \tag{16}$$

with β being the angle of the camber line with respect to the axial direction. Substituting it into Eq. (15) yields

$$p^+ - p^- = \dot{m}\frac{d\bar{V}_y}{dx} = \dot{m}\frac{d(\bar{V}_x tg\beta)}{dx} = \dot{m}\left[\bar{V}_x\frac{d(tg\beta)}{dx} + \frac{d\bar{V}_x}{dx}tg\beta\right] \tag{17}$$

where, by the incompressible mass conservation, we have

$$\frac{d\bar{V}_x}{dx} = 0 \tag{18}$$

Thus, it follows that

$$p^+ - p^- = \dot{m}\bar{V}_x\frac{d(\tan\beta)}{dx} = \dot{m}\bar{V}_x\frac{d^2y}{dx^2} = \dot{m}\bar{V}_x\cdot\beta'(x)\cdot\sec^2\beta \tag{19}$$

Equation (19) interprets the diffusion mechanism of the subsonic cascade as through changing the camber angle to make flow turning. The change in the camber angle is highly dependent on the local curvature of camber line, so we try to correlate the local force with the curvature of the camber line. The curvature is given by

$$K = \frac{y''}{(1+y'^2)^{3/2}} = \frac{\dfrac{d(\tan\beta)}{dx}}{(1+\tan^2\beta)^{3/2}} = \beta'(x)\cos\beta \tag{20}$$

Substituting K into Eq. (18), the local force in the pitchwise direction is

$$p^+ - p^- = \dot{m}\bar{V}_x\frac{d^2y}{dx^2} = \dot{m}\bar{V}_x\cdot K\cdot\sec^3\beta \tag{21}$$

Taking the derivative of x of Eq. (21), and noticing that for the given thin blade, β is also the curve angle of the suction and pressure surfaces, we obtain

$$\frac{\partial p^+}{\partial x} - \frac{\partial p^-}{\partial x} = \left(\frac{\partial p^+}{\partial l} - \frac{\partial p^-}{\partial l}\right)\frac{1}{\cos\beta} = \dot{m}\bar{V}_x\frac{d^3y}{dx^3} = \dot{m}\bar{V}_x\left[\frac{dK}{dx}\sec^2\beta + 3K^2\sec^2\beta\cdot tg\beta\right] \tag{22}$$

But the BVF on suction and pressure sides are

$$\sigma_p^+ = \frac{1}{\rho}\frac{\partial p^+}{\partial l}, \quad \sigma_p^- = -\frac{1}{\rho}\frac{\partial p^-}{\partial l} \tag{23}$$

Thus, we obtain the relationship between the averaged BVF and curvature

$$\bar{\sigma}_p = \frac{1}{2}(\sigma_p^+ + \sigma_p^-) = \frac{\dot{m}\bar{V}_x}{2\rho}\frac{d^3y}{dx^3}\cos\beta = \frac{\dot{m}\bar{V}_x}{2\rho}\left[\frac{dK}{dx}\sec^2\beta + 3K^2\sec^2\beta\cdot tg\beta\right] \tag{24}$$

Namely, the averaged BVF depends on the square of the curvature and curvature derivative. This relation makes it possible to change the curvature of the camber line to control the BVF peaks and its position.

A baseline cascade was improved based on this BVF control method. Some parameters of cascade are shown in Table 1.

Table 1 Parameters of the cascade

Inlet angle (deg)	50.6
Outlet angle (deg)	−4.4
Camber angle (deg)	55
Inlet mach number	0.75
Solidity	1.7
Chord (m)	0.068
Stagger angle (deg)	23.6

The baseline cascade was first simulated using NUMECA software with SA turbulence model. Its BVF and curvature are both plotted in Fig. 5 to compare their peak positions. The positive BVF peak on the suction side appears at 20% axial chord, the same location as that of negative curvature peak. At this position, the BVF on the pressure side is one order smaller than the BVF on the suction side, namely, $\sigma_p^- \ll \sigma_p^+$ and $\sigma_p^+ \approx 2\bar{\sigma}_p$. Subsequently, the average BVF also has a positive peak at 20% chord position, confirming that that BVF is directly associated with the square of curvature in formula of Eq. (24). The BVF peaks near LE and TE are just caused by the local great curvature change in these regions, which is inevitable but does not matter. The BVF peak at 20% chord on the suction side is what we should pay attention to, as it may cause early flow separation according to the aforementioned mechanism.

Motivated by the above observation, we carried out an inverse cascade design by shifting the centerline curvature peak more downstream, as shown in Fig. 6, but with the inlet and outlet angles of profile remaining unchanged. After calculating the revised cascade on the same mesh topology using the same turbulence model, it was found that the BVF peak at 20% chord position on the suction side is suppressed and its distribution becomes even from 20% to 60% chord (see Fig. 7). Accordingly, the adverse pressure gradient on the suction side becomes smaller than the baseline (see Fig. 8). As is well known, the reduction in the adverse pressure gradient is very beneficial for suppressing flow separation. Indeed, the comparison of Mach number distributions

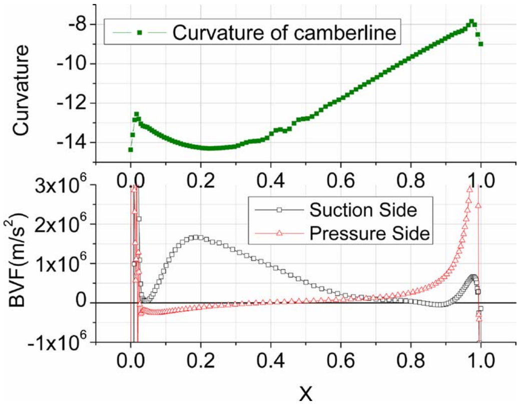

Fig. 5 BVF and curvature of the baseline

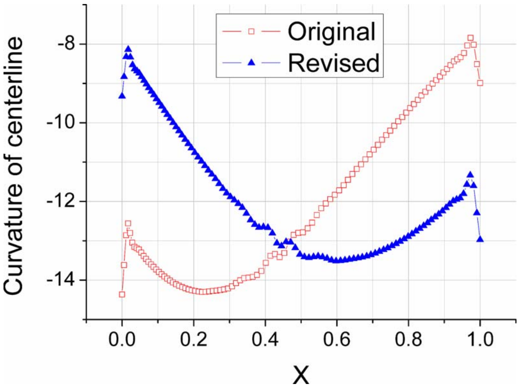

Fig. 6 Curvature comparison

in Fig. 9 illustrates that the separated-flow region of the revised cascade is much smaller than that of the baseline, and the separation point is shifted downstream, as shown by the distribution of boundary vorticity in Fig. 10.

In addition, it was found that loss coefficient of the revised cascade is decreased by 7.2% at the minimum loss incidence angle (see Fig. 11).

Although Eq. (24) was derived for incompressible flow, the mechanism of adding work and diffusion is the same for the subsonic compressor cascade, and the inverse design case study demonstrated here should still work well. It is also possible to extend the present BVF-based method to the supersonic cascade. The precompression supersonic profile is an example of controlling the curvature to reduce shock loss; but as a matter of fact, it is really to control the BVF peaks caused by the shock wave. This inverse design method based on BVF and curvature diagnosis provides a simple and effective methodology for compressor blade design without time-consuming optimization, as a supplement of the traditional design method.

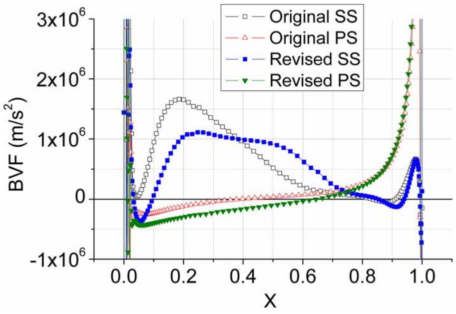

Fig. 7 BVF comparison

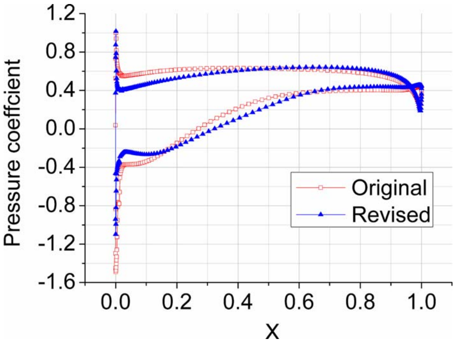

Fig. 8 Pressure coefficient comparison

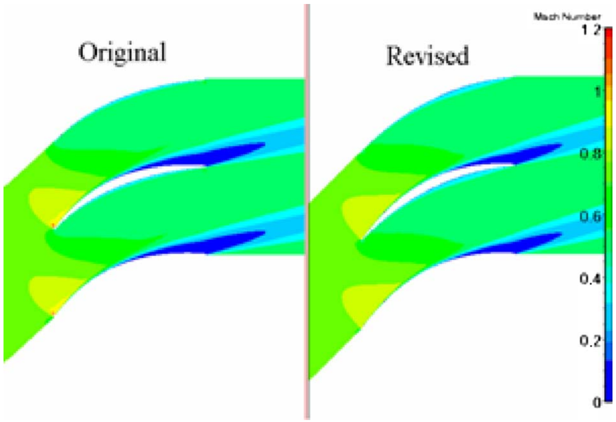

Fig. 9 Mach number distribution

4 The BVF-Based Methodology of 3D Diagnosis and Optimization

4.1 Diagnosis of Transonic Compressor Rotor. For 3D diagnosis and optimization on a compressor rotor blade, it can be based on Eq. (9), by which the loading coefficient is given by

$$\bar{H}=\frac{L_u}{(\Omega r_{\text{tip}})^2}=\left[-\frac{1}{2}\int_{S_b}\rho\bar{r}^2\sigma_{pz}drdz+\frac{1}{2}\oint_{\partial S_b}p\bar{r}^2dz\right]/\Omega \tag{25}$$

Here, the nondimensional r is given by r/r_{tip}. To understand the axial BVF component σ_{pz} more clearly, let n_θ and n_r be the circumferential and radial components of $\boldsymbol{n}$; hence, σ_{pz} can be expressed as

$$\sigma_{pz}=\frac{1}{\rho}\left(\frac{\partial p}{r\,\partial\theta}n_r-\frac{\partial p}{\partial r}n_\theta\right) \tag{26}$$

which depends on both the circumferential and radial pressure

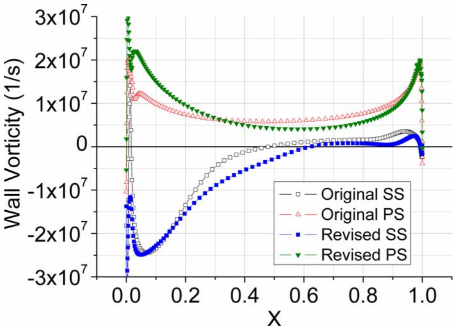

Fig. 10 Comparison of the wall vorticity

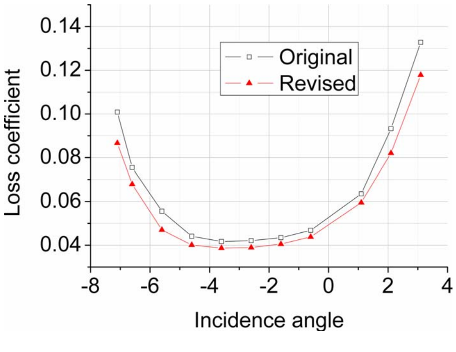

Fig. 11 Loss coefficient

Table 2 Numerical performances at peak efficiency

Mass flow rate (kg/s)	26.0
Total pressure ratio	2.36
Adiabatic efficiency (%)	89.4
Rotating speed of tip (m/s)	495.32

gradients as well as the orientation of $\boldsymbol{n}$.

Because the BVF peaks are highly localized at very narrow areas of the blade surfaces and have easily identifiable favorable or adverse effect on M_z, one's attention in optimal blade design can well be focused to these local areas.

Based on the above derived BVF, we made the flow diagnosis on a transonic fan rotor, with performance parameters shown in Table 2. The distributions of BVF and pressure on the suction and pressure blade surfaces are compared in Figs. 12 and 13, respectively.

As shown in the figures, the pressure distribution from the leading edge to the trailing edge is quite smooth, but the BVF peaks are clearly seen. On the suction side and at about 1/2 chord length of the blade, a strip of peak BVF zone extending from tip to hub can be clearly identified that obviously reflects a possible boundary-layer separation caused by a shock wave. In addition, a small peak near the trailing edge of the hub shows a small separation zone there. On the other hand, the overall distribution is satisfactory on the pressure surface of the blade.

Furthermore, the $(\boldsymbol{\sigma}_p, \boldsymbol{\tau}_w)$ alignment criterion mentioned in Sec. 2.2 can be used to verify the 3D boundary-layer separation. In both Figs. 14 and 15 we see the τ-lines convergence near the blade tip on the pressure side, which by Lighthill's criterion seems to indicate certain separation; but no BVF line turns to be aligned to any τ-lines, and thus, we may assert no boundary-layer separation on the pressure side.

In contrast, Fig. 16 shows that the τ-lines converge near 1/2 chord length on the suction side, where the ω-lines exhibit big curvature, and BVF lines are almost aligned to the τ-lines there, as indicated by Fig. 17. Hence, it is concluded that the boundary layer does separate there. This is further confirmed by the streamline pattern in the relative frame of reference on the suction the side, as shown in Figs. 18 and 19.

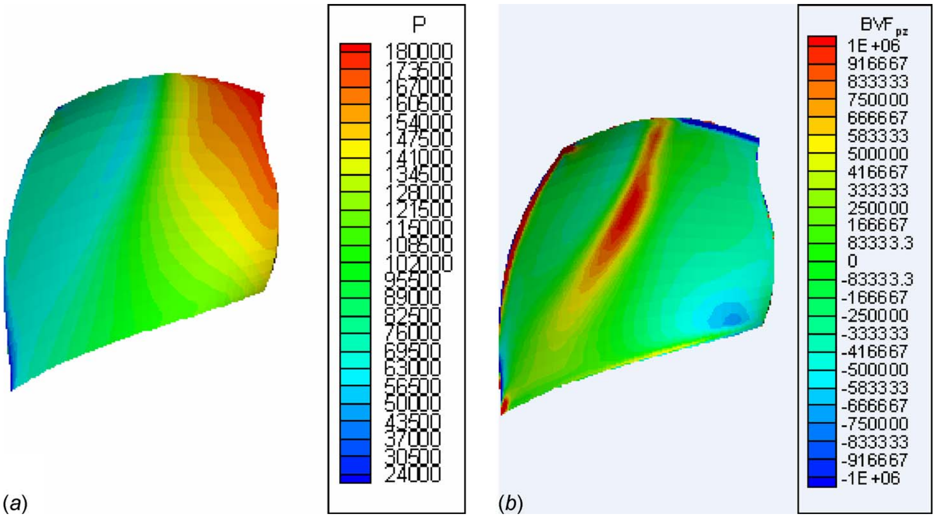

(*a*) (*b*)

Fig. 12 Distribution of pressure and BVF on the suction surface of the rotor blade: (*a*) pressure and (*b*) BVF

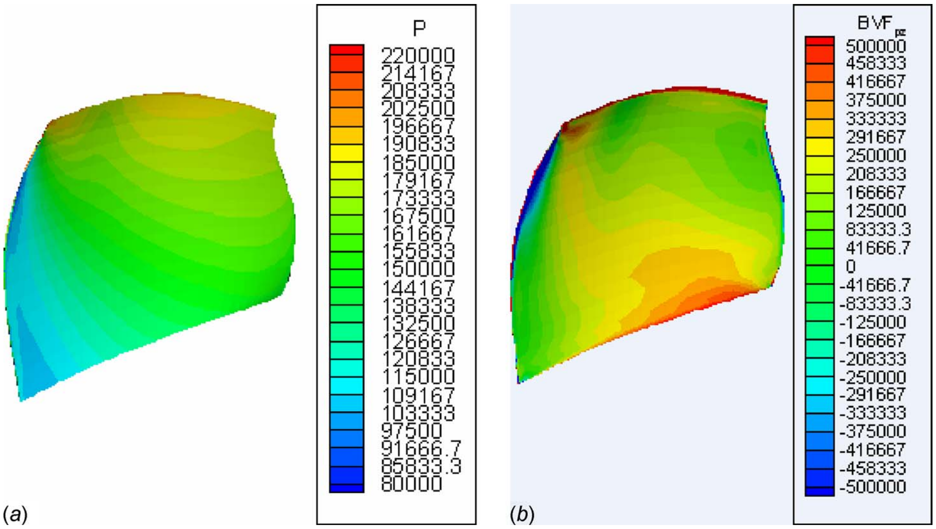

(*a*) (*b*)

Fig. 13 Distribution of pressure and BVF on the pressure surface of the rotor blade: (*a*) pressure and (*b*) BVF

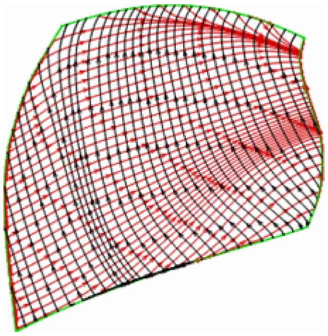

Fig. 14 (τ,ω) **on pressure side (red curve is** τ**, to the right; black curve is** ω**, upward)**

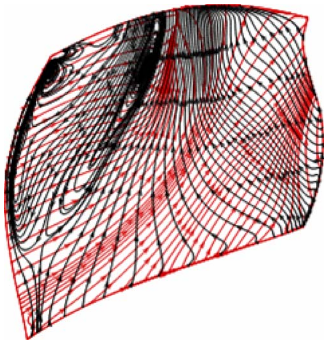

Fig. 17 (τ,σ_p) **on suction side (red curve is** τ**, mainly to the right; black curve is** σ_p**, mainly upward)**

4.2 BVF-Based Compressor Rotor Optimization. As shown in Secs. 2.2 and 2.3, the positive axial BVF makes negative contribution to the axial moment and work input (see Eq. (9)), and the BVF diagnosis may trace the physical root of separated flows on the boundary. Thus, we now seek the improvement of the axial moment of the rotor blade by optimizing the BVF distribution thereon. In this procedure, the axial moment was selected as the objective function under the constraint of fixed positions of rotor LE and TE. A simple gradient algorithm was used in the optimization process. The performance of original and optimized transonic rotors was then analyzed using NUMECA in the same mesh structure, which had $65\times49\times129$ nodes in the computational domain and $65\times49\times65$ nodes in the blade passage in circumferential, radial, and axial directions, respectively. The size of the first cells near the wall was adjusted to ensure that $Y^{+}<10$. The S-A turbulence model was applied in this study.

Figure 20 compares the axial BVF distributions on the suction sides of the original and optimized rotors, which clearly shows that not only the positive peak of axial BVF is weaker at the middle part of the blade, but also the area of this zone becomes smaller and moves more downstream than that on the original blade. Consequently, the axial moment acting on the fluid is increased by 6%.

Recalling the definition of $\boldsymbol{\sigma}_p$ in Eq. (5), it is evident that the pressure gradient has been controlled by the optimization in the local region, where the positive peak of the axial BVF is weakened. This fact can be verified through the traditional analysis. For example, the shock wave is weaker and shifted downstream, as seen from the relative Mach number contours at the middle and tip sections of the rotors in Figs. 21 and 22, and the boundary-layer separation at the tip section is obviously suppressed.

Because the optimized BVF distribution becomes better than the baseline, the rotor performance is improved considerably, as shown in Fig. 23. At the peak efficiency point, not only the pressure ratio is increased by 5.73%, but also the efficiency is increased by 1.11%. These improvements are much more significant

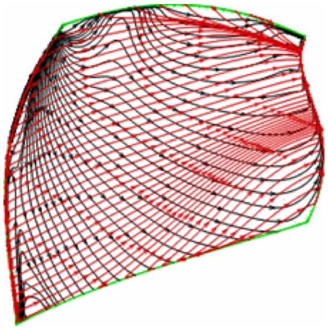

Fig. 15 (τ,σ_p) **on pressure side (red curve is** τ**, to the right; black curve is** σ_p**, mainly downward)**

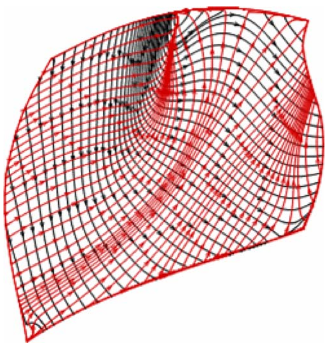

Fig. 16 (τ,ω) **on suction side (red curve is** τ**, mainly to the right; black curve is** ω**, mainly downward)**

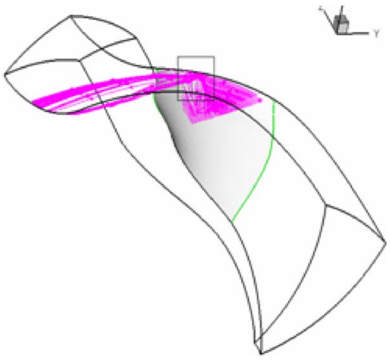

Fig. 18 Streamlines out of the suction side

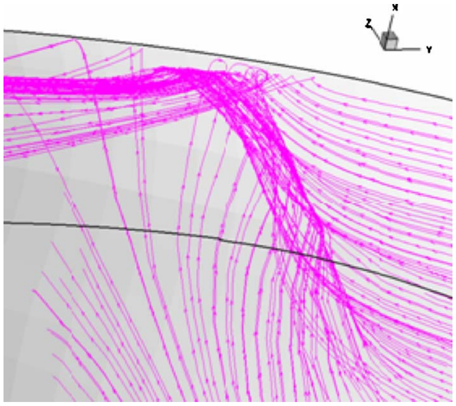

Fig. 19 Zoom in the left window

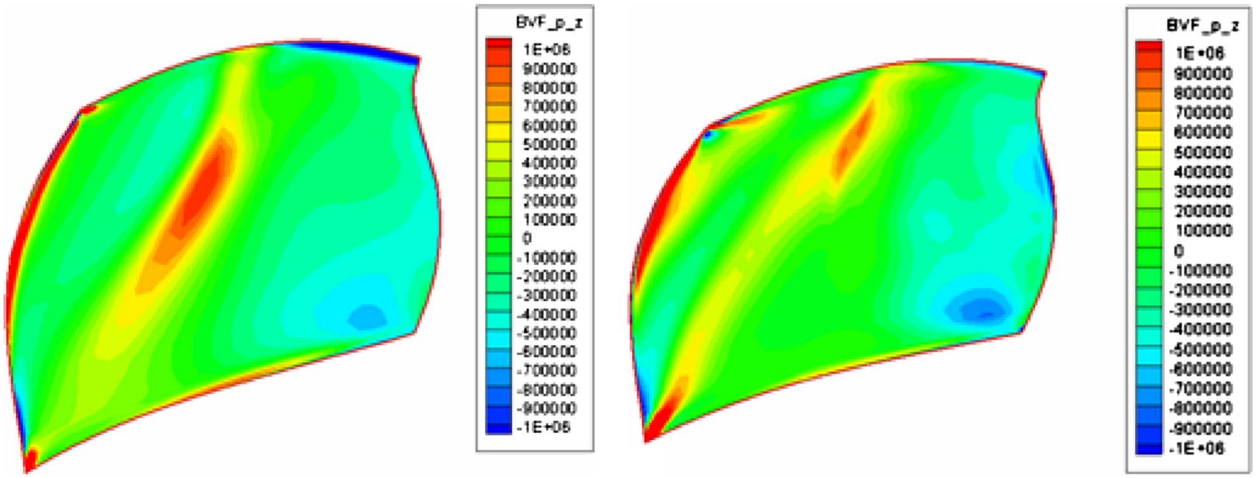

(*a*) (*b*)

Fig. 20 Axial BVF distribution on the suction side of the (*a*) original and (*b*) optimized rotors

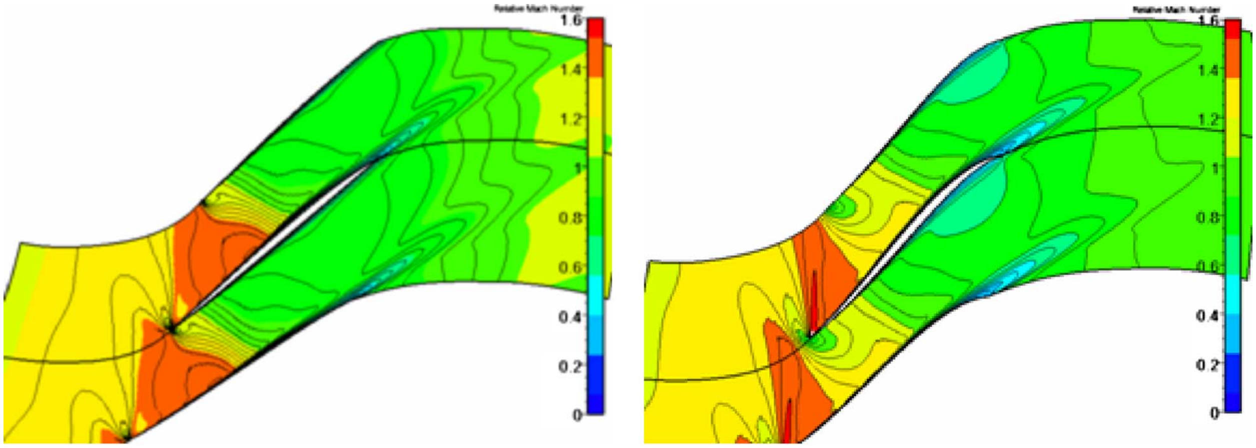

(*a*) (*b*)

Fig. 21 Comparison of relative Mach number contours at 50% span: (*a*) original and (*b*) optimized

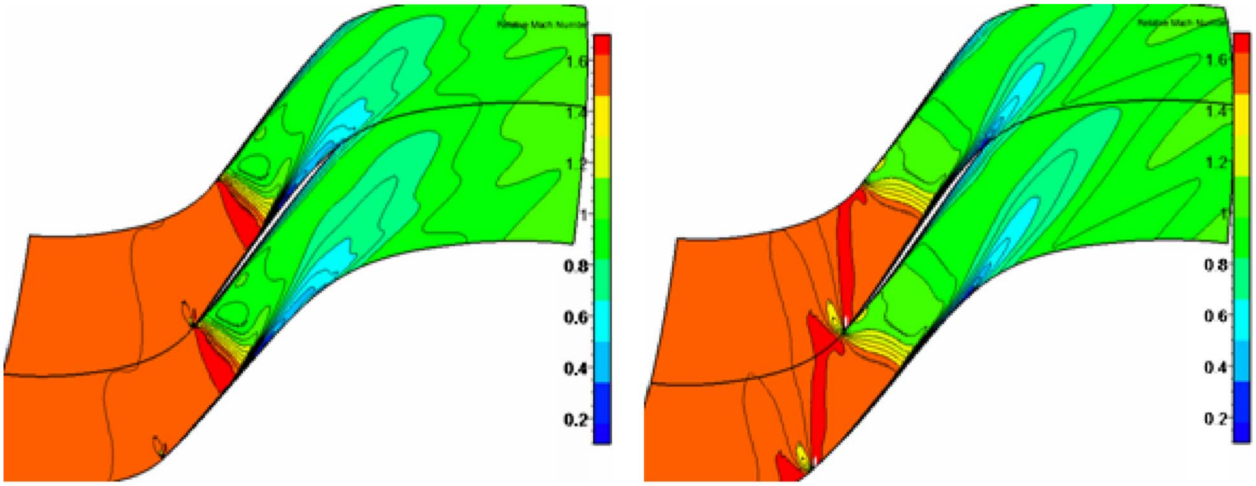

(*a*) (*b*)

Fig. 22 Comparison of relative Mach number contours at 90% span: (*a*) original and (*b*) optimized

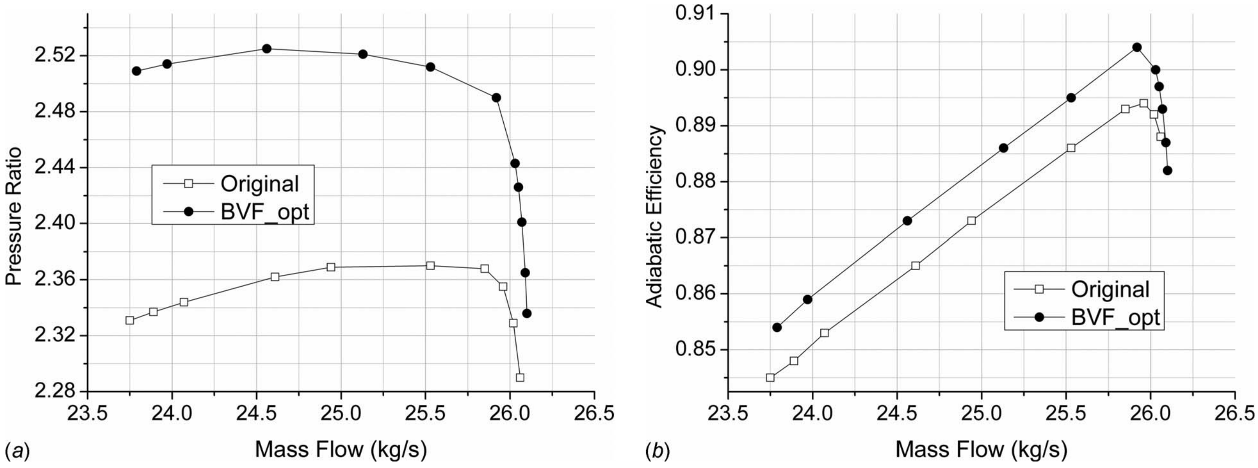

Fig. 23 Characteristics comparison: (*a*) pressure ratio and (*b*) efficiency

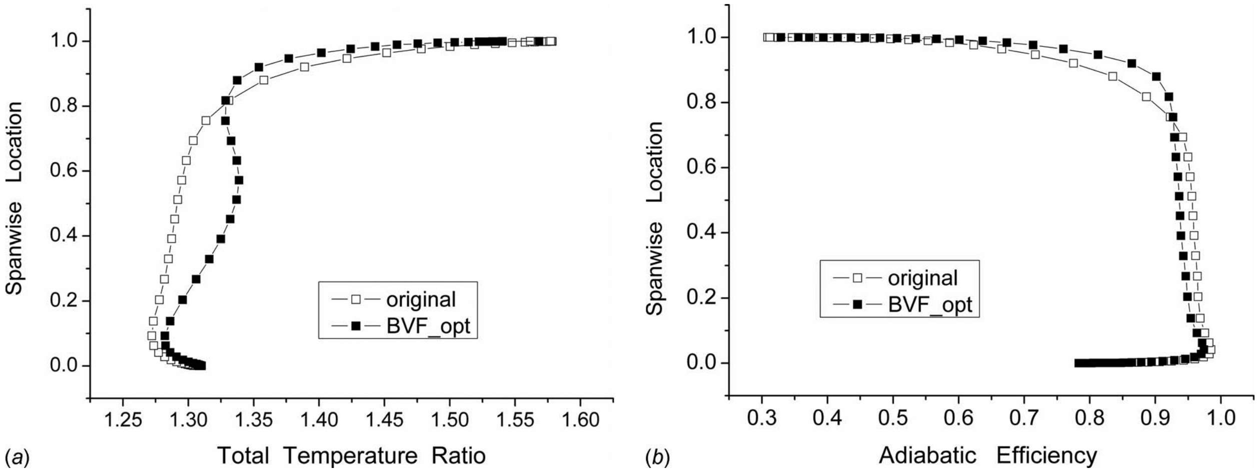

Fig. 24 Comparison of total pressure ratio and adiabatic efficiency at the rotor exit: (*a*) pressure ratio and (*b*) efficiency distributions

than that reported in Part I, where only the axisymmetric and inviscid core flows were considered. Moreover, Fig. 24(*a*) shows that the loading at midspan is greatly increased due to the suppression of the positive BVF peak at the middle sections. As we know, for transonic rotors, the efficiency is influenced largely by the supersonic sections, and the losses at the tip sections is obviously weakened as shown in Fig. 22, so the adiabatic efficiency is improved mainly at the tip section (see Fig. 24(*b*)).

This optimization example based on BVF diagnosis illustrates that controlling the BVF distribution on the blade surface can indeed improve the loading without loss of efficiency. In conventional design procedure, loading and efficiency are often two design parameters to be compromised; but now the BVF-based optimization method has guided us to focus on the physical source, and thus, provides a new methodology to improve both loading and efficiency.

5 Optimal Redesign of a Low-Speed Compressor Based on Both BVF and Circumferential Vorticity

In this section, we report the second example of diagnosis and inverse design for a low-speed, single-stage compressor rotor [9], for which the original designed performance and structure parameters is listed in Table 3.

According to the diagnosis based on the circumferential vorticity made in Part I, it is found that the peak zone of the circumferential vorticity near the casing is gradually expanding toward the channel when the flow coefficient decreases toward stall (Fig. 25), which shows that the ability of increasing pressure is sharply weakened. Therefore, in the inverse design, swept-forward blade was used to increase the load at the blade tip; meanwhile inverse bowing was adopted to improve its aerodynamic performances, to keep the circumferential vorticity within the range near the casing.

On the other hand, for this low-speed compressor blade, Fig. 26 shows three BVF peak zones on the suction and pressure surfaces. First of all, we can find the BVF peaks, the on suction side, to induce the tip and hub blockages because of the secondary flow. On the pressure side, several BVF peaks occur in the region near the trailing edge on the 80% height of blade, which reflects that the pressure gradient at this section is irregular and need to be revised in the optimal redesign. However, from the pressure dis-

Table 3 Performance of the low-speed compressor

Flow coefficient	0.574
Total pressure rise coefficient	0.32
Adiabatic efficiency (%)	85
Rotational speed (rpm)	3000
Hub tip ratio	0.75

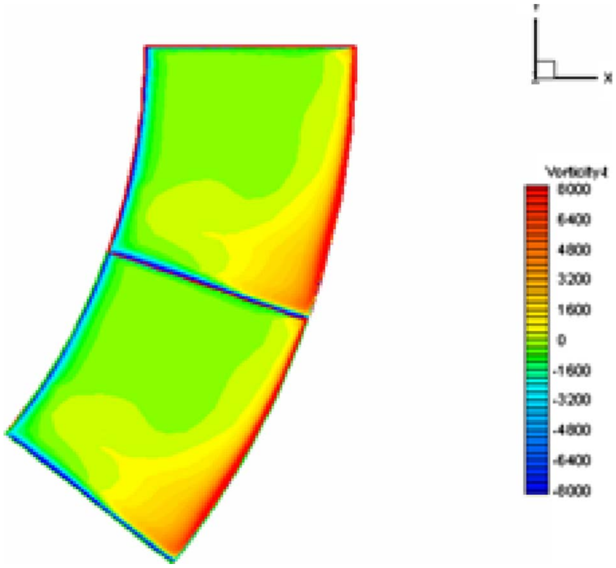

Fig. 25 Circumferential vorticity at the rotor exit

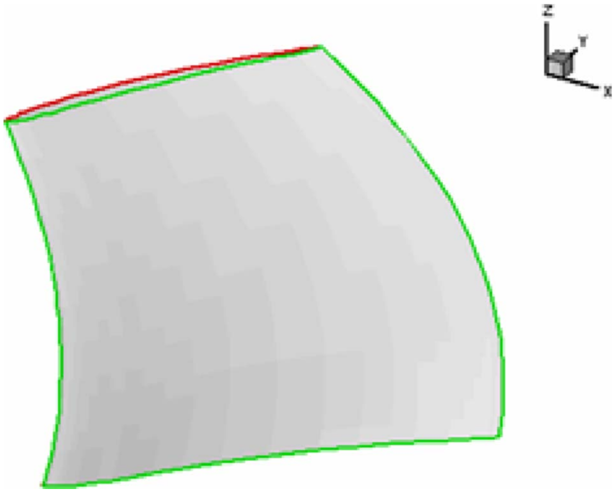

Fig. 28 Shape of the rotor of the improved design

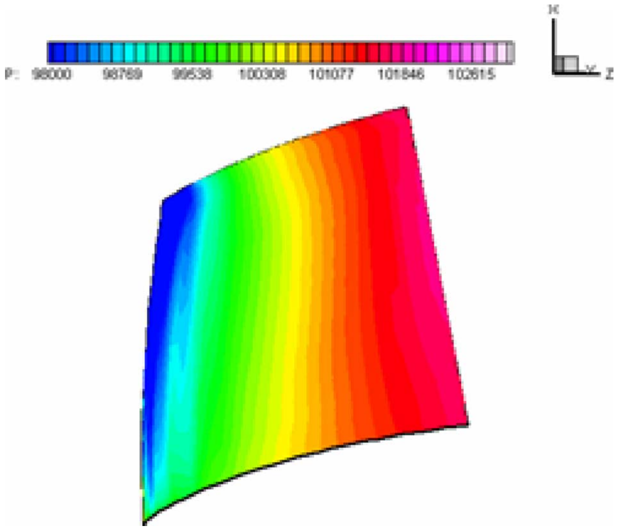

Fig. 26 BVF distribution on the (*a*) pressure and (*b*) suction sides of the rotor at low flow coefficient

tribution (Fig. 27) there is no irregularity on the blade surface, indicating again the superiority of the BVF diagnosis over the pressure diagnosis.

Figure 28 shows the redesigned blade shape based on the methodology both of BVF and circumferential vorticity, which, as mentioned above, has a swept-forward edges and inverse bowing. The numerical results show that the phenomenon of the circumferential component of vorticity expanding from the tip and casing toward the flow passage has been weakened (Fig. 29).

Meanwhile, the BVF distribution (Fig. 30) tends to be smoother; the BVF peaks, originally at the tip and hub regions on the suction side, are weakened and moved to the leading or trailing edge just due to the numerical offsets.

As shown in Fig. 31, the swept-forward redesigned compressor significantly improves the flow behavior in the range of lower flow coefficient: a greatly increased pressure rise with relatively high adiabatic efficiency. It can be concluded that, by the optimization based on both BVF and circumferential vorticity, the compressor can be redesigned to operate at higher efficiency in a wider range of flow coefficient, and the location of the peak pressure rise shows that this kind of methodology leads to a wide stall margin.

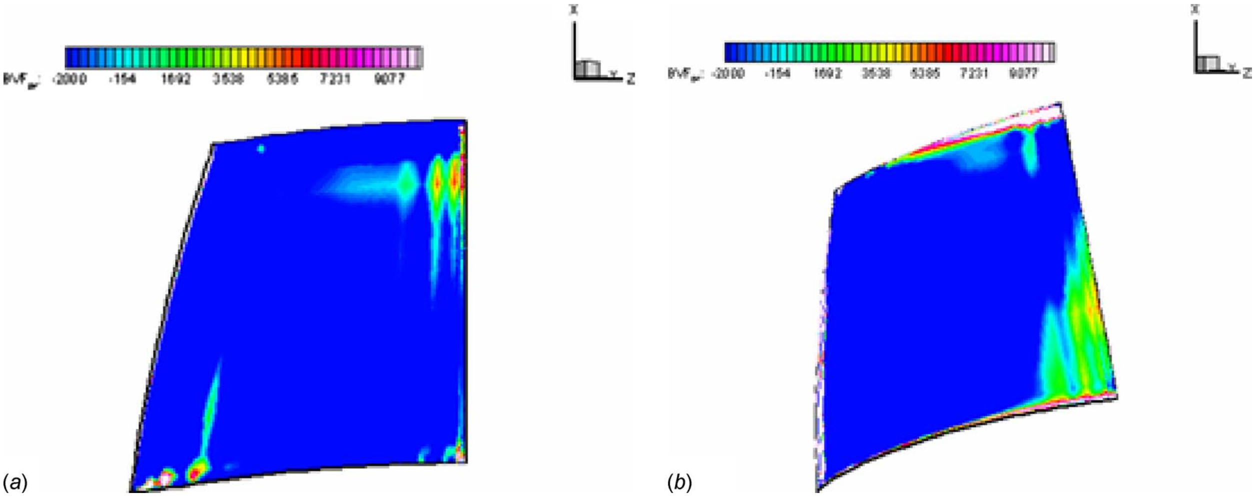

(*a*) (*b*)

Fig. 27 Static pressure on the suction side

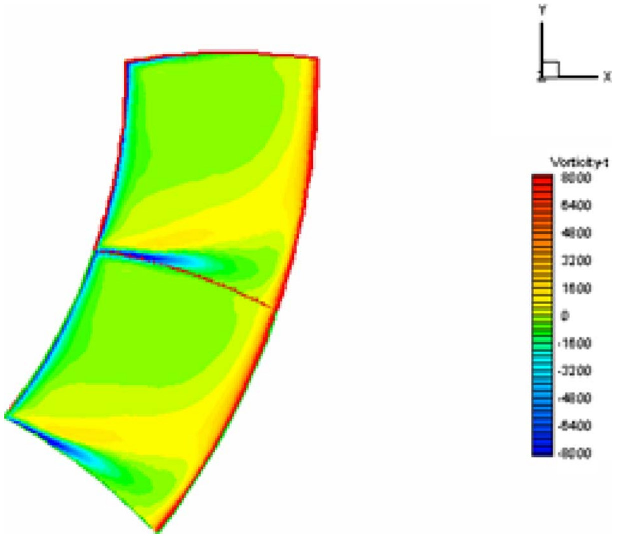

Fig. 29 Circumferential vorticity at the exit of the new rotor

6 Concluding Remarks

The key information of flow structures and dynamic processes that dominates the compressor performance is localized and magnified by the BVF-based diagnoses on the blade surface. Through analyzing the BVF distribution, especially finding its peak, one can know which key local regions cause major effects on the blade loading and possible boundary-layer separation. The worked-out examples show whether the distribution of BVF is favorable based on two intuitive criteria: first, the magnitude of BVF peak, which is hoped to be smaller, and second, the location of this BVF peak, which is hoped to be shifted away from the sensitive regions.

According to this guideline, the BVF-based optimization has been first applied to the inverse design of 2D compressor cascade. It is found that, approximately, the positive BVF peak on the suction side just locates at the position where the camberline curvature is maximum. Thus, this peak was reduced and shifted downstream by controlling that curvature distribution so that the flow separation was suppressed and cascade performance was improved. Second, a 3D transonic fan rotor was optimized by reducing the positive BVF peak and moving it downstream, so that axial moment and loading of rotor was improved without decreasing the efficiency. The optimization leads to the enhancement of pressure ratio and efficiency by 5.73% and 1.11%, respectively.

Through these examples, the methodology of inverse design and optimization related to controlling BVF peaks, which might be physically similar to the optimization of controlling velocity diffusion, has been shown to work well in applications. We attribute the advantage of the former to the localization of the BVF and its direct relation to the on-wall physical root of the vorticity.

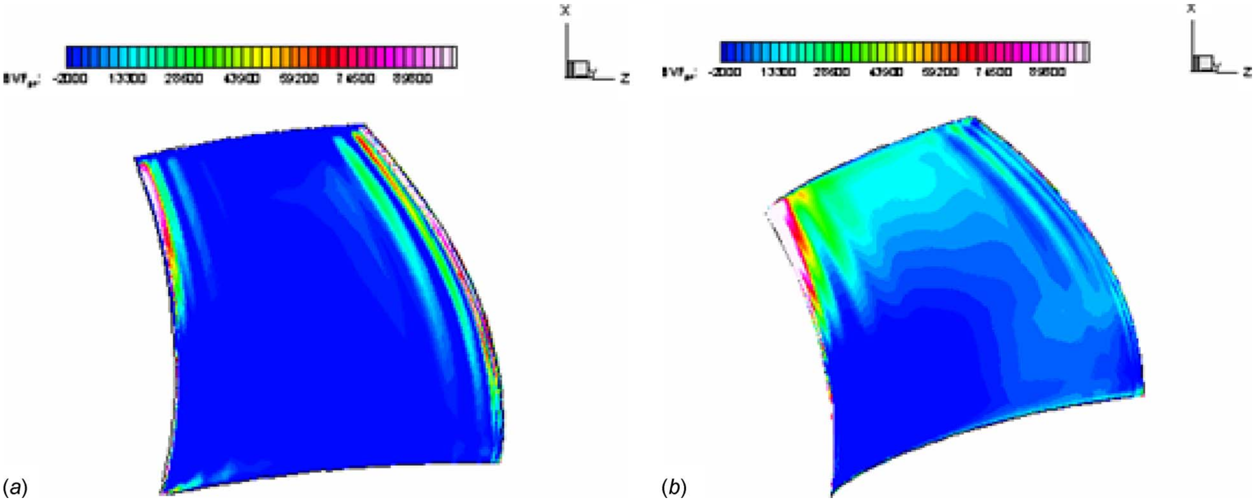

Fig. 30 Distribution of BVF on the (*b*) pressure and (*b*) suction sides of the swept-forward rotor

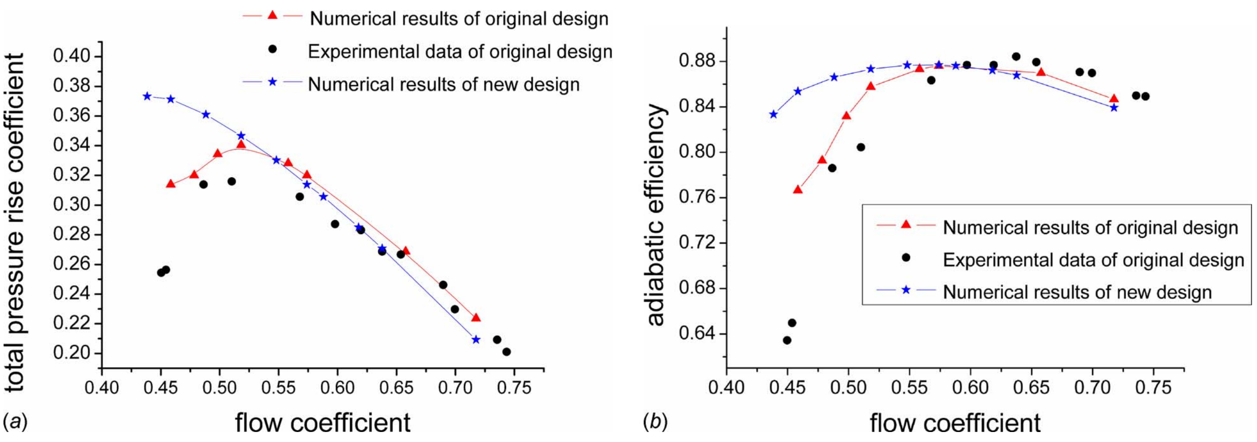

Fig. 31 Characteristics comparison of the new and original designs: (*a*) pressure ratio and (*b*) efficiency

Thus, this new methodology of diagnosis and optimal design can become a supplement to the current system of compressor aerodynamic designs.

Acknowledgment

The authors would like to acknowledge the ideas and supports from Professor Sheng Zhou. We also would like to thank the very helpful discussions with Mr. Feng Mao and Dr. Yantao Yang. The work was supported in part by National Natural Science Foundation of China (Grant Nos. 10577002 and 50176001, and Key Project No. 10532010).

Nomenclature

(r,θ,z) = cylinder coordinates with the axial z-direction; when used as subscripts denote the corresponding components of a vector
(x,y) = 2D Cartesian coordinates with the axial x-direction used in blade to blade surface
$\boldsymbol{F}$ = force exerting on blade
$\bar{H}$ = loading coefficient
K = curvature
L_u = work input per unit mass flow
$\boldsymbol{M}$ = total moment on fluids by compressor
$\dot{m}$ = mass flow
$\boldsymbol{n}$ = unit normal vector of a surface, pointing out of the fluid if at a flow boundary
p = static pressure
Re = Reynolds number
s = pitch distance
$\boldsymbol{V}$ = velocity vector
β = angle of camber line of blade with respect to axial direction
ρ = density
$\boldsymbol{\sigma}$ = boundary vorticity flux vector
ν = kinematic viscosity
$\boldsymbol{\omega}$ = vorticity
Ω = angular rotating speed
$\boldsymbol{\tau}$ = skin friction on solid surface

References

[1] Wu, J. Z., and Wu, J. M., 1996, "Vorticity Dynamics on Boundaries," Adv. Appl. Mech., **32**, pp. 119–275.
[2] Wu, J. Z., Roach, R. L., Lo, C. F., Zhu, F. L., Dowgwillo, R. M., Jiang, L. B., and Tramel, R. W., 1999, "Aerodynamic Diagnostics and Design Based on Boundary Vorticity Dynamics," Paper No. AIAA-99-3103.
[3] Wu, J. Z., and Wu, J. M., 1993, "Interaction Between a Solid Body and a Viscous Compressible Flow Field," J. Fluid Mech., **254**, pp. 183–211.
[4] Wu, J. Z., Ma, H. Y., and Zhou, M. D., 2006, *Vorticity and Vortex Dynamics*, Springer, New York.
[5] Lighthill, M. J., 1963, "Introduction: Boundary Layer Theory," *Laminar Boundary Layer*, Oxford University Press, Oxford, pp. 46–113.
[6] Wu, J. Z., Tramel, R. W., Zhu, F. L., and Yin, X. Y., 2000, "A Vorticity Dynamics Theory of Three-Dimensional Flow Separation," Phys. Fluids, **12**(8), pp. 1932–1954.
[7] Li, Q. S., and Guo, M., 2005, "Diagnosis and Design of a Low Speed Compressor Based on Local Dynamics," Prog. Nat. Sci., **15**(2), pp. 221–228.
[8] Yang, Y. T., Wu, H., Li, Q. S., Zhou, S., and Wu, J. Z., 2008, "Vorticity Dynamics in Axial Compressor Flow Diagnosis and Design," ASME J. Fluids Eng., **130**, p. 041102.
[9] Greitzer, E. M., Tan, C. S., and Graf, M. B., 2004, *Internal Flow, Concepts and Applications*, Cambridge University Press, Cambridge, pp. 145–148.

Slip Flow in the Hydrodynamic Entrance Region of Circular and Noncircular Microchannels

Zhipeng Duan
Department of Mechanical and Mechatronics Engineering,
University of Waterloo,
Waterloo, ON, N2L 3G1, Canada
e-mail: zpduan@uwaterloo.ca

Y. S. Muzychka
Faculty of Engineering and Applied Science,
Memorial University of Newfoundland,
St. John's, NL, A1B 3X5, Canada

Microscale fluid dynamics has received intensive interest due to the emergence of micro-electro-mechanical systems (MEMS) technology. When the mean free path of the gas is comparable to the channel's characteristic dimension, the continuum assumption is no longer valid and a velocity slip may occur at the duct walls. Noncircular cross sections are common channel shapes that can be produced by microfabrication. The noncircular microchannels have extensive practical applications in MEMS. The paper deals with issues of hydrodynamic flow development. Slip flow in the entrance of circular and parallel plate microchannels is first considered by solving a linearized momentum equation. It is found that slip flow is less sensitive to analytical linearized approximations than continuum flow and the linearization method is an accurate approximation for slip flow. Also, it is found that the entrance friction factor Reynolds product is of finite value and dependent on the Kn and tangential momentum accommodation coefficient but independent of the cross-sectional geometry. Slip flow and continuum flow in the hydrodynamic entrance of noncircular microchannels has been examined and a model is proposed to predict the friction factor and Reynolds product f Re for developing slip flow and continuum flow in most noncircular microchannels. It is shown that the complete problem may be easily analyzed by combining the asymptotic results for short and long ducts. Through the selection of a characteristic length scale, the square root of cross-sectional area, the effect of duct shape has been minimized. The proposed model has an approximate accuracy of 10% for most common duct shapes. [DOI: 10.1115/1.4000692]

Keywords: slip flow, entrance, microchannels, noncircular, friction

1 Introduction

Fluid flow in microchannels has emerged as an important research area. This has been motivated by their various applications such as medical and biomedical uses, computer chips, and chemical separations. The advent of micro-electro-mechanical systems (MEMS) has opened up a new research area where noncontinuum behavior is important. MEMS are one of the major advances of industrial technologies in the past decades. Micron-size mechanical and biochemical devices are becoming more prevalent both in commercial applications and in scientific research.

Microchannels are the fundamental parts of microfluidic systems. Understanding the flow characteristics of microchannel flows is very important in determining pressure distribution, heat transfer, and transport properties of the flow. Microchannels can be defined as channels whose characteristic dimensions are from 1 μm to 1 mm. Generally, above 1 mm the flow exhibits a behavior that is the same as continuum flow. The noncircular cross sections such as rectangular, trapezoidal, double-trapezoidal, triangular, and hexagonal, are common channel shapes that may be produced by microfabrication. These cross sections have wide practical applications in MEMS [1–3].

The Knudsen number (Kn) relates the molecular mean free path of gas to a characteristic dimension of the duct. Knudsen number is very small for continuum flows. However, for microscale gas flows where the gas mean free path becomes comparable with the characteristic dimension of the duct, the Knudsen number may be greater than 10^{-3}. Microchannels with characteristic lengths on the order of 100 μm would produce flows inside the slip regime as a typical mean free path of gas is approximately 70 nm at standard conditions. The slip flow regime to be studied here is classified as $0.001 < \mathrm{Kn} < 0.1$.

2 Literature Review

Rarefaction effects must be considered in gases in which the molecular mean free path is comparable to the channel's characteristic dimension. The continuum assumption is no longer valid and the gas exhibits noncontinuum effects such as velocity slip and temperature jump at the channel walls. Traditional examples of noncontinuum gas flows in channels include low-density applications such as high-altitude aircraft or vacuum technology. The recent development of microscale fluid systems has motivated great interest in this field of study. There is strong evidence to support the use of Navier–Stokes and energy equations to model the slip flow problem, while the boundary conditions are modified by including velocity slip and temperature jump at the channel walls [2,4–10].

The small length scales commonly encountered in microfluidic devices suggest that rarefaction effects are important. For example, experiments conducted by Pfahler and co-workers [11,12], Harley et al. [13], Choi et al. [14], Arkilic and co-workers [6,7], Wu et al. [15], and Araki et al. [10] on the transport of gases in microchannels confirm that continuum analyses are unable to predict flow properties in microsized devices.

Arkilic and co-workers [6,7] investigated helium flow through microchannels. The results showed that the pressure drop was less than the continuum flow results. The friction coefficient was only about 40% of the theoretical values. The significant reduction in the friction coefficient may be due to the slip flow regime, as according to the flow regime classification by Schaaf and Chambre [16], the flows studied by Arkilic and co-workers [6,7] are mostly within the slip flow regime, only bordering the transition

---

Contributed by the Fluids Engineering Division of ASME for publication in the Journal of Fluids Engineering. Manuscript received December 26, 2008; final manuscript received November 6, 2009; published online December 21, 2009. Assoc. Editor: Neelesh A. Patankar.

regime near the outlet. When using the Navier–Stokes equations with slip flow boundary conditions, the model was able to predict the flow accurately.

Araki et al. [10] investigated frictional characteristics of nitrogen and helium flows through three different trapezoidal microchannels whose hydraulic diameter is from 3 μm to 10 μm. The measured friction factor was smaller than that predicted by the conventional theory. They concluded that this deviation was caused by the rarefaction effects.

Liu et al. [9] also proved that the solution to the Navier–Stokes equation combined with slip flow boundary conditions show good agreement with the experimental data in microchannel flow.

Maurer et al. [17] conducted experiments for helium and nitrogen flows in 1.14 μm deep, 200 μm wide shallow microchannels. Flow rate and pressure drop measurements in the slip and early transition regimes were performed for averaged Knudsen numbers extending up to 0.8 for helium and 0.6 for nitrogen. The authors also provided estimates for second-order effects and found the upper limit of slip flow regime as the averaged Knudsen number equals 0.3 ± 0.1.

Colin and Aubert [18] studied slip flow in rectangular microchannels using the second-order boundary conditions proposed by Deissler [19]. In a later study, Colin et al. [20] presented experimental results for nitrogen and helium flows in a series of silicon rectangular microchannels. The authors proposed that the second-order slip flow model is valid for Knudsen numbers up to about 0.25.

A variety of researchers attempted to develop second-order slip models that can be used in the transition regime. However, there are large variations in the second-order slip coefficient [2]. The lack of a universally accepted second-order slip coefficient is a major problem in extending Navier–Stokes equations into the transition regime [21].

Jeong et al. [22] studied gaseous slip flow in rectangular microchannels by the lattice Boltzmann equation method. The effects of the aspect ratio of the channel and the outlet Knudsen number on pressure nonlinearity, slip velocity, and mass flow rate were investigated. Their results agree well with parallel plate microchannel limiting cases.

Barber and Emerson [23] conducted an investigation of gaseous slip flow at the entrance of circular and parallel plate microchannels using a two-dimensional Navier–Stokes solver. They indicated that the Knudsen number have a significant effect on the hydrodynamic entrance length to parallel plates. The hydrodynamic entrance length for parallel plates could be approximately 25% longer than the corresponding continuum solution.

For developing continuum flow ($\mathrm{Kn} \to 0$), some tabulated data or models exist for some geometries in advanced texts such as Shah and London [24]. However, for developing slip flow, only parallel plates and circular ducts are considered in the literature due to the slip boundary conditions, which make this particular hydrodynamically developing flow problem, even more complicated. A survey of the available literature indicates a shortage of information for three-dimensional entrance flows in the slip regime, such as short noncircular microchannels where the entrance region plays a very important role. There currently is no published model or tabulated data for friction factor and Reynolds number product that can be utilized by the research community. The entrance region in a microchannel is particularly of interest due to the presence of comparatively large pressure drop and heat transfer. Given that the convective heat transfer behavior in the developing region differs from that in the fully developed region, and given that many microchannel heat exchangers are short, this effect of entrance region is significant. The f_{app} Re could be significantly higher than the fully developed value of f Re. The present work is more general and the common continuum flow formulation is only a special case ($\mathrm{Kn} \to 0$) of the present proposed formulation.

3 Theoretical Analysis

One of the most fundamental problems in fluid dynamics is that of fully developed laminar flow in circular and noncircular channels under constant pressure gradient. Upon obtaining the velocity distribution $u(x,y)$ and mean velocity $\bar{u}$, the friction factor Reynolds number parameter may be defined using the simple expression denoted in some texts as the Poiseuille number

$$\mathrm{Po}_{\ell} = \frac{\bar{\tau}\ell}{\mu\bar{u}} = \frac{\left(-\dfrac{A}{P}\dfrac{dp}{dz}\right)\ell}{\mu\bar{u}} = \frac{f\ \mathrm{Re}_{\ell}}{2} \tag{1}$$

The above grouping Po is interpreted as the dimensionless average wall shear. The mean wall shear stress may also be related to the pressure gradient by means of the force balance $\bar{\tau} = -A/P dp/dz$.

When a viscous fluid enters a duct with the uniform velocity distribution at the entrance, boundary layers develop along the walls and the velocity is gradually redistributed due to the viscosity. Eventually the fluid will reach a location where the velocity is independent of the axial direction, and under such conditions the flow is termed the hydrodynamically fully developed. The hydrodynamic entrance length is defined as the duct length required to achieve a maximum velocity of 99% of that for fully developed flow. Following Sparrow et al. [25], slip flow in the entrance of circular and parallel plate microchannels is first considered by solving a linearized momentum equation, respectively. The assumptions of the present analysis can be summarized as: steady-state laminar flow, constant fluid properties, negligible body forces such as gravity, and electromagnetic. In this analysis the compressibility effects can be neglected for short microchannels. Later, we will demonstrate that the boundary layer behavior in the tube entry is substantially identical with that on a flat plate.

3.1 Circular Tubes. The equations of continuity and momentum in cylindrical coordinates are

$$\frac{1}{r}\frac{\partial}{\partial r}(rv) + \frac{\partial u}{\partial x} = 0 \tag{2}$$

$$v\frac{\partial u}{\partial r} + u\frac{\partial u}{\partial x} = -\frac{1}{\rho}\frac{dp}{dx} + \frac{\nu}{r}\frac{\partial}{\partial r}\left(r\frac{\partial u}{\partial r}\right) \tag{3}$$

It is assumed that dp/dx is independent of r, which involves idealization and has been generally applied in entrance region theoretical analyses.

By using the continuity equation (2), Eq. (3) can be rewritten as

$$\frac{\partial}{\partial x}(ru^2) + \frac{\partial}{\partial r}(ruv) = -\frac{r}{\rho}\frac{dp}{dx} + \nu\frac{\partial}{\partial r}\left(r\frac{\partial u}{\partial r}\right) \tag{4}$$

Integrating Eq. (4) with respect to r from $r=0$ to R and using the boundary conditions $v(0)=v(R)=0$, there we obtain

$$-\frac{1}{\rho}\frac{dp}{dx} = \frac{2}{R^2}\frac{\partial}{\partial x}\int_0^R ru^2 dr - \frac{2\nu}{R}\left(\frac{\partial u}{\partial r}\right)_{r=R} \tag{5}$$

Eliminating dp/dx from Eqs. (3) and (5), adding $\bar{u}(\partial u/\partial x)$ to both sides and rearranging

$$\begin{aligned} \bar{u}\frac{\partial u}{\partial x} + \frac{2\nu}{R}\left(\frac{\partial u}{\partial r}\right)_{r=R} - \frac{\nu}{r}\frac{\partial}{\partial r}\left(r\frac{\partial u}{\partial r}\right) &= (\bar{u}-u)\frac{\partial u}{\partial x} - v\frac{\partial u}{\partial r} \\ &\quad + \frac{2}{R^2}\frac{\partial}{\partial x}\int_0^R ru^2 dr \end{aligned} \tag{6}$$

The cross-sectional average of the terms on the right side of Eq. (6) is zero. This follows by integrating Eq. (6) across the section and employing that $\partial/\partial x(\int_0^R ru dr)$ is zero from the continuity equation. Hence, the right side is equated to zero as a linearizing approximation. The equation to be solved becomes

$$\frac{\nu}{r}\frac{\partial}{\partial r}\left(r\frac{\partial u}{\partial r}\right)=\bar{u}\frac{\partial u}{\partial x}+\frac{2\nu}{R}\left(\frac{\partial u}{\partial r}\right)_{r=R} \tag{7}$$

From the above analysis we obtain Targ's linearization results [24,26]. Introducing the dimensionless variables $\xi=(x/D)/(\bar{u}D/\nu)$, $\eta=r/R$, and $U=u/\bar{u}$, Eq. (7) becomes

$$\frac{1}{\eta}\frac{\partial}{\partial \eta}\left(\eta\frac{\partial U}{\partial \eta}\right)=\frac{1}{4}\frac{\partial U}{\partial \xi}+2\left(\frac{\partial U}{\partial \eta}\right)_{\eta=1} \tag{8}$$

The velocity distribution must satisfy the slip boundary condition at the walls. The local slip velocity is proportional to the local velocity gradient normal to the wall. The appropriate boundary conditions are

$$U(1,\xi)=-\frac{2-\sigma}{\sigma}2\ \mathrm{Kn}(\partial U/\partial\eta)_{\eta=1} \tag{9}$$

$$\left(\frac{\partial U}{\partial \eta}\right)_{\eta=0}=0 \tag{10}$$

$$U(\eta,0)=1 \tag{11}$$

$$U(\eta,\infty)=U_{\mathrm{fd}}(\eta) \tag{12}$$

where σ denotes tangential momentum accommodation coefficient, which is usually between 0.87 and 1 [5]. The most usual conditions correspond to $\sigma\approx 1$; therefore, σ may be assumed have a value of unity. The same procedure is valid even if $\sigma\neq 1$, defining a modified Knudsen number as $\mathrm{Kn}^*=\mathrm{Kn}(2-\sigma)/\sigma$. The Knudsen number is defined as $\mathrm{Kn}=\lambda/D_h$ and λ is the molecular mean free path.

We can write a solution of the form

$$U(\eta,\xi)=U_{\mathrm{fd}}(\eta)+V(\eta,\xi) \tag{13}$$

where $V(\eta,\xi)$ is the deviation from the fully developed flow velocity distribution. It is obvious that V approaches zero for large ξ.

Substituting Eq. (13) into Eq. (8), we find that $U_{\mathrm{fd}}(\eta)$ satisfies the equation

$$\frac{1}{\eta}\frac{\partial}{\partial \eta}\left(\eta\frac{dU_{\mathrm{fd}}}{d\eta}\right)=2\left(\frac{dU_{\mathrm{fd}}}{d\eta}\right)_{\eta=1} \tag{14}$$

and $V(\eta,\xi)$ satisfies the equation

$$\frac{1}{\eta}\frac{\partial}{\partial \eta}\left(\eta\frac{\partial V}{\partial \eta}\right)=\frac{1}{4}\frac{\partial V}{\partial \xi}+2\left(\frac{\partial V}{\partial \eta}\right)_{\eta=1} \tag{15}$$

A solution of Eq. (14) may be obtained using Eqs. (9) and (10) and the continuity condition $\int_0^1\eta U_{\mathrm{fd}}(\eta)d\eta=1/2$ [27]

$$U_{\mathrm{fd}}(\eta)=\frac{8\frac{2-\sigma}{\sigma}\mathrm{Kn}}{1+8\frac{2-\sigma}{\sigma}\mathrm{Kn}}+\frac{2}{1+8\frac{2-\sigma}{\sigma}\mathrm{Kn}}(1-\eta^2) \tag{16}$$

Equation (15) can be solved using the separation of variables method. Thus,

$$V(\eta,\xi)=F(\xi)G(\eta) \tag{17}$$

Substituting Eq. (17) into Eq. (15), we obtain

$$F_i(\xi)=C_i\exp(-4\alpha_i^2\xi) \tag{18}$$

$$\frac{1}{\eta}\frac{d}{d\eta}\left(\eta\frac{dG_i}{d\eta}\right)+\alpha_i^2G_i=2\left(\frac{dG_i}{d\eta}\right)_{\eta=1} \tag{19}$$

where α_i are the eigenvalues.

We find that a particular solution of Eq. (19) is

$$G_i^p(\eta)=\frac{2}{\alpha_i^2}\left(\frac{dG_i}{d\eta}\right)_{\eta=1} \tag{20}$$

The homogeneous equation is Bessel's equation of zero order and the solution is

$$G_i^h(\eta)=A_iJ_0(\alpha_i\eta)+B_iY_0(\alpha_i\eta) \tag{21}$$

In terms of Eq. (10), $B_i=0$, and thus the solution of Eq. (19) is

$$G_i(\eta)=G_i^p(\eta)+G_i^h(\eta)=A_iJ_0(\alpha_i\eta)+\frac{2}{\alpha_i^2}\left(\frac{dG_i}{d\eta}\right)_{\eta=1} \tag{22}$$

then

$$\left(\frac{dG_i}{d\eta}\right)_{\eta=1}=-\alpha_iA_iJ_1(\alpha_i) \tag{23}$$

Therefore, the solution for $G_i(\eta)$ is obtained

$$G_i(\eta)=\frac{A_i}{\alpha_i}[\alpha_iJ_0(\alpha_i\eta)-2J_1(\alpha_i)] \tag{24}$$

According to boundary condition Eq. (9), we find the eigenvalue α_i satisfies the following equation:

$$\alpha_iJ_0(\alpha_i)-2\left(1+\frac{2-\sigma}{\sigma}\mathrm{Kn}\ \alpha_i^2\right)J_1(\alpha_i)=0 \tag{25}$$

In addition, the coefficients A_i can be chosen so as to normalize the G_i in terms of the Sturm–Liouville orthogonality conditions, that is, $\int_0^1\eta G_i^2d\eta=0.5$

$$A_i=\left[\frac{2\alpha_i^2}{\alpha_i^2J_0^2(\alpha_i)+(\alpha_i^2-4)J_1^2(\alpha_i)}\right]^{1/2} \tag{26}$$

Thus, the G_i form a complete orthonormal set.

Applying the entrance condition, Eq. (11)

$$V(\eta,0)=1-U_{\mathrm{fd}}(\eta)=\sum_{i=1}^{\infty}C_iG_i(\eta)$$

Using the orthonormality properties of G_i, the coefficient C_i can be determined

$$C_i=\frac{2}{1+8\frac{2-\sigma}{\sigma}\mathrm{Kn}}\int_0^1\eta^3G_i(\eta)d\eta \tag{27}$$

Substituting Eq. (24) into Eq. (27), we obtain

$$C_i=\frac{A_i}{\alpha_i^3\left(1+8\frac{2-\sigma}{\sigma}\mathrm{Kn}\right)}[4\alpha_iJ_0(\alpha_i)+(\alpha_i^2-8)J_1(\alpha_i)] \tag{28}$$

Therefore,

$$\begin{aligned}V(\eta,\xi)&=\sum_{i=1}^{\infty}\frac{A_iC_i}{\alpha_i}\exp(-4\alpha_i^2\xi)[\alpha_iJ_0(\alpha_i\eta)-2J_1(\alpha_i)]\\&=\sum_{i=1}^{\infty}\frac{4\left(1+\alpha_i^2\frac{2-\sigma}{\sigma}\mathrm{Kn}\right)}{\alpha_i^2\left[1+8\frac{2-\sigma}{\sigma}\mathrm{Kn}+4\left(\alpha_i\frac{2-\sigma}{\sigma}\mathrm{Kn}\right)^2\right]}\left[\frac{J_0(\alpha_i\eta)}{J_0(\alpha_i)}\right.\\&\quad\left.-\frac{2}{2+2\alpha_i^2\frac{2-\sigma}{\sigma}\mathrm{Kn}}\right]\exp(-4\alpha_i^2\xi)\end{aligned} \tag{29}$$

Finally, the complete velocity solution is

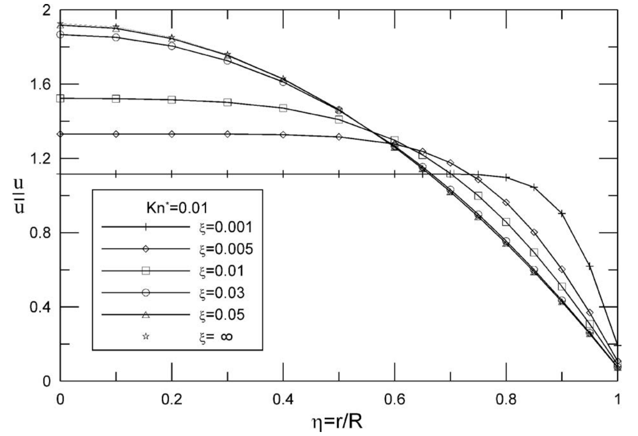

Fig. 1 Effect of ξ on the development of velocity profiles for $\mathrm{Kn}^*=0.01$ for circular tubes

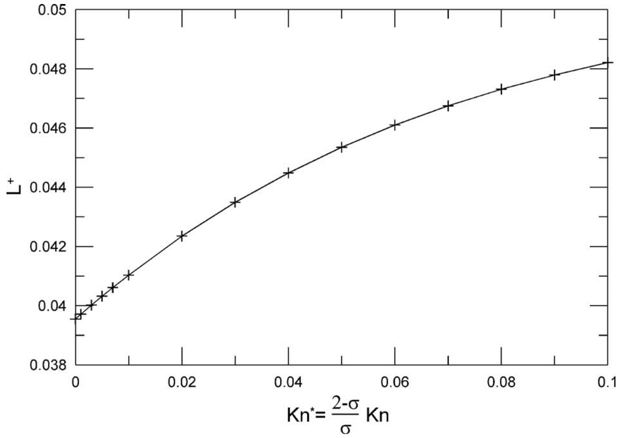

Fig. 2 Entrance length for which $U(0,\xi)=0.99U_{\mathrm{fd}}(0)$ for circular tubes

$$U(\eta,\xi)=\frac{8\frac{2-\sigma}{\sigma}\mathrm{Kn}}{1+8\frac{2-\sigma}{\sigma}\mathrm{Kn}}+\frac{2}{1+8\frac{2-\sigma}{\sigma}\mathrm{Kn}}(1-\eta^2)+\sum_{i=1}^{\infty}\frac{4\left(1+\alpha_i^2\frac{2-\sigma}{\sigma}\mathrm{Kn}\right)}{\alpha_i^2\left[1+8\frac{2-\sigma}{\sigma}\mathrm{Kn}+4\left(\alpha_i\frac{2-\sigma}{\sigma}\mathrm{Kn}\right)^2\right]}+\left[\frac{J_0(\alpha_i\eta)}{J_0(\alpha_i)}-\frac{2}{2+2\alpha_i^2\frac{2-\sigma}{\sigma}\mathrm{Kn}}\right]\exp(-4\alpha_i^2\xi) \quad (30)$$

Figure 1 shows the effect of ξ on the development of the velocity for $\mathrm{Kn}^*=0.01$. The development of the velocity distribution can be clearly portrayed by a sequence of velocity profiles at various axial positions along the pipe, as shown in Fig. 1. Near the immediate neighborhood of the entrance, the velocity is nearly flat over the entire section and drops off only near the wall. The velocity gradients are substantially smaller than in a continuum flow. With increasing distance from the entrance, the region of uniform velocity becomes smaller and the slip velocity also diminishes with the diminishing velocity gradients at the wall. The final velocity profile is a flatter parabola than the well-known Poiseuille parabola in the continuum flow. The profiles suggest the presence of an inviscid core flow, which is gradually deteriorated by the boundary layers developing along the walls of the channel. Figure 2 illustrates the role of the Reynolds number and Knudsen number on the hydrodynamic entrance length. The dimensionless hydrodynamic entrance length is a function of Reynolds number and Knudsen number. The hydrodynamic entrance length is useful when designing a microfluidic device to account for the entrance effects or choosing an appropriate location for the upstream boundary of an accurate numerical model. The values of the dimensionless entrance development length L^+ corresponding to the point where $U(0,\xi)=0.99U_{\mathrm{fd}}(0)$. They are fitted a simple correlation

$$L^+=0.0396\left[1+3.7\frac{2-\sigma}{\sigma}\mathrm{Kn}-15\left(\frac{2-\sigma}{\sigma}\mathrm{Kn}\right)^2\right] \quad (31)$$

For the continuum flow entrance length, Atkinson et al. [28] presented a simple relationship. The following equation is a linear combination of creeping flow ($\mathrm{Re}\rightarrow 0$) and boundary layer type solutions:

$$\frac{L}{D}=0.59+0.056\ \mathrm{Re} \quad (32)$$

The entrance length predicted by Eq. (32) is somewhat higher than experimental values. Chen [29] suggested a better form using the development length data of Friedmann et al. [30]

$$\frac{L}{D}=\frac{0.60}{0.035\ \mathrm{Re}+1}+0.056\ \mathrm{Re} \quad (33)$$

The entrance length does not vanish as Re approaches zero. It still takes about 0.6 tube diameter. Finally, we present a relationship for slip flow entrance length

$$\frac{L}{D}=\frac{0.60}{0.035\ \mathrm{Re}+1}+0.0396\ \mathrm{Re}\left[1+3.7\frac{2-\sigma}{\sigma}\mathrm{Kn}-15\left(\frac{2-\sigma}{\sigma}\mathrm{Kn}\right)^2\right] \quad (34)$$

where we use the first term of Chen's development length formula [29] in order to take into account the effect of creeping flow ($\mathrm{Re}\rightarrow 0$). Sreekanth [31] calculated the entrance lengths of his experiments and found that they agree with values predicted by the expression $L^+=C/4$, where C has a value between 0.15 and 0.2 depending on the Kn. Therefore, Sreekanth's experiments [31] approximately agree with Eq. (31).

The pressure drop between the entrance and any station downstream can be found by integrating the momentum equation. Equation (5) can be written as

$$-\frac{1}{4\left(\frac{1}{2}\rho\bar{u}^2\right)}\frac{dp}{d\xi}=\frac{\partial}{\partial\xi}\int_0^1\eta U^2(\eta,\xi)d\eta-4\left(\frac{\partial U}{\partial\eta}\right)_{\eta=1} \quad (35)$$

Under fully developed conditions, the inertia terms in Eq. (35) disappear. Therefore,

$$\frac{1}{4\left(\frac{1}{2}\rho\bar{u}^2\right)}\frac{dp}{d\xi}=4\left(\frac{\partial U_{\mathrm{fd}}}{\partial\eta}\right)_{\eta=1} \quad (36)$$

Equation (36) is integrated between 0 and ξ, giving

$$\frac{[p(0)-p(\xi)]_{\text{fd}}}{\frac{1}{2}\rho\bar{u}^2} = -16\int_0^{\xi} \left(\frac{\partial U_{\text{fd}}}{\partial \eta}\right)_{\eta=1} d\xi = \frac{64\xi}{1+8\frac{2-\sigma}{\sigma}\text{Kn}} \tag{37}$$

It is convenient to report the pressure drop in a developing flow as equal to that for a fully developed flow plus a correction term $K(\xi)$ representing additional pressure drop, which exceeds the fully developed pressure drop. Thus,

$$\frac{p(0)-p(\xi)}{\frac{1}{2}\rho\bar{u}^2} = \frac{64\xi}{1+8\frac{2-\sigma}{\sigma}\text{Kn}} + K(\xi) \tag{38}$$

Integrating Eq. (35) between 0 and ξ, we can obtain the following expression:

$$\frac{p(0)-p(\xi)}{\frac{1}{2}\rho\bar{u}^2} = 4\left[\int_0^1 \eta U^2 d\eta - \frac{1}{2} - 4\int_0^{\xi}\left(\frac{\partial U}{\partial \eta}\right)_{\eta=1} d\xi\right] \tag{39}$$

Thus,

$$\begin{aligned} K(\xi) &= 4\left[\int_0^1 \eta U^2 d\eta - \frac{1}{2} - 4\int_0^{\xi}\left(\frac{\partial V}{\partial \eta}\right)_{\eta=1} d\xi\right] \\ &= \frac{4}{3\left(1+8\frac{2-\sigma}{\sigma}\text{Kn}\right)^2} \\ &\quad - 8\sum_{i=1}^{\infty} \frac{[3-\exp(-4\alpha_i^2\xi)]\exp(-4\alpha_i^2\xi)}{\alpha_i^2\left(1+8\frac{2-\sigma}{\sigma}\text{Kn}+4\left(\alpha_i\frac{2-\sigma}{\sigma}\text{Kn}\right)^2\right)} \end{aligned} \tag{40}$$

From an inspection of Eq. (40), it is found that $K(0)$ is zero and $K(\infty)$ is given by

$$K(\infty) = \frac{4}{3\left(1+8\frac{2-\sigma}{\sigma}\text{Kn}\right)^2} \tag{41}$$

which is the fully developed value of incremental pressure drop factor.

Substituting Eq. (40) into Eq. (38), the apparent friction factor Reynolds product for circular tubes can be obtained

$$\begin{aligned} f_{\text{app}}\ \text{Re}_{D_h} &= \frac{16}{1+8\frac{2-\sigma}{\sigma}\text{Kn}} + \frac{1}{3\xi\left(1+8\frac{2-\sigma}{\sigma}\text{Kn}\right)^2} \\ &\quad - 2\sum_{i=1}^{\infty} \frac{(3-\exp(-4\alpha_i^2\xi))\exp(-4\alpha_i^2\xi)}{\alpha_i^2\xi\left(1+8\frac{2-\sigma}{\sigma}\text{Kn}+4\left(\alpha_i\frac{2-\sigma}{\sigma}\text{Kn}\right)^2\right)} \end{aligned} \tag{42}$$

Effect of Kn on f_{app} Re for developing laminar flow is illustrated in Fig. 3. It is seen that the effect of increasing Kn is to decrease apparent friction factor. The eigenvalues α_i are given in Table 1. The eigenvalues possess the characteristic that $\alpha_{i+1}-\alpha_i \to \pi$ as i becomes large. It is found that twenty eigenvalues are sufficient accurate for all values of ξ of interest. The negative exponentials cause rapid convergence, especially if ξ is not too small. As an illustration, for practical application $\xi=0.01$, only three terms are required. Thirty eigenvalues should be used when ξ is very small ($\xi=0.0001$).

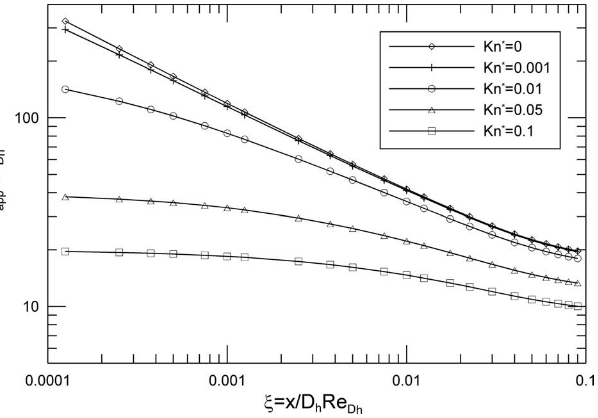

Fig. 3 Effect of Kn* on f_{app} Re for developing laminar flow for circular tubes

3.2 Parallel Plates. Next, we consider the flow in hydrodynamic entrance region under slip conditions between parallel plate microchannels. The microchannel height is $2h$ and there is symmetry about $y=0$. The equations of continuity and momentum in Cartesian coordinates are

$$\frac{\partial u}{\partial x} + \frac{\partial v}{\partial y} = 0 \tag{43}$$

$$u\frac{\partial u}{\partial x} + v\frac{\partial u}{\partial y} = -\frac{1}{\rho}\frac{dp}{dx} + \nu\frac{\partial^2 u}{\partial y^2} \tag{44}$$

It is assumed that dp/dx is independent of y, which involves idealization.

Using continuity Eq. (43), we can rewrite Eq. (44) as

$$\frac{\partial u^2}{\partial x} + \frac{\partial (uv)}{\partial y} = -\frac{1}{\rho}\frac{dp}{dx} + \nu\frac{\partial^2 u}{\partial y^2} \tag{45}$$

Integrating Eq. (45), with respect to y from $y=0$ to h and using the boundary conditions $v(0)=v(h)=0$, there we obtain

Table 1 Eigenvalues obtained from Eq. (25)

	Eigenvalues			
i	Kn*=0	Kn*=0.01	Kn*=0.05	Kn*=0.1
1	5.13562	5.03806	4.74142	4.51606
2	8.41724	8.25817	7.81634	7.54591
3	11.61984	11.40186	10.85911	10.59026
4	14.79595	14.52101	13.91224	13.66206
5	17.95982	17.62986	16.98106	16.75353
6	21.11700	20.73409	20.06384	19.85810
7	24.27011	23.83646	23.15780	22.97149
8	27.42057	26.93845	26.26044	26.09100
9	30.56920	30.04095	29.36979	29.21488
10	33.71652	33.14447	32.48437	32.34199
11	36.86286	36.24934	35.60308	35.47152
12	40.00845	39.35572	38.72508	38.60294
13	43.15345	42.46372	41.84973	41.73582
14	46.29800	45.57337	44.97654	44.86989
15	49.44216	48.68466	48.10514	48.00491
16	52.58602	51.79754	51.23522	51.14072
17	55.72963	54.91198	54.36656	54.27718
18	58.87302	58.02790	57.49896	57.41420
19	62.01622	61.14522	60.63226	60.55168
20	65.15927	64.26388	63.76635	63.68956

$$-\frac{1}{\rho}\frac{dp}{dx} = \frac{1}{h}\frac{\partial}{\partial x}\int_0^h u^2 dy - \frac{\nu}{h}\left(\frac{\partial u}{\partial y}\right)_{y=h} \tag{46}$$

Eliminating dp/dx from Eqs. (44) and (46), adding $\bar{u}(\partial u/\partial x)$ to both sides and rearranging

$$\bar{u}\frac{\partial u}{\partial x} + \frac{\nu}{h}\left(\frac{\partial u}{\partial y}\right)_{y=h} - \nu\frac{\partial^2 u}{\partial y^2} = (\bar{u}-u)\frac{\partial u}{\partial x} - v\frac{\partial u}{\partial y} + \frac{1}{h}\frac{\partial}{\partial x}\int_0^h u^2 dy \tag{47}$$

The cross-sectional average of the terms on the right side of Eq. (47) is zero. This follows by integrating Eq. (47) across the section and employing that $\partial/\partial x(\int_0^h u dy)$ is zero from the continuity equation. Hence, the right side is equated to zero as a linearizing approximation. The equation thus to be solved becomes

$$\nu\frac{\partial^2 u}{\partial y^2} = \bar{u}\frac{\partial u}{\partial x} + \frac{\nu}{h}\left(\frac{\partial u}{\partial y}\right)_{y=h} \tag{48}$$

Also, from the above analysis we obtain Targ's linearization results [24,26]. Introducing the dimensionless variables $\xi = (x/D_h)/(\bar{u}D_h/\nu)$, $\eta = y/h$, and $U = u/\bar{u}$, Eq. (48) becomes

$$\frac{\partial^2 U}{\partial \eta^2} = \frac{1}{16}\frac{\partial U}{\partial \xi} + \left(\frac{\partial U}{\partial \eta}\right)_{\eta=1} \tag{49}$$

The appropriate boundary conditions are

$$U(1,\xi) = -\frac{2-\sigma}{\sigma}4\ \mathrm{Kn}(\partial U/\partial \eta)_{\eta=1} \tag{50}$$

$$\left(\frac{\partial U}{\partial \eta}\right)_{\eta=0} = 0 \tag{51}$$

$$U(\eta,0) = 1 \tag{52}$$

$$U(\eta,\infty) = U_{\mathrm{fd}}(\eta) \tag{53}$$

We can write a solution of the form

$$U(\eta,\xi) = U_{\mathrm{fd}}(\eta) + V(\eta,\xi) \tag{54}$$

Substituting Eq. (54) into Eq. (49), we find that $U_{\mathrm{fd}}(\eta)$ satisfies the equation

$$\frac{d^2 U_{\mathrm{fd}}}{d\eta^2} = \left(\frac{dU_{\mathrm{fd}}}{d\eta}\right)_{\eta=1} \tag{55}$$

and $V(\eta,\xi)$ satisfies the equation

$$\frac{\partial^2 V}{\partial \eta^2} = \frac{1}{16}\frac{\partial V}{\partial \xi} + \left(\frac{\partial V}{\partial \eta}\right)_{\eta=1} \tag{56}$$

A solution of Eq. (55) may be obtained using Eqs. (50) and (51) and the continuity condition $\int_0^1 U_{\mathrm{fd}}(\eta)d\eta = 1$ [27]

$$U_{\mathrm{fd}}(\eta) = \frac{12\frac{2-\sigma}{\sigma}\mathrm{Kn}}{1+12\frac{2-\sigma}{\sigma}\mathrm{Kn}} + \frac{1.5}{1+12\frac{2-\sigma}{\sigma}\mathrm{Kn}}(1-\eta^2) \tag{57}$$

Equation (56) can be solved using separation of variables method. Thus,

$$V(\eta,\xi) = F(\xi)G(\eta) \tag{58}$$

Substituting Eq. (58) into Eq. (56), we obtain

$$F_i(\xi) = C_i \exp(-16\alpha_i^2\xi) \tag{59}$$

$$\frac{d^2 G_i}{d\eta^2} + \alpha_i^2 G_i = \left(\frac{dG_i}{d\eta}\right)_{\eta=1} \tag{60}$$

where α_i are the eigenvalues.

We find that a particular solution of Eq. (60) is

$$G_i^{p}(\eta) = \frac{1}{\alpha_i^2}\left(\frac{dG_i}{d\eta}\right)_{\eta=1} \tag{61}$$

The solution of the homogeneous equation is

$$G_i^{h}(\eta) = A_i\cos(\alpha_i\eta) + B_i\sin(\alpha_i\eta) \tag{62}$$

In terms of Eq. (51), $B_i=0$, and thus the solution of Eq. (60) is

$$G_i(\eta) = G_i^{p}(\eta) + G_i^{h}(\eta) = A_i\cos(\alpha_i\eta) + \frac{1}{\alpha_i^2}\left(\frac{dG_i}{d\eta}\right)_{\eta=1} \tag{63}$$

then

$$\left(\frac{dG_i}{d\eta}\right)_{\eta=1} = -\alpha_i A_i\sin(\alpha_i) \tag{64}$$

Therefore, the solution for $G_i(\eta)$ is obtained

$$G_i(\eta) = \frac{A_i}{\alpha_i}[\alpha_i\cos(\alpha_i\eta) - \sin(\alpha_i)] \tag{65}$$

According to boundary condition Eq. (50), we find the eigenvalue α_i satisfies the following equation:

$$\tan(\alpha_i) = \frac{\alpha_i}{1+4\alpha_i^2\frac{2-\sigma}{\sigma}\mathrm{Kn}} \tag{66}$$

Also, the coefficient A_i can be chosen in order to normalize the G_i in terms of the orthogonality conditions, that is $\int_{-1}^{1} G_i^2 d\eta = 1$

$$A_i = -\frac{1}{\sin(\alpha_i)}\left[1+12\frac{2-\sigma}{\sigma}\mathrm{Kn} + 16\left(\alpha_i\frac{2-\sigma}{\sigma}\mathrm{Kn}\right)^2\right]^{-1/2} \tag{67}$$

Applying the entrance condition, Eq. (52)

$$V(\eta,0) = 1 - U_{\mathrm{fd}}(\eta) = \sum_{i=1}^{\infty} C_i G_i(\eta)$$

Using the orthonormality properties of G_i, the coefficients C_i can be determined

$$C_i = \frac{1.5}{1+12\frac{2-\sigma}{\sigma}\mathrm{Kn}}\int_{-1}^{1}\eta^2 G_i(\eta)d\eta \tag{68}$$

Substituting Eq. (65) into Eq. (68), we obtain

$$C_i = \frac{2A_i\sin(\alpha_i)}{\alpha_i} \tag{69}$$

Therefore,

$$\begin{aligned} V(\eta,\xi) &= \sum_{i=1}^{\infty}\frac{2A_i^2\sin(\alpha_i)}{\alpha_i^2}[\alpha_i\cos(\alpha_i\eta) - \sin(\alpha_i)]\exp(-16\alpha_i^2\xi) \\ &= \sum_{i=1}^{\infty}\frac{2[\alpha_i\cos(\alpha_i\eta) - \sin(\alpha_i)]\exp(-16\alpha_i^2\xi)}{\alpha_i^2\sin(\alpha_i)\left[1+12\frac{2-\sigma}{\sigma}\mathrm{Kn} + 16\left(\alpha_i\frac{2-\sigma}{\sigma}\mathrm{Kn}\right)^2\right]} \end{aligned} \tag{70}$$

Finally, the complete velocity solution is

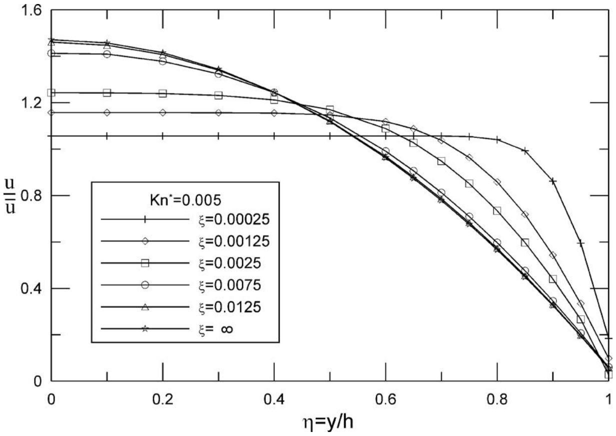

Fig. 4 Effect of ξ on the development of velocity profiles for $\mathrm{Kn}^*=0.005$ for parallel plates

$$U(\eta,\xi)=\frac{12\frac{2-\sigma}{\sigma}\mathrm{Kn}}{1+12\frac{2-\sigma}{\sigma}\mathrm{Kn}}+\frac{1.5}{1+12\frac{2-\sigma}{\sigma}\mathrm{Kn}}(1-\eta^2)+\sum_{i=1}^{\infty}\frac{2[\alpha_i\cos(\alpha_i\eta)-\sin(\alpha_i)]\exp(-16\alpha_i^2\xi)}{\alpha_i^2\sin(\alpha_i)\left[1+12\frac{2-\sigma}{\sigma}\mathrm{Kn}+16\left(\alpha_i\frac{2-\sigma}{\sigma}\mathrm{Kn}\right)^2\right]}\tag{71}$$

Figure 4 shows the effect of ξ on the development of the velocity for $\mathrm{Kn}^*=0.005$. The development of the flow is illustrated by a sequence of velocity profiles, as shown in Fig. 4. As with the circular tube, it is seen that the profiles in the immediate neighborhood of the entrance have a distinct flat portion in the region away from the channel wall. This may be interpreted as corresponding to an inviscid core flow. Due to continuity, retardation near the wall must cause the core flow to increase. With increasing distance from the entrance, the action of viscosity at the walls or boundary layers developing along the walls tends to deteriorate the core, and the flat potion contracts. Figure 5 illustrates the dimensionless entrance development length L^+ as a function of Kn $(0.001\leq\mathrm{Kn}\leq 0.1)$. The values of L^+ corresponding to the point where $U(0,\xi)=0.99U_{\mathrm{fd}}(0)$. They are fitted a simple correlation

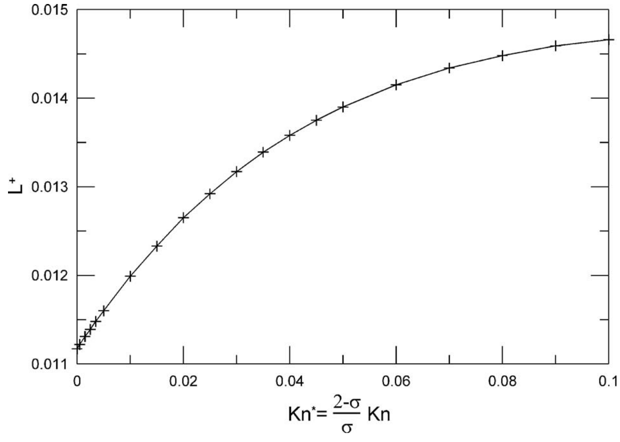

Fig. 5 Entrance length for which $U(0,\xi)=0.99U_{\mathrm{fd}}(0)$ for parallel plates

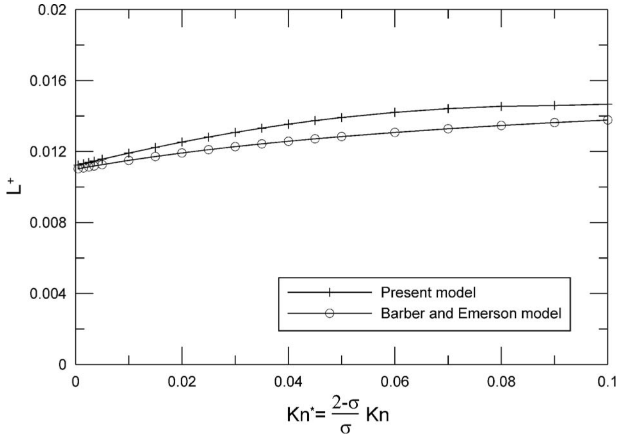

Fig. 6 Entrance length comparison for the Barber and Emerson [23] numerical model

$$L^+=0.0112\left[1+6.7\frac{2-\sigma}{\sigma}\mathrm{Kn}-37\left(\frac{2-\sigma}{\sigma}\mathrm{Kn}\right)^2\right]\tag{72}$$

For the continuum flow entrance length, Atkinson et al. [28] suggested a relationship

$$\frac{L}{D_h}=0.3125+0.011\ \mathrm{Re}\tag{73}$$

Chen [29] proposed an equation similar to Eq. (33)

$$\frac{L}{D_h}=\frac{0.315}{0.0175\ \mathrm{Re}+1}+0.011\ \mathrm{Re}\tag{74}$$

Finally, we suggest a relationship for slip flow entrance length

$$\frac{L}{D_h}=\frac{0.315}{0.0175\ \mathrm{Re}+1}+0.0112\ \mathrm{Re}\left[1+6.7\frac{2-\sigma}{\sigma}\mathrm{Kn}-37\left(\frac{2-\sigma}{\sigma}\mathrm{Kn}\right)^2\right]\tag{75}$$

where we use the first term of Chen's development length formula [29], Eq. (74). It is seen that the effect of slip is to increase the entrance length.

Barber and Emerson [23] also suggested a curve fitted model using numerical data

$$\frac{L}{D_h}=\frac{0.332}{0.0271\ \mathrm{Re}+1}+0.011\ \mathrm{Re}\left(\frac{1+14.78\frac{2-\sigma}{\sigma}\mathrm{Kn}}{1+9.78\frac{2-\sigma}{\sigma}\mathrm{Kn}}\right)\tag{76}$$

Figure 6 shows the comparison between present analytical model Eq. (75) and the Barber and Emerson numerical model Eq. (76) [23]. The difference between present analytical model and Barber and Emerson numerical model [23] is less than 8%.

The pressure drop between the entrance and any station downstream can be found by integrating the momentum equation. Equation (46) may be written as

$$-\frac{1}{2\left(\frac{1}{2}\rho\bar{u}^2\right)}\frac{dp}{d\xi}=\frac{\partial}{\partial\xi}\int_0^1 U^2(\eta,\xi)d\eta-16\left(\frac{\partial U}{\partial\eta}\right)_{\eta=1}\tag{77}$$

Under fully developed conditions, the inertia terms in Eq. (77) disappear. Therefore,

$$\frac{1}{2\left(\frac{1}{2}\rho\bar{u}^2\right)}\frac{dp}{d\xi} = 16\left(\frac{\partial U_{\mathrm{fd}}}{\partial \eta}\right)_{\eta=1} \tag{78}$$

Equation (78) is integrated between 0 and ξ, giving

$$\frac{[p(0)-p(\xi)]_{\mathrm{fd}}}{\frac{1}{2}\rho\bar{u}^2} = -32\int_0^{\xi}\left(\frac{\partial U_{\mathrm{fd}}}{\partial \eta}\right)_{\eta=1} d\xi = \frac{96\xi}{1+12\frac{2-\sigma}{\sigma}\mathrm{Kn}} \tag{79}$$

Thus,

$$\frac{p(0)-p(\xi)}{\frac{1}{2}\rho\bar{u}^2} = \frac{96\xi}{1+12\frac{2-\sigma}{\sigma}\mathrm{Kn}} + K(\xi) \tag{80}$$

Integrating Eq. (77) between 0 and ξ, we can obtain the following expression:

$$\frac{p(0)-p(\xi)}{\frac{1}{2}\rho\bar{u}^2} = 2\left[\int_0^1 U^2 d\eta - 1 - 16\int_0^{\xi}\left(\frac{\partial U}{\partial \eta}\right)_{\eta=1} d\xi\right] \tag{81}$$

Therefore,

$$\begin{aligned} K(\xi) &= 2\left[\int_0^1 U^2 d\eta - 1 - 16\int_0^{\xi}\left(\frac{\partial V}{\partial \eta}\right)_{\eta=1} d\xi\right] \\ &= \frac{0.8}{\left(1+12\frac{2-\sigma}{\sigma}\mathrm{Kn}\right)^2} \\ &\quad - 4\sum_{i=1}^{\infty}\frac{[3-\exp(-16\alpha_i^2\xi)]\exp(-16\alpha_i^2\xi)}{\alpha_i^2\left[1+12\frac{2-\sigma}{\sigma}\mathrm{Kn}+16\left(\alpha_i\frac{2-\sigma}{\sigma}\mathrm{Kn}\right)^2\right]} \end{aligned} \tag{82}$$

From an inspection of Eq. (82), it is found that $K(0)$ is zero and $K(\infty)$ is given by

$$K(\infty) = \frac{0.8}{\left(1+12\frac{2-\sigma}{\sigma}\mathrm{Kn}\right)^2} \tag{83}$$

Substituting Eq. (82) into Eq. (80), the apparent friction factor Reynolds product for parallel plates can be obtained

$$\begin{aligned} f_{\mathrm{app}}\ \mathrm{Re}_{D_h} &= \frac{24}{1+12\frac{2-\sigma}{\sigma}\mathrm{Kn}} + \frac{1}{5\xi\left(1+12\frac{2-\sigma}{\sigma}\mathrm{Kn}\right)^2} \\ &\quad - \sum_{i=1}^{\infty}\frac{(3-\exp(-16\alpha_i^2\xi))\exp(-16\alpha_i^2\xi)}{\alpha_i^2\xi\left[1+12\frac{2-\sigma}{\sigma}\mathrm{Kn}+16\left(\alpha_i\frac{2-\sigma}{\sigma}\mathrm{Kn}\right)^2\right]} \end{aligned} \tag{84}$$

Effect of Kn on f_{app} Re for developing laminar flow is illustrated in Fig. 7. It is seen that the effect of increasing Kn is to decrease apparent friction factor. The eigenvalues are determined from Eq. (66). It is found that twenty eigenvalues are sufficient accurate for all values of ξ of interest. The negative exponentials cause rapid convergence, especially when ξ is not too small. As an illustration, for practical application $\xi=0.01$, only two terms are required. When ξ is very small ($\xi=0.0001$), 20 eigenvalues should be employed.

Shapiro et al. [32], Shah and London [24], and Muzychka and Yovanovich [33] showed that Eq. (85) may be used to compute the friction factor for the short duct of most noncircular ducts ($\xi \leq 0.001$) for continuum flow (Kn → 0). All numerical results obtained from Eq. (42) or Eq. (84) almost reduce to their continuum limit Eq. (85) in the limit Kn → 0. The maximum difference is less than 3.9%

$$(f_{\mathrm{app}}\ \mathrm{Re}_{\ell})_c = \frac{3.44}{\sqrt{\xi}} \tag{85}$$

For slip flow, Fig. 8 also demonstrates that very near the inlet of circular and parallel plate ducts ($\xi \leq 0.001$), f_{app} Re is nearly equivalent and independent of duct shape. This is a further proof of the reliability of the proposed solutions. At the entrance of the duct, the velocity boundary layer starts developing at each wall under the imposed flow acceleration. As long as the thickness of the boundary layer is small compared with the duct dimensions, the boundary layers from different walls do not affect each other appreciably. This explains the reason why very near the inlet of ducts, f_{app} Re is nearly equivalent and independent of duct shape. Therefore, Eq. (42) or Eq. (84) may be used to compute the friction factor for the very short duct of noncircular shape. As the boundary layer develops further downstream ($\xi > 0.001$), the effects of geometry become more pronounced and the solutions for

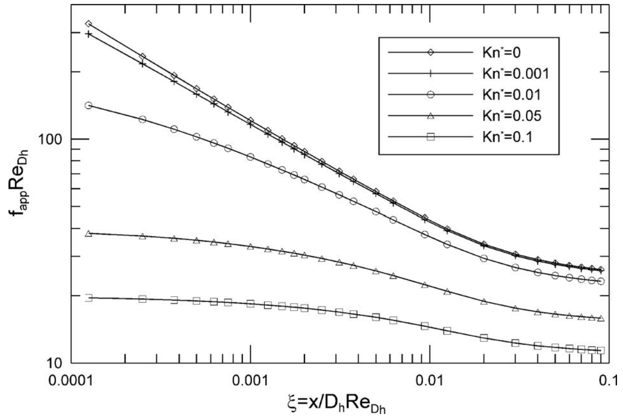

Fig. 7 Effect of Kn* on f_{app} Re for developing laminar flow for parallel plates

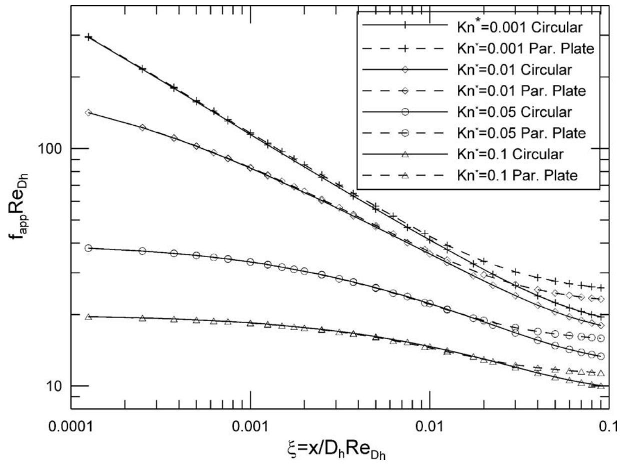

Fig. 8 Comparison of f_{app} Re for different Kn* between circular tubes and parallel plates

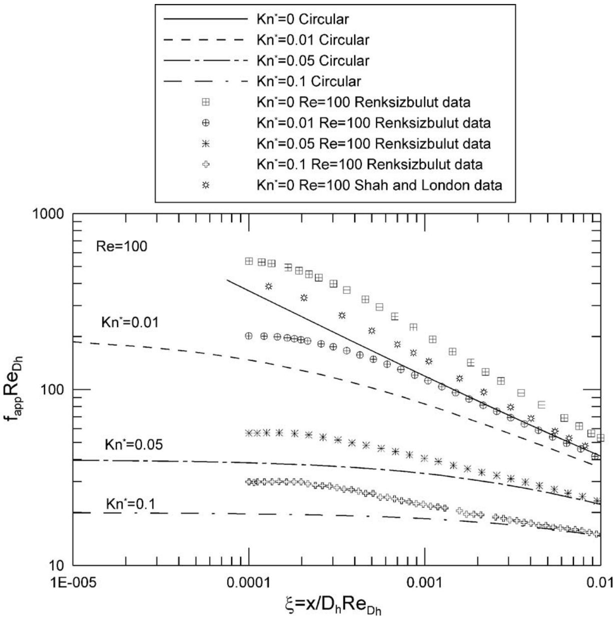

Fig. 9 Comparison of f_{app} Re for the numerical data by Renksizbulut et al. [35] for Re=100

circular tubes and parallel plates Eq. (42) or Eq. (84) are no longer valid for noncircular ducts.

Furthermore, the asymptotic limit of f_{app} Re for $\xi \rightarrow 0$ can be obtained by substituting velocity slip boundary condition into Eq. (1)

$$f_{app}\ \mathrm{Re} = \frac{2\bar{\tau}D_h}{\mu\bar{u}} = \frac{2\dfrac{\mu u}{\lambda\dfrac{2-\sigma}{\sigma}}D_h}{\mu\bar{u}} = \frac{u}{\bar{u}}\frac{2}{\mathrm{Kn}^*} \xrightarrow[\xi\rightarrow 0]{} \frac{2}{\mathrm{Kn}^*} \qquad (86)$$

After we cancel the common factors 2 and D_h we can write for the mean wall shear the following fundamental relationship:

$$\bar{\tau} = \frac{\mu\bar{u}}{\lambda\dfrac{2-\sigma}{\sigma}}$$

which is a fundamental relation for slip flow at the entrance. The foregoing relation can be obtained directly in a simple manner by application of scaling analysis to the slip boundary condition and Newton's law of viscosity. Yu and Ameel [34] gave the similar asymptotic limit of Nusselt number for slip flow heat transfer at the entrance of a conduit. The universal entrance Nusselt number expression is independent of the cross-sectional geometry and valid for any conduit geometry. This is consistent with the conclusions of the present hydrodynamic study.

Slip flow in the entrance region of rectangular microchannels was investigated numerically by Renksizbulut et al. [35]. Figure 9 demonstrates the comparison between Eq. (42) and the numerical data by Renksizbulut et al. [35] for different Knudsen numbers. The numerical data from Shah and London [24] for continuum flow are included in this figure. When $\xi=10^{-5}$ and $\mathrm{Kn}^*=0.1$, 0.05, and 0.01, f_{app} Re=19.9, 39.5, and 185.6, respectively, for the present analysis. Therefore, present analytical results agree very well with the asymptotic limiting values, whereas the results of Renksizbulut et al. [35] are in poor agreement with the asymptotic limiting values. This indicates that the linearization method is an accurate approximation for slip flow. It is found that the numerical data by Renksizbulut et al. [35] for square microchannels overpredict the values of f_{app} Re.

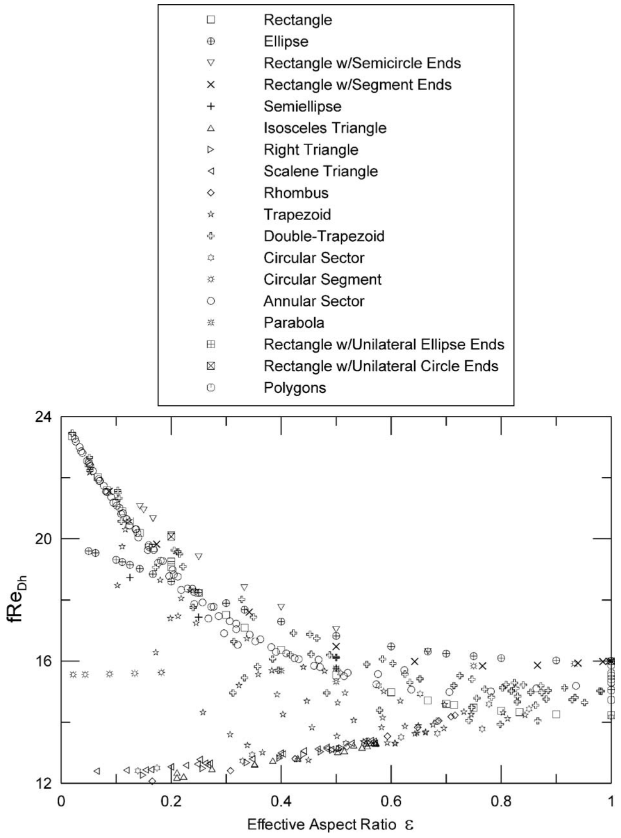

Fig. 10 Fully developed f Re_{D_h} for noncircular ducts [37]

3.3 General Model. For circular tubes, the choice of the length scale in the definition of Reynolds number is obvious. However, for noncircular ducts, the question always arises of what to use as the correct length scale. Although it is customary to use the hydraulic diameter, this choice is widely believed to be incorrect. Muzychka and Yovanovich [33] showed that the square root of cross-sectional area is more appropriate than the hydraulic diameter for nondimensionalizing the laminar continuum flow data. Duan and Muzychka [36] demonstrated that the same conclusion can be extended to the slip flow regime. Figures 10 and 11 [37] show that the square root of cross-sectional area is a more effective characteristic length scale than the hydraulic diameter for nondimensionalizing the fully developed laminar flow data. The data for some noncircular ducts reported as f Re_{D_h} are plotted versus the effective aspect ratio ε in Fig. 10. Some data increase with increasing values of ε while other values decrease with increasing values of ε. The next step in the comparisons is to convert all data from f Re_{D_h} to f $\mathrm{Re}_{\sqrt{A}}$ and replot versus the effective aspect ratio. When this is done, as shown in Fig. 11, all data follow closely a similar trend where the values decrease with increasing values of ε. It was found that the use of the hydraulic diameter in laminar flow situations yields greater scatter in results as compared with the use of $\sqrt{A}$ as a characteristic length scale. When $\sqrt{A}$ is used, the effect of the duct shape become minimized, and all of the laminar flow data can be predicted using a simple model based on the solution for the rectangular duct. That means dimensionless average wall shear stress can be made a weak function of duct shape.

If the friction factor Reynolds product for circular tubes is recast using $\sqrt{A}$ as a characteristic length scale in f $\mathrm{Re}_{\sqrt{A}}$, the following relationship is obtained:

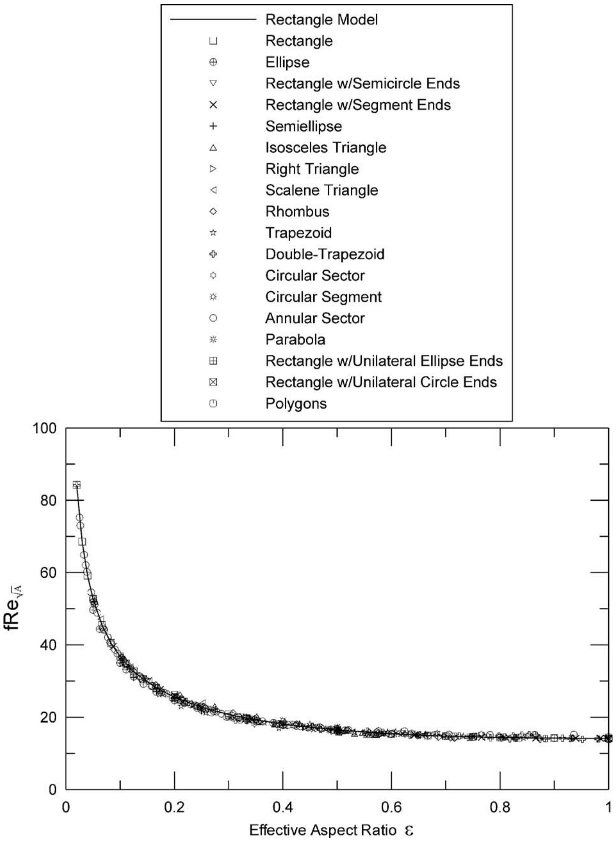

Fig. 11 Fully developed $f\ \mathrm{Re}_{\sqrt{A}}$ for noncircular ducts [37]

$$f_{\mathrm{app}}\ \mathrm{Re}_{\sqrt{A}} = \frac{16\frac{P}{4\sqrt{A}}}{1+8\frac{2-\sigma}{\sigma}\mathrm{Kn}} + \frac{4\sqrt{A}}{P}\left[\frac{1}{3\xi\left(1+8\frac{2-\sigma}{\sigma}\mathrm{Kn}\right)^2} - 2\sum_{i=1}^{\infty}\frac{\left(3-\exp\left(-\left(\frac{P}{4\sqrt{A}}\right)^2\alpha_i^2\xi\right)\right)\exp\left(-\left(\frac{P}{4\sqrt{A}}\right)^2\alpha_i^2\xi\right)}{\alpha_i^2\xi\left(1+8\frac{2-\sigma}{\sigma}\mathrm{Kn}+4\left(\alpha_i\frac{2-\sigma}{\sigma}\mathrm{Kn}\right)^2\right)}\right] \tag{87}$$

where

$$\xi = \frac{x}{\sqrt{A}\ \mathrm{Re}_{\sqrt{A}}}$$

For short duct asymptote ($\xi < 0.001$), we only consider the second term of right hand side of Eq. (87)

$$f\ \mathrm{Re}_{\sqrt{A}} = \frac{4\sqrt{A}}{P}\left[\frac{1}{3\xi\left(1+8\frac{2-\sigma}{\sigma}\mathrm{Kn}\right)^2} - 2\sum_{i=1}^{\infty}\frac{\left(3-\exp\left(-\left(\frac{P}{4\sqrt{A}}\right)^2\alpha_i^2\xi\right)\right)\exp\left(-\left(\frac{P}{4\sqrt{A}}\right)^2\alpha_i^2\xi\right)}{\alpha_i^2\xi\left(1+8\frac{2-\sigma}{\sigma}\mathrm{Kn}+4\left(\alpha_i\frac{2-\sigma}{\sigma}\mathrm{Kn}\right)^2\right)}\right] \tag{88}$$

Table 2 Definitions of effective aspect ratio [37]

Geometry	Effective aspect ratio
Regular polygons	$\varepsilon = 1, \quad N \geq 4$
Simple singly connected	$\varepsilon = \frac{b}{a}$
Trapezoid	$\varepsilon = \left[\left(\frac{2b}{a+c}\right)^n + \left(\frac{a+c}{2b}\right)^n\right]^{-1/n}, \quad n = 1.7$
Arbitrary triangle	$\varepsilon = \left[\left(\frac{2b}{a}\right)^n + \left(\frac{2a}{b}\right)^n\right]^{-1/n}, \quad n = 0.53$
Double-trapezoid	$\varepsilon = \left[\left(\frac{a+c}{2b}\right)^n + \left(\frac{1+\frac{c}{a}}{\frac{2a}{b}}\right)^n\right]^{-1/n}, \quad n = 2.8$
Rhombus	$\varepsilon = \left[\left(\frac{2b}{a}\right)^n + \left(\frac{2a}{b}\right)^n\right]^{-1/n}, \quad n = 0.68$
Circular annulus	$\varepsilon = \frac{1-r^*}{\pi(1+r^*)}$

Equation (88) is nearly independent of the duct shape and may be used to calculate the friction factor Reynolds product for the short asymptote of most noncircular ducts for slip flow.

The friction factor Reynolds product $f\ \mathrm{Re}$ for slip flow in long noncircular microchannels has been proposed by the authors [36] as follows:

$$f\ \mathrm{Re}_{\sqrt{A}} = \frac{1}{1+(11.97-10.59\varepsilon+8.49\varepsilon^2-2.11\varepsilon^3)\frac{2-\sigma}{\sigma}\mathrm{Kn}} \times \frac{12}{\sqrt{\varepsilon}(1+\varepsilon)\left[1-\frac{192\varepsilon}{\pi^5}\tanh\left(\frac{\pi}{2\varepsilon}\right)\right]} \tag{89}$$

The definition of aspect ratio proposed by Muzychka and Yovanovich [33] and Duan and Yovanovich [37] is summarized in Table 2 for a number of geometries. The aspect ratio for regular polygons is unity. The aspect ratio for most singly connected ducts is taken as the ratio of the maximum width to maximum length such that $0 < \varepsilon < 1$. For the trapezoid duct, double-trapezoid duct, triangle duct, rhombic duct, and the doubly connected duct, simple expressions have been derived to relate the characteristic dimensions of the duct to a width to length ratio.

A general model is now proposed using the Churchill and Usagi [38] asymptotic correlation method. The model takes the form

$$f\ \mathrm{Re}_{\sqrt{A}} = [(f\ \mathrm{Re}_{\sqrt{A}})^n_{\mathrm{long}} + (f\ \mathrm{Re}_{\sqrt{A}})^n_{\mathrm{short}}]^{1/n} \tag{90}$$

where n is a superposition parameter determined by comparison with numerical, analytical, and experimental data over the full range of ξ. Using the results provided by Eqs. (88) and (89), and the general expression, Eq. (90), the following model is proposed:

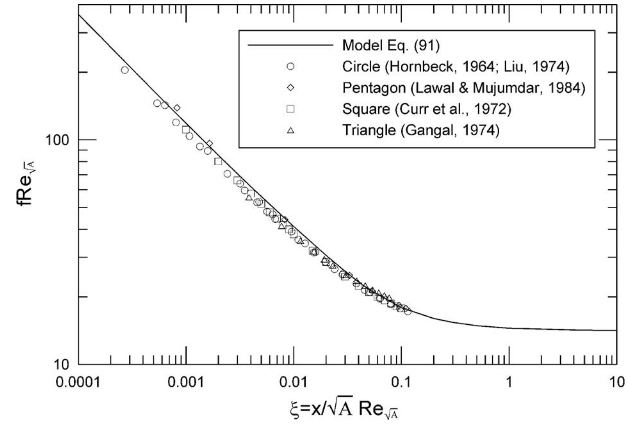

Fig. 12 Comparison of $f\ \mathrm{Re}_{\sqrt{A}}$ for polygonal ducts

$$f\ \mathrm{Re}_{\sqrt{A}} = \left(\frac{1}{1 + (11.97 - 10.59\varepsilon + 8.49\varepsilon^2 - 2.11\varepsilon^3)\frac{2-\sigma}{\sigma}\mathrm{Kn}} \times \frac{12}{\sqrt{\varepsilon}(1+\varepsilon)\left[1 - \frac{192\varepsilon}{\pi^5}\tanh\left(\frac{\pi}{2\varepsilon}\right)\right]} \right) + \frac{4\sqrt{A}}{P}\left(\frac{1}{3\xi\left(1 + 8\frac{2-\sigma}{\sigma}\mathrm{Kn}\right)^2} - 2\sum_{i=1}^{\infty} \frac{\left(3 - \exp\left(-\left(\frac{P}{4\sqrt{A}}\right)^2 \alpha_i^2 \xi\right)\right)\exp\left(-\left(\frac{P}{4\sqrt{A}}\right)^2 \alpha_i^2 \xi\right)}{\alpha_i^2 \xi\left(1 + 8\frac{2-\sigma}{\sigma}\mathrm{Kn} + 4\left(\alpha_i\frac{2-\sigma}{\sigma}\mathrm{Kn}\right)^2\right)} \right) \quad (91)$$

Using the available analytical data for circular tubes and parallel plates, and the available data in the literature [39–43] for continuum flow, it is found that the value n, which minimizes the root mean square difference, lies in the range $1.0 < n < 1.2$ with a convenient value $n \approx 1$ for most common noncircular microchannels. When the geometric characteristic aspect ratio $P/4\sqrt{A}$ is close to 2 or greater, $n = 1.1$ or 1.2 will yield a better approximation.

4 Results and Discussion

Figure 12 demonstrates the comparison between the proposed model Eq. (91) and the available data in the literature for continuum flow. It is found that the difference between the model and available data is less than 9.6%. Therefore, experimental, analytical, and numerical results for continuum flow do support the validity of the present model.

Furthermore, Fig. 13 presents the comparison between the proposed model Eq. (91) and the analytical solution of circular ducts Eq. (87). The model predictions are in agreement with analytical solution within 1%.

Niazmand et al. [44] and Renksizbulut et al. [35] numerically investigated slip flow in the entrance region of rectangular microchannels. The Reynolds number range is from 0.1 to 100. Figure 14 demonstrates the comparison between the proposed model and the numerical data by Niazmand et al. [44] for Re = 100 and $\xi > 0.005$. It is found that the difference between the model and the numerical data by Niazmand et al. [44] is from 8% to 18%. The difference decreases with an increase in Knudsen number. This indicates that the slip flow is less sensitive to analytical linearized approximations than the continuum flow. It is noted, however, that the numerical data by Niazmand et al. [44] overpredict the values of f Re.

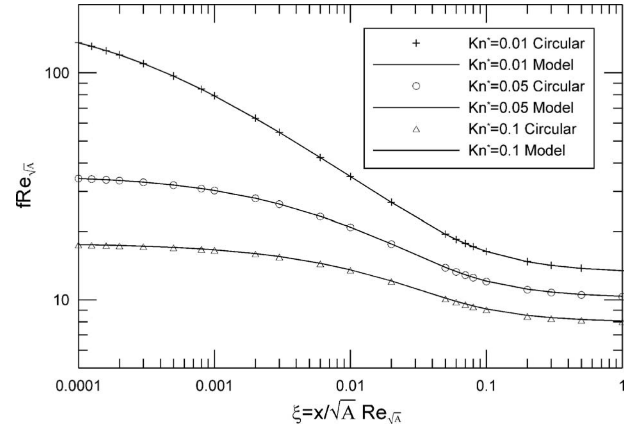

Fig. 13 Comparison of $f\ \mathrm{Re}_{\sqrt{A}}$ for circular tubes

It is found that Eq. (91) characterizes the developing slip flow in noncircular microchannels. The maximum deviation of exact values is approximately less than 10%. The proposed model correctly approaches the $\xi \to 0$ and $\xi \to \infty$ asymptotes. The friction factor Reynolds product may be predicted from Eq. (91), provided an appropriate definition of the aspect ratio is chosen.

5 Conclusion

This paper investigated slip flow and continuum flow in noncircular microchannels. A model was developed for predicting the friction factor Reynolds product in noncircular microchannels for developing slip flow and continuum flow. The present model took advantage of the selection of a more appropriate characteristic length scale square root of flow area to develop a simple model. As for developing slip flow, no solutions or graphical and tabulated data exist for most geometries, this developed model may be used to predict friction factor and pressure drop of developing slip flow in noncircular microchannels such as rectangular, annular, elliptical, trapezoidal, double-trapezoidal, triangular, rhombic, hexagonal, octagonal, and circular segment microducts. The developed model approaches the slip flow asymptote for developing and fully developed flows. The accuracy of the developed model was approximately within 10%. The developed model is simple and founded on theory, and it may be used by the research com-

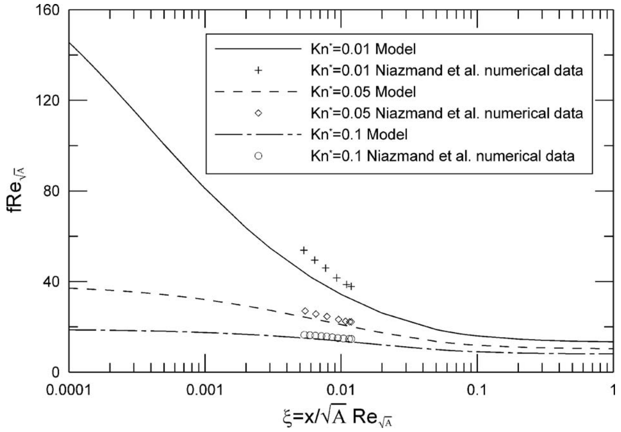

Fig. 14 Comparison of $f\ \mathrm{Re}_{\sqrt{A}}$ for the numerical data by Niazmand et al. [44]

munity for the practical engineering design of microchannels. The developed analytical model is useful for a number of reasons. These include: (1) introduction of interesting and unique solution techniques, (2) an indication of the effect of various independent parameters, (3) an indication of trends expected from related numerical data and future experiments, and (4) very easy to utilize by the research community.

It may be pointed out that the linearization schemes do not take into account the effect of the transverse flow rigorously, although they predict fairly well the friction factor Reynolds number product. Quarmby [45] showed that the transverse velocity is very much reduced in the entrance region as the Knudsen number increases. Since the present linear solutions do not take into account the effect of the transverse flow rigorously, they will clearly be more correct for slip flow where transverse velocity is less significant. Therefore, the present linearization method is an accurate approximation for slip flow.

The paper deals with issues of hydrodynamic flow development, which are not well understood in other geometries. It is found that slip flow is less sensitive to analytical linearized approximations than continuum flow and the linearization method is a quite accurate approximation for slip flow. Also, it is found that the entrance friction factor Reynolds product is of finite value and dependent on the Kn and tangential momentum accommodation coefficient but independent of the cross-sectional geometry. This paper also examined the effects of the Knudsen number on the hydrodynamic entrance length for circular tubes and parallel plates.

Acknowledgment

The authors would like to express their appreciation to professors Michael Yovanovich and Richard Culham for their suggestions, which helped them in improving the quality of this paper. The authors acknowledge the support of the Natural Sciences and Engineering Research Council of Canada (NSERC).

Nomenclature

A = flow area, m^2
a = major semi-axis of an ellipse or a rectangle, m
a = base width of a trapezoidal, triangular, double-trapezoidal, or rhombic duct, m
b = minor semi-axis of an ellipse or a rectangle, m
b = height of a trapezoidal, triangular, double-trapezoidal, or rhombic duct, m
c = short side of a trapezoidal or double-trapezoidal duct, m
D = diameter of circular tubes, m
D_h = hydraulic diameter, $=4A/P$
f = Fanning friction factor, $=\tau/((1/2)\rho\bar{u}^2)$
h = half height of a parallel plate channel, m
K = incremental pressure drop factor
Kn = Knudsen number, $=\lambda/D_h$
Kn* = modified Knudsen number, $=\mathrm{Kn}(2-\sigma)/\sigma$
L = hydrodynamic entrance length, m
L^+ = dimensionless hydrodynamic entrance length, $=L/D_h\ \mathrm{Re}_{D_h}$
ℓ = arbitrary length scale
n = correlation parameter
P = perimeter, m
Po = Poiseuille number, $=\bar{\tau}\ell/\mu\bar{u}$
p = pressure, N/m^2
Re = Reynolds number, $=\ell\bar{u}/\nu$
R = radius, m
r = radial coordinate in the cylindrical coordinate system, m
r^* = dimensionless radius ratio, $=r_i/r_o$
r_i = inner radius of a concentric duct, m
r_o = outer radius of a concentric duct, m
U = dimensionless velocity, $=u/\bar{u}$
u, v = velocity components, m/s
$\bar{u}$ = average velocity, m/s
V = dimensionless developing velocity
x, y = Cartesian coordinates, m

Greek Symbols

α = eigenvalue
ε = nominal and effective aspect ratios
η = dimensionless channel coordinate
λ = molecular mean free path, m
μ = dynamic viscosity, N s/m^2
ν = kinematic viscosity, m^2/s
ξ = dimensionless duct length, $=x/\ell\ \mathrm{Re}_\ell$
ρ = density, kg/m^3
σ = tangential momentum accommodation coefficient
τ = wall shear stress, N/m^2

Subscripts

$\sqrt{A}$ = based upon the square root of flow area
app = apparent
c = continuum
D_h = based upon the hydraulic diameter
fd = fully developed
ℓ = based upon the arbitrary length ℓ

References

[1] Ged-el-Hak, M., 2001, *MEMS Handbook*, CRC, Boca Raton, FL.
[2] Karniadakis, G. E., Beskok, A., and Aluru, N., 2005, *Microflows and Nanoflows*, Springer, New York.
[3] Nguyen, N. T., and Wereley, S. T., 2003, *Fundamentals and Applications of Microfluidics*, Artech House, London.
[4] Eckert, E. G. R., and Drake, R. M., 1972, *Analysis of Heat and Mass Transfer*, McGraw-Hill, New York.
[5] Rohsenow, W. M., and Choi, H. Y., 1961, *Heat, Mass, and Momentum Transfer*, Prentice-Hall, New Jersey.
[6] Arkilic, E. B., Breuer, K. S., and Schmidt, M. A., 1994, "Gaseous Flow in Microchannels," *Application of Microfabrication to Fluid Mechanics*, Vol. FED-197, ASME, New York, pp. 57–66.
[7] Arkilic, E. B., Breuer, K. S., and Schmidt, M. A., 1997, "Gaseous Slip Flow in Long Microchannels," J. Microelectromech. Syst., **6**(2), pp. 167–178.
[8] Pong, K., Ho, C., Liu, J., and Tai, Y., 1994, "Nonlinear Pressure Distribution in Uniform Microchannels," *Application of Microfabrication to Fluid Mechanics*, Vol. FED-197, ASME, New York, pp. 51–56.
[9] Liu, J., Tai, Y. C., and Ho, C. M., 1995, "MEMS for Pressure Distribution Studies of Gaseous Flows in Microchannels," Proceedings of the IEEE International Conference on Micro Electro Mechanical Systems, Amsterdam, The Netherlands, pp. 209–215.
[10] Araki, T., Kim, M. S., Hiroshi, I., and Suzuki, K., 2000, "An Experimental Investigation of Gaseous Flow Characteristics in Microchannels," *Proceedings of the International Conference on Heat Transfer and Transport Phenomena in Microscale*, G. P. Celata, ed., Begell House, New York, pp. 155–161.
[11] Pfahler, J., Harley, J., Bau, H., and Zemel, J. N., 1990, "Gas and Liquid Transport in Small Channels," *Micromechanical Sensors, Actuators, and Systems*, Vol. DSC-19, ASME, New York, pp. 149–157.
[12] Pfahler, J., Harley, J., Bau, H., and Zemel, J. N., 1991, "Gas and Liquid Flow in Small Channels," *Micromechanical Sensors, Actuators, and Systems*, Vol. DSC-32, ASME, New York, pp. 49–58.
[13] Harley, J., Huang, Y., Bau, H., and Zemel, J. N., 1995, "Gas Flows in Micro-Channels," J. Fluid Mech., **284**, pp. 257–274.
[14] Choi, S. B., Barron, R. F., and Warrington, R. O., 1991, "Fluid Flow and Heat Transfer in Microtubes," *Micromechanical Sensors, Actuators, and Systems*, Vol. DSC-32, ASME, New York, pp. 123–134.
[15] Wu, S., Mai, J., Zohar, Y., Tai, Y. C., and Ho, C. M., 1998, "A Suspended Microchannel With Integrated Temperature Sensors for High Pressure Flow Studies," Proceedings of the IEEE Workshop on Micro Electro Mechanical Systems, Heidelberg, Germany, pp. 87–92.
[16] Schaaf, S. A., and Chambre, P. L., 1961, *Flow of Rarefied Gases*, Princeton University Press, New Jersey.
[17] Maurer, J., Tabeling, P., Joseph, P., and Willaime, H., 2003, "Second-Order Slip Laws in Microchannels for Helium and Nitrogen," Phys. Fluids, **15**, pp. 2613–2621.
[18] Aubert, C., and Colin, S., 2001, "High-Order Boundary Conditions for Gaseous Flows in Rectangular Microducts," Microscale Thermophys. Eng., **5**, pp. 41–54.
[19] Deissler, R. G., 1964, "An Analysis of Second-Order Slip Flow and Temperature-Jump Boundary Conditions for Rarefied Gases," Int. J. Heat

Mass Transfer, **7**, pp. 681–694.
[20] Colin, S., Lalonde, P., and Caen, R., 2004, “Validation of a Second-Order Slip Flow Model in Rectangular Microchannels,” Heat Transfer Eng., **25**, pp. 23–30.
[21] Barber, R. W., and Emerson, D. R., 2006, “Challenges in Modeling Gas-Phase Flow in Microchannels: From Slip to Transition,” Heat Transfer Eng., **27**, pp. 3–12.
[22] Jeong, N., Lin, C. L., and Choi, D. H., 2006, “Lattice Boltzmann Study of Three-Dimensional Gas Microchannel Flows,” J. Micromech. Microeng., **16**, pp. 1749–1759.
[23] Barber, R. W., and Emerson, D. R., 2001, “A Numerical Investigation of Low Reynolds Number Gaseous Slip Flow at the Entrance of Circular and Parallel Plate Microchannels,” ECCOMAS Computational Fluid Dynamics Conference, Swansea, Wales, UK.
[24] Shah, R. K., and London, A. L., 1978, *Laminar Flow Forced Convection in Ducts*, Academic, New York.
[25] Sparrow, E. M., Lundgren, T. S., and Lin, S. H., 1962, “Slip Flow in the Entrance Region of a Parallel Plate Channel,” *Proceedings of the Heat Transfer and Fluid Mechanics Institute*, Stanford University Press, Stanford, pp. 223–238.
[26] Sparrow, E. M., Lin, S. H., and Lundgren, T. S., 1964, “Flow Development in the Hydrodynamic Entrance Region of Tubes and Ducts,” Phys. Fluids, **7**, pp. 338–347.
[27] Kennard, E. H., 1938, *Kinetic Theory of Gases*, McGraw-Hill, New York.
[28] Atkinson, B., Brocklebank, M. P., Card, C. C. H., and Smith, J. M., 1969, “Low Reynolds Number Developing Flows,” AIChE J., **15**, pp. 548–553.
[29] Chen, R. Y., 1973, “Flow in the Entrance Region at Low Reynolds Numbers,” ASME J. Fluids Eng., **95**, pp. 153–158.
[30] Friedmann, M., Gillis, J., and Liron, N., 1968, “Laminar Flow in a Pipe at Low and Moderate Reynolds Numbers,” Appl. Sci. Res., **19**, pp. 426–438.
[31] Sreekanth, A., 1969, “Slip Flow Through Long Circular Tubes,” *Proceedings of the Sixth International Symposium on Rarefied Gas Dynamics*, L. Trilling and H. Y. Wachman, eds., Academic, New York, pp. 667–680.
[32] Shapiro, A. H., Siegel, R., and Kline, S. J., 1954, “Friction Factor in the Laminar Entry Region of a Smooth Tube,” Proceedings of the US Second National Congress of Applied Mechanics, New York, pp. 733–741.
[33] Muzychka, Y. S., and Yovanovich, M. M., 2002, “Laminar Flow Friction and Heat Transfer in Non-circular Ducts and Channels: Part I-Hydrodynamic Problem,” Compact Heat Exchangers, A Festschrift on the 60th Birthday of Ramesh K. Shah, Grenoble, France, pp. 123–130.
[34] Yu, S. P., and Ameel, T. A., 2001, “A Universal Entrance Nusselt Number for Internal Slip Flow,” Int. Commun. Heat Mass Transf., **28**(7), pp. 905–910.
[35] Renksizbulut, M., Niazmand, H., and Tercan, G., 2006, “Slip-Flow and Heat Transfer in Rectangular Microchannels With Constant Wall Temperature,” Int. J. Therm. Sci., **45**, pp. 870–881.
[36] Duan, Z. P., and Muzychka, Y. S., 2007, “Slip Flow in Non-circular Microchannels,” Microfluid. Nanofluid., **3**, pp. 473–484.
[37] Duan, Z. P., and Yovanovich, M. M., 2009, “Pressure Drop for Laminar Flow in Microchannels of Arbitrary Cross-Sections,” Semi-Therm 25 Semiconductor Thermal Measurement and Management Symposium, San Jose, CA.
[38] Churchill, S. W., and Usagi, R., 1972, “A General Expression for the Correlation of Rates of Transfer and Other Phenomena,” AIChE J., **18**, pp. 1121–1128.
[39] Hornbeck, R. W., 1964, “Laminar Flow in the Entrance Region of a Pipe,” Appl. Sci. Res., Sect. A, **13**, pp. 224–232.
[40] Liu, J., 1974, “Flow of a Bingham Fluid in the Entrance Region of an Annular Tube,” MS thesis, University of Wisconsin, Madison.
[41] Lawal, A., and Mujumdar, A. S., 1984, “Forced Convection Heat Transfer to a Power Law Fluid in Arbitrary Cross-Section Ducts,” Can. J. Chem. Eng., **62**, pp. 326–333.
[42] Curr, R. M., Sharma, D., and Tatchell, D. G., 1972, “Numerical Predictions of Some Three Dimensional Boundary Layers in Ducts,” Comput. Methods Appl. Mech. Eng., **1**, pp. 143–158.
[43] Gangal, M. K., 1974, “Some Problems in Channel Flow,” Ph.D. thesis, University of Calgary, Calgary, Alberta, Canada.
[44] Niazmand, H., Tercan, G., and Renksizbulut, M., 2005, “Entrance Region Flows in Rectangular Microchannels With Constant Wall Temperature,” Proceedings of the Third International Conference on Minichannels and Microchannels, Toronto, Canada, Paper No. ICMM2005-75064.
[45] Quarmby, A., 1968, “A Finite Difference Analysis of Developing Slip Flow,” Appl. Sci. Res., **19**, pp. 18–33.

K. C. Sahu[1]
Department of Chemical Engineering,
Indian Institute of Technology Hyderabad,
Yeddumailaram 502205, Andhra Pradesh, India
e-mail: ksahu@iith.ac.in

O. K. Matar
Department of Chemical Engineering,
Imperial College London,
South Kensington Campus,
London SW7 2AZ, UK
e-mail: o.matar@imperial.ac.uk

Stability of Plane Channel Flow With Viscous Heating

The linear stability analysis of pressure-driven flow undergoing viscous heating through a channel is considered. The walls of the channel are maintained at different constant temperatures and Nahme's law is applied to model the temperature dependence of the fluid viscosity. A modified Orr–Sommerfeld equation coupled with a linearized energy equation is derived and solved using an efficient spectral collocation method. Our results indicate that increasing the influence of viscous heating is destabilizing. It is also shown that the critical Reynolds number decreases by one order of magnitude with increase in the Nahme number. An energy analysis is conducted to understand the underlying physical mechanism of the instability. [DOI: 10.1115/1.4000847]

1 Introduction

The study of flows of viscous fluids with temperature-dependent properties is of great interest in lubrication, tribology, food processing, instrumentation, and viscometry. In the polymer processing industries [1], viscous heating plays an important role as many fluids in such applications strongly depend on temperature because of the coupling between the energy and momentum equations causing profound changes in the flow structure [2–8]. Although a large number of studies have examined the effect of temperature-dependent fluid viscosity and wall heating on flow stability, which have included boundary-layer [9–12], Couette [13–19], channel [20–25], and pipe flows [26,27], viscous heating in Poiseuille channel flow has received far less attention. The main objective of the present paper therefore is to examine the linear stability of pressure-driven channel flow with viscous heating and asymmetrically heated walls.

In literature, the effect of viscous heating has been studied using either Arrhenius-type relationships (see Refs. [16,28]) or a Nahme-type law (see Refs. [15,17–19,29] for instance) to model the temperature-viscosity relationship. Davis et al. [28] and Eldabe et al. [16] used an Arrhenius-type relationship and a Nahme-type law, respectively, to study plane Couette flow and showed that the graph of shear rate against shear stress is monotonic for fluids, which are less sensitive to temperature (as considered in the present study) and S shape for fluids, which are highly sensitive to temperature. The latter also compared the results obtained using both relationships.

The linear stability of channel flow with wall heating was studied by Potter and Graber [20] and Pinarbasi and Liakopoulos [24] who found that the temperature differences between the walls was always destabilizing; this finding was later confirmed by Schäfer and Herwig [21] via an asymptotic analysis of a similar problem. Unlike the above studies, Wall and Wilson [23] and Sameen and Govindarajan [22] rescaled the governing equations using the viscosity of the fluid at the hot wall and the average viscosity across the channel, respectively. Their results, in contradiction to those in Refs. [20,21] indicated that the temperature difference between the walls was stabilizing. Using a transient growth analysis, Sameen and Govindarajan [22] showed that the Prandtl number (taken to be negligible in the linear stability analysis [23]) had a large destabilizing influence. They also studied the effect of buoyancy and found that the Poiseuille–Rayleigh–Bénard mode, which appears at a moderate Grashof number, merged with the Poiseuille mode at high Grashof number. Carrière and Monkewitz [25] showed that the flow was absolutely unstable at very low Reynolds numbers and high Grashof numbers. In all the above studies, the effect of viscous heating, whose study is the main objective of the present paper, was neglected.

The effect of viscous heating in Couette flows was considered by several authors [15,5,17]. They found that the critical Reynolds number decreases as the viscous heating increases. A similar conclusion was also found in Taylor–Couette systems by several authors theoretically [30–33] and experimentally [34,35]. They found that the coupling between the velocity perturbations and the base state temperature gradient is the main mechanism of instability, as it gives rise to spatially inhomogeneous temperature fluctuations, which in turn reduce the local viscosity thereby decreasing the dissipation energy of the disturbances. For very large Pr, Thomas et al. [30] also derived an analytical expression for the critical Reynolds number as a function of the Nahme and Prandtl numbers. Pinarbasi and Imal [29] studied the effect of viscous heating of inelastic fluid flow through a symmetrically heated channel, finding that viscous heating had a destabilizing influence. Of particular interest here is the work of Costa and Macedonio [6], who studied the effect of viscous heating with temperature-dependent viscosity in a symmetrically heated channel flow by linear stability analysis and direct numerical simulations. They found that in certain regimes, viscous heating can trigger and sustain secondary rotational flows. In the present paper, the effect of viscous heating on Poiseuille flow in an *asymmetrically* heated channel is studied, which appears not to have been done previously.

The rest of this paper is organized as follows. The details of the problem formulation are provided in Sec. 2 and the results of the linear stability analysis are presented in Sec. 3. The concluding remarks are provided in Sec. 4.

2 Formulation of the Problem

The pressure-driven, two-dimensional (2D) channel flow of a Newtonian and incompressible fluid with viscous heating is considered, as shown in Fig. 1. The walls are maintained at (different) constant temperatures; $\Delta T \equiv T_u - T_l$, where T_u is the temperature at the top wall. A rectangular coordinate system (x,y) is used to model this flow where x and y denote the horizontal and vertical coordinates. The rigid and impermeable channel walls are located at $y=-H$ and $y=H$. The following Nahme-type viscosity-temperature relationship [36,15,8] is used that approximates the variation in viscosity of many liquids over a wide range of temperature:

---

[1] Corresponding author.

Contributed by the Fluids Engineering Division of ASME for publication in the JOURNAL OF FLUIDS ENGINEERING. Manuscript received June 1, 2009; final manuscript received December 7, 2009; published online January 12, 2010. Assoc. Editor: Ugo Piomelli.

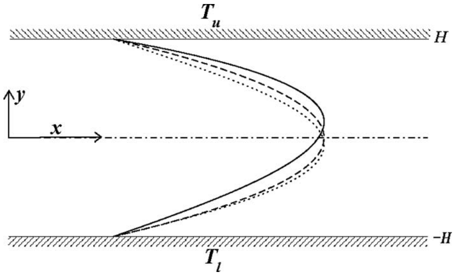

Fig. 1 Schematic diagram of the channel; bottom and top walls are maintained at different, constant temperatures, T_l and T_u, respectively. Also shown here are profiles of the steady, horizontal velocity component generated with Na=0.86, r_T=1 (solid line), Na=0.86, r_T=−0.5 (dotted line), and Na=0, r_T=0 (dashed line).

$$\mu = \mu_l \exp\left[-\frac{\beta(T-T_l)}{T_l}\right] \tag{1}$$

where β is a dimensionless activation energy parameter that stands for the sensitivity of the viscosity to temperature variation; for liquids, β is a positive number and μ_l is the value of the viscosity at T_l.

The following scaling is employed in order to render these equations dimensionless:

$$(x,y) = H(\tilde{x},\tilde{y}), \quad t = \frac{H}{U_m}\tilde{t}, \quad (u,v) = U_m(\tilde{u},\tilde{v}), \quad p = \frac{\mu_l U_m}{H}\tilde{p} \tag{2}$$

$$T = \frac{\tilde{T}T_l}{\beta} + T_l, \quad \mu = \tilde{\mu}\mu_l$$

where u and v denote the horizontal and vertical velocity components and p, ρ, and t denote pressure, density, and time, respectively. The tildes designate dimensionless quantities and U_m is the maximum value of the horizontal velocity component. With the usual Boussinesq approximation, the dimensionless governing equations (after dropping tildes from all nondimensional terms) are then given by

$$\frac{\partial u}{\partial x} + \frac{\partial v}{\partial y} = 0 \tag{3}$$

$$\mathrm{Re}\left[\frac{\partial u}{\partial t} + u\frac{\partial u}{\partial x} + v\frac{\partial u}{\partial y}\right] = -\frac{\partial p}{\partial x} + \left\{\frac{\partial}{\partial x}\left[2\mu\frac{\partial u}{\partial x}\right] + \frac{\partial}{\partial y}\left[\mu\left(\frac{\partial u}{\partial y} + \frac{\partial v}{\partial x}\right)\right]\right\} \tag{4}$$

$$\mathrm{Re}\left[\frac{\partial v}{\partial t} + u\frac{\partial v}{\partial x} + v\frac{\partial v}{\partial y}\right] = -\frac{\partial p}{\partial y} + \left\{\frac{\partial}{\partial x}\left[\mu\left(\frac{\partial u}{\partial y} + \frac{\partial v}{\partial x}\right)\right] + \frac{\partial}{\partial y}\left[2\mu\frac{\partial v}{\partial y}\right]\right\} - \frac{\mathrm{Gr}}{\mathrm{Re}}T \tag{5}$$

$$\mathrm{RePr}\left[\frac{\partial T}{\partial t} + u\frac{\partial T}{\partial x} + v\frac{\partial T}{\partial y}\right] = \mathrm{Na}\mu\left[2\left\{\left(\frac{\partial u}{\partial x}\right)^2 + \left(\frac{\partial v}{\partial y}\right)^2\right\} + \left(\frac{\partial u}{\partial y} + \frac{\partial v}{\partial x}\right)^2\right] + \left[\frac{\partial^2 T}{\partial x^2} + \frac{\partial^2 T}{\partial y^2}\right] \tag{6}$$

where $\mathrm{Re}(\equiv \rho U_m H/\mu_l)$, $\mathrm{Na}(\equiv \beta\mu_l U_m^2/\kappa T_l)$, $\mathrm{Pr}(\equiv c_p\mu_l/\kappa)$, and $\mathrm{Gr}(\equiv \alpha_0 T_l g H^3/\beta\nu^2)$ are the Reynolds, Nahme, Prandtl, and Grashof numbers, respectively; $\nu(\equiv \mu_l/\rho)$ is a kinematic viscosity while κ, c_p, g, and α_0 are coefficient of thermal conductivity, specific heat capacity at constant pressure, the acceleration due to gravity, and the thermal expansion coefficient, respectively. It can be seen that the equations of motion and energy are coupled by the temperature dependence of the viscosity. The extent of coupling increases with Na, which is the product of β and the Brinkman number $(\mathrm{Br} \equiv \mu_l U_m^2/\kappa T_l)$.

2.1 Basic State. The base state whose linear stability characteristics will be analyzed, corresponds to a steady, parallel, fully developed flow with vertical thermal stratification.

$$\frac{d}{dy}\left[\mu_0\frac{dU}{dy}\right] = G \tag{7}$$

$$\frac{d^2T_0}{dy^2} + \mathrm{Na}\mu_0\left(\frac{dU}{dy}\right)^2 = 0 \tag{8}$$

where U, G, T_0, and μ_0 represent the horizontal velocity component, constant horizontal pressure gradient, temperature, and viscosity for the basic state. The dimensionless viscosity-temperature relationship for the basic state is given by

$$\mu_0(T_0) = \exp(-T_0) \tag{9}$$

The coupled Eqs. (7) and (8) are solved using a fourth-order Runge–Kutta method and validated against solutions generated using MATLAB with the following boundary conditions:

$$U = 0 \quad \text{at } y = \pm 1 \tag{10}$$

$$T_0 = 0 \quad \text{at } y = -1 \quad \text{and} \quad T_0 = r_T \quad \text{at } y = 1 \tag{11}$$

where $r_T = \beta\Delta T/T_l$.

The basic state velocity profiles obtained above for a constant pressure gradient are then rescaled by the maximum horizontal velocity U_m. Typical basic state profiles of the second derivative of the horizontal velocity component (U'') and temperature (T_0) for different Na when r_T=1 and r_T=−0.5 are shown in Figs. 2(*a*)–2(*d*), respectively. An inspection of Figs. 2(*a*) and 2(*c*) reveals that the tendency of the profiles to become inflectional (U''=0 for a value of y in the channel) increases with Na; the profile is inflectional for Na>0.8 approximately indicating that the flow in inviscidly unstable [37] for these parameter values. These features also indicate that increasing Na is expected to exert a destabilizing influence on the flow. As expected, it can be seen that the inflectional point always lies near the cold wall.

2.2 Linear Stability Analysis. We examine the temporal linear stability of the base state obtained by solving Eqs. (7) and (8) to infinitesimal, 2D disturbances using a normal modes analysis by expressing each flow variable as the sum of a base state and a 2D perturbation [38,39],

$$(u,v,p,T,\mu)(x,y,t) = [U(y),0,P(y),T_0(y),\mu_0(y)] + \mathrm{Real}\{(\hat{u},\hat{v},\hat{p},\hat{T},\hat{\mu})(y)\exp(\imath[\alpha x - \omega t])\}, \tag{12}$$

where the hat decoration designates the perturbation quantities. In Eq. (12), $\hat{\mu} = (d\mu_0/dT_0)\hat{T}$ represents the perturbation viscosity, α is the disturbance wavenumber (real), and ω is a complex frequency. The amplitude of the velocity disturbances are then reexpressed in terms of a streamfunction: $(\hat{u},\hat{v}) = (\psi', -\imath\alpha\psi)$, where the prime denotes differentiation with respect to y. The substitution of Eq. (12) into Eqs. (3)–(6) followed by subtraction of the base state equations, subsequent linearization, and elimination of the pressure perturbation yields the following coupled ordinary differential eigenvalue equations (following the suppression of the hat decoration):

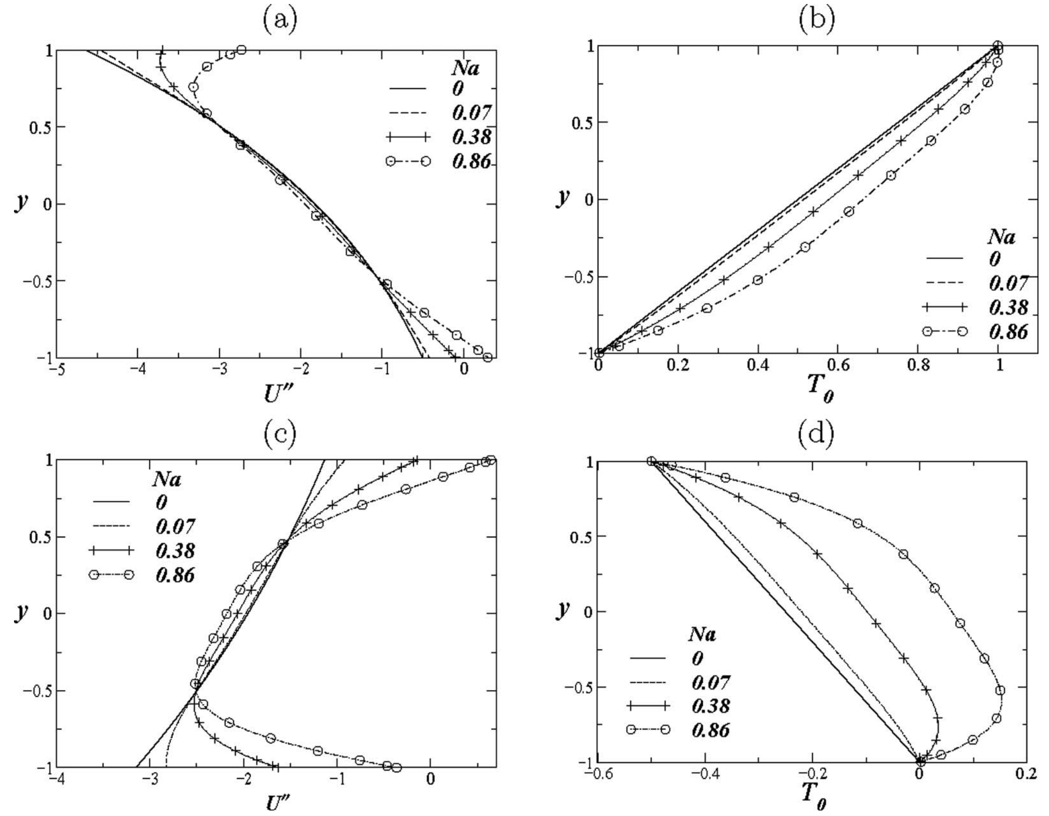

Fig. 2 **Basic state profiles of the second derivative of the horizontal component of the velocity (U'') and temperature (T_0) for different Na when $r_T=1$ and $r_T=-0.5$ are shown in (*a*) and (*b*) and (*c*) and (*d*), respectively**

$$\begin{aligned}\imath\alpha[(\psi''-\alpha^2\psi)(U-c)-\psi U''] &= \frac{1}{\mathrm{Re}}\Bigg[\mu_0(\psi''''-2\alpha^2\psi''+\alpha^4\psi)+2\frac{d\mu_0}{dT_0}T_0'(\psi'''-\alpha^2\psi')\\ &\quad+\frac{d\mu_0}{dT_0}T_0''(\psi''+\alpha^2\psi)+\frac{d^2\mu_0}{dT_0^2}(T_0')^2(\psi''+\alpha^2\psi)+\frac{d\mu_0}{dT_0}(U'T''\\ &\quad+2U''T'+\alpha^2U'T+U'''T)+2\frac{d^2\mu_0}{dT_0^2}T_0'U'T'+\frac{d^2\mu_0}{dT_0^2}T_0''U'T\\ &\quad+\frac{d^3\mu_0}{dT_0^3}(T_0')^2U'T+2\frac{d^2\mu_0}{dT_0^2}T_0'U''T\Bigg]+\frac{\mathrm{Gr}}{\mathrm{Re}^2}\imath\alpha T\end{aligned} \tag{13}$$

$$\imath\alpha[(U-c)T-\psi T_0'] = \frac{1}{\mathrm{RePr}}[T''-\alpha^2T]+\frac{\mathrm{Na}}{\mathrm{RePr}}2U'\mu_0(\psi''+\alpha^2\psi) \tag{14}$$

where $c(\equiv\omega/\alpha)$ is a complex phase speed of the disturbance. Note that a given mode is unstable if $\omega_i>0$, stable if $\omega_i<0$, and neutrally stable if $\omega_i=0$. The minimum Reynolds number in the neutral stability curve (contour of $c_i=0$ in α against Re plot) is referred to here as a "critical" Reynolds number $\mathrm{Re}_{\mathrm{cr}}$. In the limit $(\mathrm{Na}\rightarrow 0)$, these equations reduce to those of Sameen and Govindarajan [22]; and in the limit $(\mathrm{Na},\mathrm{Gr})\rightarrow 0$, we obtained the stability equations of Wall and Wilson [23]. We can also recover the Orr–Sommerfeld equation for the special case of $T=0$ and $\mu_0=1$.

The eigenvalue c and the eigenfunctions ψ and T are obtained via the solution of Eqs. (13) and (14) using the Chebyshev spectral collocation method [40], accomplished by the specification of the collocation points chosen to be the Chebyshev Gauss–Lobatto points defined as $y_k=\cos(k\pi/N)$, where $k=(1,N)$ subject to the following boundary conditions:

$$\psi=\psi'=T=0 \quad \text{at } y=\pm 1 \tag{15}$$

where N is the order of Chebyshev polynomials.

The eigenvalue problem is then recast into the following matrix form:

$$\begin{bmatrix}\mathcal{A}_{11} & \mathcal{A}_{12}\\ \mathcal{A}_{21} & \mathcal{A}_{22}\end{bmatrix}\begin{bmatrix}\psi\\ T\end{bmatrix}=c\begin{bmatrix}\mathcal{B}_{11} & \mathcal{B}_{12}\\ \mathcal{B}_{21} & \mathcal{B}_{22}\end{bmatrix}\begin{bmatrix}\psi\\ T\end{bmatrix} \tag{16}$$

and solved using the public domain software LAPACK. A similar technique has previously been used to study the stability of flow through a diverging pipe [40] and interfacial stability of non-Newtonian fluid flow through a channel [39]. The results obtained from the above linear stability analysis are discussed below.

3 Results and Discussion

We begin the presentation of our results by demonstrating their convergence the on refinement of the spatial-mesh. Evidence of this is provided in Fig. 3 in which we plot the neutral stability curves for $r_T=1$, $\mathrm{Pr}=1$, $\mathrm{Gr}=100$, and $\mathrm{Na}=0.86$. The parameter values chosen are characteristic of a situation when the top channel wall is maintained at a higher temperature than that of the bottom wall, with some typical values of Prandtl and Grashof numbers. In this case, one would expect the flow to be more unstable than isothermal channel (e.g., Refs. [22,23]). It can be seen that the curves are indistinguishable for different values of the order of Chebyshev polynomials N. Thus, $N=121$ is used to generate the rest of the stability results in this paper. The neutral stability curve for $r_T=0$, $\mathrm{Gr}=0$, and $\mathrm{Na}=0$, which corresponds to the isothermal flow through a channel, is shown by a dotted line.

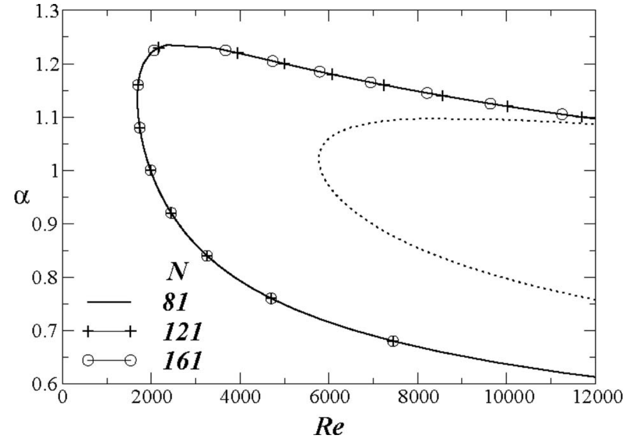

Fig. 3 The effect of increasing the order of Chebyshev polynomials (N) on the neutral stability curve with $r_T=1$, Pr=1, Gr=100, and Na=0.86. The dotted line shows the neutral stability curve for $r_T=0$, Gr=0, and Na=0, which corresponds to isothermal flow through a channel; the critical Reynolds number for this case is 5772.2.

It can be seen that the critical Reynolds number obtained for this case is 5772.2, which is the same as that of isothermal channel flow [41]. This inspires further confidence in the predictions of our numerical procedure.

In Fig. 4, we investigate the effect of varying r_T, which is equivalent to increasing the temperature difference between the channel walls in the absence of viscous heating and gravity. An inspection of Fig. 4(*a*) reveals that an increase in r_T destabilizes the flow. This observation is the same as that of Ref. [20] and opposite to the finding in Refs. [22,23]. However, this difference is due to the fact that unlike the present study, the authors in Refs. [22,23] used the viscosity at the hot wall (μ_{hot}) as the reference viscosity while scaling the governing equations. It can be seen in Fig. 4(*b*) that the present results agree with those of the latter studies, when we redefine the Reynolds number based on μ_{hot}, $\text{Re}_H=\rho U_m H/\mu_{\text{hot}}$. Since viscosity of liquid decreases with increasing temperature, the location of the maximum velocity is shifted toward the hot wall, as can also be seen in Fig. 1. This makes the profile less (more) inflectional ($U''=0$) near the hot (cold) wall. It can also be seen in Fig. 4(*b*) that the neutral stability curves for $r_T=0.5$ and -0.5 are indistinguishable when the Reynolds number is defined based on μ_{hot}, Re_H. This result indicates that the neutral stability curves are symmetrical in r_T for this set of parameters, however, we will see below that this is not true for nonzero Na.

In the rest of this paper, we concentrate on studying the effects of the Nahme number. In Figs. 5(*a*) and 5(*b*), we plot numerically generated dispersion curves (ω_i against α curves) for different values of Na with $r_T=1$ and $r_T=-0.5$, respectively. The rest of the parameter values are $\text{Re}=10^4$, Pr=1, and Gr=100. The dispersion curves for the symmetrically heated channel ($r_T=0$, Na=0.86)

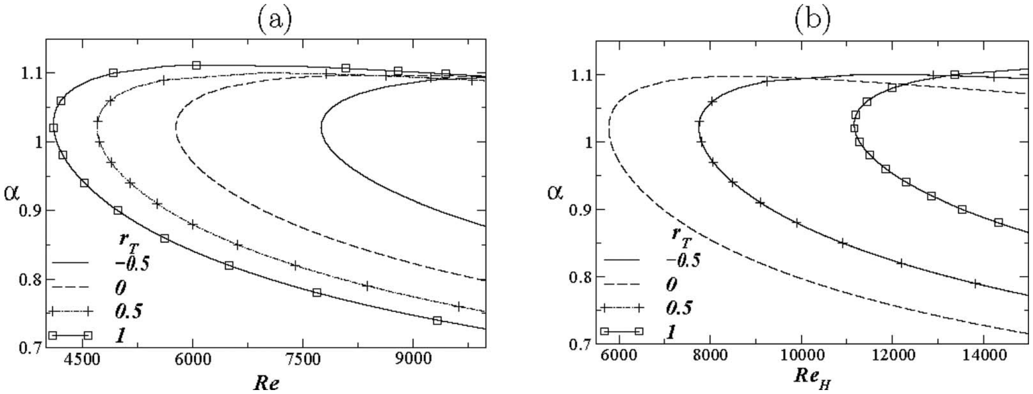

Fig. 4 Stability boundaries for different values of r_T. The rest of the parameter values are Pr=0, Gr=0, and Na=0. In Fig. 4(*b*), $\text{Re}_H \equiv U_m \rho H/\mu_{\text{hot}}$. Note that the curves associated with $r_T=-0.5$ and $r_T=0.5$ in panel (*b*) are indistinguishable.

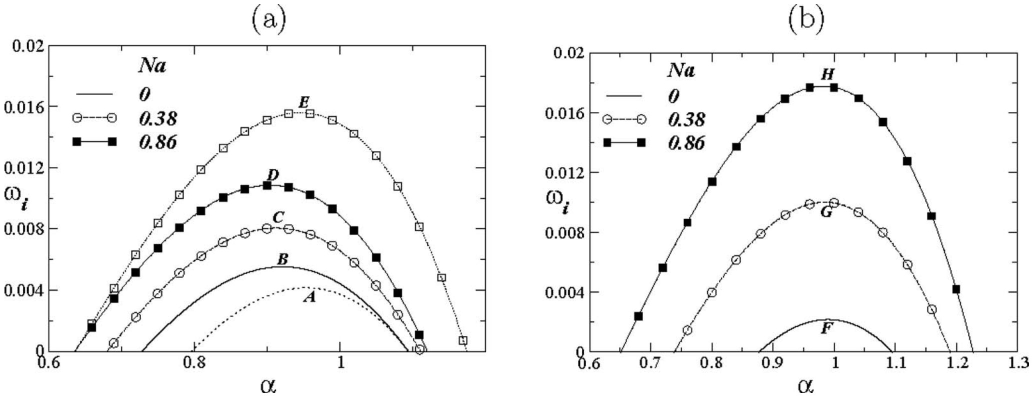

Fig. 5 The effect of varying the Na on the dispersion curves for $r_T=1$ (*a*) and $r_T=-0.5$ (*b*). The rest of the parameter values are $\text{Re}=10^4$, Pr=1, and Gr=100. The dotted line and the line with the open squares represent the dispersion curves for isothermal channel ($r_T=0$, Na=0) and symmetrically heated channel flow ($r_T=0$, Na=0.86). The labels A–E and F–H are used to designate the maxima in the dispersion curves in (*a*) and (*b*), respectively; the energy budgets associated with the points labeled A–E and F–H are provided in Tables 1 and 2, respectively.

Table 1 Energy budgets for the points labeled A–E in Fig. 5(*a*)

Point	REY/KIN	DIS/KIN
A	0.0193	0.0110
B	0.0197	0.0082
C	0.0243	0.0078
D	0.0295	0.0074
E	0.0410	0.0100

Table 2 Energy budgets for the points labeled F–H in Fig. 5(*b*)

Point	REY/KIN	DIS/KIN
F	0.0168	0.013
G	0.0319	0.0124
H	0.0468	0.0117

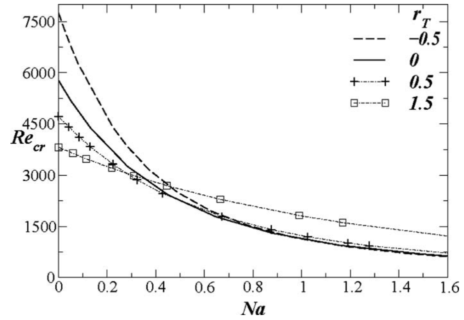

Fig. 6 Variation in the critical Reynolds number with Na for different values of r_T. The rest of the parameter values are Pr =1 and Gr=100.

and isothermal channel ($r_T=0$, Na=0) are also shown in Fig. 5(*a*). The dispersion curves depicted in Fig. 5 are paraboloidal, and $\omega_i>0$ over a finite band of wavenumbers, indicating the presence of a linear instability. It can be seen in Figs. 5(*a*) and 5(*b*) that increasing Na is destabilizing, leading to an increase in the maximal growth rate and to a wider range of wavenumbers over which the flow is unstable for both $r_T=1$ and $r_T=-0.5$. An inspection of Fig. 5(*a*) also reveals that in the presence of viscous heating, the flow through a symmetrically heated (isothermal) channel is more (less) unstable than that of the corresponding asymmetrically heated channel.

In order to gain further insight into the mechanisms underlying the instabilities discussed in the foregoing, we have carried out an analysis of the "energy budget" [38,42] (see Appendix for details). A similar analysis was also performed recently by Sahu and coworkers [39,43] and Sevlam et al. [44] for immiscible non-Newtonian, miscible channel flows and miscible core annular flows, respectively. The energy "budgets" associated with points A–E and F–H, which correspond to the most dangerous modes of the dispersion curves in Figs. 5(*a*) and 5(*b*) are given in Tables 1 and 2, respectively. An inspection of Tables 1 and 2 reveals that the contribution arising from the spatially averaged "Reynolds stress" term, *REY* (viscous dissipation term, *DIS*) increases (decreases) with increase in Na, which makes the flow more unstable. A similar mechanism of instability was found earlier by several authors [30–32] in Taylor–Couette systems. It can also be seen in Table 1 that the contribution arising from the spatially averaged REY (DIS) associated with point A is lower (higher) than that associated with point B, indicating that isothermal channel flow is less unstable than that in an asymmetrically heated channel. A similar comparison of the "energies" associated with points D and E reveals that flow in a symmetrically heated channel is more unstable than that in an asymmetrically heated channel when Na =0.86.

Finally, in Fig. 6 we investigate the variation in critical Reynolds number, defined as the value of Re at which $\omega_i=0$ with Na for different values of r_T. It can be seen that Na is destabilizing for all positive values of r_T investigated in the present work; the "isothermal" critical Reynolds number decreases by an order of magnitude with increasing Na. An inspection of Fig. 6 also reveals that r_T is destabilizing for Na smaller than a critical value Na_c (that depends on the rest of the parameters) but stabilizing above this value. To understand the physical mechanism of this behavior, we plot the dispersion curves for Na=0.1 and 1.1 and Re$=10^4$ in Figs. 7(*a*) and 7(*b*), respectively. The rest of the parameter values are the same as those used to generate Fig. 6. It can be seen in Figs. 7(*a*) and 7(*b*) that increasing r_T is destabilizing for Na=0.1 and stabilizing for Na=1.1. We also found (not shown) that with the increase in r_T, the Reynolds stress reduces near the cold wall and increases near the hot wall indicating that production near the hot wall is more important than that of the cold wall for the instability; dissipation, however, is almost identical in all the cases.

The destabilizing characteristics of r_T for Na=0.1 can be explained by inspection of the energy budgets of the points labeled A–D, associated with the most dangerous mode in Fig. 7(*a*), which are listed in Table 3. An inspection of Table 3 indicates that the magnitude of the spatially averaged energy dissipation, DIS, decreases with increasing r_T in contrast to that of REY, which remains approximately constant for the range of r_T considered. Similarly, inspection of the energy budgets of the points labeled E–H, associated with the most dangerous mode in Fig. 7(*b*),

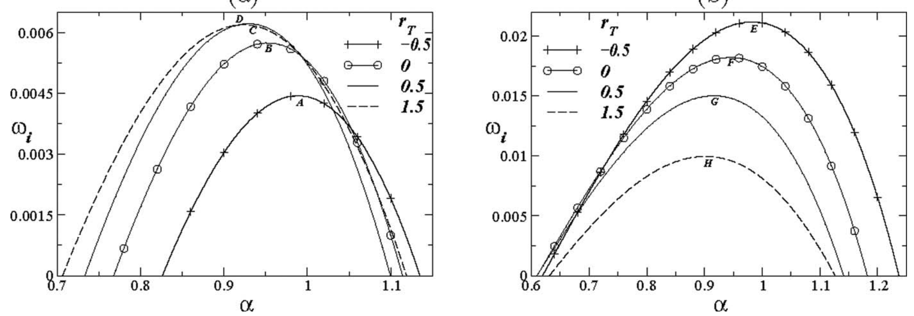

Fig. 7 The effect of varying r_T on the dispersion curves for Na=0.1 (*a*) and Na=1.1 (*b*). The rest of the parameter values are same as those used to generate Fig. 6. The labels A–H are used to designate the maxima in the dispersion curves; the energy budgets associated with these points are provided in Tables 3 and 4.

Table 3 Energy budgets for the points labeled A–D in Fig. 7(*a*)

Point	REY/KIN	DIS/KIN
A	0.0211	0.0128
B	0.0222	0.0108
C	0.022	0.0094
D	0.02	0.0071

Table 4 Energy budgets for the points labeled E–H in Fig. 7(*b*)

Point	REY/KIN	DIS/KIN
E	0.0529	0.011
F	0.0459	0.0095
G	0.0385	0.0083
H	0.026	0.0078

which are listed in Table 4, reveals that REY decreases with increasing r_T. The spatially averaged DIS also decreases but with a slower rate.

4 Conclusions

We have investigated the effect of viscous heating parameterized by a suitably defined Nahme number, Na, on the linear stability of a pressure-driven channel flow with a temperature-dependent viscosity; both symmetrically and asymmetrically heated channel walls are considered. The viscosity-temperature dependence is modeled by a Nahme-type relationship. The modified Orr–Sommerfeld equation for the disturbance streamfunction coupled to a linearized energy equation is derived and solved using a spectral collocation method. Our results indicate that increasing the value of Na, which increases the relative significance of viscous heating, promotes instability. We have also found that increasing r_T, which corresponds to an increase in the temperature difference between the two walls, is more (less) destabilizing for low (high) values of Na.

Acknowledgment

The authors acknowledge the fruitful discussions with Professor Rama Govindarajan. K.S. thanks Uttam Doraswami, Francesco Coletti, and Lennon Ó Náraigh of Imperial College London for their help and encouragement. We also thank the EPSRC for their support through Grant Nos. EP/E046029/1 and EP/D503051 and the DTI through Grant No. TP//ZEE/6/1/21191.

Appendix: Energy Balance

Here we have carried out an energy budget analysis as given in Refs. [38,42]. A similar analysis was also performed recently by Sahu and co-workers [39,43] and Sevlam et al. [44] for immiscible non-Newtonian, miscible channel flows, and miscible core annular flows, respectively. The energy equation is derived by taking the inner product of the horizontal and vertical components of the Navier–Stokes equations with their respective velocity components. The resultant equation is then averaged over the wavelength $2\pi/\alpha$ and integrated over the height of channel.

$$2\omega_i(\mathrm{KIN}) = \mathrm{REY\text{-}DIS} \tag{A1}$$

where

$$\mathrm{KIN} = \int_{-1}^{1} \frac{1}{4}(uu^* + vv^*)dy \tag{A2}$$

$$\mathrm{REY} = -\int_{-1}^{1} \frac{1}{4}U'(uv^* + u^*v)dy \tag{A3}$$

$$\mathrm{DIS} = \int_{-1}^{1} \frac{\mu_0}{\mathrm{Re}}\left[\alpha^2 uu^* + \frac{1}{2}(u' + \imath\alpha v)(u^{*\prime} - \imath\alpha v^*) + v'v^{*\prime}\right]dy \tag{A4}$$

where the superscript * denotes complex conjugate, KIN represents the spatially averaged disturbance kinetic energy, REY denotes the spatially averaged Reynolds stress term, which determines the rate of production of energy due to transfer of energy from the base flow to the disturbances, and DIS corresponds to the spatially averaged viscous dissipation of energy. The above equation allows one to isolate the mechanisms by which energy is transferred from the base flow to the disturbances.

References

[1] Pearson, J. R. A., 1985, *Mechanics of Polymer Processing*, Elsevier, London.
[2] Pearson, J. R. A., 1977, "Variable-Viscosity Flows in Channels With High Heat Generation," J. Fluid Mech., **83**, pp. 191–206.
[3] Ockendon, H., 1979, "Channel Flow With Temperature-Dependent Viscosity and Internal Viscous Dissipation," J. Fluid Mech., **93**, pp. 737–746.
[4] Ockendon, H., and Ockendon, J., 1977, "Variable-Viscosity Flows in Heated and Cooled Channels," J. Fluid Mech., **83**, pp. 177–190.
[5] Wylie, J. J., and Huang, H., 2007, "Extensional Flows With Viscous Heating," J. Fluid Mech., **571**, pp. 359–370.
[6] Costa, A., and Macedonio, G., 2005, "Viscous Heating Effects in Fluids With Temperature-Dependent Viscosity: Triggering of Secondary Flows," J. Fluid Mech., **540**, pp. 21–38.
[7] Pinarbasi, A., and Ozalp, C., 2005, "Influence of Variable Thermal Conductivity and Viscosity for Nonisothermal Fluid Flow," Phys. Fluids, **17**, p. 038109.
[8] Pinarbasi, A., and Ozalp, C., 2001, "Effect of Viscosity Models on the Stability of a Non-Newtonian Fluid in a Channel With Heat Transfer," Int. Commun. Heat Mass Transfer, **28**(3), pp. 369–378.
[9] Wazzan, A. R., Okamura, T. T., and Smith, A. M. O., 1968, "The Stability of Water Flow Over Heated and Cooled Flat Plates," Trans. ASME, Ser. C: J. Heat Transfer, **99**, pp. 109–114.
[10] Lauchle, G. C., and Gurney, G. B., 1984, "Laminar Boundary-Layer Transition on a Heated Underwater Body," J. Fluid Mech., **144**, pp. 79–101.
[11] Tritton, D. J., 1963, "Transition to Turbulence in the Free Convection Boundary Layers on an Inclined Heated Plate," J. Fluid Mech., **16**(3), pp. 417–435.
[12] Hu, J., Ben Hadid, H., Henry, D., and Mojtabi, A., 2008, "Linear Temporal and Spatio-Temporal Stability Analysis of a Binary Liquid Film Flowing Down an Inclined Uniformly Heated Plate," J. Fluid Mech., **599**, pp. 269–298.
[13] Herbert, D. M., 1963, "On the Stability of Visco-Elastic Liquids in Heated Plane Couette Flow," J. Fluid Mech., **17**(3), pp. 353–359.
[14] Strazisar, A. J., Reshotko, E., and Prahl, J. M., 1977, "Experimental Study of the Stability of Heated Laminar Boundary Layers in Water," J. Fluid Mech., **83**(2), pp. 225–247.
[15] Sukanek, P. C., Goldstein, C. A., and Laurence, R. L., 1973, "The Stability of Plane Channel Flow With Viscous Heating," J. Fluid Mech., **57**, pp. 651–670.
[16] Eldabe, N. T. M., El-Sabbagh, M. F., and El-Sayed(Hajjaj), M. A.-S., 2007, "The Stability of Plane Couette Flow of a Power-Law Fluid With Viscous Heating," Phys. Fluids, **19**, p. 094107.
[17] Yueh, C. S., and Weng, C. I., 1996, "Linear Stability Analysis of Plane Couette Flow With Viscous Heating," Phys. Fluids, **8**(7), pp. 1802–1813.
[18] Becker, L. E., and McKinley, G. H., 2000, "The Stability of Viscoelastic Creeping Plane Shear Flows With Viscous Heating," J. Non-Newtonian Fluid Mech., **92**, pp. 109–133.
[19] Ho, T. C., Denn, M. M., and Anshus, B. E., 1977, "Stability of Low Reynolds Number Flow With Viscous Heating," Rheol. Acta, **16**, pp. 61–68.
[20] Potter, M. C., and Graber, E., 1972, "Stability of Plane Poiseuille Flow With Heat Transfer," Phys. Fluids, **15**(3), pp. 387–391.
[21] Schäfer, P., and Herwig, H., 1993, "Stability of Plane Poiseuille Flow With Temperature Dependent Viscosity," Int. J. Heat Mass Transfer, **36**, pp. 2441–2448.
[22] Sameen, A., and Govindarajan, R., 2007, "The Effect of Wall Heating on Instability of Channel Flow," J. Fluid Mech., **577**, pp. 417–442.
[23] Wall, D. P., and Wilson, S. K., 1996, "The Linear Stability of Channel Flow of Fluid With Temperature Dependent Viscosity," J. Fluid Mech., **323**, pp. 107–132.
[24] Pinarbasi, A., and Liakopoulos, A., 1995, "Role of Variable Viscosity in the Stability of Channel Flow," Int. Commun. Heat Mass Transfer, **22**, pp. 837–847.
[25] Carrière, P., and Monkewitz, P., 1999, "Convective Versus Absolute Instability in Mixed Rayleigh–Benard–Poiseuille Convection," J. Fluid Mech., **384**, pp. 243–262.
[26] Yao, L. S., 1978, "Entry Flow in a Heated Straight Tube," J. Fluid Mech., **88**(3), pp. 465–483.
[27] Joseph, D. D., 1964, "Variable Viscosity Effects on the Flow and Stability of Flow in Channels and Pipes," Phys. Fluids, **7**, p. 1761.
[28] Davis, S. H., Kriegsmann, G. A., Laurence, R. L., and Rosenblat, S., 1983, "Multiple Solutions and Hysteresis in Steady Parallel Viscous Flows," Phys. Fluids, **26**(5), pp. 1177–1182.

[29] Pinarbasi, A., and Imal, M., 2005, "Viscous Heating Effects on the Linear Stability of Poiseuille Flow of an Inelastic Fluid," J. Non-Newtonian Fluid Mech., **127**, pp. 67–71.

[30] Thomas, D. G., Sureshkumar, R., and Khomami, B., 2004, "Thermo-Mechanical Instabilities in Dean and Taylor–Couette Flows: Mechanisms and Scaling Laws," J. Fluid Mech., **517**, pp. 251–279.

[31] Thomas, D. G., Sureshkumar, R., and Khomami, B., 2003, "Influence of Fluid Thermal Sensitivity on the Thermo-Mechanical Stability of the Taylor–Couette Flow," Phys. Fluids, **15**(11), pp. 3308–3317.

[32] Al-Mubaiyedh, U. A., Sureshkumar, R., and Khomami, B., 1999, "Influence of Energetics on the Stability of Viscoelastic Taylor–Couette Flow," Phys. Fluids, **11**(11), pp. 3217–3226.

[33] Al-Mubaiyedh, U. A., Sureshkumar, R., and Khomami, B., 2002, "The Effect of Viscous Heating on the Stability of Taylor–Couette Flow," J. Fluid Mech., **462**, pp. 111–132.

[34] White, J. M., and Muller, S. J., 2002, "Experimental Studies on the Stability of Newtonian Taylor–Couette Flow in the Presence of Viscous Heating," J. Fluid Mech., **462**, pp. 133–159.

[35] White, J., and Muller, S., 2000, "Viscous Heating and the Stability of Newtonian and Viscoelastic Taylor–Couette Flows," Phys. Rev. Lett., **84**, pp. 5130–5133.

[36] Nahme, R., 1940, "Beiträge zur hydrodynamischen theorie der lagerreibung," Ing. -Arch., **11**, pp. 191–209.

[37] Rayleigh, L., 1879, "On the Stability of Certain Fluid Motions," Proc. London Math. Soc., **s1–11**, pp. 57–72.

[38] Govindarajan, R., L'vov, V. S., and Procaccia, I., 2001, "Retardation of the Onset of Turbulence by Minor Viscosity Contrasts," Phys. Rev. Lett., **87**, p. 174501.

[39] Sahu, K. C., Valluri, P., Spelt, P. D. M., and Matar, O. K., 2007, "Linear Instability of Pressure-Driven Channel Flow of a Newtonian and Herschel–Bulkley Fluid," Phys. Fluids, **19**, p. 122101.

[40] Sahu, K. C., and Govindarajan, R., 2005, "Stability of Flow Through a Slowly Diverging Pipe," J. Fluid Mech., **531**, pp. 325–334.

[41] Orszag, S. A., 1983, "Accurate Solution of the Orr–Sommerfeld Stability Equation," J. Fluid Mech., **128**, pp. 347–385.

[42] Boomkamp, P. A. M., and Miesen, R. H. M., 1996, "Classification of Instabilities in Parallel Two-Phase Flow," Int. J. Multiphase Flow, **22**, pp. 67–88.

[43] Sahu, K. C., Ding, H., Valluri, P., and Matar, O. K., 2009, "Linear Stability Analysis and Numerical Simulation of Miscible Channel Flows," Phys. Fluids, **21**, p. 042104.

[44] Selvam, B., Merk, S., Govindarajan, R., and Meiburg, E., 2007, "Stability of Miscible Core—Annular Flows With Viscosity Stratification," J. Fluid Mech., **592**, pp. 23–49.

Effect of Grooves on Cavitation Around the Body of Revolution

Yongjian Li
e-mail: yj-li03@mails.tsinghua.edu.cn

Haosheng Chen

Jiadao Wang

Darong Chen
e-mail: chendr@mail.tsinghua.edu.cn

State Key Laboratory of Tribology,
Tsinghua University,
Beijing 100084, China

Cavitation occurs widely in hydraulic machines, water and underwater vehicles, and lots of other equipments operating with liquids. Much research has been carried out to find out the factors affecting the degree of cavitation for better control of this phenomenon. In this study, the effects of grooves distributed around the body of revolution on cavitation are investigated using experimental and numerical methods. The experimental results show that the position and shape of the cavity clouds are affected by the dimensions of the grooves. A numerical simulation using the finite volume method indicates that the grooves influence the pressure distribution in the whole flow field and induce significant pressure fluctuation. The minimum pressure in each groove occurs on the top of the groove's "windward" edge and decreases as the groove width is increased. Comparing the experimental and numerical results, it is found that cavitation is closely related to the local pressure of the fluid. Multiple grooves around the body of revolution induce pressure fluctuation. The groove width affects the amplitude and interval of the fluctuation and consequently influences the distribution of cavitation. [DOI: 10.1115/1.4000648]

Keywords: cavitation, body of revolution, computational fluid dynamic

1 Introduction

Cavitation is the vaporization of liquids under the effect of depressurization. This occurs in most hydraulic machines, water and underwater vehicles, and other equipments operating with liquids [1–3]. It usually induces vibration and noise, causes erosion, and reduces the performance of the devices. Much research has been carried out to find out which factors affect cavitation. It has been proved that the geometric structure of the surface, from the shape in macroscale to the roughness in microscale, plays an important role in cavitation [1–4]. The original research in this area chiefly focused on the influence of the macrogeometries, such as the head-forms of the bodies [5], the shape of the hydrofoils [6], and so on. Later, special attention was paid to the effects of single and multiple bulges or crevices by a series of researchers, including Holl [7,8], Benson [9], and Arndt and Ippen [4]. They carried out experiments to detect the inception of cavitation and summarized several prediction formulas. Investigations have been performed to determine the cavitation effects of the surface roughness [10,11]. Stutz [12] and Coutier-Delgosha et al. [13] studied the influence of roughness on sheet cavitation separately. Coutier-Delgosha et al. found that the roughness decreased the cavity length and increased the oscillation frequency of the fluid. Numerical methods have also been used to analyze the cavitation effect of roughness. Bayada et al. [14,15] and Harp and Salant [16] investigated the cavitation on a rough surface with the average flow model, and obtained the percent area where cavitation appeared. But only statistical results can be obtained with these models.

Drag reduction [17,18] is one of the more important topics with regard to cavitation affecting underwater vehicles and weapons, most of which have, approximately, shapes of revolution. In order to investigate the effects of cavitation on surface drag, understanding is required of not only the inception and development of cavitation but also the shape, distribution, and stability of the cavities [19,20]. Geometric structures on the surface have proved to be one of the most effective methods to control cavitation. However, most research concerning the geometric effect on cavitation have been either to prevent or delay the inception of cavitation by designed geometric structures, or to enhance cavitation by specially shaped devices. Seldom has attention been paid to the control of the distribution of cavities around the object by artificial geometric structures, such as riblets or grooves. The control of the cavities by surface grooves for drag reduction is the ultimate objective of this research project and this article principally focuses on the effects of grooves on cavity distribution.

Experiments in a water tunnel were carried out and numerical simulations were conducted to investigate the influence of groove width on cavitation and cavity distribution. Experimental results showed that grooves with different widths caused different distributions of cavities. The numerical results indicated that the pressure distribution around the object varied as the groove width increased. Extremely low pressure, which was generated by the separation of the flow behind the top end of the groove's windward edge, was the principal reason for the occurrence of cavitation. Cavity clouds expand along the flow direction, and their sizes were determined by the groove widths and their positions. This conclusion makes it possible to adjust the distribution of cavities around bodies of revolution by the design of the surface grooves.

2 Experimental Researches

2.1 Experimental Methods. Experiments were carried out in the water tunnel at the State Key Laboratory of Tribology, China, as shown schematically in Fig. 1(*a*). The operating fluid was tap

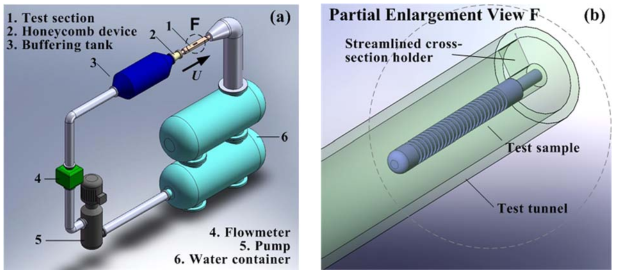

Fig. 1 Schematic of the water tunnel used in the State Key Laboratory of Tribology (China)

Contributed by the Fluids Engineering Division of ASME for publication in the Journal of Fluids Engineering. Manuscript received June 30, 2008; final manuscript received October 28, 2009; published online December 15, 2009. Assoc. Editor: Theodore Heindel.

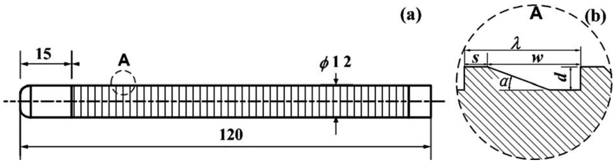

Fig. 2 Schematic of the samples: (*a*) the size of the sample and (*b*) shape of the grooves

Table 1 Parameters of Nikon D50 camera

Sensor	Resolution	Shutter speed range	Continuous shooting	Lens type
CCD	6×10^6	$1/4000\sim30$ s	2.5 frame/s	Interchangeable Nikon F-mount

water. It was pumped to a buffering tank and then was driven to the test section through a contracting duct. The test section was 300 mm in length with an inner diameter of 30 mm. In front of the test section inlet, a honeycomb component was installed to reduce the turbulent intensity of the flow. The sample was fixed on a holder placed at the end of the test section, as shown in Fig. 1(*b*). The cross section of the holder was streamlined to reduce its influence on the flow.

As shown in Fig. 2, the size of the sample was 120 mm long and 12 mm across. The head of the sample was made similar to a MK46 torpedo, which is widely used in many countries [21,22], and circumferential grooves were made on the samples, as shown in Fig. 2(*b*). The shape of the cross section of the groove was quadrilateral. In order to enhance cavitation, the windward edge was perpendicular to the axis of the body, which narrows the flow down suddenly in each wavelength of the grooves. Four dimensions describe the shape and distribution of the grooves: the space between the adjacent grooves, the "leeward" edge angle of the grooves α, groove width w, and groove depth d.

Samples with different grooves were tested in the water tunnel, and photos were captured with a Nikon D50 camera to compare the cavity cloud distributions. The effects of the groove width were then analyzed.

The camera was fixed perpendicular to the water tunnel. This camera is a digital single-lens reflex camera, which has a 23.7×15.6 mm^2 image sensor with 6.1×10^6 effective pixels. It can shoot 2.5 frames/s in continuous mode and it has the auto-focus function. Its parameters are listed in Table 1.

In the set of experiments, all the dimensions of the grooves were the same except for the groove width w and the number of the grooves. These dimensions are listed in Table 2.

The initial temperature of the water was kept constant in all the experiments. The velocity of the flow at the test section inlet was set to be 24 m/s, according to the reported speed of the MK46 torpedo, by adjusting the output frequency of the pump's transducer. The pressures in the buffering tank were tested and kept constant at 1.8 MPa.

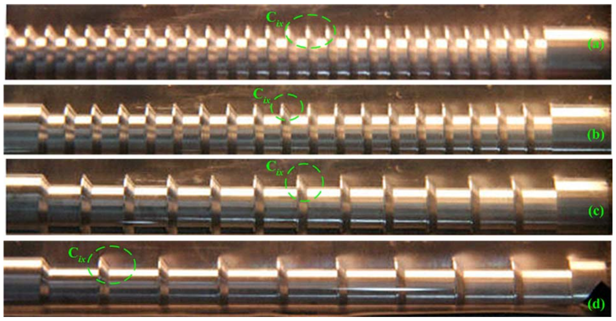

Fig. 3 Cavity cloud around the samples with different w in the tests: (*a*) No. 1 $w=3.0$ mm, (*b*) No. 2 $w=4.5$ mm, (*c*) No. 3 $w=7.5$ mm, and (*d*) No. 4 $w=10.5$ mm

2.2 Experimental Results. Photos of the samples were captured during dynamically stable flow (Fig. 3). Figure 4(*a*) shows the enlarged view of part of one groove. In both Figs. 3 and 4(*a*), light colored regions can be seen around the connecting part of the grooves, which start from the top of the windward edge, cover the space between the grooves, extend almost to the bottom of the groove along the "leeward" edge, and spread to a certain distance along the flow direction. It is reasonable to deduce that the fluids in these regions are water with many small cavities. Because of the camera's resolution, a single cavity with distinguishable boundaries could not be observed. However, due to the nature of the vapor/water mixture, the observed cavities reflect more light than the surrounding water. So, the regions where cavities exist are lighter in color in the photos. We name these regions as the cavity clouds and name the starting point of each cavity cloud as the cavitation starting point.

In Fig. 3, the first cavitation starting points occurring along the flow direction in sample Nos. 1–3 are all almost in the middle of the grooved section, while that in sample No. 4 occurs closer to the body's head.

Because the difference in brightness between the cavity clouds and the surrounding water regions is quite significant, image processing methods could be adopted to analyze the distribution of the cavity clouds. First, the colored photographs were changed into gray scale images. Then the distributions of the gray scale value of these images were obtained by an image processing program, as shown in Fig. 4(*b*). There were two peaks in the gray scale value curve, which respectively represented the high reflective region induced by the sample and the low reflective region caused by the surrounding water, i.e., the dark background. So, the area between the two peaks could be regarded as the representation of the cavity cloud. Here, lower and higher threshold values were chosen according to the gray scale value curve. In the case shown in Fig. 4, they were 90 and 240. Afterwards, the boundary between the cavity cloud and the surrounding water were attained by image processing analysis according to the lower threshold value, as shown in Fig. 4(*c*). However, it should be noted that the boundary between the cavity cloud and the sample cannot be identified solely on the higher threshold value, as the value only represents the boundary of the highlighted parts on the sample. But

Table 2 Parameters of samples in tests on effect of the groove width on cavitation

No.	s (mm)	w (mm)	d (mm)	α (deg)	N (number of grooves)
1	0.5	3.0	1.5	45	28
2	0.5	4.5	1.5	45	19
3	0.5	7.5	1.5	45	12
4	0.5	10.5	1.5	45	9

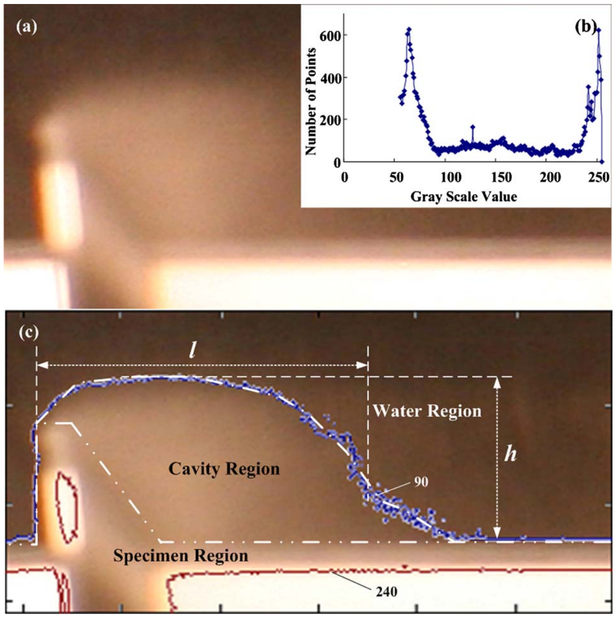

Fig. 4 Image processing for cavity cloud identification

the boundary of the sample is easily demonstrated according to its geometric parameters. Finally, the area of the cavity cloud was identified by image processing.

We use the method above to analyze the cavity clouds around the samples. The areas of the cavity clouds with respect to the position on the sample are illustrated in Fig. 5.

As shown in Figs. 5 and 3, when comparing the groove widths from 7.5 mm to 10.5 mm, the first cavitation position of sample No. 4 is located forward of that for sample No. 3. The areas of the cavity clouds in the groove at the same positions along the samples are larger with wider grooves. The uncertainty of the data shown in Fig. 5 is attributed to the resolution of the camera and the image processing. Here, the uncertainly caused by the camera is $\pm 0.197\ \mathrm{mm}^2$ (95%), and the approximation of the uncertainty contribution from image processing is $\pm 0.052\ \mathrm{mm}^2$ (95%) using the sequential perturbation method [23]. So the uncertainty in the experiment result is $\pm 0.204\ \mathrm{mm}^2$ (95%).

3 Numerical Simulation

Knowledge of the pressure distribution is indispensable for the interpretation of cavitation [24]. But it is extremely difficult to measure this pressure distribution on the surface with complex small geometric structures as it is usually too elaborate for the researchers to carry out the measurement along the grooved or ribbed surface. Until now, no measurements being generally accepted have emerged. So, numerical calculations are necessary.

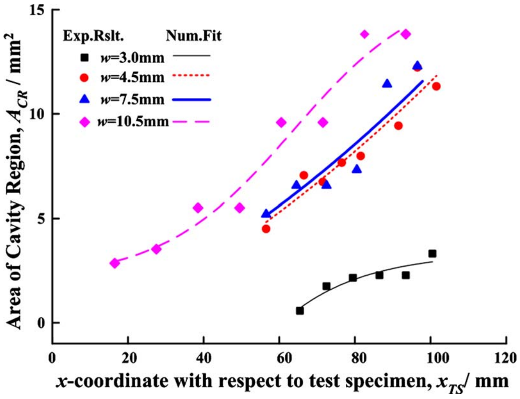

Fig. 5 Areas of cavity region with respect to the position on the sample

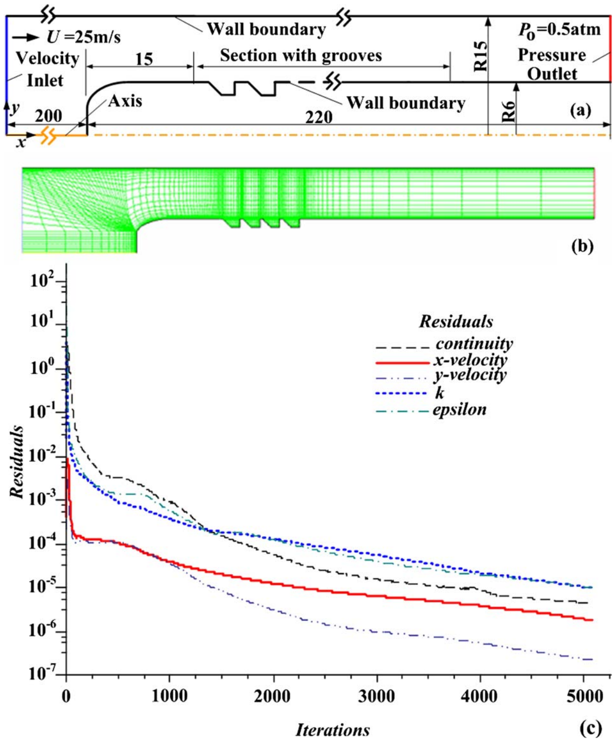

Fig. 6 Simulation model: (*a*) schematic of the model with dimension and boundary conditions, (*b*) mesh of model, and (*c*) residuals of the numerical results

The Computational Fluid Dynamics (CFD) software FLUENT was adopted to analyze these cases. It solves the equations governing the motion of fluids based on the finite volume method (FVM) [25], which is one of the most popular numerical discretization methods used in CFD. Here, Reynolds averaged Navier–Stokes equations (RANS) [26] were used to simulate the turbulent flow. The turbulent models were based on the Re-Normalization Group (RNG) k-ε model and the pressure gradient effect is considered. QUICK format is employed in the discretization of momentum equations, PRESTO format is used to discretize the pressure terms, and SIMPLEC algorithm is applied in the coupling of the pressure and velocity. A second order upwind scheme is conducted in the solving process of k and ε. References [25–29] have introduced the details of the numerical algorithms mentioned above.

The simulation domain was modeled to match the test section of the water tunnel. Since the test samples and the water tunnel were axisymmetric, a two-dimensional half body domain was used to simplify the computations (Fig. 6(*a*)). For this simulation, an inlet velocity of 25 m/s was used. This value was approximately the same as the upstream velocity set during the experiments. The proximity of the wall boundary conditions were found to result in an increased flow velocity of about 30 m/s around the body. The right side of the domain was the pressure outlet, and the pressure there was set to be 0.5 atm according to the test condition. The boundary conditions of the other sides of the domain were illustrated in Fig. 6(*a*).

Under the conditions mentioned above, the Reynolds number of the flow Re is 7.5×10^5. The turbulent kinetic energy k is $0.816\ \mathrm{m}^2/\mathrm{s}^2$, and the turbulent dissipation ratio ε is $57.7\ \mathrm{m}^2/\mathrm{s}^3$.

The mesh of the model is shown in Fig. 6(*b*). The grid size increased from the wall to the center of the flow field and the growth factor is about 1.02. The total grid number was about

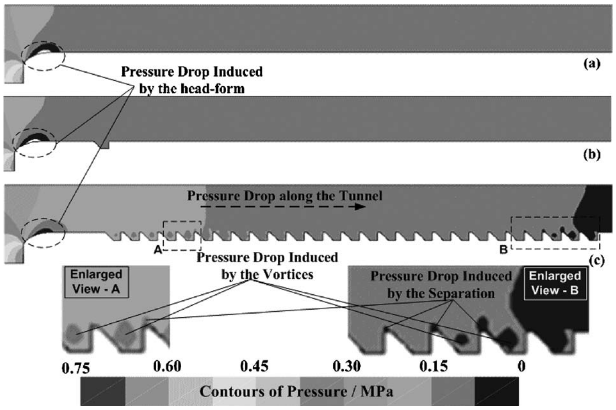

Fig. 7 Pressure distribution: (*a*) smooth surface, (*b*) surface with single groove, and (*c*) surface with distributed grooves

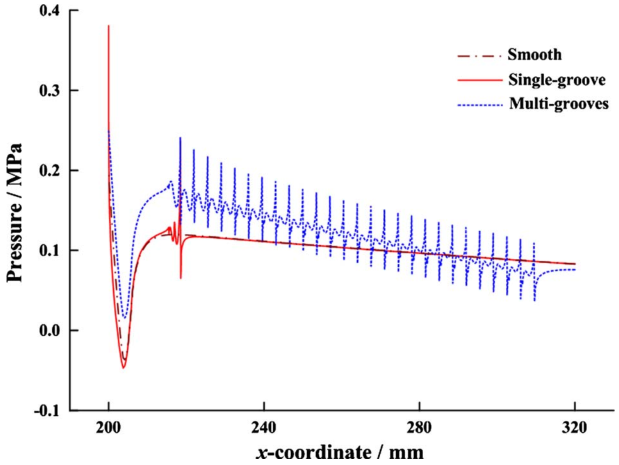

Fig. 8 Pressure distribution comparison between surface with single groove and distributed grooves

65,000 and the minimum grid size is about $3.5 \times 3.5\ \mu\text{m}^2$, which is small enough that the pressure distribution barely changed when the mesh was four times as fine as the case shown in Fig. 6(*b*).

The residual definitions are used for judging convergence. The criterion requires that the residuals decrease to 10^{-5} for the continuity, momentum, and turbulent equations. The variations in the residuals are shown in Fig. 6(*c*). The residuals of the continuity, *x*-velocity, *y*-velocity, turbulent kinetic energy, and dissipation rate all reached the convergence criteria and the pressure of the flow field almost kept constant after about 5000 iteration steps.

The pressure distributions around the body have been paid special attention, as they influence the cavitation process directly and also as they are affected by the surface grooves greatly. As a simplification, only the single-phase cases are taken into consideration. Although this simplification makes the numerical results attained less reflective of the real situation, it reduces the computation load and its results are still usable for prediction of cavitation.

In Secs. 3.1 and 3.2, a basic comparison of the pressure distributions induced by smooth surface, single groove, and distributed grooves is first made to figure out the special effect of distributed grooves. Then, the influence of the groove width is studied in detail to determine whether it is possible to adjust the distribution of the cavities by the design of the surface grooves.

3.1 Comparison Among Smooth Surface, Single Groove, and Multiple Grooves. Numerical simulations were carried out to obtain the pressure distribution around the bodies of revolution with a smooth surface, with a single groove, and with multiple grooves. The dimensions of the groove were the same as in sample No. 1, as listed in Table 2. The boundary conditions of the simulations were the same as those mentioned above.

Figure 7(*a*) represents the numerical results of the pressure distribution around the smooth sample. Figures 7(*b*) and 7(*c*) show results of the case with single groove and that with multiple grooves. Comparing Figs. 7(*a*) and 7(*b*), the effect of a single groove is only obvious in its vicinity and local pressure fluctuation. However, as shown in Fig. 7(*c*), the multiple grooves make the whole flow field quite different from that without grooves. The pressure becomes higher around the head of the body while it gets lower at the tail area of the body. It can also be observed that local low pressure regions induced by the vortices appear in the grooves.

Figure 8 shows the pressure variation along the models' surface. It is obvious that the distributed grooves change the whole pressure distribution of the flow field and induce pressure fluctuation around each groove.

Four distinct pressure drop effects can be seen in Fig. 7. First, there is the overall pressure drop along the tunnel from the dissipation effect of the side wall and the sample's surface. Second, there is the pressure drop induced by the head-form of the body of revolution. Third, there are the pressure drops caused by the vortices in the grooves. Finally, there is the pressure drop taking place as a result of the flow separation. It should be noted that sometimes the pressure drop from the head-form is a combined effect of the increase in the flow velocity around the body of revolution as the flow channel narrows, and the separation of the flow.

According to Figs. 7 and 8, the distributed grooves enhance the variation in pressure along the tunnel and reduce the pressure drop around the head of the body. The most specific effects of the grooves are pressure reduction caused by the vortices in the grooves and the separation at the top of the groove's windward edge.

3.2 Comparison of the Effect of the Grooves' Width on Cavitation. To completely investigate the effect of the dimensions of grooves on cavitation, so many factors should be taken into account that it is impossible to go over all of them in one article. However, the width-to-depth ratio of grooves (or width-to-height ratio of riblets) has been researched extensively [30–32]. It has been proved that this ratio is one of the most influential factors of the geometric structure that affect the flow patterns and the mass and heat transfer process. Here, the depth of each groove was fixed and the width was varied from 3.0 mm to 10.5 mm. The geometric dimensions of the computational models are listed in Table 2. The boundary conditions of the calculation domain were the same as what has been mentioned in Sec. 3.1. The results

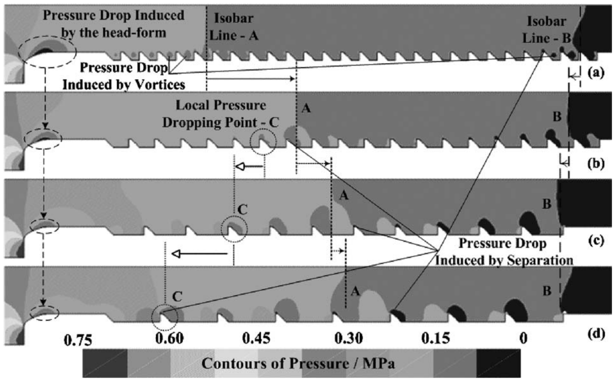

Fig. 9 Pressure distribution around the body of revolution with different groove widths

obtained were compared with those of the experiments in Sec. 2.

The numerical simulation results are shown in Fig. 9. The pressure distribution around the bodies of revolution varies with the difference in the groove width. Compared with the pressure distribution around the smooth sample shown in Fig. 7(*a*), pressure at the head of the body with grooves is significantly greater, and the magnitude of the difference is greater with increased groove width. Correspondingly, the pressures at the tails of the bodies are lower with an increase in the groove width. From Fig. 9, it can be found that the isobar-line A is repositioned farther toward the tails of the bodies while the isobar-line B is moved in the opposite direction.

Figure 9 also shows that as the groove width is increased, the local pressure on the top of the windward edge of the grooves is decreased. As mentioned above, depressurizations at these positions are usually caused by the separation of the flow. In Fig. 9, the darkest regions have pressures low enough for cavitation inception. The larger the groove width, the shorter the distance from the head of the body to the first cavitation starting point.

The center of the vortex is another position where local low pressure is generated, as shown in Figs. 9(*a*) and 7(*c*). Compared with the depressurization caused by the separation, the significance of the low pressure induced by the vortex is decreased as the groove width is increased.

Figure 10 shows the pressure distribution on the bodies. With the presence of grooves, the pressure on the surface fluctuates significantly. The pressure distributions around the grooved section of the samples are wavelike curves. They are different in shape but their wavelengths are the same as that of the grooves in each case. The mean absolute pressure is reduced along the flow direction from the effect of the side wall. The amplitude of the pressure fluctuation is closely related to the groove width. The wider the groove, the larger the amplitude.

The relationship between the pressure distribution and cavitation is analyzed by the application of a common index, which is the cavitation number (σ), which has been widely used in research on cavitation. It is defined in Eq. (1) [1–3] and used to evaluate the potential of the flow to cavitate. It expresses the relationship between the difference of a local absolute pressure from the vapor pressure and the kinetic energy per volume. The smaller it is, the more easily the fluid cavitates. In order to discuss the cavitation effect influenced by the pressure, a nondimensional parameter, which is the pressure coefficient C_p, is also defined, as shown in Eq. (2) [1–3]:

$$\sigma = \frac{p_\infty - p_v}{0.5\rho V_\infty^2} \tag{1}$$

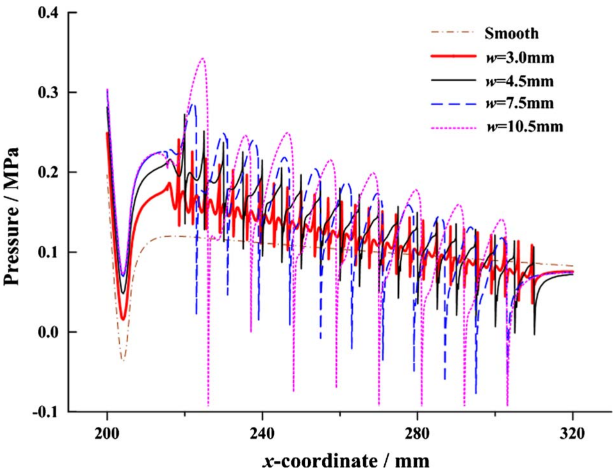

Fig. 10 **Pressure distribution curves around the body of revolution with different groove widths**

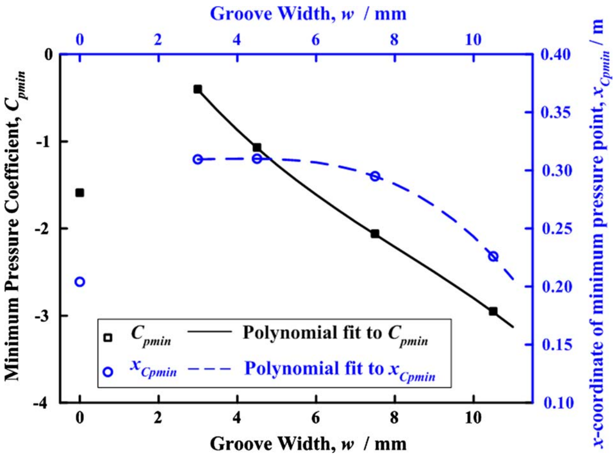

Fig. 11 **$C_{p\,\min}$ and position of $C_{p\,\min}$ in *x*-direction of body of revolution with different groove widths**

$$C_p = \frac{p - p_\infty}{0.5\rho V_\infty^2} \tag{2}$$

where p_v is the vapor pressure of fluid, p is the local pressure at the selected point, p_∞ is the upstream pressure, ρ is the density of the fluid, and V_∞ is the upstream velocity.

In this case, the upstream pressure and velocity were measured in the tests, where $p_\infty = 0.135$ MPa and $V_\infty = 25$ m/s. The operation fluid is water, and the temperature in the tests is $25 \pm 2\,^\circ\text{C}$. $\rho = 1 \times 10^3$ kg/m^3 and $p_v = 3564$ Pa. According to Eq. (1), the cavitation number in this case is 0.421.

According to the research results on cavitation [1–3], when $C_p < -\sigma$, cavitation will occur. In the case that the upstream pressure, upstream velocity, temperature, and the density of the fluid are constant, σ is invariable, so C_p can be adopted to characterize the cavitation capability of any point in the flow. The minimum C_p, $C_{p\,\min}$, and the areas of the regions where C_p is smaller than $-\sigma$ ($A_{C_p < -\sigma}$) are used to evaluate the cavitation effect of groove width, as shown in Figs. 10 and 11. The results for the smooth surface case ($w = 0$) were plotted in the figures for comparison.

As the groove width is increased, the minimum pressure coefficient decreases, and the position of the minimum pressure coefficient point moves forward toward the head of the body of revolution. In the cases where w is 3 mm or 4.5 mm, the minimum pressure coefficients are obviously larger than that of samples without grooves. Figure 12 shows the area where $C_p < -\sigma$, and that is the area of the flow where cavitation should occur. As the groove width is increased, the area of cavitation the region is quickly enlarged.

Both experiments and numerical simulations have been performed to investigate the effect of the distributed grooves on cavitation. Photos of the experiments, which showed the cavity clouds distribution around the bodies, have been obtained and numerical simulations have been carried out to analyze the pressure distribution around the bodies, taking into account the effect of distributed grooves. By comparing the numerical results to the experimental results, it is found that the local pressure obtained by the numerical simulation can be used to predict the positions of the cavitation.

4 Discussion

In this paper, only the effect of groove width is analyzed. However, as shown in other research on effects of grooves [33–35], cavitation is affected by the other geometric and spacing parameters of the grooves, such as the depth and the distribution. Further experiments and analysis should focus on the cavitation effect of those parameters.

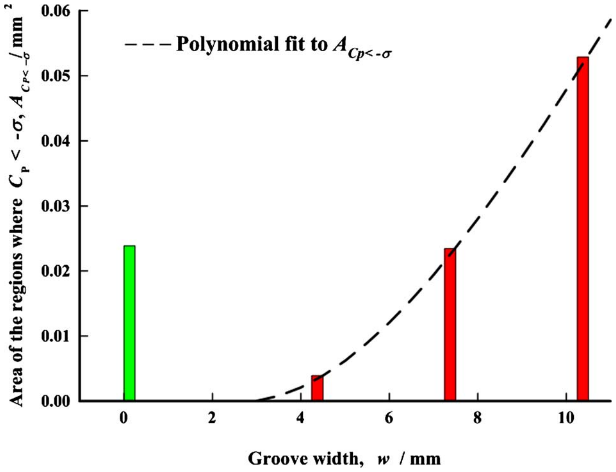

Fig. 12 Area of the regions where $C_p<-\sigma$ of body of revolution with different groove widths

Another important thing that should be noted is that the numerical simulation is performed under the assumption that the water is pure. As the real water in nature always contains microsolid or gaseous nuclei [1–3], cavitation may occur when the pressure is higher than its vapor pressure [36,37]. Cavitation occurs more readily in experiments than in the numerical simulation, such as the case of the sample with 3 mm wide grooves in Secs. 2.2 and 3.2. Moreover, the numerical results are obtained in the single-phase model. When the pressure around the body of revolution drops down below the vapor pressure, cavities will generate and move downstream. They will influence the pressure downstream and the properties of the fluid. More precise results can be achieved using a multiphase model.

The principal objective of this article is to obtain knowledge of the distribution of cavities influenced by the grooves. This concerns the inception, motion, and stability of the cavities. On one hand, the grooves enhance the pressure drop in certain local regions, which may enhance cavitation inception, while on the other hand, the fluctuations of the pressure may reduce the stability of the cavities and induce more collapses. Full knowledge of the synthesized effect requires further studies.

5 Conclusion

The effect of the distributed grooves on cavitation around the body of revolution were investigated both by experimental and numerical methods. The following conclusions can be drawn.

The numerical simulation results indicated that the distributed grooves enhance the variation in pressure along the tunnel. With the existence of the grooves, the pressure on the surface fluctuates significantly. The flow separation and vortices induced by the grooves will make the local pressure drop down greatly.

Numerical results also indicated that the pressure distribution is influenced by the groove width. As the groove width is increased, the amplitude of the pressure fluctuation around the grooved section rises rapidly. When all the other parameters of the groove are held constant, the wider the groove, the lower the local pressure on the top of the windward edge.

Both the experimental and numerical results show that the cavitation starting position and the distribution of cavities change as the groove width is varied. As cavitation is closely related to the pressure distribution, the minimum local pressure points, which usually appear on the top of the windward edge of the grooves, should be the cavitation starting points. When the minimum pressure is low enough, cavitation will occur and the cavity cloud will spread from the starting point to a certain distance downstream. The numerical results appear to be in good agreement with the experimental results.

As shown above, numerical methods can be used to obtain more information about the effects of grooves on cavitation. Multiple grooves affect the whole flow field and change the distribution of the cavity clouds. The parameters of the grooves make it possible to adjust the spatial distribution of cavitation by the design of the grooves.

Acknowledgment

The authors would like to thank Yubei Xie, Xiaodi Li, and Gang Zhou for their contributions toward this work. This work is supported by National Basic Research Program of China (Grant No. 2007CB707702) and National Natural Science Foundation of China (Grant No. 50975158).

References

[1] Lecoffre, Y., 1999, *Cavitation: Bubble Trackers*, A. A. Balkema, Brookfield, VT.
[2] Knapp, R. T., Daily, J. W., and Hammitt, F. G., 1981, *Cavitation*, Water Conservancy Press, Beijing, China.
[3] Huang, J. T., 1991, *Theory and Application of Cavitation and Cavitation Erosion*, Tsinghua University Press, Beijing, China.
[4] Arndt, R., and Ippen, A. T., 1967, "Cavitation Near Surfaces of Distributed Roughness," MIT Hydrodynamics Laboratory, Report No. 104.
[5] Ceccio, S. L., and Brennen, C. E., 1992, "Dynamics of Attached Cavities on Bodies of Revolution," ASME J. Fluids Eng., **114**, pp. 93–99.
[6] Zhang, M.-D., Wang, G.-Y, Zhang, Z., and Gao, Y.-Y., 2006, "Cavitation Inception in Turbulent Flows Around a Hydrofoil," Journal of Beijing Institute of Technology, **15**(4), pp. 393–396.
[7] Holl, J. W., 1965, "The Estimation of the Effect of Surface Irregularities on the Inception of Cavitation," *Cavitation in Fluid machinery*, ASME, New York, pp. 3–15.
[8] Holl, J. W., 1960, "The Inception of Cavitation on Isolated Surface Irregularities," ASME J. Basic Eng., **82**, pp. 169–183.
[9] Benson, B. W., 1966, "Cavitation Inception on Three Dimensional Roughness Elements," DTMB, Report No. 2104.
[10] Chang, J. C., Huang, S. B., and Lin, C. B., 2006, "Effects of Inlet Surface Roughness, Texture, and Nozzle Material on Cavitation," Atomization Sprays, **16**, pp. 299–318.
[11] Arndt, R., and Ippen, A. T., 1968, "Rough Surface Effects on Cavitation Inception," ASME J. Basic Eng., **90**, pp. 249–261.
[12] Stutz, B., 2003, "Influence of Roughness on the Two-Phase Flow Structure of Sheet Cavitation," ASME J. Fluids Eng., **125**, pp. 652–659.
[13] Coutier-Delgosha, O., Devillers, J. F., Leriche, M., and Pichon, T., 2005, "Effect of Wall Roughness on the Dynamics of Unsteady Cavitation," ASME J. Fluids Eng., **127**, pp. 726–733.
[14] Bayada, G., Martin, S., and Vazquez, C., 2005, "An Average Flow Model of the Reynolds Roughness Including a Mass-Flow Preserving Cavitation Model," ASME J. Tribol., **127**, pp. 793–802.
[15] Bayada, G., Martin, S., and Vazquez, C., 2006, "Micro-Roughness Effects in (Elasto) Hydrodynamic Lubrication Including a Mass-Flow Preserving Cavitation Model," Tribol. Int., **39**, pp. 1707–1718.
[16] Harp, S. R., and Salant, R. F., 2001, "An Average Flow Model of Rough Surface Lubrication With Inter-Asperity Cavitation," ASME J. Tribol., **123**, pp. 134–143.
[17] Cao, W., Wei, Y., Wang, C., Zou, Z., and Huang, W., 2006, "Current Status, Problems and Applications of Supercavitation Technology," Advances in Mechanics, **36**(4), pp. 571–579.
[18] Bai, L., Chen, D.-R., Li, X.-D., Wang, J.-D., Zou, G., and Xie, Y.-B., 2006, "Experimental Study and Numerical Simulation on Drag Reduction of the Underwater Vehicle Based on Surface Profile Design," Journal of Experimental Mechanics, **21**(5), pp. 661–666.
[19] Amromin, E., and Mizine, I., 2003, "Partial Cavitation as Drag Reduction Technique and Problem of Active Flow Control," Mar. Technol., **40**(3), pp. 181–188.
[20] Chen, H. S., Li, J., and Chen, D. R., 2006, "Study of Drag Forces on a Designed Surface in Bubbly Water Lubrication Using Electrolysis," ASME J. Fluids Eng., **128**(6), pp. 1383–1389.
[21] Valerio, G., 1986, "Reliability Improvement Through Environmental Tests and Defect Reduction Programs," Proceedings, Annual Technical Meeting—Institute of Environmental Sciences, pp. 36–39.
[22] Li, C. Y., 1999, "MK46 Torpedo of USA," Modern Ships, **1**, pp. 35–37.
[23] Figliola, R. S., and Beasley, D. E., 2000, *Theory and Design for Mechanical Measurements*, Wiley, New York.
[24] Kuiper, G., 1981, *Cavitation Inception on Ship Propeller Models*, Netherlands Ship Model Basin, The Netherlands.
[25] Ferziger, J. H., and Peric, M., 1996, *Computational Methods for Fluid Dynamics*, Springer, Berlin.
[26] Versteeg, H. K., and Malalasekera, W., 2007, *An Introduction to Computational Fluid Dynamics*, Pearson Education Limited, England.
[27] Hayase, T., Humphrey, J., and Greif, R., 1992, "A Consistently Formulated QUICK Scheme for Fast and Stable Convergence Using Finite-Volume Iterative Calculation Procedures," J. Comput. Phys., **98**, pp. 108–118.

[28] Van Doormaal, J. P., and Raithby, G. G., 1984, “Enhancement of the SIMPLE Method for Predicting Incompressible Fluid Flows,” Numer. Heat Transfer, **7**, pp. 147–163.

[29] Patankar, S. V., and Spalding, D. B., 1972, “A Calculation Procedure for Heat, Mass and Momentum Transfer in Three-Dimensional Parabolic Flows,” Int. J. Heat Mass Transfer, **15**, pp. 1787–1806.

[30] Cui, J., Patel, V. C., and Lin, C.-L., 2003, “Large-Eddy Simulation of Turbulent Flow in a Channel With Rib Roughness,” Int. J. Heat Fluid Flow, **24**, pp. 372–388.

[31] Leonardi, S., Orlandi. P., Djenidi, L., and Antonia, R., 2003, “Structure of Turbulent Channel Flow With Square Bars on One Wall,” Proceedings of the Third International Symposium on Turbulence and Shear Flow Phenomena, Sendai, Japan, pp. 123–128.

[32] Miyake, Y., Tsujimoto, K., and Nakaji, M., 2001, “Direct Numerical Simulation of Rough-Wall Heat Transfer in a Turbulent Channel flow,” Int. J. Heat Fluid Flow, **22**, pp. 237–244.

[33] Chen, H., Chen, D., and Li, Y., 2006, “Investigation on Effect of Surface Roughness Pattern to Drag Force Reduction Using Rotary Rheometer,” ASME J. Tribol., **128**, pp. 131–138.

[34] Naterer, G. F., Glockner, P. S., Thiele, D., Chomokovski, S., Venn, G., and Richardson, G., 2005, “Surface Micro-Grooves for Near-Wall Energy and Flow Control: Application to Aircraft Intake De-Icing,” J. Micromech. Microeng., **15**, pp. 501–513.

[35] Du, X. W., Zou, J., Fu, X., Ji, H., and Yang, H. Y., 2007, “Effect of Throttling Grooves Structure on Cavitation Noise,” Zhejiang Daxue Xuebao, **41**, pp. 456–465.

[36] Trevena, D. H., 1987, *Cavitation and Tension in Liquids*, Adam Hilger, Philadelphia, PA.

[37] Hammitt, F. G., 1980, *Cavitation and Multiphase Flow Phenomena*, McGraw-Hill, New York.

Modeling Blockage of Particles in Conduit Constrictions: Dense Granular-Suspension Flow

A. J. Parry
Department of Modeling and Simulation,
Schlumberger Riboud Product Center,
1 Rue Henri Becquerel,
Clamart 92140, France
e-mail: aparry@clamart.oilfield.slb.com

O. Millet
Laboratoire d'Etude des Phénomènes de Transfert
et d'Instantanéité: Agro-Ressources et Bâtiment,
Université de la Rochelle,
Avenue Michel Crepeau,
Cedex 1,
La Rochelle 17042, France

This paper presents a numerical simulation study of dense granular-suspension flow in a conduit with constriction. An empirical function of solid concentrations and Reynolds number prescribes the force between a particle and the fluid. This simplification reduces the computing load of the fine flow-field details around each particle. In the fluid-momentum equation, a source term distributes the force over the particle volume. The study addresses particle-laden flow at constant liquid-flow rate. Two different algorithms of the interparticle contact show that the bridging phenomenon causing the blockage of the particles persists in the presence of the fluid flow. While the particles are in movement, there are frequent interparticle and particle-wall impacts and vigorous fluctuations of the net reaction force on the wall from the particle phase. There is close correlation between the component of this reaction oriented in the flow direction and the rate of change in the pressure drop across the constricted conduit. [DOI: 10.1115/1.4000691]

Keywords: nonsmooth contact dynamics, discrete element method, fluid-particle coupling, blockage, arching

1 Introduction

Dense granular-suspension flows occur in solid-transport processes and in nature, such as in underwater avalanches. Examples in the oil industry are proppant transport for well fractures to control their opening [1], solids transport to form gravel packs that filter out sand flow [2], and management of drilling cuttings [3]. Interparticle contact and fluid-particle forces influence dense granular-suspension flows. Force chains created between particle-contact points affect the mixture dynamics. This dynamics can lead to conduit blockage near a constriction. Current design practices often use empirical criteria to maintain a minimal particle flow. These empirical relationships provide a minimal ratio of constriction width to particle size. There is a need to complement the experiments with new general-purpose numerical simulation methods. This article presents such numerical simulations of a concentrated suspension of particles in a fluid flowing through a constricted conduit (Fig. 1).

A bridging event requires a calculation framework capable of representing the particle geometry and contact configuration. We choose the discrete element method (DEM) in favor of the continuum model [4] because of the ability to model directly the contact interactions. In the smooth DEM [5], spring-dashpot connectors between particles model the contact interaction. High stiffness prevents interpenetration of particles. Explicit time integration solves the system of equations. The high stiffness leads to high natural frequencies and the requirement of small timesteps to maintain stability of the time integration. In the nonsmooth contact dynamics (NSCD) method [6], shock laws using restitution coefficients and the Coulomb unilateral contact law model the contact. The partly implicit time integration causes less constraint on the timestep size.

Some coupling methods for fluid and particle motions use fictitious domain techniques [7,8]. The simulated details of the flow around the particles require fine meshes to obtain accurate fluid-particle interaction forces. An alternative technique is the particle-source-in-cell method [9]. This method accounts for interphase exchange by empirical, lumped correlations. In its original form, the particles are smaller than the fluid mesh size. The force transfer between the particle and the fluid happens within the fluid volume element (or cell) occupied by the particle center.[1] The coupling technique adopted here is the particle-source-in-cell method extended to particle sizes larger than the fluid cells.

Section 2 explains the Lagrangian particle tracking and fluid-particle-motion coupling. The variables for the particle-contact kinematics parameterize the smooth DEM and NSCD methods. The coupling strategy considers that the fluid occupies the whole flow domain, including the particle volumes, and that the force acting from a particle to the fluid acts uniformly over the particle volume. Flow simulations around closely packed sphere arrays and spheres in the proximity of the walls measure the effectiveness of the coupling technique. Section 3 describes and discusses simulations of the blockage of particles in a conduit constriction.

2 Description of Model

2.1 Particle Kinematics. Consider the kinematics of a pair of spherical particles in contact, as depicted in Fig. 2. The position vector of the center of particle i is $\boldsymbol{x}_i$ and that of particle j is $\boldsymbol{x}_j$, measured from a fixed global frame of reference (x_1, x_2, x_3). The unit vectors aligned with the global frame are $\boldsymbol{x}_1$, $\boldsymbol{x}_2$, and $\boldsymbol{x}_3$.

At the contact point, the relative velocity $\boldsymbol{U}_{i/j}$ of particle i with respect to particle j is calculated from the particle translational $\boldsymbol{U}$ and rotational velocities $\boldsymbol{\omega}$, and the particle radius r using the formula

$$\boldsymbol{U}_{i/j} = \boldsymbol{U}_i + r_i\boldsymbol{n} \times \boldsymbol{\omega}_i - \boldsymbol{U}_j + r_j\boldsymbol{n} \times \boldsymbol{\omega}_j \tag{1}$$

$\boldsymbol{n} = (\boldsymbol{x}_i - \boldsymbol{x}_j)/|\boldsymbol{x}_i - \boldsymbol{x}_j|$ is the unit vector directed from the center of particle j to the center of particle i.

Let us define a fixed local frame of reference (n, u, v) at the contact point. The n-axis is aligned with $\boldsymbol{n}$. The u- and v-axes are in the plane containing the contact point and normal to $\boldsymbol{n}$. There is a choice in the orientation of these axes within the plane. In this

---

Contributed by the Fluids Engineering Division of ASME for publication in the JOURNAL OF FLUIDS ENGINEERING. Manuscript received December 10, 2008; final manuscript received November 6, 2009; published online January 7, 2010. Assoc. Editor: Neelesh A. Patankar.

[1] A refinement of this transfer uses a weighted projection [10].

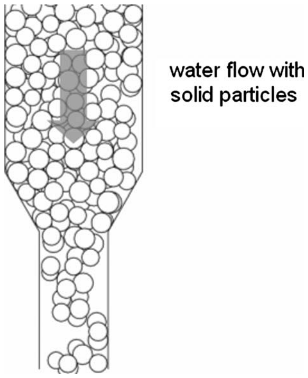

Fig. 1 Dense granular-suspension flowing through a conduit constriction; combined solid-solid and solid-fluid interactions

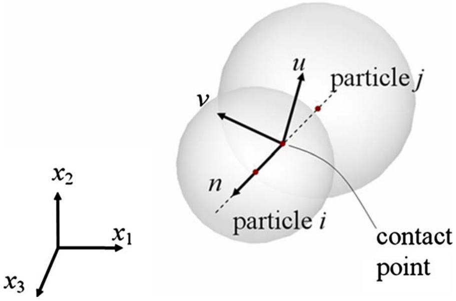

Fig. 2 Figure showing particle *i* in contact with particle *j*; local normal-tangential coordinates at contact point; normal unit vector collinear with particle centers

work the orientation of the unit vectors defining the direction of the axes $\boldsymbol{u}$- and $\boldsymbol{v}$-axes is determined from the rule

$$\begin{cases} \boldsymbol{v} = (\boldsymbol{x}_2 \times \boldsymbol{n})/|\boldsymbol{x}_2 \times \boldsymbol{n}|, & |\boldsymbol{x}_2 \times \boldsymbol{n}| \leq b \\ \boldsymbol{v} = (\boldsymbol{x}_3 \times \boldsymbol{n})/|\boldsymbol{x}_3 \times \boldsymbol{n}|, & |\boldsymbol{x}_2 \times \boldsymbol{n}| > b, \quad \text{where } 0 < b < 1 \end{cases}$$

$$\boldsymbol{u} = \boldsymbol{v} \times \boldsymbol{n} \tag{2}$$

which circumvents the possibility of singularities due to alignment of $\boldsymbol{n}$ with either $\boldsymbol{x}_2$ or $\boldsymbol{x}_3$. The choice of value of b within the range specified is arbitrary and a value of 0.9 was set.

The transformation matrix T expresses the relative velocity in the local coordinates, as follows:

$$\boldsymbol{U}_{i/j}^{\text{local}} = \begin{bmatrix} U_n \\ U_u \\ U_v \end{bmatrix} = T^t \boldsymbol{U}_{i/j} = \begin{bmatrix} n_1 & u_1 & v_1 \\ n_2 & u_2 & v_2 \\ n_3 & u_3 & v_3 \end{bmatrix}^t \boldsymbol{U}_{i/j} \tag{3}$$

2.2 Smooth Discrete Element Method. The integration of the particle-phase motion equations over the timestep $\delta t = t^{n+1} - t^n$ in the smooth discrete element method [5] is described here. The position $\boldsymbol{x}$ and angle $\boldsymbol{\theta}$ of a particle at the end of the timestep is determined from its position, angle, translational velocity $\boldsymbol{U}$, rotational velocity, $\boldsymbol{\omega}$, translational acceleration $\boldsymbol{a}$, and rotational acceleration $\dot{\boldsymbol{\omega}}$ at the beginning of the timestep, as follows:

$$\begin{aligned} \boldsymbol{x}_i^{n+1} &= \boldsymbol{x}_i^n + \delta t \boldsymbol{U}_i^n + \frac{(\delta t)^2}{2} \boldsymbol{a}_i^n \\ \boldsymbol{\theta}_i^{n+1} &= \boldsymbol{\theta}_i^n + \delta t \boldsymbol{\omega}_i^n + \frac{(\delta t)^2}{2} \dot{\boldsymbol{\omega}}_i^n \end{aligned} \tag{4}$$

Contact between particles i and j is detected by measuring the occurrence of interpenetration

$$h = -|\boldsymbol{x}_i^{n+1} - \boldsymbol{x}_j^{n+1}| + r_i + r_j \tag{5}$$

When $h > 0$, there is contact between particles i and j. In the case of contact with a wall, $r_j = 0$. There are n_c contacts associated with each particle.

The velocities at the mid-timestep level $t^{n+1/2}$ are determined from velocities and accelerations at the beginning of the timestep

$$\begin{aligned} \boldsymbol{U}_i^{n+1/2} &= \boldsymbol{U}_i^n + \frac{\delta t}{2} \boldsymbol{a}_i^n \\ \boldsymbol{\omega}_i^{n+1/2} &= \boldsymbol{\omega}_i^n + \frac{\delta t}{2} \dot{\boldsymbol{\omega}}_i^n \end{aligned} \tag{6}$$

Several terms and parameters are required to describe the particle kinetics. $\boldsymbol{F}_i$ is the fluid force acting on the particle (Sec. 2.4). The particle mass is m_i and the angular inertia about its center of mass is I_i. The fluid and particle densities are ρ_f and ρ_i, respectively. The gravitational acceleration is $\boldsymbol{g}$. Newton's second law of motion applied to the particle provides the accelerations at the end of the timestep t^{n+1} as follows:

$$\boldsymbol{a}_i^{n+1} = \frac{1}{m_i} \left(\left[\boldsymbol{F}_i + m_i \left(1 - \frac{\rho_f}{\rho_i} \right) \boldsymbol{g} \right] + \sum_{l=1}^{n_c} \boldsymbol{S}_i \right) \tag{7}$$

$$\dot{\boldsymbol{\omega}}_i^{n+1} = \frac{1}{I_i} \sum_{l=1}^{n_c} (-r\boldsymbol{n} \times \boldsymbol{S})_i. \tag{8}$$

where $\Sigma_{l=1}^{n_c} \boldsymbol{S}_i$ is the sum of all contact reactions acting on the particle. The calculation of the contact reactions is described later.

The calculation of velocities at the end of the timestep is as follows:

$$\begin{aligned} \boldsymbol{U}_i^{n+1} &= \boldsymbol{U}_i^{n+1/2} + \frac{\delta t}{2} \boldsymbol{a}_i^{n+1} \\ \boldsymbol{\omega}_i^{n+1} &= \boldsymbol{\omega}_i^{n+1/2} + \frac{\delta t}{2} \dot{\boldsymbol{\omega}}_i^{n+1} \end{aligned} \tag{9}$$

We are now ready to initiate a new timestep for the particle phase. The calculation of the motion of the particle phase is continued over the required number of timesteps.

The calculation of reaction for contact l acting from particle j to particle i is now described [11–13]. Hertz stiffness and damping coefficients are defined using the modulus of elasticity E and the Poisson's ratio υ

$$k = \frac{4}{3} \left(\frac{1 - \upsilon_i^2}{E_i} + \frac{1 - \upsilon_j^2}{E_j} \right)^{-1} \sqrt{Rh}, \quad \eta = 2\sqrt{kM} \tag{10}$$

where $R = (r_i r_j / r_i + r_j)$, $M = (m_i m_j / m_i + m_j)$, and h is defined in Eq. (5).

In the case where the contact involves a wall, $k = (4/3)(E_i / 1 - \upsilon_i^2)\sqrt{r_i h}$ and $\eta = 2\sqrt{k m_i}$.

The calculation of contact reaction is as follows:

$$\begin{aligned} \boldsymbol{S} &= T(S_n, S_u, S_v)^t \\ S_n &= \max\{0, kh + \eta U_n\} \\ S_u &= -\min\{K\sqrt{U_u^2 + U_v^2}, \mu_C S_n\} \frac{U_u}{\sqrt{U_u^2 + U_v^2}} \\ S_v &= -\min\{K\sqrt{U_u^2 + U_v^2}, \mu_C S_n\} \frac{U_v}{\sqrt{U_u^2 + U_v^2}} \end{aligned} \tag{11}$$

The Coulomb friction law relates the tangential reaction force to the normal reaction force, using the coefficient of friction μ_C. The regularization parameter K is set to 10^9 for the present work. The transformation matrix T and the relative velocities expressed in the local coordinates $[U_n \;\; U_u \;\; U_v]^t$ are defined in Eq. (3).

2.3 Contact Dynamics Method With Bipotential. This section outlines the method to advance the particle-phase motion over the timestep $\delta t = t^{n+1} - t^n$ using the NSCD method. The algorithm and method follow [14], using a bipotential in the contact relationships. This bipotential relates the relative velocities to the reactions. Explicit time integration determines the coordinates and orientations of the particles at the mid-timestep, as follows:

$$\boldsymbol{x}_i^{n+1/2} = \boldsymbol{x}_i^n + \frac{\delta t}{2}\boldsymbol{U}_i^n \tag{12}$$

$$\boldsymbol{\theta}_i^{n+1/2} = \boldsymbol{\theta}_i^n + \frac{\delta t}{2}\boldsymbol{\omega}_i^n \tag{13}$$

The analog of Eq. (5), at $t^{n+1/2}$, determines the number of contacts n_c associated with each particle.

The equations-of-motion for all particles are solved to determine the new translational $\boldsymbol{U}^{n+1}$ and rotational $\boldsymbol{\omega}^{n+1}$ velocities at the end of the timestep

$$\boldsymbol{U}_i^{n+1} = \boldsymbol{U}_i^n + \frac{1}{m_i}\left(\left[\boldsymbol{F} + m\left(1 - \frac{\rho_f}{\rho}\right)\boldsymbol{g}\right]\delta t + \sum_{l=1}^{n_c}\boldsymbol{S}\right)_i^{n+1} \tag{14}$$

$$\boldsymbol{\omega}_i^{n+1} = \boldsymbol{\omega}_i^n + \frac{1}{I_i}\left(\sum_{l=1}^{n_c}(-r\boldsymbol{n} \times \boldsymbol{S})\right)_i^{n+1} \tag{15}$$

where $(\Sigma_{l=1}^{n_c}\boldsymbol{S})_i^{n+1}$ is the sum of the translational contact impulses acting on the particle.

An iterative Gauss–Seidel procedure updates the impulses to account for the new velocities at t^{n+1}. The impulses are initialized to zero or to the values from the previous timestep, if the contacts persist. The loop, with counter q, solves the equations-of-motion until convergence of the impulse values. Convergence is considered when ε, as defined below, attains a sufficiently small value

$$\varepsilon = \frac{\displaystyle\sum_i \sum_{l=1}^{n_c}(\boldsymbol{S}^q - \boldsymbol{S}^{q-1})^2}{\displaystyle\sum_i \sum_{l=1}^{n_c}(\boldsymbol{S}^q)^2} \tag{16}$$

There are three possible contact conditions. Contacts can be separating, sticking, or sliding. The impulse for contact l acting from particle j to particle i is updated in five steps [14], as follows:

Step 1. Transform the relative velocities $\boldsymbol{U}_{i/j}^n$ and $\boldsymbol{U}_{i/j}^{n+1}$ from global to local coordinates using Eq. (3). Similarly, transform the impulse of the contact from global to local coordinates using the transformation matrix T defined in Eq. (3) as follows:

$$[S_n \;\; S_u \;\; S_v]^t = T^t[S_1^q \;\; S_2^q \;\; S_3^q]^t \tag{17}$$

Step 2. The normal and tangential momentum-restitution coefficients e_n and e_t are experimentally determined parameters. Along with the local relative velocities, they define the "formal" velocities in the local coordinates for the contact, as follows:

$$[W_n \;\; W_u \;\; W_v]^t = \left[\frac{U_n^{n+1} + e_n U_n^n}{1 + e_n} \quad \frac{U_u^{n+1} + e_t U_u^n}{1 + e_t} \quad \frac{U_v^{n+1} + e_t U_v^n}{1 + e_t}\right]^t \tag{18}$$

Step 3. Predict the impulse $[\tau_n \;\; \tau_u \;\; \tau_v]^t$ using the formula

$$[\tau_n \;\; \tau_u \;\; \tau_v]^t = [S_n \;\; S_u \;\; S_v]^t - \lambda[(W_n + \mu_C W_t) \;\; W_u \;\; W_v]^t \tag{19}$$

where $\lambda = (1 + e_n)m_i/(1 + m_i/m_j)$, $W_t = \sqrt{W_u^2 + W_v^2}$, and μ_C is the coefficient of Coulomb friction. In the case where the contact involves a wall, $\lambda = (1 + e_n)m_i$.

Step 4. Correct the impulse $[S_n \;\; S_u \;\; S_v]^t$ according to the *contact status*

if $\mu_C\tau_t < -\tau_n$, then separating out and set

$$[S_n \;\; S_u \;\; S_v]^t = 0 \tag{20}$$

else

if $\tau_t \leq \mu_C\tau_n$, then contact with sticking and set

$$[S_n \;\; S_u \;\; S_v]^t = [\tau_n \;\; \tau_u \;\; \tau_v]^t \tag{21}$$

else, *contact with sliding* and set

$$[S_n \;\; S_u \;\; S_v]^t = [\tau_n \;\; \tau_u \;\; \tau_v]^t + \left[\mu_C\frac{\tau_t - \mu_C\tau_n}{1 + \mu_C^2} \quad -\frac{\tau_u}{\tau_t}\frac{\tau_t - \mu_C\tau_n}{1 + \mu_C^2} \quad -\frac{\tau_v}{\tau_t}\frac{\tau_t - \mu_C\tau_n}{1 + \mu_C^2}\right]^t \tag{22}$$

where $\tau_t = \sqrt{\tau_u^2 + \tau_v^2}$.

Step 5. Transform the impulse from local to global coordinates while applying the under-relaxation factor γ to stabilize the update, as follows:

$$\boldsymbol{S}^{q+1} = \gamma T[S_n \;\; S_u \;\; S_v]^t + (1 - \gamma)\boldsymbol{S}^q \tag{23}$$

This iterative method determines the new velocities and updates the contact impulses. The contact treatment combines in an efficient way the Coulomb unilateral contact law for the interparticle friction and shock using momentum-restitution coefficients (normal and tangential).

The Gauss–Seidel loop terminates when the impulses for all contact pairs have converged. The particle coordinate and orientation at the end of the timestep are determined for all particles from

$$\begin{aligned}\boldsymbol{x}_i^{n+1} &= \boldsymbol{x}_i^{n+1/2} + \frac{\delta t}{2}\boldsymbol{U}_i^{n+1} \\ \boldsymbol{\theta}_i^{n+1} &= \boldsymbol{\theta}_i^{n+1/2} + \frac{\delta t}{2}\boldsymbol{\omega}_i^{n+1}\end{aligned} \tag{24}$$

We are now ready to initiate the next particle-phase timestep. The calculation of the motion of the particle phase continues for the required number of timesteps.

The implementation of the particle dynamics algorithm was validated by testing against the series of validation cases described in Ref. [14]. These tests check the tangential and normal interactions.

2.4 Fluid-Particle Interaction Force. It is possible to split the fluid-particle interaction force into a series of forces associated with distinct physical processes such as steady drag and lift forces and the unsteady inertial and viscous forces [12], each described by empirical or theoretical relations. The present work retains only the steady drag term to describe the fluid-particle interaction force in the particle equation of motion (Eq. (7) and (14)). Also, flow induced torque is neglected. These simplification are justified by the predominance of the steady drag force when the particles block near a constriction. The drag force is expressed using the fluid density ρ_f, the diameter d, the drag coefficient C_D, and the relative velocity of the fluid with respect to the particle

$$\boldsymbol{F} = \frac{\pi d^2 \rho_f}{8} C_D |\boldsymbol{V} - \boldsymbol{U}|(\boldsymbol{V} - \boldsymbol{U}) \tag{25}$$

where $\boldsymbol{V}$ is the fluid velocity and $\boldsymbol{U}$ is the particle velocity, evaluated at time level $n+1/2$ for the smooth DEM and $n+1$ for the NSCD method. Several empirical drag-force correlations are available. (Massol et al. [16] gave a comparison and analysis of several drag-coefficient formulae, for high solid volume fractions, moderate values of Reynolds number, and various packing arrangements.) In this work, we use the correlation of Wen and Yu [15]

$$\left\{\begin{array}{ll} C_D = (1-\alpha)^{-1.7}\dfrac{24}{\mathrm{Re}_s}(1+0.15\,\mathrm{Re}_s^{0.687}), & \mathrm{Re}_s \le 1000 \\ & \qquad \alpha \le 0.59 \\ C_D = (1-\alpha)^{-1.7}0.44, & \mathrm{Re}_s > 1000 \end{array}\right. \tag{26}$$

where Re_s is the particle Reynolds number defined using superficial fluid velocity. The superficial fluid velocity in a volume containing both fluid and solids is the volume-averaged fluid velocity, taking the fluid velocity to be zero in the portions of the volume occupied by solids. α is the particle-volume concentration. Section 2.5.4 explains the overall fluid and particle time integration schemes and indicates when α and $\boldsymbol{V}$ are evaluated.

2.5 Coupling of Particle and Fluid Motion

2.5.1 Fluid-Flow Equations and Solution Method. In the calculation procedure, the fluid occupies the whole flow domain, including the particle volumes. The particles interact with the fluid through the interaction forces. The fluid-momentum equation in a particle volume is extended by a source term that enforces $-\boldsymbol{F}$ (Eq. (25)) onto the fluid. The momentum source is the dominant effect on the fluid, justifying the simplification.

We evaluate the pressure gradient in a closed column containing fluid and particles. This evaluation serves to verify that the coupling treatment correctly predicts buoyancy effects in two limiting scenarios, as follows:

(1) The particles do not touch the wall and descend at their terminal velocities. In this case, the pressure gradient supports the weight of the mixture. Under terminal velocity, Eq. (7) and (14) reduces to

$$-\boldsymbol{F} = m\left(1 - \frac{\rho_f}{\rho}\right)\boldsymbol{g}$$

The source term replaces the fluid weight by the particle weight in the particle volume, as required.

(2) The wall or base supports the particles, and the fluid is stationary. In this hydrostatic case, the pressure gradient corresponds to the gradient in a fluid with no particles. In the case of stationary particles, Eq. (7) and (14) reduces to

$$-\boldsymbol{F} = 0$$

The source term preserves the fluid weight in the particle volumes, as required.

The fluid-flow algorithm used here is the finite volume method [17] of the commercially available software FLUENT [18]. Finite volumes subdivide the flow domain. The method conserves integrated mass and momentum for each finite volume. Here, the algorithm treats the fluid as incompressible. Euler's implicit technique performs the time integration. A standard high Reynolds number, two-equation turbulence model with wall functions is employed to include the effects of turbulence on the fluid flow. The drag-force relation (Eq. (25)) uses the time-averaged fluid velocity, as opposed to the instantaneous value, taking into account turbulent fluctuations.[2]

2.5.2 Local Calculation of Fluid Velocity and Particle Concentration. We now describe the method used to calculate the local fluid velocity and particle concentration around a particle in the suspension flow. These quantities are required in the fluid force expression (Eq. (25)) for the particle. The method determines the averaged local behavior, taking into account strong variations in the fluid velocity and concentration between adjacent particles.

To begin with, the particle-volume fraction field is calculated for the finite-volume cells (or elements). This is approximated numerically, as described in the three stages, as follows.

(1) Initialize the volume of solids V_{sj} to zero for all cells j.
(2) Discretize the volume of each particle into small elements δV. For each element i, find the cell j within which the element center resides and calculate $V_{sj} = V_{sj} + \delta V_i$.
(3) The solid volume fraction in each cell is calculated by $\alpha_j = V_{sj}/V_j$, where V_j is the cell volume j.

Next, the local fluid velocity and solid volume fraction around a particle is calculated for each particle in turn, using the following procedure.

Designate the maximal averaging volume for the particle, here chosen to be a sphere extending two times the particle radius from its center. Discretize this maximal averaging volume into small volume elements δV. Initialize the local particle based variables—the local solids volume fraction α, the local fluid velocity $\boldsymbol{V}$, and the sum of volume elements V for the particle—to zero. For each element δV_i, find the cell j within which the element center resides and calculate

$$\alpha = \alpha + \alpha_j \delta V_i$$

$$\boldsymbol{V} = \boldsymbol{V} + \boldsymbol{V}_j \delta V_i$$

$$V = V + \delta V_i$$

where $\boldsymbol{V}_j$ is the fluid velocity in the cell j. Elements that do not reside within a cell are outside of the flow domain and are not included in the summations. Then calculate the local particle variables as

$$\alpha = \alpha / V$$

---

[2] Although not pursued in this work, methods are available to include the effects of instantaneous turbulent velocity fluctuations on the drag [12].

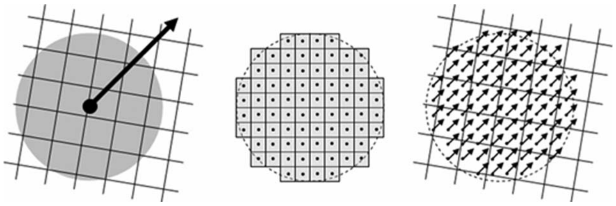

Fig. 3 Distribution of the particle-fluid force onto multiple fluid cells: schematic of the particle on multiple fluid cells with force acting from particle to fluid (left), particle discretized into small cubes and force distributed uniformly onto the cubes (middle), and projection of the cube forces onto fluid cells (right)

$$\boldsymbol{V} = \frac{\boldsymbol{V}}{V(1-\alpha)}$$

Note that the cell-based velocities $\boldsymbol{V}_j$ are considered as superficial velocities.

2.5.3 Projection of Particle Forces Onto the Fluid Mesh. A source term in the fluid-momentum equation serves to transmit the interphase force (Eq. (25)) for each particle to the fluid. The force acts uniformly over the particle volume. Figure 3 explains the procedure for force projection onto the fluid mesh. Figure 3 (left) shows a 2D representation of the particle superimposed on a fluid mesh and the force vector acting from the particle to the fluid. The particle volume is discretized into small subvolumes. A particle-volume discretization is shown in Fig. 3 (middle). Each subvolume contributes its proportional share to the total force. This subvolume force acts on the fluid element in which its center resides (Fig. 3, right). The fluid-momentum equations are modified to account for the particle forces acting in each finite volume.

Next, we measure the usefulness of the empirical fluid-particle force correlation and explore the effectiveness of the hypothesis of using only forces within the fluid, neglecting particle volumes, to represent the fluid-particle coupling. A range of simulations are done on three configurations: flows through fixed arrays of close packed spheres, flow around fixed isolated spheres near walls, and flow through fixed spheres in the flow configuration studied in Sec. 3. These configurations will be treated in turn.

We consider three different packing structures of equally sized spheres: cubic, body-centered-cubic (bcc), and face-centered-cubic (fcc) arrangements. The solid volume fraction α is 0.511 in each structure. The flows investigated were aligned with the structures and had superficial Reynolds numbers Re_s of 10 and 8000. We compare the resolved geometry simulations results with those of the force-projection method, which is denoted as unresolved geometry method. Use of periodic boundary conditions allowed reduction in the flow domain size to a unit cell for each structure.

Table 1 lists the drag forces obtained by the resolved and unresolved methods. The normalization employs the true average superficial fluid velocity V_s. Also shown are the drag values obtained by direct input of Re_s, V_s, and α into the drag correlation (Eq. (26)). The resolved simulation results show good agreement with the correlation at low Re_s, with up to 1.19 times the force from the direct application of the correlation. At higher Re_s, there is notable difference between the resolved cubic-structure result and those of the bcc or fcc results. The comparison between the correlation and the resolved results at higher Re_s also show notable difference. The resolved force values range from 0.2 to 0.58 times the value from the direct application of the correlation. There is clearly a need for more in-depth information on drag coefficients of close packed structures at high Re_s. This important aspect is not considered further in this article.

The unresolved technique uses an iterative coupled scheme, where information on the local flow velocity and solid concentration is used to determine the drag force from application of the correlation equation. This drag force is projected onto the fluid cells, which, in turn, affects the fluid velocity. For the purposes of determination of local fluid velocity and particle-volume fraction and the projection of fluid-particle force onto the fluid cells, it is required to discretize the particle volume and the spherical-averaging volume. The particle and averaging spheroid are discretized into subelements of length 1/30th the particle radius or averaging volume radius. For the cubic-structure unresolved simulations, a range of fluid mesh densities have been investigated with cell sizes ranging from 0.1 to 0.67 times the sphere radius. The unresolved technique provides results showing good agreement with the correlation at low Re_s and reasonably good agreement at high Re_s. The forces range from 0.88 to 1.11 times the direct correlation values in the laminar flow simulations and the forces range from 0.69 to 0.92 times the direct correlation values in the turbulent flow simulations. The fluid cell size test carried out for the cubic structure indicates that the unresolved method can be applied with coarse fluid meshes without significant loss of precision.

In order to study the flow around a fixed sphere in the proximity

Table 1 Drag force in cubic, body-centered-cubic, and face-centered-cubic structures

			$\frac{F}{d^2\rho_f V_s^2}$	
			$\mathrm{Re}_s=10$, $\alpha=0.511$	$\mathrm{Re}_s=8000$, $\alpha=0.511$
Correlation (Eq. (25))			23.003	2.4382
	Packing structure	No. of cells		
Resolved	Cubic	174,383	21.858 (0.95)[a]	1.4139 (0.58)
	bcc	345,848	24.732 (1.08)	0.5131 (0.21)
	fcc	646,244	27.372 (1.19)	0.4971 (0.20)
		$\delta L_{\mathrm{cell}}/R$		
Unresolved	Cubic	0.1	23.725 (1.03)	1.688 (0.69)
		0.2	23.257 (1.01)	1.715 (0.70)
		0.4	22.908 (1.0)	1.754 (0.72)
		0.67	25.630 (1.11)	2.231 (0.92)
	bcc	0.2	20.351 (0.88)	1.744 (0.72)
	fcc	0.2	22.066 (0.96)	1.915 (0.79)

[a] Ratio of resolved or unresolved force to correlation force.

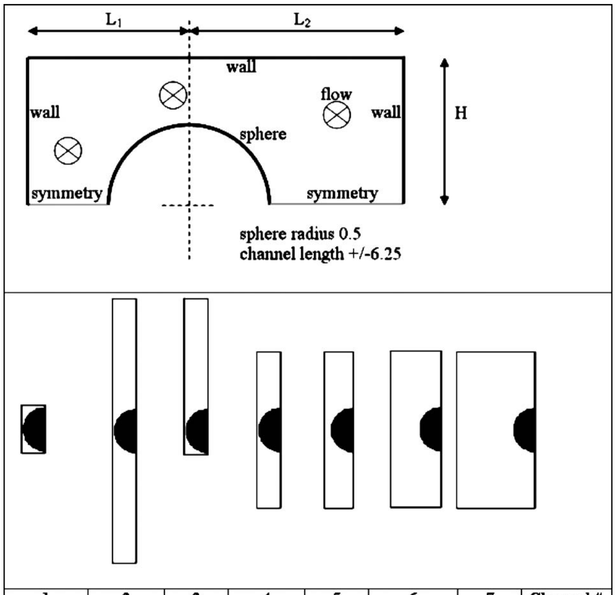

1	2	3	4	5	6	7	Channel #
0.5625	3.125	0.5625	1.8438	1.8438	1.8438	1.8438	L_1
0.5625	3.125	3.125	1.8438	1.8438	1.8438	1.8438	L_2
0.5625	0.5625	0.5625	0.5625	0.6875	1.1875	1.8438	H
0.2306	0.1624	0.1894	0.1617	0.1423	0.1254	0.1254	α

Fig. 4 Parameters for the wall proximity tests. Channel of length is equal to 12.5 sphere diameters, containing a single sphere at mid-length. The channel section parameters are L_1, L_2, and H (top). Seven sections are studied (middle and bottom). The solid volume fraction α was calculated according to Sec. 2.5.2 (bottom).

of walls, a channel containing a sphere is simulated with both resolved and unresolved methods. The parameters defining the channel dimensions and wall distances are shown in Fig. 4. As in the previous test, the particle volume (or spherical-averaging volume) is discretized into subelements of length 1/30th of the particle radius (or averaging volume radius). Uniform flow profiles are imposed on the inlet to the channel, which is placed 6.25 sphere diameters upstream on the sphere. The solids volume fractions using the procedure in Sec. 2.5.2 with a maximal averaging volume of twice the sphere radius are also indicated in the last row of the table. Figure 5 shows the normalized streamwise components of the force acting on the whole sphere. At the high Re_s flows studied, the unresolved method underpredicts the resolved-method force in channel 1 by a factor of 0.7. For the other channels, the unresolved method overpredicts the resolved-method forces by factors of 1.4–1.8.

The performance of the unresolved method in the flow configuration of Sec. 3 is now studied. The spheres are fixed in their initial position and the vertical component of the steady state drag force is calculated using the resolved and unresolved methods. The geometry, physical, and model parameters are described in Secs. 3.1–3.3. The flow corresponds to a sphere-based superficial Reynolds number of 8000. The number of cells for the resolved simulations are 4.3×10^6. In Fig. 6 the force values of selected particles are listed. There is reasonable agreement between the resolved and unresolved methods.

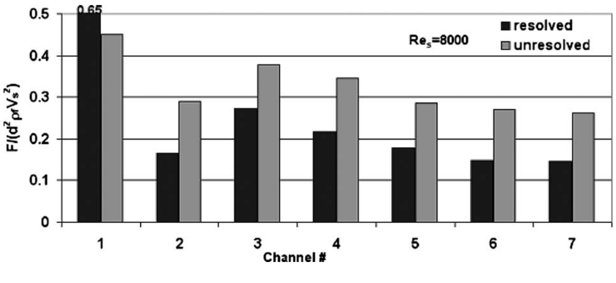

Fig. 5 Wall proximity test, streamwise component of drag force; resolved and unresolved methods (Re_s=8000)

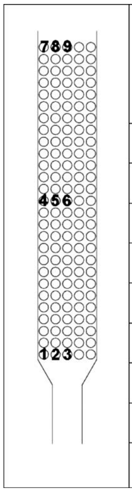

Particle #	Re_s=8000		
	$F_{resolved}$ [N]	$F_{unresolved}$ [N]	$\frac{F_{unresolved}}{F_{resolved}}$
1	0.0293	0.0248	0.8459
2	0.0396	0.0302	0.7618
3	0.0408	0.0329	0.8069
4	0.0278	0.0319	1.1491
5	0.0288	0.0328	1.1406
6	0.0386	0.0330	0.8571
7	0.0336	0.0293	0.8734
8	0.0348	0.0300	0.8604
9	0.0344	0.0300	0.8700

Fig. 6 Drag forces on particles corresponding to the configuration studied in Sec. 3; test with particles fixed in the initial positions Resolved and unresolved methods (Re_s=8000)

2.5.4 Coupling of Fluid- and Particle-Flow Solvers. An explicit time-marching method couples the fluid and particle motions during the time integration over the fluid-flow timestep $\delta t = t^{m+1} - t^m$ (Fig. 7). The mean particle-fluid interaction forces calculated during the previous timestep $\langle \boldsymbol{F} \rangle^{m-1\to m}$ determine the fluid field. In turn, the new fluid velocity field $\boldsymbol{V}^{m+1}$ and the previous particle-volume fraction field α^m determine the particle field. This two-step process is repeated in the next fluid-flow timestep. The particle-motion stage is subdivided into a number of smaller timesteps to permit the calculation of multiple impacts during a single fluid timestep.

3 Granular-Suspension Flow in Conduit With Constriction

3.1 Configuration. A granular suspension of 135 spherical 8 mm particles in water flows in a conduit with constriction. Figure 8 shows the dimensions of the channel and constriction in the form of a 60 deg convergent constriction. The depth of the flow domain is 9 mm. Initially, the particles are arranged as a rectangle in the upper part of the channel equidistant from the walls. The horizontal and vertical interparticle spacing is 10 mm.

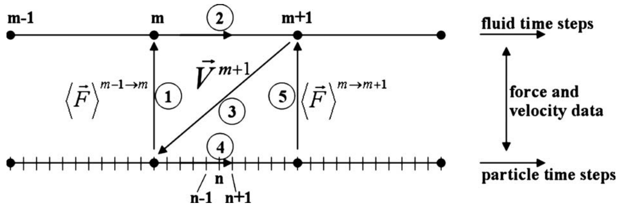

Fig. 7 Fluid and particle-phase coupling sequences. Exchange of data between fluid (top line) and particle (bottom line) solvers.

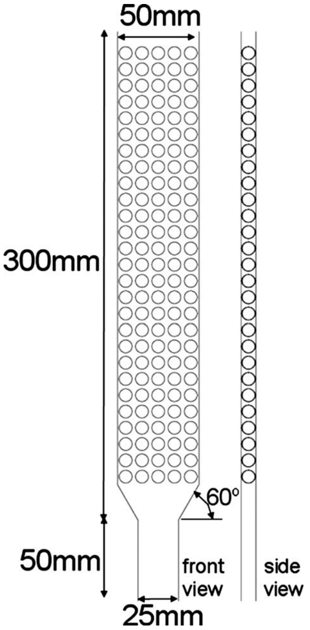

Fig. 8 Geometry and initial particle configuration: 135 particles of 8 mm diameter

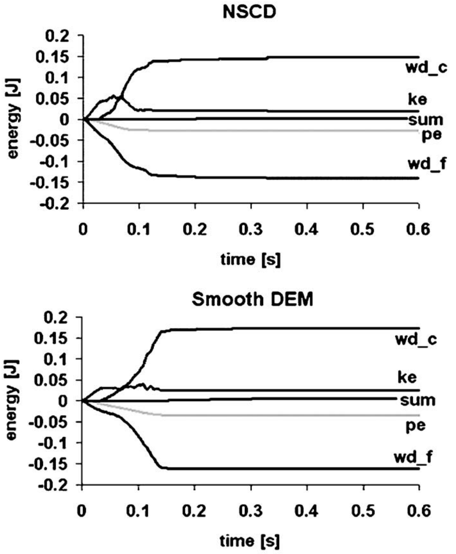

Fig. 9 Particle-phase-energy balance for NSCD (top) and smooth DEM (bottom): ke=kinetic energy, pe=potential energy, wd_f=work done on particles by fluid, wd_c=energy dissipated by particle interaction, and sum=ke+pe−wd_f+wd_c

3.2 Properties. The water is at ambient conditions. The particle density is twice that of water. The Coulomb friction coefficient for the interparticle and wall contacts (including front and back walls) is $\mu_C=0.6$. For the NSCD method, the normal and tangential restitution coefficients for the interparticle and all wall contacts are $e_n=0.0$ and $e_t=1.0$. For the smooth DEM method, the particle Young's modulus and Poisson's ratio used in Eq. (10) are $E=200$ MPa and $\upsilon=0.3$, respectively. The Young's modulus describes a relatively flexible solid such as low-density polyethylene. This parameter of the smooth DEM method controls the interpenetration of particles. Combined with the particle mass, it controls the timestep size allowed. For the present smooth DEM simulations, the level of interpenetration remains below 0.1 mm.

3.3 Algorithm Settings. The domain is discretized with a structured mesh of $30\times 200\times 6$ finite volumes in the width, height, and depth directions, respectively. The fluid cell size corresponds to 0.375 times the radius of the spheres. The timestep size for the fluid-flow algorithm is 0.0005 s. The NSCD method uses 1000 substeps, and the smooth DEM uses 20,000 substeps. The fluid enters the domain at the top with a velocity of 1 m/s. The initial fluid velocity is 1 m/s downward throughout the domain, whereas initially, the particles are at rest. This situation gives for the particles an initial superficial Reynolds number Re_s of 8000. The downward gravitational acceleration is included.

The convergence criterion for the fluid-flow solver is the normalized residual level of 1×10^{-6} for all the flow variables. For the particle phase using the NSCD method, the Gauss–Seidel loop is terminated when the convergence tolerance in Eq. (16) is below 0.01 or the number of iterations exceed 1000. The under-relaxation factor for the impulse update (γ of Eq. (23)) is 0.5. Each particle volume is discretized into small cubes of edge length $r/10$ for the fluid-source-term calculations (Sec. 2.5.3). The zone of radius $2r$ for the averaging of the superficial fluid velocity (Sec. 2.5.2) is discretized into cubes of side $2r/10$. The resolution of the projection volume corresponds to 0.024% of the particle volume, and likewise, the resolution of the averaging volume corresponds to 0.024% of the averaging volume.

3.4 Discussion of Results. Figure 9 shows the evolution of energy trade-offs for the particle phase. The trade-off happens between kinetic and potential energies, work done by the fluid-to-particle forces, and energy dissipated by particle interaction. Particles that have left the domain through the outlet contribute no further to the energy exchange. At about 0.15 s, the particle flow jams, rapidly bringing the energy exchange to a halt. For the smooth DEM, a very small change in total energy during the simulation indicates a good temporal resolution for the particle equations-of-motion. The energy balance is not a sufficient quality

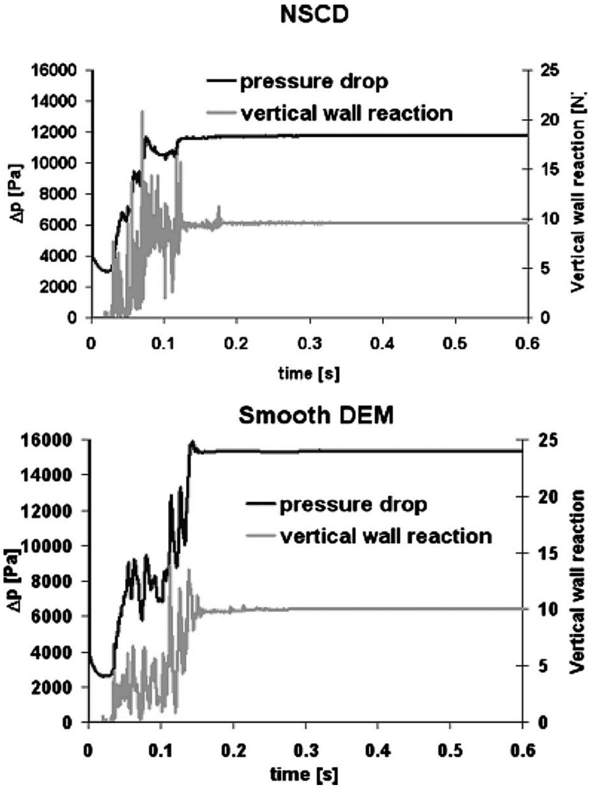

Fig. 10 Evolution of the pressure drop and total particle-wall reaction for the NSCD (top) and smooth DEM (bottom)

measure of the time integration for the NSCD method, since the implicit nature of the time integration assures energy balance even for a coarse time resolution. For the NSCD method, time-grid-independence tests were carried out to ensure that a sufficiently small timestep was employed. The energy evolution curves in Fig. 9 indicate a similar repartition of the energy components for the two simulation methods. The kinetic energy of the particle phase does not return to zero after jamming, since some of the particles have left the domain.

Figure 10 shows the evolution of pressure drop between the inlet and outlet and the vertical component of reaction force due to both particle frictions along the vertical conduit walls and impact on the convergent section, averaged over the fluid timestep. The onset of the flow generates a high-pressure drop, followed by a small decrease until the particle slug encounters the constriction at about 0.05 s. The pressure drop then builds up until jamming occurs. From that moment on, the pressure drop and wall force stay constant. While the particles are flowing, the wall force fluctuates, indicating the erratic dynamics of the multiple contacts.

Figure 11 displays the time derivative of the pressure drop and particle-wall reaction. In both the NSCD and smooth DEM methods, there is a clear correlation between the rate of change in the pressure drop and particle-wall reaction. The pressure drop fluctuations depend principally on the fluid-particle interaction force. In such situations, the temporal derivative of the fluid-momentum equation renders the difference between the fluid and particle accelerations proportional to the time derivative of the pressure drop. Particle and fluid accelerations result from the contact dynamics.

Results from both the smooth DEM and NSCD methods show blocking of the particles at about 0.11 s. Figure 12 show some results from the smooth DEM method at 0.75 s. The left plot shows the fluid velocity in the central plane of the duct with channeling, where the fluid-flow chooses the path of least resistance. The middle plot shows fluid velocity of the cells adjacent to the walls and shows that the magnitudes are higher than on the mid-plane. The right plot shows the corresponding particle configuration, indicating the normal and tangential contact reactions with line thickness proportional to reaction magnitude.

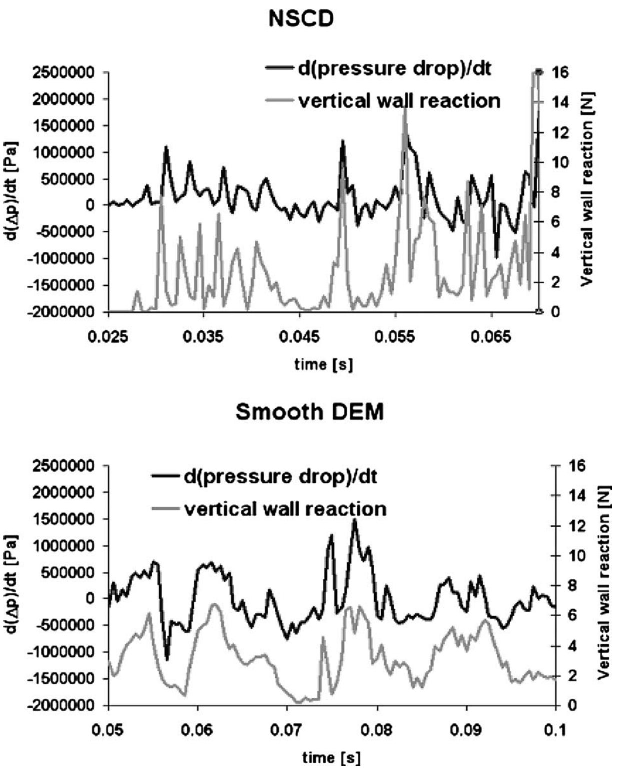

Fig. 11 Time rate of change in the system pressure drop with total particle-wall vertical reaction for the NSCD (top) and smooth DEM (bottom)

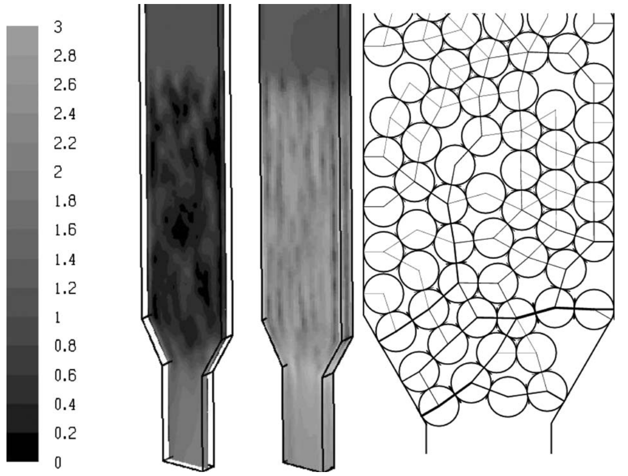

Fig. 12 Fluid speed (left: legend in m/s) and particle configuration in bridged state (right), showing force chains; smooth DEM method at 0.75 s

The accuracy of the present coupling strategy depends on the quality of the transfer laws used between the fluid and particle phases. The method is attractive, since a fine fluid mesh is not required to predict the interphase forces. The computation time of the coupled fluid-particle problem is quite similar to a dry-particle simulation. Regarding computational resources for the algorithm, serial versions of the NSCD and smooth DEM codes both take approximately 24 h on a 2.33 GHz processor PC to complete the above simulations, with 9 mm domain thickness.

3.4.1 Further Simulations. A further simulation is carried out with a flow domain of 50 mm depth, instead of 9 mm. The particles are arranged in simple cubic configuration with 10 mm spacing, so that the initial positions are as they were previously but with five layers of particles, in the depth direction, instead of one. The number of fluid cells in the depth direction is 30. We use the smooth DEM method with the same parameters and settings as were previously used. Figure 13 displays the strong correlation between the rate of change in the pressure drop and vertical-wall reaction. Also shown is the repartition of mechanical energy of the particle phase as a function of time and the conservation of total energy of the particle phase, and front and right-side views of the particle configuration at 0.215 s.

4 Conclusions

The two coupled fluid-particle calculation methods studied can both capture the bridging blockage of the particles in dense granular-suspension flow in conduits with constrictions.

Both methods predict a strong correlation between the temporal change in the pressure drop and the streamwise component of wall reaction due to the particle-phase contact. As the transported particles become jammed during blockage and bridging, the streamwise pressure gradient increases rapidly, while the fluid seeps through the gaps between the slowly moving or stationary particles.

The use of an algebraic formula for fluid-particle interaction forces is attractive, from the computational resource viewpoint, since the fine details of the local flow fields around particles need not be resolved. The accuracy of the method directly depends on the ability of the force correlations to predict the particle-fluid forces. Experimental evaluation of drag coefficients at high Reynolds numbers would be valuable for implementation into the

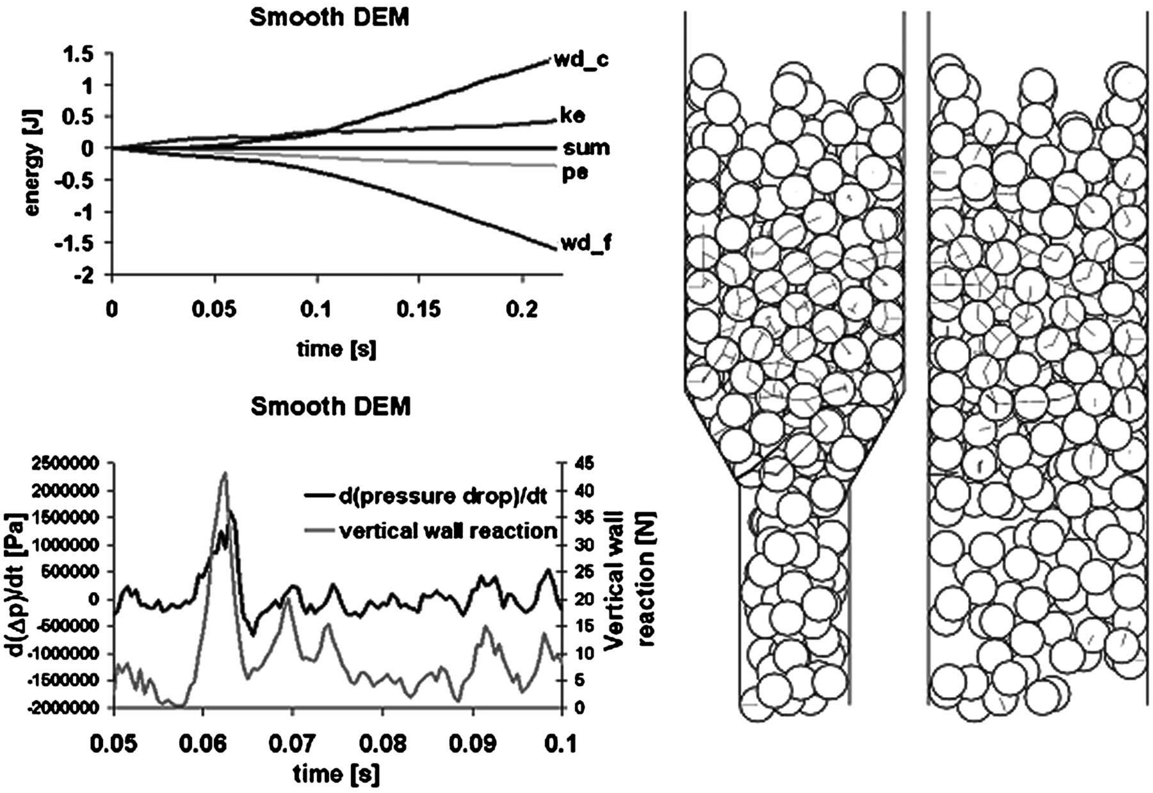

Fig. 13 Smooth DEM in deep geometry: graph showing correlation of the rate of change in the system pressure drop with wall vertical reaction (left bottom), evolution of energy repartition (left top), and particle configuration at 0.215 s (right)

method described in this paper. The effects of unsteadiness (added mass effects) and high solids volume fraction on the drag forces require to be evaluated.

Acknowledgment

The authors acknowledge the helpful discussions with Professor A. Hamdouni of the Université de la Rochelle and J. Fortin of the Université de Picardie Jules Verne INSSET. A.J.P. is grateful for the advice given by his Schlumberger colleagues, M. G. Luling and B. J. A. Zielinska.

Nomenclature

List of Symbols

a = particle translational acceleration ($\mathrm{ms^{-2}}$)
b = constant, $0<b<1$
C_D = drag coefficient for sphere, 1
d = particle diameter (m)
E = Young's modulus ($\mathrm{N\ m^{-2}}$)
e_n = momentum-restitution coefficient, normal direction, 1
e_t = momentum-restitution coefficient, tangential direction, 1
$\boldsymbol{F}$ = force from fluid to particle (N)
$\boldsymbol{g}$ = gravitational acceleration ($\mathrm{ms^{-2}}$)
h = distance of interpenetration of two particles (m)
I = moment of inertia of sphere about center of mass, $=md^2/10$ ($\mathrm{kg\ m^2}$)
K = regularization parameter (Eq. (11)) ($\mathrm{N\ m^{-1}\ s}$)
k = stiffness (Eq. (10)) ($\mathrm{N\ m^{-1}}$)
M = reduced mass of particles i and j (Eq. (10)) (kg)
m = mass of sphere, $=\pi\rho\ d^3/6$ (kg)
n_c = number of contacts associated with each particle
R = reduced radius of particles i and j (Eq. (10)) (kg)
Re_s = superficial Reynolds number, based on slip velocity, $=\rho_f(1-\alpha)|\boldsymbol{V}-\boldsymbol{U}|d/\mu$, 1
r = particle radius (m)
$\boldsymbol{S}$ = translational contact impulse or reaction force (N s or N)
T = matrix of direction cosines for contact point coordinates, 1
t = time (s)
$\boldsymbol{U}$ = particle translational velocity ($\mathrm{m\ s^{-1}}$)
$\boldsymbol{V}$ = fluid velocity ($\mathrm{m\ s^{-1}}$)
V = volume
$\boldsymbol{W}$ = formal velocities for contact pair in local coordinates ($\mathrm{m\ s^{-1}}$)
$\boldsymbol{x}$ = particle position vector (m)

Greek Letters

α = volume concentration of the particle phase, 1
ε = convergence criterion for the impulses, 1
γ = under-relaxation factor for the impulse update, 1
η = damping coefficient ($\mathrm{N\ m^{-1}\ s}$)
λ = numerical parameter in impulse predictor-corrector scheme (kg)
μ = fluid dynamic viscosity ($\mathrm{kg\ m^{-1}\ s^{-1}}$)
μ_C = Coulomb friction coefficient, 1
υ = Poisson's ratio, 1
$\boldsymbol{\theta}$ = particle rotational angle (rad)
ρ_f = fluid density ($\mathrm{kg\ m^{-3}}$)

ρ = particle density (kg m^{-3})
$\boldsymbol{\tau}$ = translational contact impulse (N s)
$\boldsymbol{\omega}$ = particle rotational velocity (rad s^{-1})

Superscripts

local = local coordinate system
m = flow solver timestep index
n = particle solver timestep index
q = Gauss–Seidel loop counter
t = transpose of a matrix

Subscripts

c = contact index
f = fluid
i = index of particle
j = index of particle in contact with particle i
m = flow solver timestep index
n = particle solver timestep index
s = particle or superficial
t = tangential

References

[1] Nolte, K. G., 1988, "Fluid Flow Considerations in Hydraulic Fracturing," Paper No. SPE 18537.
[2] Gruesbeck, C., Salathiel, W. M., and Echols, E. E., 1979, "Design of Gravel Packs in Deviated Wellbores," Paper No. SPE 6805, pp. 109–115.
[3] Leising, L. J., and Walton, I. C., 2002, "Cuttings-Transport Problems and Solutions in Coiled-Tubing Drilling," Paper No. SPE 77261.
[4] Jackson, R., 2000, *The Dynamics of Fluidized Particles*, Cambridge University Press, Cambridge.
[5] Cundall, P. A., and Stack, O. D. L., 1979, "A Discrete Numerical Model for Granular Assemblies," Geotechnique, **29**, pp. 47–65.
[6] Jean, M., and Moreau, J.-J., 1991, *Dynamics of Elastic or Rigid Bodies With Frictional Contact: Numerical Methods*, Publications du L.M.A., Berlin, Vol. 124, pp. 9–29.
[7] Glowinski, R., Pan, T. W., Helsa, T. I., Joseph, D. D., and Périaux, J., 2001, "A Fictitious Domain Approach to the Direct Simulation of Incompressible Viscous Flow Past Moving Rigid Bodies: Application to Particulate Flow," J. Comput. Phys., **169**(2), pp. 363–426.
[8] Megally, A., Laure, P., and Coupez, T., 2004, "Direct Simulation of Rigid Fibers in Viscous Fluid," Proceedings of the Third International Symposium on Two-Phase Flow Modelling and Experimentation, Pisa.
[9] Crowe, C. T., Sharma, M. P., and Stock, D. E., 1977, "The Particle-Source-in Cell (PSI-Cell) Model for Gas Droplet Flows," ASME J. Fluids Eng., **99**, pp. 325–332.
[10] Garg, R., Narayanan, C., Lakehal, D., and Subramaniam, S., 2007, "Accurate Numerical Estimation of Interphase Momentum Transfer in Lagrangian-Eulerian Simulations of Dispersed Two-Phase Flows," Int. J. Multiphase Flow, **33**, pp. 1337–1364.
[11] Tsuji, Y., Tanaka, T., and Ishida, T., 1992, "Lagrangian Numerical Simulation of Plug Flow of Cohesionless Particles in a Horizontal Pipe," Powder Technol., **71**, pp. 239–250.
[12] Crowe, C. T., Sommerfield, M., and Tsuji, Y., 1998, *Multiphase Flow With Droplets and Particles*, CRC, Boca Raton, FL.
[13] Maugis, D., 2000, *Contact, Adhesion and Rupture of Elastic Solids*, Springer-Verlag, Berlin.
[14] Fortin, J., Millet, O., and de Saxcé, G., 2005, "Numerical Simulation of Granular Materials by an Improved Discrete Element Method," Int. J. Numer. Methods Eng., **62**, pp. 639–663.
[15] Wen, C. Y., and Yu, Y. H., 1966, "Mechanics of Fluidization," Chem. Eng. Prog., Symp. Ser., **62**, pp. 100–111.
[16] Massol, A., Simonin, O., and Poinsot, T., 2004, "Steady and Unsteady Drag and Heat Transfer in Fixed Arrays of Equal Sized Spheres," CERFACS, Technical Report No. TR/CFD/04/13.
[17] Ferziger, J. H., and Perić, M., 2002, *Computational Methods for Fluid Dynamics*, Springer, New York.
[18] Fluent Inc., 2006, FLUENT 6.3 User's Guide.

Liquid Sheet Breakup in Gas-Centered Swirl Coaxial Atomizers

V. Kulkarni

D. Sivakumar

C. Oommen

Department of Aerospace Engineering,
Indian Institute of Science,
Bangalore,
Karnataka 560012, India

T. J. Tharakan
Liquid Propulsion Systems Centre,
Indian Space Research Organization,
Valiamala,
Thiruvananthapuram 695547, India

The study deals with the breakup behavior of swirling liquid sheets discharging from gas-centered swirl coaxial atomizers with attention focused toward the understanding of the role of central gas jet on the liquid sheet breakup. Cold flow experiments on the liquid sheet breakup were carried out by employing custom fabricated gas-centered swirl coaxial atomizers using water and air as experimental fluids. Photographic techniques were employed to capture the flow behavior of liquid sheets at different flow conditions. Quantitative variation on the breakup length of the liquid sheet and spray width were obtained from the measurements deduced from the images of liquid sheets. The sheet breakup process is significantly influenced by the central air jet. It is observed that low inertia liquid sheets are more vulnerable to the presence of the central air jet and develop shorter breakup lengths at smaller values of the air jet Reynolds number Re_g. *High inertia liquid sheets ignore the presence of the central air jet at smaller values of* Re_g *and eventually develop shorter breakup lengths at higher values of* Re_g. *The experimental evidences suggest that the central air jet causes corrugations on the liquid sheet surface, which may be promoting the production of thick liquid ligaments from the sheet surface. The level of surface corrugations on the liquid sheet increases with increasing* Re_g. *Qualitative analysis of experimental observations reveals that the entrainment process of air established between the inner surface of the liquid sheet and the central air jet is the primary trigger for the sheet breakup.* [DOI: 10.1115/1.4000737]

Keywords: gas-centered coaxial atomizers, liquid sheets, jet/sheet breakup, sprays

1 Introduction

It has always been the endeavor of all engineers working in spray combustion to transform bulk liquid (fuel and/or oxidizer) into tiny droplets. A decrease in the size of liquid droplets results in better combustion quality parameters such as combustion efficiency, heat release, exhaust gas emissions, etc. Spray formation is accomplished in a liquid propellant engine by means of an atomizer present inside the engine combustion chamber. A successful atomizer design must provide high quality of atomization needed to ensure an efficient combustion process. For liquid propellant rocket (LPR) applications, several atomizer configurations are being currently employed and the most commonly used configurations are the impinging type [1,2] and the coaxial type [3–7]. A coaxial type atomizer comprises of an inner orifice surrounded by an outer orifice and it has been used with both liquid/gas [3,4,7] and liquid/liquid type propellant combinations [5,6]. The present investigation of gas-centered coaxial swirl atomizer falls under the category of liquid/gas coaxial atomizers.

Gas-centered swirl atomizers have been studied under two major configurations: the premixing type and the coaxial type. In the premixing type, the liquid flows over the inner wall of the gaseous orifice by passing it through tangential ports and a mixing process between the liquid and the gas occurs inside the gaseous orifice. In the coaxial type, the liquid and the gas flow via two different orifices arranged coaxially. Figure 1 illustrates a schematic of a coaxial type gas-centered swirl atomizer. The atomizer, as illustrated in the figure, discharges a central gaseous jet surrounded by an annular swirling liquid sheet. Soller et al. [8] studied the combustion behavior of sprays discharging from gas-centered swirl coaxial atomizers and found that the coaxial type atomizers exhibit superior combustor wall compatibilities compared with that of the premixing type in the context of wall thermal stress levels. Sprays discharging from the coaxial type gas-centered swirl atomizers bend toward the spray axis, thereby reducing the thermal load experienced on the walls of combustor [9].

Spray formation in atomizers is governed by the breakup behavior of liquid jet or sheet discharging from the atomizer orifices [10]. In gas-centered swirl coaxial atomizers, the physical process by which the outer liquid sheet interacts with the central gas jet and the role of the central gas jet in the breakup of the liquid sheet into drops are key factors in determining the quality of atomization. The fundamental mechanisms governing the breakup of a liquid sheet injected into still ambient air are well documented in the current literature. The comprehensive experimental study by Dombrowski and Fraser [11] revealed the influence of flow and orifice parameters such as liquid properties, velocity of the liquid sheet, turbulence at the orifice exit, etc., on the breakup of liquid sheets. The breakup occurs via the interaction of the liquid sheet with the surrounding gas medium [12–14]. The aerodynamic shear developed over the surfaces of the liquid sheet causes waves to grow and these waves separate from the liquid sheet in the form of ligaments, which subsequently disintegrated into droplets [15,16]. Two types of waves aid the sheet breakup: sinuous and dilational [17]. Sinuous waves are produced when the two surfaces of the liquid sheet oscillate in phase with each other and dilational waves result from the out-of-phase motion of the two surfaces. Several theoretical studies have been reported on the propagation of these waves in liquid sheets and their influence on the sheet stability, and a recent review summarizes the outcomes of these investigations [18].

The influence of coflowing air on the breakup behavior of liquid sheets, particularly planar liquid sheets, has been studied extensively. Mansour and Chigier [19] studied the disintegration mechanism of liquid sheets discharging from a slit type orifice in

---

Contributed by the Fluids Engineering Division of ASME for publication in the Journal of Fluids Engineering. Manuscript received December 14, 2008; final manuscript received November 24, 2009; published online January 12, 2010. Assoc. Editor: Theodore Heindel.

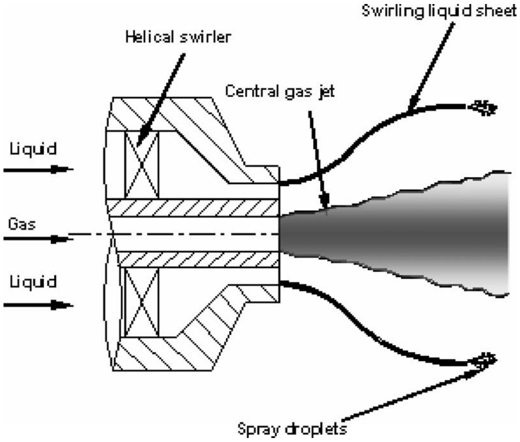

Fig. 1 A schematic of jets discharging from a gas-centered swirl coaxial atomizer

the presence of coflowing air. The airflow over the surfaces of the liquid sheet augments the formation of cellular structures (thin liquid membrane bounded by thick ligaments) in the liquid sheet. In a similar study, Stapper et al. [20] suggested that the cellular type breakup occurs at higher relative velocities between the liquid sheet and the coflowing air jet. A much finer experimental study on the formation of cellular structures in liquid sheets by Park et al. [21] showed that their presence is attributed to the unstable sinuous waves developing over the liquid sheet. The cellular type breakup results in wider drop size histograms as the thin membranes of cellular structures generate finer spray droplets and the rims seen at the periphery of cellular structures generate larger diameter droplets. A classification of disintegration regimes for liquid sheets with low air velocities discharging from a coaxial airblast atomizer was done by Adzic et al. [22]. The authors identified three major disintegration regimes: Kelvin–Helmholtz regime, cellular regime, and atomization regime. A systematic study on the role of coflowing air on the liquid sheet behavior was carried out by Lozano et al. [23] by including the effect of air boundary layer and air viscosity in the stability analysis of the liquid sheet. The authors suggested that the air velocity mostly determines the oscillatory behavior of the liquid sheet and the theoretical predictions on the characteristics of sheet oscillation improve with the inclusion of air viscosity in the analysis. A general observation in these studies is that the flow characteristics of coflowing air play a dominant role in the disintegration of the liquid sheet sandwiched between the air sheets.

The present experimental study deals with the breakup phenomena of swirling liquid sheets discharging from gas-centered swirl coaxial atomizers. The primary objective is to understand how the central gas jet aids the breakup process of such liquid sheets and the subsequent spray formation. The breakup of swirling liquid sheets without the coflowing gas jet has been studied extensively in the context of pressure swirl atomizers, and Lefebvre [10] provides a comprehensive summary on the breakup process of such simple swirling liquid sheets. In the present work, a gas jet exists in the aircore of the abovementioned simple swirling liquid sheets. The effect of the central gas jet on the sheet behavior is significantly different from the role played by still ambient air, and such an interaction process between the central gas jet and the swirling liquid sheet is not fully understood in the current literature. Note that several of the published works on gas-centered swirl coaxial atomizers confined their attention to the analysis of combustion related aspects [7–9]. A systematic experimental investigation is carried out in the present work to document the influence of central gas jet on the breakup behavior of the outer swirling liquid sheet by conducting cold flow experiments at ambient atmospheric conditions with air and water as working fluids.

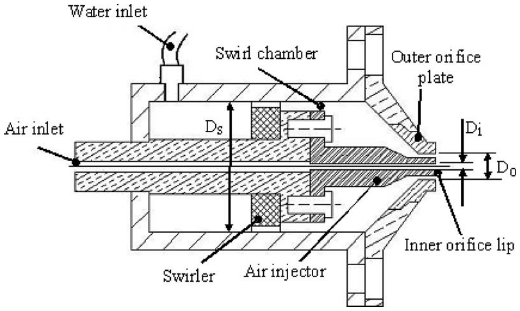

Fig. 2 A schematic of the gas-centered swirl coaxial atomizer used in the present study

2 Experimental Details

A schematic of the gas-centered swirl coaxial atomizer used in this study is shown in Fig. 2. Major components of the atomizer configuration are highlighted in the figure. The outer orifice plate consisted of a converging portion and an orifice. Diameter of the outer orifice D_o and that of the inner (central) orifice D_i were kept at 4.4 mm and 2.4 mm, respectively. Lip thickness of the inner orifice was kept at 0.3 mm, which resulted in an orifice gap of 0.7 mm for the outer orifice. Swirling motion to the flowing liquid was imparted by passing the liquid through rectangular shaped helical passages present over the periphery of the swirler. Two different atomizer configurations ($CA1$ and $CA2$) were studied by varying the geometrical parameters of the swirler. The width w of the rectangular helical passage was kept at 1.0 mm for both $CA1$ and $CA2$. The depth h of the helical passage was kept differently for the atomizer configurations as 0.5 mm for $CA1$ and 1.0 mm for $CA2$. The number of helical passages in the swirler n was fixed at 6 for both the atomizer configurations. The swirling intensity of the outer pressure swirl atomizer was characterized in terms of swirl number S, which was estimated in the present study using the relation

$$S = \frac{\pi D_o D_s}{4nwh} \tag{1}$$

where D_s is the diameter of the swirl chamber [5,6]. The estimated values of S for the atomizer configurations $CA1$ and $CA2$ were 25.7 and 12.3, respectively. A standard spray test facility was used to carry out the experiments. The facility consisted of a large stainless steel tank containing water kept under a particular pressure by means of a compressed air supply and an air pressure regulator. Flexible tubes capable of withstanding high pressures were used to carry the experimental liquid to the atomizer assembly. Tubes similar in nature, drawn from the compressed air supply, were used to deliver air at a given mass flow rate which was estimated by employing an orifice flow meter. A filter was employed between the liquid storage tank and the atomizer assembly to arrest contaminants present in the liquid. Necessary needle valves along with pressure gauges were connected in the flow lines to keep the fluid flow at steady operational conditions.

The flow behavior of liquid sheets was characterized by capturing images of liquid sheets using photographic techniques. A Nikon D1X digital camera with diffused backlighting system was used to take photographs of the liquid sheets. The pixel resolution of the camera was 2000 × 1312. The diffused backlighting system consisted of a strobe lamp, and each flash from the strobe lamp had lasted for about 12 μs, which became the time resolution for imaging. The measurements obtained from the image analysis are: the half spray cone angle of spray at the orifice exit θ, the radial spread of spray SW at different locations in the spray axis, the breakup length of the liquid sheet L_b, and the two-dimensional surface profile of the liquid sheet. Figure 3 shows the details of θ, L_b, and SW on a typical image of the outer swirling liquid sheet.

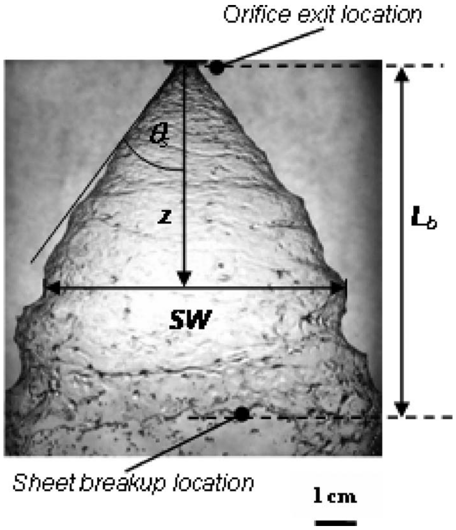

Fig. 3 A typical image of the outer liquid sheet illustrating the details of θ, L_b, and SW

Table 1 Uncertainty estimates

Quantity	Source of uncertainty	Net uncertainty (%)
m_l	Measurement resolution (1%) Repeatability (0.12–4.03%)	1–4.15
m_g	Measurement resolution (0.030%) Repeatability (0.22–4.3%)	1.75–4.68
$(\Delta P)_l$	Measurement resolution (2%) Repeatability (1.67–3.57%) Calibration (0.13–1.27%)	2.6–4.28
$(\Delta P)_g$	Measurement resolution (0.02%) Repeatability (0.83–6.67%) Calibration (1.71–5.16%)	1.9–8.42
L_b	Breakup point identification (0.09–0.109%) Repeatability (1.35–10.75%)	1.35–10.75
SW	Spray width point identification (0.53–2.31%) Repeatability (3.05–7.69%)	3.1–8.03

An image processing algorithm was developed to deduce the two-dimensional surface profile of the liquid sheet in the form of plots from the high resolution images of liquid sheets. The algorithm identifies the bounding pixels of spray contour at different Z locations (counted in terms of pixels) from the orifice exit. The locations of the bounding pixels in the digital image were carefully extracted so that the data can be plotted using a graphical software. These profiles were analyzed systematically to understand the surface perturbations and ligaments developing from the liquid sheets.

The flow condition of the outer liquid sheet was expressed in terms of Weber number We_l as

$$\mathrm{We}_l = \frac{\rho_l U_l^2 t_f}{\sigma} \tag{2}$$

where ρ_l is the liquid density (998 kg/m^3), σ is the surface tension (0.0728 N/m), U_l is the axial velocity of the liquid sheet at the orifice exit, and t_f is the thickness of the liquid sheet at the orifice exit. The value of t_f was estimated using an analytical relation reported in the literature [10] as

$$t_f = 3.66\left(\frac{D_o m_l \mu_l}{\rho_l (\Delta P)_l}\right)^{0.25} \tag{3}$$

where m_l is the liquid mass flow rate, $(\Delta P)_l$ is the injection pressure drop across the outer orifice, and μ_l is the liquid dynamic viscosity (1.003×10^{-3} kg/ms). The axial velocity of the liquid sheet at the orifice exit, U_l was estimated from the mass conservation as

$$U_l = \frac{m_l}{\rho_l \pi t_f (D_o - t_f)} \tag{4}$$

The flow condition of the central air jet was expressed in terms of Reynolds number Re_g as

$$\mathrm{Re}_g = \frac{\rho_g U_g D_i}{\mu_g} \tag{5}$$

where ρ_g is the air density (1.2 kg/m^3), U_g is the axial velocity of the gas jet at the orifice exit, and μ_g is the air dynamic viscosity (1.81×10^{-5} kg/ms). The value of U_g was estimated from the mass conservation as

$$U_g = \frac{4 m_g}{\rho_g \pi D_i^2} \tag{6}$$

where m_g is the air mass flow rate.

The uncertainty estimates for primary measurements are presented in Table 1. The uncertainty estimates for derived measurements like spray contraction parameter, nondimensionalized breakup length, etc., can be determined from Table 1. The calculation for net uncertainty was based on the procedure described by Moffat [24].

3 Results and Discussion

3.1 Visual Observations on the Breakup of the Outer Liquid Sheet by the Central Air Jet.

Figure 4 illustrates the images of outer swirling liquid sheets discharging from the gas-centered swirl coaxial atomizer *CA*1 with different combinations of outer liquid sheet and central air jet flow conditions. An image row in the figure corresponds to the cases of increasing Re_g for a constant We_l and an image column corresponds to the cases of increasing We_l for a constant Re_g. It is evident from the image rows of Fig.

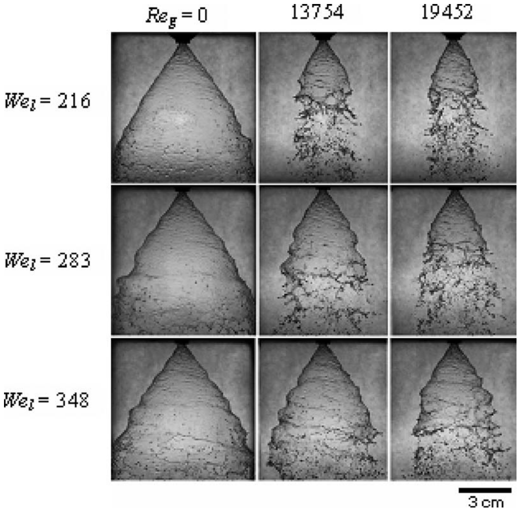

Fig. 4 Images of liquid sheets discharging from the gas-centered swirl coaxial atomizer *CA*1 ($S=25.7$) for different combinations of We_l and Re_g

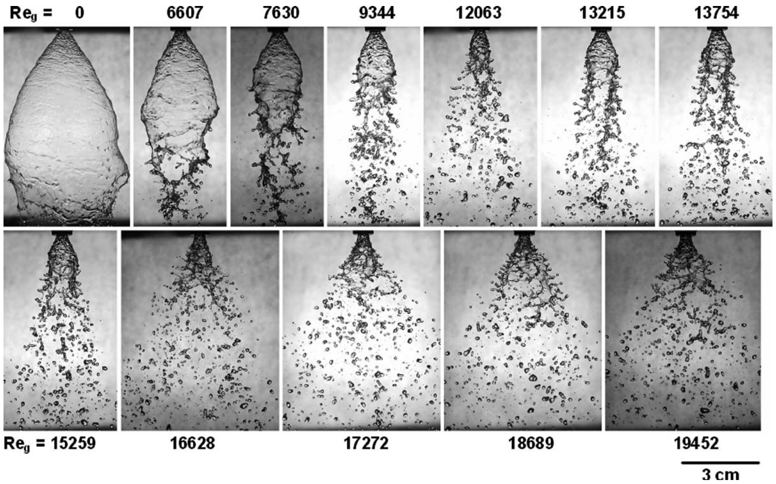

Fig. 5 The influence of the central air jet on the flow behavior of the outer liquid sheet with $We_l = 114$ discharging from the gas-centered swirl coaxial atomizer *CA*2 ($S = 12.3$). We_l remains constant for all the images shown in this figure.

4 that for a given We_l, an increase in Re_g destabilizes the outer liquid sheet and decreases the breakup length of the liquid sheet (L_b). In a similar manner, an increase in We_l for a given Re_g increases L_b. Detailed analysis on the sheet breakup process was carried out by constructing image sequences for a particular We_l, however with varying Re_g. Figure 5 shows a sequence of images illustrating the breakup of the outer liquid sheet with $We_l = 114$ under different central air jet flow conditions. The image at the leftmost top corner of Fig. 5 corresponds to the liquid sheet without any central air jet. The presence of the central air jet with low Re_g pulls the liquid sheet toward the spray axis, as seen in the second and third images off of the top row of Fig. 5 and results in a shift in the sheet breakup location toward the orifice exit. The central air jet impinges directly on the inner surface of the liquid sheet at slightly higher Re_g conditions, which may be leading to the generation of chunks of liquid masses immediately after the breakup. The liquid sheet collapses dramatically with further increase in Re_g, as seen in the images of Fig. 5 and the breakup of the liquid sheet occurs in the near region of the orifice exit. High resolution images illustrating the breakup of the liquid sheet at higher values of Re_g are given in Fig. 6. The axisymmetric conical shape of the outer liquid sheet, as observed in the lower values of Re_g, is no longer seen at these higher values of Re_g and the sheet breakup occurs in a more complex manner. Discrete liquid sheets bounded by thick rims are dominantly seen at these flow conditions.

The images given in Fig. 5 show an increase in the radial spread of spray with increasing Re_g particularly in the higher range of Re_g (see the last five images of Fig. 5). An intense mixing between the liquid sheet and the central air jet in the near region of the orifice exit occurs at these flow conditions because the jet boundaries are closer to each other than ever before. Note that the inertia of the central air jet in the near region of the orifice exit is proportional to $\rho_g U_g^2$, which is two orders of magnitude larger than that of the liquid sheet, $\rho_l U_l^2$ at higher values of Re_g given in Fig. 5. The increase in radial spread with increasing Re_g at higher values of Re_g may be a direct consequence of momentum exchange between the jets. A closer interaction between the liquid sheet and the central air jet in the near region of the orifice exit under these flow conditions may result in a violent breakup of liquid masses.

Figures 7(*a*)–7(*c*) show the two-dimensional surface profiles of liquid sheets discharging from the gas-centered swirl coaxial atomizer *CA*2 for different combinations of We_l and Re_g. In general surface corrugations seen on the liquid sheet increases with increasing Re_g and this effect is more pronounced for low inertia liquid sheets. The liquid sheets with lower inertia are showing more surface corrugations for a given increase in Re_g, and higher inertia liquid sheets need a larger increase in Re_g to develop simi-

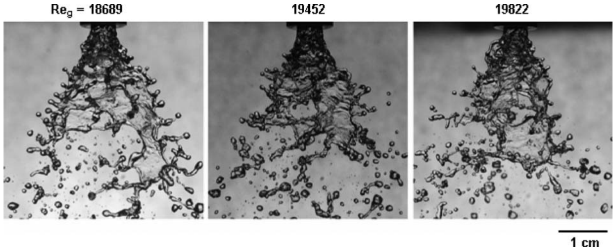

Fig. 6 High resolution images illustrating the violent and complex breakup of the liquid sheet by the central air jet in the near region of the orifice exit. Atomizer configuration is *CA*2 ($S = 12.3$) and $We_l = 114$.

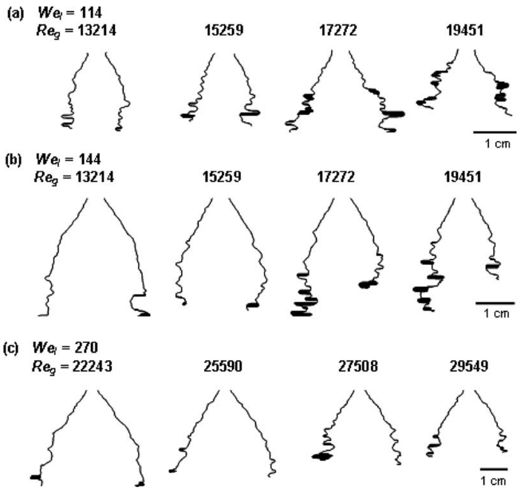

Fig. 7 Enlarged view of the two-dimensional surface profiles of liquid sheets discharging from the gas-centered swirl coaxial atomizer *CA*2 ($S = 12.3$) with different combinations of We_l and Re_g: (*a*) $We_l = 114$, (*b*) $We_l = 144$, and (*c*) $We_l = 270$

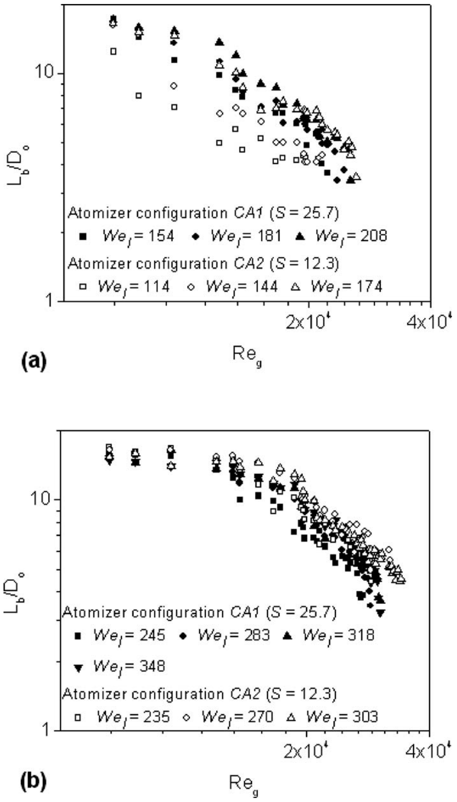

Fig. 8 Quantitative variation in L_b with Re_g for different values of We_l: (*a*) low values of We_l and (*b*) moderate and high values of We_l

lar levels of surface corrugations. Qualitatively this can be seen by comparing the profiles given in Fig. 7(*a*) (or Fig. 7(*b*)) with that of Fig. 7(*c*). Note that the profiles of liquid sheets given in Fig. 7(*c*) correspond to higher values of Re_g compared with those of Figs. 7(*a*) and 7(*b*). The dark patches seen in a surface profile correspond to the presence of thick liquid masses, for example, liquid ligaments, and indicate the termination of a smooth liquid sheet. The profile analysis of liquid sheets with increasing Re_g reveals that the dark patches appear more in the case of low inertia liquid sheets. This suggests that the low inertia liquid sheets are prone to develop thick liquid ligaments during the sheet breakup process. Interestingly it is observed that even at very high values of Re_g, an intact liquid sheet is always present in the near region of the orifice exit and the sheet breakup occurs at distances one or two times the outer orifice diameter from the orifice exit. This can be understood from the sheet surface profiles given in Figs. 7(*a*)–7(*c*). In the present gas-centered swirl coaxial atomizers, the liquid sheet at the orifice exit is separated from the central air jet by the inner orifice lip and a meaningful interaction between the liquid sheet and the central air jet is expected to happen a few millimeters away from the orifice exit.

3.2 Quantitative Variation in L_b With Flow Conditions.

The breakup process of outer liquid sheets is analyzed further by deducing quantitative measurements of L_b from the spray images. Figures 8(*a*) and 8(*b*) show the quantitative variation in L_b with Re_g for different values of We_l. Each data point in Figs. 8(*a*) and 8(*b*) corresponds to the arithmetic average of L_b values measured from a set of a minimum of three images captured during repeated experimental runs at a given test condition. The variation in L_b with Re_g clearly shows that the central air jet destabilizes the outer liquid sheet. For low inertia liquid sheets, the influence of the central air jet on L_b is seen even at low values of Re_g, as illustrated in Fig. 8(*a*). The variation in L_b with Re_g for high inertia liquid sheets given in Fig. 8(*b*) shows that the breakup length remains unaltered in the lower values of Re_g and drastic changes in L_b are seen at higher Re_g. Figures 8(*a*) and 8(*b*) also show that the decrease in L_b with increasing Re_g is more rapid for low inertia liquid sheets and is gradual for high inertia liquid sheets. The measurements of L_b given in Figs. 8(*a*) and 8(*b*) do not show any significant influence of S on the sheet breakup length for the atomizer configurations studied.

3.3 Physical Insights on the Sheet Breakup Process.

The breakup process of liquid sheets in gas-centered swirl coaxial atomizers is influenced by several physical events. Since a swirling liquid sheet diverges away from the spray axis, it is essential to bring the liquid sheet closer to the boundary of the central air jet in order to establish an effective interaction process between the liquid sheet and the central air jet. This process is accomplished by the central air jet itself. The presence of the air jet inside the core of the outer swirling liquid sheet establishes an entrainment process of air between the central air jet and the inner surface of the outer liquid sheet. The air entrainment process reduces the local pressure over the inner surface of the outer liquid sheet and thereby increases the pressure difference across the liquid sheet P_e-P_i, where P_e and P_i are, respectively, the pressures at the outside and inside surfaces of the outer liquid sheet. For a given P_e, an increase in P_e-P_i makes the liquid sheet move toward the spray axis. A stronger air entrainment process, or higher Re_g, increases P_e-P_i and the spray continues to contract with increasing Re_g. Such a spray contraction with increasing Re_g can be seen from the spray photographs given in Fig. 4.

In the present work a nondimensionalized spray contraction parameter ξ is used to illustrate the trends of spray contraction with Re_g and is expressed as

$$\xi = \frac{(SW)_{\mathrm{Re}_g=0} - (SW)_{\mathrm{Re}_g}}{(SW)_{\mathrm{Re}_g=0}} \tag{7}$$

where $(SW)_{\mathrm{Re}_g=0}$ and $(SW)_{\mathrm{Re}_g}$ correspond to the spray widths for liquid sheets with $\mathrm{Re}_g=0$ and $\mathrm{Re}_g \neq 0$, respectively. The variation in ξ with Re_g for the liquid sheets with different We_l is shown in Figs. 9(*a*) and 9(*b*). Since the liquid sheet is conical in nature, the variation in ξ with Re_g is presented in the figure for different axial distances (Z) from the orifice exit. The measurements given in Fig. 9(*a*) clearly suggest that the liquid sheets with lower We_l exhibit a sharp increase in the spray contraction with increasing Re_g compared with higher inertia liquid sheets. In other words, low inertia liquid sheets are more vulnerable to the presence of the central air jet and high inertia liquid sheets do not recognize the presence of the central air jet in the lower values of Re_g. Such a sharp increase in the spray contraction helps the liquid sheet to initiate a more active interaction with the central air jet.

The second physical event to influence the sheet breakup process is the development of surface corrugations, which aid the generation of liquid ligaments from the sheet surface. Quantitative characterization of surface corrugations is done by estimating the tortuosity of the liquid sheet profile. Tortuosity of the liquid sheet profile at any two points in the profile is defined as the ratio of the length of the curved line profile between the two points to the least distance between the two points and is a measure of corrugations on the sheet profile exist between the two points. The value of tortuosity is always greater than 1 and increases with increasing levels of sheet profile corrugations. Assuming that the digitized points of the sheet profile are given in the *x*-*y* coordinate system as (x_1,y_1), $(x_2,y_2),\ldots,(x_k,y_k),\ldots,$ and (x_n,y_n), where subscripts 1 and n correspond to the first and last points of the sheet profile curve, the tortuosity of the liquid sheet profile can be estimated as

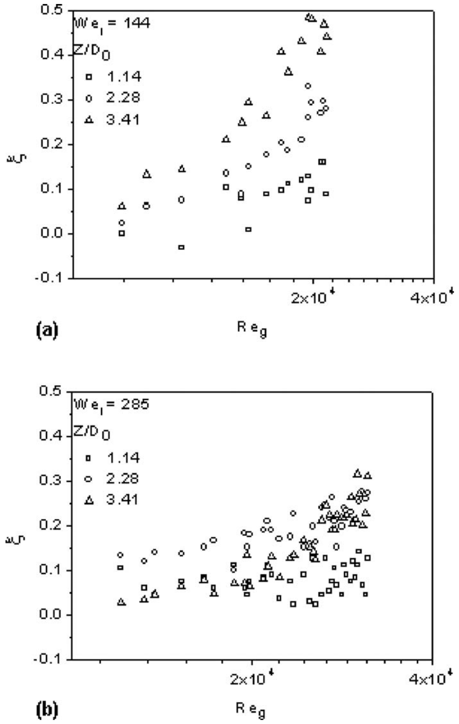

Fig. 9 Variation in spray contraction parameter ξ with Re_g for different values of We_l at different axial locations (*Z*) from the orifice exit (*a* and *b*). Atomizer configuration is *CA*2 (*S*=12.3).

$$\text{tortuosity} = \frac{\sum_{k=1}^{n-1} \sqrt{(x_{k+1}-x_k)^2+(y_{k+1}-y_k)^2}}{\sqrt{(x_n-x_1)^2+(y_n-y_1)^2}} \tag{8}$$

Attention must be given to ensure that the numerator was accurate enough to represent the total length of the curve. Figure 10 shows the variation in tortuosity of the liquid sheet profile with Re_g for different values of We_l. The variation in tortuosity is almost insignificant for the liquid sheets with very low values of Re_g ($<10{,}000-15{,}000$), as seen in Fig. 10. A steep increase in the tortuosity with Re_g is observed for low inertia liquid sheets in the moderate values of Re_g, as highlighted by the measurements marked with open symbols in Fig. 10 and the rise in tortuosity is somewhat gradual for relatively high inertia liquid sheets (see the measurements marked with filled symbols in Fig. 10).

The third physical event to influence the sheet breakup process is the direct impingement of the central air jet on the inner surface of the liquid sheet and the subsequent mixing process between the liquid sheet and the central air jet. This event starts once the outer liquid sheet meets the boundary of the central air jet and generally occurs at high values of Re_g. The dynamics of the liquid sheet at these flow conditions is very complicated and is marked by features such as substantial reduction in the liquid sheet breakup length, generation of thick liquid ligaments and droplet clusters, cellular patterns on the surface of the liquid sheet, ejection of ligaments and droplets in the transverse direction, etc. The images shown in Fig. 6 are typical of this event. More systematic experiments are needed to ascertain these facts in a quantitative manner.

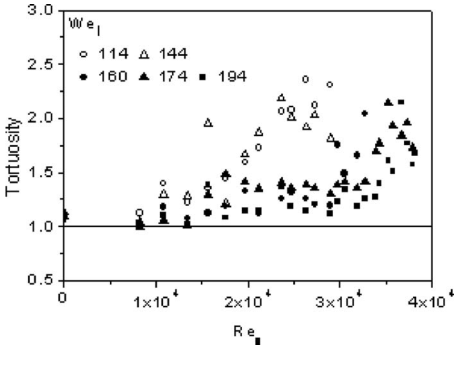

Fig. 10 Variation in tortuosity of the liquid sheet profile with Re_g for liquid sheets with different We_l discharging from the gas-centered swirl coaxial atomizer *CA*2 (*S*=12.3)

The quantitative variation in L_b with Re_g given in Figs. 8(*a*) and 8(*b*) shows that the breakup process of liquid sheets discharging from gas-centered swirl coaxial atomizers is primarily determined by the flow parameters We_l and Re_g. The influence of Re_g on the sheet breakup is very significant for low inertia liquid sheets, whereas such behavior is observed only at higher values of Re_g for high inertia liquid sheets. It is interesting to observe that low inertia liquid sheets disintegrate at lower values of Re_g. Note that low inertia liquid sheets discharging from a simple pressure swirl atomizer exhibit a longer breakup length and it is quite normal to presume that these liquid sheets require more energy for their breakup and the subsequent atomization process. A reverse trend is observed in the gas-centered swirl coaxial atomizers. This behavior is attributed to the fact that low inertia liquid sheets are more vulnerable to the entrainment process developed between the central air jet and the liquid sheet. High inertia liquid sheets are relatively less influenced by the entrainment process, which resulted in almost an insignificant variation in L_b with Re_g in the lower values of Re_g, as seen in Fig. 8(*b*). Analysis of spray images revealed that the breakup of the liquid sheet is faster if the liquid sheet exists near the spray axis. This was observed for all values of We_l. Thus the primary trigger for the sheet breakup may be the intensity of entrainment process developed between the liquid sheet and the central air jet.

4 Conclusions

An experimental study on the breakup behavior of the outer swirling liquid (water) sheet by the central gas (air) jet discharging from custom fabricated gas-centered swirl coaxial atomizers has been reported. The analysis of spray pictures captured using conventional photographic techniques reveals that the presence of the central air jet in the core of the swirling liquid sheet significantly changes the breakup behavior of the liquid sheet. At low values of the air jet Reynolds number, the interaction process between the liquid sheet and the central air jet develops corrugations on the surface of the liquid sheet. For a given low inertia liquid sheet, the level of sheet corrugations, described in the present work in terms of tortuosity of the sheet profile, increases with an increasing air jet Reynolds number. A reduced effect of the central air jet on the surface corrugations is observed for high inertia liquid sheets. The breakup region of the liquid sheet is marked by features such as ejection of liquid ligaments from the sheet surface, localized droplet clusters, increased surface corrugations on the liquid sheet, and cellular structures (thin membrane of the liquid sheet surrounded by a thick rim) on the liquid sheet. Quantitative measurements of the liquid sheet breakup length suggest that the breakup length of low inertia liquid sheets decreases with an increasing air jet Reynolds number and the decrease in sheet breakup length is less severe for high inertia liquid sheets. The present flow configuration of liquid and air jets creates an air entrainment process between the inner surface of the liquid sheet and the central air jet. The entrainment process helps to bring the liquid sheet and the central air jet closer to each other, and thereby develops a more active interaction between the jets. A high inertia central air jet aids to develop a stronger air entrainment process and hence brings the liquid sheet nearer to the spray axis. This results in the direct impingement of the air jet on the liquid sheet and the breakup length of the liquid sheet decreases steeply at high inertia air jet conditions.

Acknowledgment

This work was supported by Space Technology Cell, Indian Institute of Science under Grant No. ISTC/MAE/SK/179.

References

[1] Ryan, H. M., Anderson, W. E., Pal, S., and Santoro, R. J., 1995, "Atomization Characteristics of Impinging Liquid Jets," J. Propul. Power, **11**, pp. 135–145.

[2] Ashgriz, N., Brocklehurst, W., and Talley, D., 2001, "Mixing Mechanisms in a Pair of Impinging Jets," J. Propul. Power, **17**, pp. 736–749.

[3] Mayer, W. O. H., 1994, "Coaxial Atomization of a Round Liquid Jet in a High Speed Gas Stream: A Phenomenological Study," Exp. Fluids, **16**, pp. 401–410.

[4] Rahman, S. A., Pal, S., and Santoro, R. J., 1995, "Swirl Coaxial Atomization: Cold-Flow and Hot-Fire Experiments," AIAA Paper No. 95-0381.

[5] Sivakumar, D., and Raghunandan, B. N., 1996, "Jet Interaction in Liquid-Liquid Coaxial Injectors," ASME J. Fluids Eng., **118**, pp. 329–334.

[6] Sivakumar, D., and Raghunandan, B. N., 1998, "Hysteric Interaction of Conical Liquid Sheets From Coaxial Atomizers: Influence on the Spray Characteristics," Phys. Fluids, **10**, pp. 1384–1397.

[7] Cohn, R. K., Strakey, P. A., Bates, R. W., Talley, R. G., Muss, J. A., and Johnson, C. W., 2003, "Swirl Coaxial Injector Development," AIAA Paper No. 2003-0124.

[8] Soller, S., Wagner, R., Kau, H.-P., Martin, P., and Maeding, C., 2005, "Characterization of Main Chamber Injectors for GOX/Kerosene in a Single Element Rocket Combustor," AIAA Paper No. 2005-3750.

[9] Muss, J. A., Johnson, C. W., Cheng, G. C., and Cohn, R., 2003, "Numerical Cold Flow and Combustion Characterization of Swirl Coaxial Injectors," AIAA Paper No. 2003-0125.

[10] Lefebvre, A. H., 1989, *Atomization and Sprays*, Hemisphere, New York.

[11] Dombrowski, N., and Fraser, R. P., 1954, "A Photographic Investigation Into the Disintegration of Liquid Sheets," Philos. Trans. R. Soc. London, **247**, pp. 101–130.

[12] Squire, H. B., 1953, "Investigation of the Instability of a Moving Liquid Film," Br. J. Appl. Phys., **4**, pp. 167–169.

[13] Taylor, G. I., 1959, "The Dynamics of Thin Sheets of Fluid. II Waves on Fluid Sheets," Proc. R. Soc. London, Ser. A, **253**, pp. 296–312.

[14] Taylor, G. I., 1959, "The Dynamics of Thin Sheets of Fluid. III Disintegration of Fluid Sheets," Proc. R. Soc. London, Ser. A, **253**, pp. 313–321.

[15] Dombrowski, N., and Johns, W. R., 1963, "The Aerodynamic Instability and Disintegration of Viscous Liquid Sheets," Chem. Eng. Sci., **17**, pp. 291–305.

[16] Clark, C. J., and Dombrowski, N., 1972, "Aerodynamic Instability and Disintegration of Inviscid Liquid Sheets," Proc. R. Soc. London, Ser. A, **329**, pp. 467–478.

[17] Hagerty, W., and Shea, J. F., 1955, "A Study of the Stability of Moving Liquid Film," ASME J. Appl. Mech., **22**, pp. 509–514.

[18] Lin, S. P., 2003, *Breakup of Liquid Sheets and Jets*, Cambridge University Press, London.

[19] Mansour, A., and Chigier, N., 1990, "Disintegration of Liquid Sheets," Phys. Fluids A, **2**, pp. 706–719.

[20] Stapper, B. E., Sowa, W. A., and Samuelsen, G. S., 1992, "An Experimental Study of the Effects of Liquid Properties on the Breakup of a Two-Dimensional Liquid Sheet," ASME J. Eng. Gas Turbines Power, **114**, pp. 39–45.

[21] Park, J., Huh, K. Y., Li, X., and Renksizbulut, M., 2004, "Experimental Investigations on Cellular Breakup of a Planar Liquid Sheet From an Air-Blast Nozzle," Phys. Fluids, **16**, pp. 625–632.

[22] Adzic, M., Carvalho, I. S., and Heitor, M. V., 2001, "Visualization of the Disintegration of an Annular Liquid Sheet in a Coaxial Air Blast Injector at Low Atomizing Air Velocities," Optical Diagnostics in Engineering, **5**, pp. 27–38.

[23] Lozano, A., Barreras, F., Hauke, G., and Dopazo, C., 2001, "Longitudinal Instabilities in an Air-Blasted Liquid Sheet," J. Fluid Mech., **437**, pp. 143–173.

[24] Moffat, R. J., 1988, "Describing the Uncertainties in Experimental Results," Exp. Therm. Fluid Sci., **1**, pp. 3–17.

Effect of Capsule Density and Concentration on Pressure Drops of Spherical Capsule Train Conveyed by Water

Deniz Ulusarslan
Department of Mechanical Engineering,
Yıldız Technical University,
34349 Istanbul, Turkey
e-mail: ulusars@yildiz.edu.tr

This experimental investigation concerns the hydraulic transport of a spherical capsule train, whose density is equal to that of water (relative density; s = 1), in horizontal pipes. In a system where the carrier fluid is water, pressure drops of two phase flow and capsule velocities were measured at 0.2–1.0 m/s bulk velocities and 5–20% capsule transport concentrations. The results found were compared with the pressure gradient (pressure drops per unit length) ratios ($(\Delta P/L)_m/(\Delta P/L)_w$) *measured for less dense capsules. The capsule velocity and the velocity ratio* (V_c/V_b) *increased with increasing the bulk velocity. As concentration increases, the pressure gradient of the capsule-water mixture increases. For all concentrations, the pressure gradient ratio decreases (getting closer to 1) with increasing bulk velocity. This result is similar to that of capsules with less relative density. However, the pressure gradient ratio of the capsule flow with less density is higher than that of capsules with equal density at constant transport concentrations. The reason for this difference is that the capsules with a density equal to that of water move along the axis of the pipe for a longer time. When capsules with equal density are used, the mass flow rate will remain the same, but energy consumption will decrease.*
[DOI: 10.1115/1.4000738]

Keywords: two phase flow, spherical capsule train, hydraulic capsule pipelining, pressure drop, velocity ratio

1 Introduction

Spherical ice capsule applications for pipelines of district cooling systems increase the cooling capacity. However, it is critical to know the parameters and characteristics of the relevant flow before building such pipelines.

Flow parameters and flow patterns concerning the utilization of granulated ice-water or snow-water mixtures (slurry flow) in cooling systems were examined by various authors [1–4]. The size of ice particles was a maximum of 12 mm, and ice concentration did not exceed 25%. However, capsule flow can ensure a maximum ice concentration of approximately 43% when the diameter ratio ($k=d/D$) is 0.8. Kawada et al. [1] reported potential blocking problems in the flow of ice-water slurry. In ice-water slurry flows, the fact that ice particles tend to cluster at especially low velocities and proceed in the form of bed flows contacting the upper wall of pipes at a high rate increases the pressure gradient. Therefore, it is necessary to operate at bulk velocities that minimize the pressure gradient for slurry flows. The fact that particles within ice-water slurry flows tend to disperse or accumulate in pipeline joints cause various blocking problems to arise and excessive pressure drops to take place. However, such problems do not arise in capsule flows.

Utilization of spherical ice capsules filling 80–90% of the pipe's diameter will be an innovation and will ensure a number of advantages.

- Since ice capsules are large in terms of dimension, they will be able to stay frozen for a longer time. Melting will be even slower if the capsules are put in a plastic casing. Plastic casings will prevent the adhesion and abrasion of ice capsules.
- Ice concentration and bulk velocity values reached during the flow are much higher than the concentration and bulk velocity values reached during the ice-water slurry flow. Therefore, the cooling capacity of the system will increase.
- Since the pipelines used for heating purposes will be used for cooling in summer, no new investment will be required. Pipelines installed to carry water can be used for the flow of the ice and water mixture in summer, so that water and cooling demands will be met together.
- Blocking problems arising from dispersion of particles in ice-water slurry flows will be prevented.
- Since the spherical capsules have only point contact with the pipe wall during the flow, losses arising from friction (surface to surface) will decrease. Particles will neither disperse nor accumulate at low velocities so that there will be no critical velocity limit for slurry flows.
- The spherical form of capsules prevents the blocking of pipe joints and ensures local losses to minimize.

The objective of this experimental investigation is to recognize flow behavior of spherical capsules with various relative densities, i.e., ice capsules with different densities ($s=0.87$-1.0-1.1) to find out the capsule density, pipe geometry, and flow conditions, which minimize pressure gradients. Previous investigations conducted in this field were related to flow behaviors of spherical capsules with less density ($s=0.87$) [5,6]. This investigation focuses on pressure gradients and velocity ratios of capsules with equal density ($s=1$). Flow characteristics of capsules with different densities were compared. This investigation was conducted at 0.2–1.0 m/s bulk velocities and 5–20% capsule transport concentrations.

Contributed by the Fluids Engineering Division of ASME for publication in the Journal of Fluids Engineering. Manuscript received March 27, 2009; final manuscript received November 12, 2009; published January 12, 2010. Assoc. Editor: Theodore Heindel.

2 Literature Review

The first studies on capsules were conducted in the early 1960s by a group of researches at the Alberta Research Center in Canada. For most of the studies, densities of the materials considered to be carried through pipelines were higher than or equal to the density of the carrier liquid. Until the first half of the 1970s, studies focused on characteristics of the flow behaviors of single cylindrical capsules (with flat or rounded ends) or spherical capsules placed in vertical or mostly horizontal pipes with a circular cross section.

Button and Ma [7] examined the movements of four types of spheres. The principal components were a 95.6 mm inner diameter horizontal transparent pipe fitted with a device for the introduction and release of the spheres and a stationary film multiflash photographic arrangement to record the spheres' trajectory. The sphere diameters were 9.47 mm, 12.55 mm, 15.75 mm, and 18.9 mm; the four densities were 1300 $\mathrm{kg/m^3}$, 1620 $\mathrm{kg/m^3}$, 2100 $\mathrm{kg/m^3}$, and 2710 $\mathrm{kg/m^3}$; and water velocities ranged from 1.21 m/s to 4.55 m/s. They presented the geometric and kinematic trajectories of a single sphere carried by the water, and expressed the drag and lift coefficients.

Garg [8] expressed the behavior of a single cylindrical capsule (relative density=2, length=2.5 m) in a horizontal pipe with an inner diameter of 101.6 mm. Capsule velocity, shear force, energy requirements, pressure ratio variation, and friction factor were investigated. A theoretical analysis for a rigid, straight, cylindrical, flat-ended capsule moving parallel to the horizontal pipe wall by taking into account the effects of friction between the capsule and pipe surfaces and of nonuniform clearance (between the bottom of the capsule and the pipe wall) over the capsule length was presented. The theory of hydrodynamic lubrication was used to determine the force acting on the capsule due to the wedging action produced by the nonuniform clearance over the capsule length. Average velocity ranged from 0.3 m/s to 2.5 m/s; diameter ratio of the capsule to the pipe was 0.9 to 0.95.

Since the studies were conducted with a single capsule, the increase in the pressure gradient was very small. Therefore, the pressure gradient measurements were conducted later on systems with capsule trains. Studies with single capsules were limited to the distribution of the forces affecting the capsule's surface and to the measurements of the velocities of the capsule. The carrier liquid was mostly water, but some researchers added a polymer in the water to increase its viscosity or used it as carrier liquid oils having various viscosities in order to measure in a more viscous medium [9–11]. Factors affecting the velocity ratio ($R_v = V_c/V_b$) of the capsule-carrier liquid movement, and to what extent the turbulence structure damps when more viscous liquids are used, were investigated. The addition of polymers or surfactants generally decreased pressure drops (drag reduction effect) [12].

Since capsule pipelines involve the continuous flow of capsules and their mutual effects in commercial practices, measurements made by using a single capsule do not give sufficient information about a capsule train. Therefore, studies were directed to capsule trains in the second half of the 1970s. However, the number of capsules that formed the train was limited in the studies. The early studies conducted to determine both the flow mechanism of a single capsule and the behavior of a capsule train used a capsule (or a capsule train) fixed or suspended inside the pipe for liquid flow. The studies revealed that the pressure gradient increases as the density of the carried material increases.

Seaba and Xu [13,14] investigated the pressure gradient for a capsule train-water flow in a pipe with a 50.1 mm inner diameter. The lift of velocity and capsule and total pressure gradients were presented. The capsule train consisted of five capsules with a total length of 0.5 m. Each capsule had a relative density of 1.3, aspect ratio (length of capsule divided by capsule diameter) of 2–4, and a diameter ratio equal to 0.75.

In a study conducted on the hydrodynamics of moving capsules, Vlasak [15] used capsules of anomalous shapes (i.e., cylindrical capsules with helical grooves carved on them) and having densities higher than that of the carrier liquid, and set up a special delivery mechanism to ensure the capsule train to be continuously moving within the system. Literature does not include a study conducted on the flow of a spherical capsule train whose density is equal to that of the carrier liquid for use in cooling systems.

The noses of cylindrical capsules tend to rise up at very high velocities [16]; it makes it difficult for them to pass through pipe joints. Spherical ice capsules were considered appropriate for the pipelines of cooling systems. Properties of the flows of capsule-water mixtures whose density is less than that of water must be known well before installing the pipelines of a cooling system. To do this, a number of experimental investigations and models are necessary.

In this experimental investigation, spherical capsules made of polypropylene material whose density is equal to that of water were used. It was conducted at a diameter ratio of 0.8, capsule transport concentrations ranging from 5% to 20%, and flow velocities of $1.2 \times 10^4 < \mathrm{Re} < 10^5$. Experimental findings concerning pressure drop and capsule movements were collected.

3 Dimensional Analysis

Buckingham's π method was used for dimensional analysis. Independent variable parameters of the system are capsule velocity (V_c), capsule diameter (d), capsule length (l), capsule density (ρ_c), capsule shape factor (B), the mean distance between capsules (l_c), the roughness of the capsule surface (e_c), the roughness of the pipe surface (e_p), pipe diameter (D), pipe inclination (θ), the rigidity factor of the pipe material (KS_p) and the rigidity factor of the capsule material (KS_c), the lubrication factor of the carrier liquid (water) influencing friction between capsule and pipe wall (c), the density of the carrier liquid (ρ_w), dynamic viscosity of water (μ_w), and the average velocity of capsule and carrier liquid flowing together (bulk velocity) (V_b). L refers to the length of the pipe in the measuring line; the pressure drop of the mixture per unit length (pressure gradient) depends on the independent variables of the system

$$\left(\frac{\Delta P}{L}\right)_m = f(V_c,d,l,\rho_c,B,l_c,e_c,e_p,D,L,\theta,KS_c,KS_p,c,\rho_w,\mu_w,V_b) \tag{1}$$

With reference to previous papers [6,11,15,17,18], for the presented case, i.e., the train of spherical capsules of the same density as carrier liquid (water), conveyed in a straight horizontal pipe, the aspect ratio (l/d) is $d/d=1$, capsule shape factor (B), the roughness of the capsule surface (e_c) and pipe surface (e_p) [11], the pipe inclination (θ), the rigidity factors (KS_p) and (KS_c), and the lubrication factor (c) [17] can be ignored.

Thus, the parameters of the system's independent variables are

$$V_c \quad \text{or} \quad \left(\frac{\Delta P}{L}\right)_m = f(V_b,D,d,\rho_c,\rho_w,\mu_w,l_c,g) \tag{2}$$

The system can be described by seven dimensionless numbers composed of eight independent variables, and the velocity ratio and the dimensionless pressure gradient can be written with reference to the literature [6,11,15,17] as a function of those five dimensionless numbers

$$\frac{V_c}{V_b} = f\left(\frac{d}{D},\frac{\rho_c}{\rho_w},\frac{V_b\rho_w D}{\mu_w},\frac{V_b^2}{gd},\frac{d}{l_c}\right) \tag{3}$$

$$\frac{V_b^2\rho_w}{D}\left(\frac{\Delta P}{L}\right)_m^{-1} = f\left(\frac{d}{D},\frac{\rho_c}{\rho_w},\frac{V_b\rho_w D}{\mu_w},\frac{V_b^2}{gd},\frac{d}{l_c}\right) \tag{4}$$

In accordance with the results of the dimensional analysis, the dimensionless numbers of the system were written as an expression of the dimensionless pressure gradient ($(\Delta P/L)_m D/\rho_w V_b^2$) or

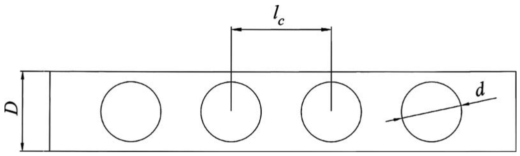

Fig. 1 Schematic diagram of distance between capsules

as a function of the velocity ratio ($R_v = V_c/V_b$). Dimensionless numbers are diameter ratio ($k = d/D$), the relative density of the capsule ($s = \rho_c/\rho_w$), Reynolds number ($\mathrm{Re} = V_b \rho_w D/\mu_w$), the Froude number of the capsule ($\mathrm{Fr} = V_b^2/gd$), and the expression that yields in situ concentration (d/l_c) (Fig. 1.), which describes the part of the pipe occupied by the capsule. In situ concentration is relative to linear filling of the capsules in the train (d/l_c), and the volumetric in situ concentration was determined to be

$$C_{\text{in-situ}} = \frac{2}{3} k^2 \frac{d}{l_c} \tag{5}$$

Diameter ratio ($k = 0.8$) and the relative density of the capsule ($s = 1.0$) are constant in the conducted experiments. Investigations carried out by using a single spherical capsule in equal density reported that the influence of the Froude number is negligible [18]. The density of the spheres used in this investigation's system was near to that of water. Therefore, the Froude number was not taken into account. In this case, the velocity ratio and the dimensionless pressure gradient could be expressed as a function of the Reynolds number (Re) and the capsule transport concentration C_{tr} only

$$\frac{V_c}{V_b} = f\left(\frac{V_b \rho_w D}{\mu_w}, \frac{d}{l_c}\right) = f(\mathrm{Re}, C_{\text{tr}}) \tag{6}$$

$$\left(\frac{V_b^2 \rho_w}{D}\left(\frac{\Delta P}{L}\right)_m^{-1}\right) = f\left(\frac{V_b \rho_w D}{\mu_w}, \frac{d}{l_c}\right) = f(\mathrm{Re}, C_{\text{tr}}) \tag{7}$$

4 Experimental Setup

An experimental setup similar to actual capsule pipelines was created [5,6]. The test section was formed by means of horizontal plexiglass pipes 6 m long and with a 0.1 m inner diameter. Pressure drop measurements were carried out on the 4 m section of the plexiglass pipe. Two pressure taps were connected through piezometric hoses to the ends of a differential pressure transmitter used for measuring pressure drops with a distance (L) of 4 m between them. This transmitter was able to measure pressure changes at a range of 0–10 kPa, with an accuracy of 0.5%. Two fiber optic sensors were installed on the measuring section with a distance of 0.1 m between them. Signals transmitted from the printed circuit board to the computer were determined by means of a special software to calculate capsule velocities, the number of capsules that would constitute in situ and transport concentrations, and the distance between the capsules. Capsules passing through the measuring section were refed into the system through a sieve installed on the tank to ensure the continuous flow of the capsule train. Capsules comprising the train were rigid, in spherical shape, with a relative density of 1, and a diameter of 0.08 m. The temperature of the water circulating within the system during the tests was $20 \pm 2°\mathrm{C}$. Pressure drops were measured at the $1.2 \times 10^4 < \mathrm{Re} < 10^5$ range and under transport concentrations of 5–20%.

5 Experimental Parameters

5.1 Capsule Transport Concentration, C_{tr}. Volumetric capsule concentration can be determined in terms of transport concentration and in situ concentration. Transport concentration is defined as the ratio of the volumetric flow rate of the solid materials moving in the system to the total flow rate

$$C_{\text{tr}} = \frac{Q_c}{Q_w + Q_c} \tag{8}$$

In situ concentration refers to the ratio of the capsule volume to the total volume in the pipe, which was 1 m long. Results of the test indicate that the flow velocities of the phases are very close to each other, $V_c \approx V_b$. Therefore, the in situ concentration $C_{\text{in-situ}}$ was considered to be equal to transport concentration C_{tr} in data processing

$$C_{\text{tr}} = \frac{C_{\text{in-situ}} V_c}{V_b} \cong C_{\text{in-situ}} \tag{9}$$

5.2 Bulk Velocity, V_b. The mean velocity reached while the capsules and water flow together yields the bulk velocity

$$V_b = \frac{Q_w + Q_c}{A} \tag{10}$$

where A is the cross section of the pipe in the measuring section, and Q_w and Q_c are volumetric flow rate of water and capsules, respectively.

5.3 Velocity Ratio, R_v. The velocity ratio is defined as the capsule velocity to bulk velocity ratio

$$R_v = \frac{V_c}{V_b} \tag{11}$$

where V_c is the velocity of the capsule, found by evaluating the sensor signals transmitted to the computer.

5.4 Pressure Gradient Ratio, R_p. The pressure gradient ratio is defined as the ratio of the pressure gradient occurring in the two phase mixture flow (capsule train and water) to the pressure gradient occurring in the single phase water flow

$$R_P = \frac{(\Delta P/L)_m}{(\Delta P/L)_w} \tag{12}$$

6 Experimental Results

6.1 Pressure Gradient of Single-Phase Water Flow. Pressure drops measured during the water flow helped to determine the hydraulic properties of the pipe located in the measuring line. Pressure drops and corresponding velocities were put in the Darcy–Weisbach equation to calculate the friction coefficient (λ) of the pipe. It was indicated that the pipe used in the measuring section was hydraulically smooth.

6.2 Velocity Ratio of the Capsule Train. Capsule velocity increased with the increase in the bulk velocity (see Fig. 2). Under nearly all conditions, the capsules traveled concentrically in the pipe due to the density of the capsules. This mechanism avoids the frictional forces between the capsule and pipe walls. The capsules moved along the pipe's axis where maximum flow velocity occurs, with less rolling movement. When $\mathrm{Re} > 2.5 \times 10^4$, the velocity of the capsule is higher than that of the mixture, $V_c/V_b > 1$ (see Fig. 3).

It was observed that for flows of capsules with diameter ratios of 0.8 at bulk velocities 0.2–1.0 m/s, the effect of the capsule's concentration on the velocity ratio is relatively low for higher flow velocities (see Fig. 3.), but it is significant for low velocities. Figure 4 shows the relationship between the velocity ratio and Re number of the mixture at different transport concentrations. For constant transport concentrations, the velocity ratio increased with

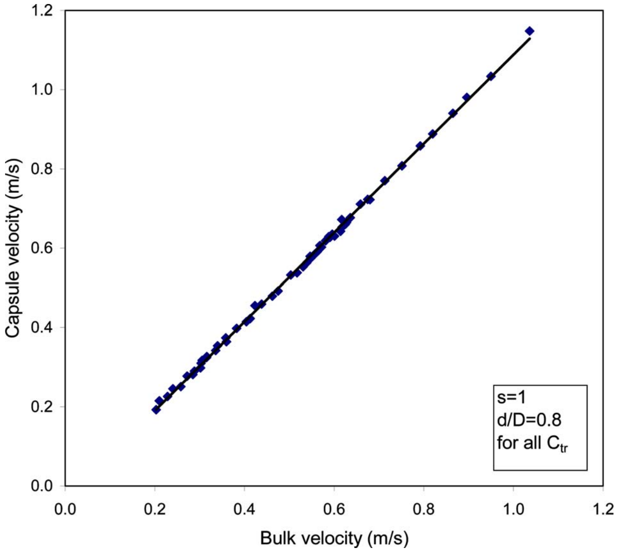

Fig. 2 Relation between bulk velocity and capsule velocity

the increase in the bulk velocity (the difference in V_c/V_b for $C_{\text{tr}}=5\%$, and Re=20,000 and 100,000 (see Fig. 4(*a*)) is: $V_c/V_b=0.95$ and 1.11, i.e., about 16.8%).

6.3 Pressure Gradient of the Capsule Train-Water Flow. Pressure drops occurring at different bulk velocities and capsule concentrations were measured. It was observed that, due to the presence of the solid phase, pressure gradients of the capsule flow are higher than the single phase water flow. As concentration increases, the pressure gradient of the capsule-water mixture increases (see Fig. 5).

The pressure gradient ratio significantly increases as the concentration increases at constant bulk velocities and especially at lower velocities. At constant transport concentrations, the pressure gradient ratio decreases (getting closer to 1) with increasing bulk velocity. The variation in the pressure gradient ratio with bulk velocity at different concentrations is presented in Fig. 6.

The capsules with the same density as the carrier liquid moved in the center of the pipe without contact with the pipe wall. But especially at lower velocities, capsules jumped from the pipe axis (for very short time). At that moment, the capsules rotated partially. Characteristics of the pressure gradient curves (in Fig. 6) at different capsule concentrations are very similar. However, the pressure gradient ratio increases with increasing capsule transport concentrations. Additional losses caused by the partial rotation and jumping movement of the capsules are effective in this increment. As bulk velocity increased, the spheres traveled concentrically in the pipe without rolling.

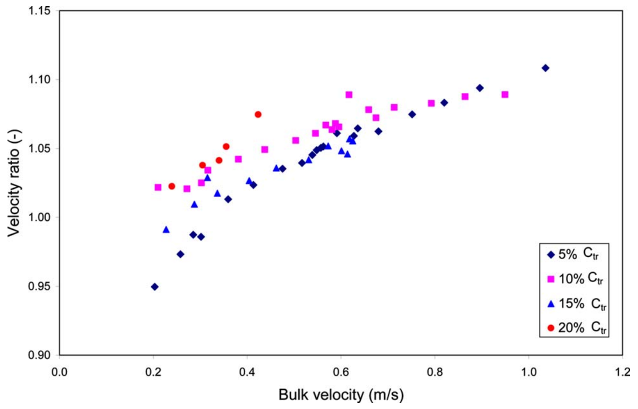

Fig. 3 Variation in velocity ratio with bulk velocity

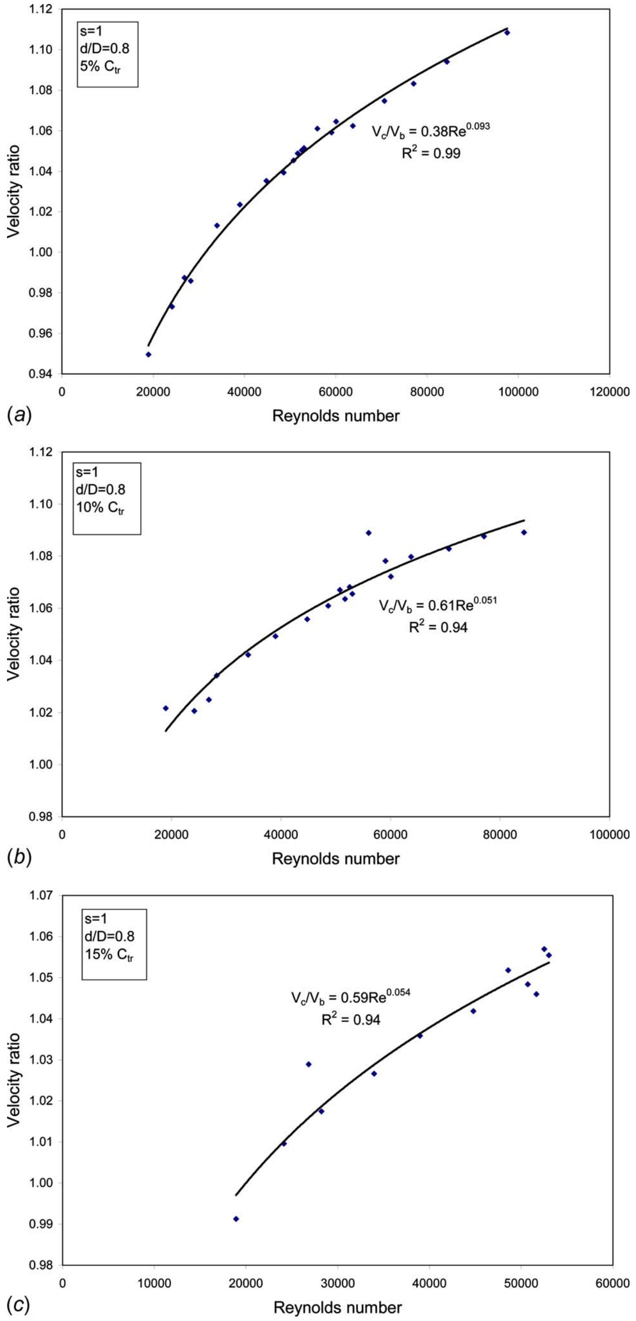

Fig. 4 Relation between the velocity ratio and Re number of mixture

At constant transport concentration and constant bulk velocities, the pressure gradient ratio for the capsules with equal density is less than that of the capsules with low density. The reason for this difference is that the capsules rotate less and move along the pipe axis for a longer period of time. Thus, additional frictions caused by the rotational movement of the capsules decrease (see Fig. 7).

6.4 Friction Coefficient of Capsule Train-Water Flow. During the tests, pressure drops caused by the capsule-water flow at each flow rate were measured and used in a Darcy–Weisbach equation to calculate the friction coefficient (λ) of the capsule flow. A change in the coefficients of friction, based on the experi-

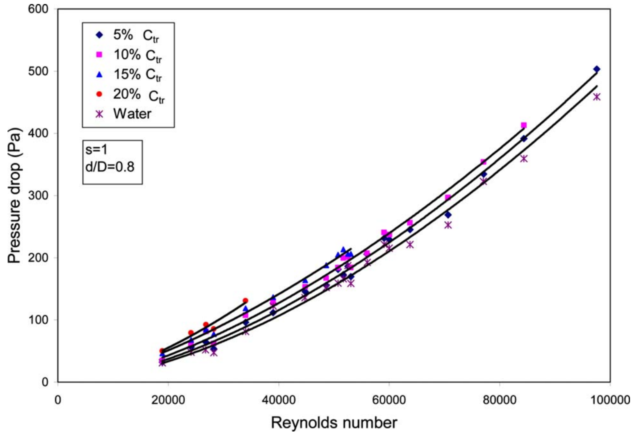

Fig. 5 Relation between $(\Delta P/L)_m$ and Re number of mixture based on experiments

ments with the Re number for the mixture, is given in Fig. 8.

It was observed that, due to the presence of the solid phase, friction coefficients of the capsule flow are higher than those for the water alone. Additional losses caused by the partial rotation and jumping of the capsules have an impact on the difference in friction coefficient. Figure 8 shows the relationship between the friction coefficient and Re number of the mixture at different concentrations.

7 Conclusion

This experimental investigation was conducted on spherical ice capsule applications for cooling systems. Its objective was to find the ice capsule density, which minimizes the pressure drops of the spherical capsule train flow. In a system where the carrier fluid is water, the pressure drops and velocities were measured at 0.2–1.0 m/s bulk velocities and 5–20% capsule transport concentrations. The following results were found.

- Capsule velocity increased with increasing bulk velocity for the capsules with equal density. For constant transport concentrations, velocity ratio increased with the increase in the bulk velocity.
- Due to the presence of the solid phase, pressure gradients of capsule flows are higher than those of the single phase water flow.

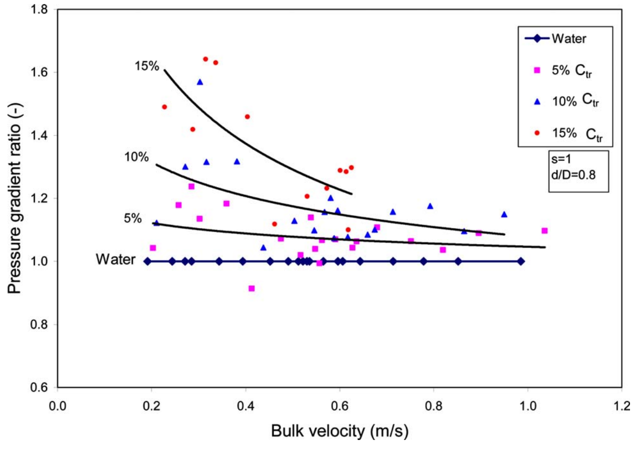

Fig. 6 Variation in pressure gradient ratio with bulk velocity and concentration

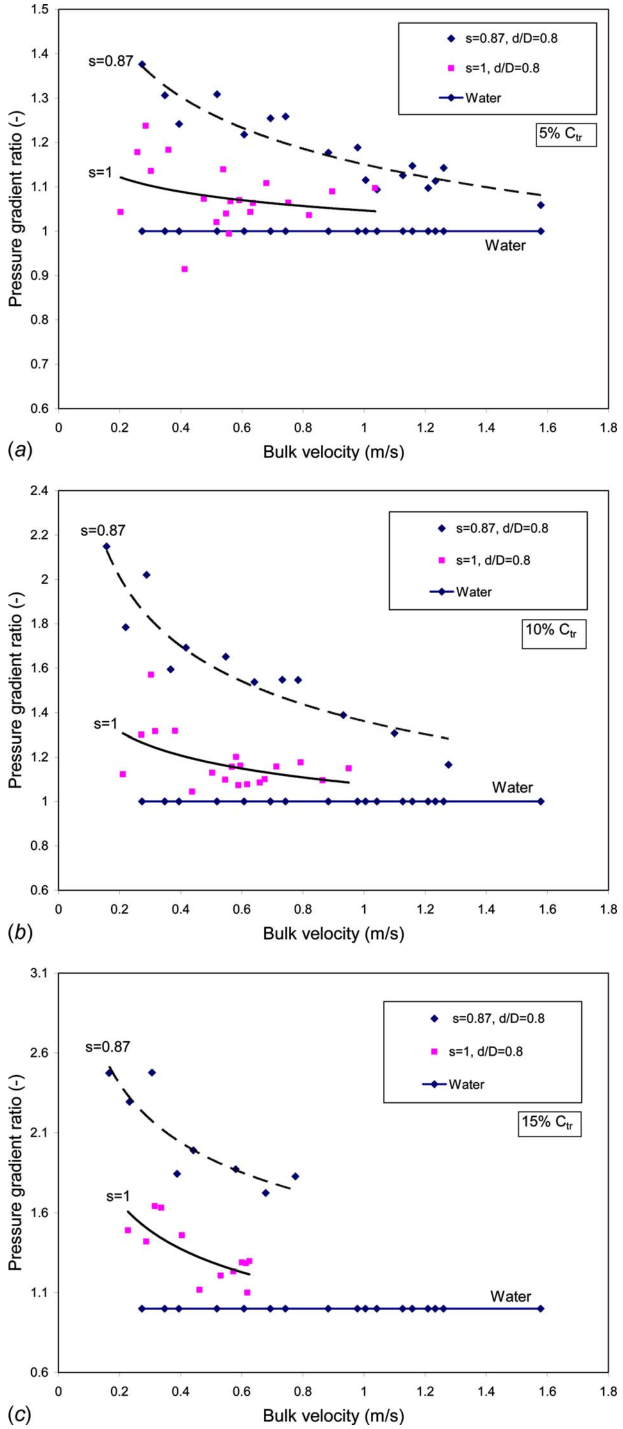

Fig. 7 Comparison of pressure gradient ratios for different capsule density

- At lower bulk velocities, pressure gradient ratios increase with increasing concentration. This result is similar to that of the capsules with density that is less than that of the carrier liquid.
- As bulk velocity increases, the pressure gradient ratio tends to get close to 1 at all concentrations.
- Friction coefficient values for the flow of the capsule train-water (for constant Reynolds number) are higher than those for the single phase water flow because of additional losses (caused by the partial rotation and jumping movement of the capsules).

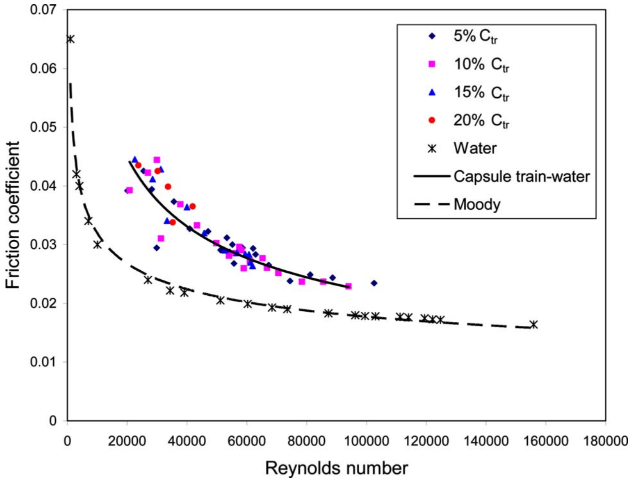

Fig. 8 Darcy–Weisbach friction factor versus Reynolds number of mixture

- At constant transport concentration and at constant bulk velocities, the pressure ratio of the capsules with equal density is less than that of the capsules with less density. The reason for this difference is the fact that the capsules with equal density rotate less and move along the axis of the pipe for a longer period of time. Thus, additional frictions caused by the rotational movement of the capsules decrease and energy consumption decreases. Therefore, the use of capsules with equal density is more advantageous.
- Further experimental investigations are being conducted to determine flow characteristics at higher bulk velocities, higher capsule concentrations, and different capsule diameters and densities.

Nomenclature

A = cross sectional area of the pipe
B = capsule shape factor
c = lubrication factor
C_{tr} = transport concentration
$C_{\text{in-situ}}$ = in situ concentration
d = capsule outer diameter
D = pipe inner diameter
e = surface roughness
Fr = Froude number
k = capsule to pipe diameter ratio (d/D)
KS = rigidity factor
l_c = mean distance between capsules
l = length of cylindrical capsules
l/D = aspect ratio of capsule (for cylindrical capsule)
L = length of measurement section
Q = flow rate
ΔP = pressure drop
$(\Delta P/L)$ = pressure gradient
Re = Reynolds number
R_v = velocity ratio
R_P = pressure gradient ratio
s = relative density of capsule (ρ_c/ρ_w)
V = velocity

Subscripts

c = capsule
m = mixture
p = pipe
w = water
b = bulk

Greek Letters

λ = friction coefficient
θ = pipe inclination angle
ρ = density
μ = dynamic viscosity

References

[1] Kawada, Y., Shirakashi, M., and Yamada, S., 1999, "Flow Characteristics of Ice-Water Slurry in a Horizontal Circular Pipe," *Proceedings of the Third ASME-JSME Joint Fluids Engineering Conference*, July 18–23, San Francisco, CA, pp. 1–5.
[2] Snoek, C. W., Walosik, S., and Gupta, R. P., 1993, "Ice Slurry Transport for District Cooling Networks," *Hydrotransport 12*, Proceedings of the 12th International Conference on Slurry Handling and Pipeline Transport, Brugge, Belgium, Mechanical Engineering Publications, London, 28–30 September, pp. 511–524.
[3] Takahashi, H., Masuyama, T., and Kawashima, T., 1991, "Flow Properties for Slurries of Particles With Densities Close to That of Water," *Proceedings of the First ASME-JSME Fluid Engineering Conference*, Liquid-Solid Flows, FED, Vol. 118, pp. 103–108.
[4] Kawada, Y., Tsukada, Y., Kobayashi, M., and Shirakashi, M., 1998, "Measurement of Properties of Ice Particles in Water Affecting Ice-Water Mixture Flow in Pipes," *Proceedings of Fourth KSME-JSME Liquids Engineering Conference*, Oct. 18–21, Pusan, Korea (South), pp. 373–376.
[5] Ulusarslan, D., and Teke, I., 2005, "An Experimental Investigation of the Capsule Velocity, Concentration Rate and the Spacing Between the Capsules for Spherical Capsule Train Flow in a Horizontal Circular Pipe," Powder Technol., **159**, pp. 27–34.
[6] Ulusarslan, D., and Teke, I., 2006, "An Experimental Determination of Pressure Drops in the Flow of Low Density Spherical Capsule Train Inside Horizontal Pipes," Exp. Therm. Fluid Sci., **30**, pp. 233–241.
[7] Button, B. L., and Ma, T. H., 1975, "Hydraulic Transport of Single Spheres in a Horizontal Pipe," ASME J. Fluids Eng., **97**, pp. 243–245.
[8] Garg, V. K., 1977, "Capsule Pipelining—An Improved Theoretical Analysis," ASME J. Fluids Eng., **99**, pp. 763–771.
[9] Ellis, H. S., Kruyer, J., and Roehl, A. A., 1975, "The Hydrodynamics of Spherical Capsules," Can. J. Chem. Eng., **53**, pp. 119–125.
[10] Kruyer, J., and Ellis, H. S., 1974, "Predicting the Required Liquid Throughput From the Capsule Velocity and Capsule Pressure Gradient in Capsule Pipelines," Can. J. Chem. Eng., **52**, pp. 215–221.
[11] Round, G. F., and Bolt, L. H., 1965, "The Pipeline Flow of Capsules—Part 8—An Experimental Investigation of the Transport in Oil of Single, Denser Than Oil, Spherical and Cylindrical Capsules," Can. J. Chem. Eng., **43**, pp. 197–205.
[12] Vlasak, P., 1995, "The Toms Effect in Capsule-Liquid Flows," *Proceedings of the Eight International Freight Pipeline Society Symposium*, Pittsburgh, PA, pp. 93–98.
[13] Seaba, J., and Xu, G., 1995, "Capsule Transport in Coal Slurry Medium," ASME J. Fluids Eng., **117**, pp. 691–695.
[14] Seaba, J., and Xu, G., 1996, "A Novel Method to Measure Capsule Pressure Gradient in a Pipeline," ASME J. Fluids Eng., **118**, pp. 867–870.
[15] Vlasak, P., 1999, "An Experimental Investigation of Capsules of Anomalous Shape Conveyed by Liquid in a Pipe," Powder Technol., **104**, pp. 207–213.
[16] Feng, J., Huang, P. Y., and Joseph, D. D., 1995, "Dynamic Simulation of the Motion of Capsules in Pipelines," J. Fluid Mech., **286**, pp. 201–227.
[17] Ellis, H. S., 1964, "The Pipeline Flow of Capsules—Part 3—An Experimental Investigation of the Transport by Water of Single Cylindrical and Spherical Capsules With Density Equal to That of the Water," Can. J. Chem. Eng., **42**, pp. 1–8.
[18] Ellis, H. S., and Bolt, L. H., 1964, "The Pipeline Flow of Capsules—Part 7—An Experimental Investigation of the Transport by Two Oils of Single Cylindrical and Spherical Capsules With Density Equal to That of the Oil," Can. J. Chem. Eng., **42**, pp. 201–210.

Assessment of the Performance of Acoustic and Mass Balance Methods for Leak Detection in Pipelines for Transporting Liquids

Jaqueline Costa Martins

Paulo Seleghim, Jr.[1]
e-mail: seleghim@sc.usp.br

School of Engineering of São Carlos,
University of São Paulo,
Av. Trabalhador São-Carlense, 400,
13566-590 São Carlos, SP, Brazil

On-line leak detection is a main concern for the safe operation of pipelines. Acoustic and mass balance are the most important and extensively applied technologies in field problems. The objective of this work is to compare these leak detection methods with respect to a given reference situation, i.e., the same pipeline and monitoring signals acquired at the inlet and outlet ends. Experimental tests were conducted in a 749 m long laboratory pipeline transporting water as the working fluid. The instrumentation included pressure transducers and electromagnetic flowmeters. Leaks were simulated by opening solenoid valves placed at known positions and previously calibrated to produce known average leak flow rates. Results have clearly shown the limitations and advantages of each method. It is also quite clear that acoustics and mass balance technologies are, in fact, complementary. In general, an acoustic leak detection system sends out an alarm more rapidly and locates the leak more precisely, provided that the rupture of the pipeline occurs abruptly enough. On the other hand, a mass balance leak detection method is capable of quantifying the leak flow rate very accurately and of detecting progressive leaks. [DOI: 10.1115/1.4000736]

1 Introduction

The transportation of petrochemical products through pipelines is the most common option in both industrial applications involving long distances and in distribution networks, in which a product must be delivered to a number of processes or customers. Due to safety and environmental reasons, the operation of such pipelines must include an on-line leak detection system (LDS), which promptly detects and assesses the occurrence of a leak, particularly if the transported product is toxic or inflammable. Such a need is absolutely clear in view of the significant number of accidents that have occurred, usually with serious economical and environmental consequences. According to Papadakis et al. [1], the most common causes of leak accidents in gas or oil pipelines are related to corrosion, mechanical failure, inappropriate operation, ground movement, and external human actions such as a clumsy machine operator. (Theft is also an important example of external human action.)

The techniques currently applied cover a large variety of methods, ranging from visual inspection to sophisticated hardware/software based specialist systems. It is commonly agreed that no single method is universally applicable (see Refs. [2,3]) fundamentally because operational, economical, and safety issues can be completely different from one application to another. Focusing on LDS's requiring on-line instrumentation installed at the ends of the pipeline, or, at least, at a few locations kilometers apart from each other, these techniques can be grouped into the two following categories: (1) fast signal processing based methods and (2) slow process signal based methods.

Among the fast signal processing techniques, probably the most applied method relies on detecting the presence of pressure waves associated with the flow transient caused by the appearance of the leak (see Ref. [4]). Dedicated acquisition and processing hardware, as well as the corresponding firmware, are necessary to detect the presence of characteristic waveforms embedded in pressure signals. As these waveforms travel along the pipeline at the velocity of sound, such methods are often called "acoustic" but the term is misleading. Actually there exists true acoustic methods based on detecting the noise caused by the leak with the help of microphones, but this is a different technological category (inspection). Waves caused by a sudden leakage have very low central frequencies, within approximately 0.5–2 Hz, which characterizes them as subsonic. Generally speaking, acoustic LDS's are applicable to liquid, gas, and some multiphase pipelines, are fast, and can locate the leak accurately, but the precision of the estimated leak flow rate is poor. Another important characteristic is that an acoustic LDS is not suited for detecting gradually developing leaks (progressive), although pressure waves associated with hydraulic transients have been used to inspect the pipeline for existing abnormalities (see Refs. [5,6]).

A slow process signal method, such as the ones based on SCADA (Supervisory Control and Data Acquisition) signals, was early proposed by Siebert [7] in 1981. The method was based on a statistical analysis and was tested on pipeline for transporting gasoline and natural gas. The reported leak sensitivities were around 0.2% and 5.0% of the nominal flow rate, the detection time in both cases was a few hours, and the localization error was about 20 km. Probably the first mass balance based method was proposed by Ellul [8] in 1989 and was capable of detecting a 0.5% leak in 3–6 h. The underlying idea sustaining these methods is the concept of deviation from a characteristic dynamic state associated with normal pipe operation. More precisely, the canonical flow variables and their temporal derivatives constitute a state space, in which all normal operation states are represented by characteristic trajectories. Any anomalous operating condition is identified as an uncharacteristic trajectory and may indicate a leak. This is a very powerful and universal concept and, actually, may be applied not only to leak detection problems, but to any kind of fault detection application and to multiphase flow regime identification (see Ref. [9]). Within these ideas, a rigorous mathematical formulation of the mass balance LDS was proposed by Stouffs

---

[1] Corresponding author.

Contributed by the Fluids Engineering Division of ASME for publication in the Journal of Fluids Engineering. Manuscript received September 15, 2008; final manuscript received November 16, 2009; published online January 12, 2010. Assoc. Editor: Theodore Heindel.

and Giot [2] in 1993, who also highlighted the importance of the packing term and the influence of intrinsic errors on the minimum detection threshold. A good review on the subject can be found in Ref. [10].

The basic motivation of this work arises from the very delicate problem of specifying a LDS. This is so because previous practical experiences are associated with countless specific application conditions to which a great number of different techniques have been applied. In the absence of a more systematic theoretical background, this choice involves high uncertainties, and a successful application credited to a sensible specification is, possibly, the result of having a lot of chance. (A very favorable application condition, for example.) Thus, the main objective of this work is to perform a comparative test between two important on-line leak detection techniques. Since the acoustic and mass balance methods are capable of satisfying different requirements and, to some extent, are suited to different conditions, a benchmark problem has been defined to which both methods are applicable. Objective common performance characteristics were defined in order to assess the performance of each LDS, as follows: detection delay, leak location error, and leak mass flow rate error.

2 Leak Detection Based on Acoustic Sensing

The sudden structural failure of a pipeline originates a leak that engenders a hydrodynamic transient that propagates upstream and downstream relatively to the flow. The absolute propagation speed is determined by the local values of the flow average velocity and wave celerity, which, for a given liquid, are determined by the local flow pressure and temperature. This transient is characterized by pressure and velocity oscillations reflecting the evolution to a new dynamic equilibrium between pressure (elastic) and inertia energy modes. Thus, detecting the rupture of the pipeline becomes a problem of detecting a specific waveform embedded in pressure, velocity, or any other monitoring signal. This is a very well defined problem in signal analysis and there are several methods that can be applied, depending on the specificities of the problem. Usual approaches are simple correlative filters (see Ref. [11]) or, more recently, the so-called neural filters (see Ref. [12]), which have the property of autonomously learning new waveforms. For instance, if $P_{\text{in}}(t)$ is the pressure signal measured at the inlet end of the pipeline, and if $\psi(t)$ is the waveform associated with the leak, the following correlation signal $r(t)$ is defined (see Ref. [11]):

$$r(t) = \frac{1}{\displaystyle\int_{t-T}^{t} \psi(\tau)^2 d\tau \cdot \int_{t-T}^{t} P_{\text{in}}(\tau)^2 d\tau} \left[\int_{t-T}^{t} P_{\text{in}}(\tau - t) \cdot \psi(\tau) d\tau \right]^4 \tag{1}$$

in which T denotes the temporal support of the sought waveform. It is evident that $0 \le r(t) \le 1$ and $r(t)=1$ only if $P_{\text{in}}(t)$ matches $\psi(t)$ locally. An alarm is then triggered if the correlation signal exceeds a predefined convenient threshold. Figure 1 shows the pressure signals measured at both ends of a 2 km oil pipeline during a simulated leak test.

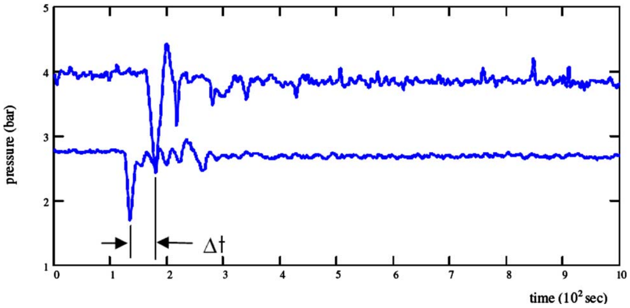

Fig. 1 Characteristic pressure waveforms during a simulated leak test

Once these pulses are detected at both ends of the pipeline, the delay ΔT between them is used to determine the leak location ℓ, according to the equation

$$\Delta t = \int_0^{\ell} \frac{dx}{U(x) - a(x)} - \int_{\ell}^{L} \frac{dx}{U(x) + a(x)} \tag{2}$$

It is clear that to solve for Eq. (2) it is necessary to provide the average flow velocity and the acoustic propagation velocity profiles, which are functions of the flow pressure and temperature. For example, mass conservation implies that $U(x)$ should change to compensate for the density and diameter variations due to thermal or elastic expansion of the pipe. To explicit this relation it would be necessary to solve for a set of coupled differential equations relating mass, momentum, and elastic energy conservation principles, that is, a coupled fluid-structure problem. However, if the flow velocity is small compared with the acoustic propagation velocity (generally the case in liquids) and if pipe diameter variations can be neglected because of a low working pressure or due to very rigid pipe walls, and both applies to our experimental conditions, important simplifying hypothesis can be assumed. Therefore, a simplified version of Eq. (2) can be solved by assuming average constant values for $a(x)$ and $U(x)$, which, after integration, results

$$\ell = \left(\Delta T - \frac{L}{\bar{a} + \bar{U}} \right) \left(\frac{\bar{a}^2 + \bar{U}^2}{2\bar{a}} \right) \tag{3}$$

The equations leading to an estimation of the leak flow rate start from calculating the amplitude of the negative (rarefaction) pressure pulse with the help of Joukowsk's equation

$$\Delta P_0 = \rho a \Delta U \tag{4}$$

In Eq. (4), ΔP_0 and ΔU denote the pulse amplitude and the variation in the average flow velocity due to and at the location of the leak respectively. A very important property of this wave is its ability to propagate through long distances (due to an intrinsic low attenuation) and, also, to easily surpass obstacles such as curves, valves, etc. This is so because of the huge wavelength, which varies between a few hundred to a thousand meters in most practical pipeline applications. In the case shown above, the central frequency of the wave is about 1.8 Hz and the speed of sound was determined as 1230 m/s, resulting in a wavelength λ of 683 m approximately, according to the fundamental wave equation.

The amplitude of the pressure wave reduces progressively as it propagates along the pipeline, away from the leak spot. Acoustic attenuation is a complex phenomenon and is still poorly understood, particularly at low frequencies. Most of the information found in the open literature concerns high frequencies within the ultrasound range in single or multiphase media (see Ref. [13]). Chuanhu et al. [3] presented a linear analysis of the governing Navier–Stokes equations and showed that viscous dissipation plays an important role in acoustic attenuation. Experimental evidences also suggest that dissolved gas, turbulence, and the flow regime in multiphase flows are important aspects influencing acoustic attenuation.

The basic equation accounting acoustic attenuation of one-dimensional waves is (see Ref. [13]):

$$\Delta P(x) = \Delta P_0 \exp(-\alpha x) \tag{5}$$

in which $\Delta P(x)$ represents the amplitude of the pressure pulse at distance x from the leak location and α is the attenuation coefficient. A classic empirical correlation, developed by Duck et al. [14] in 1998, can be used to illustrate the long distances reached by low frequency waves

$$\alpha = \beta \omega^n \tag{6}$$

where ω is the wave frequency in Hz, and β and n are constants determined empirically for specific fluids. Considering a water pipeline, for which $\beta \approx 1.89$ dB/cm and $n \approx 1$, the resulting attenuation coefficient according to Eq. (6) for a 1.8 Hz wave is $\alpha \approx 10^{-14}$ m^{-1}. Equation (5) implies that the pressure pulse should propagate through 10^{13} m to experience an attenuation of 50% in its amplitude, i.e., more than the earth-moon distance! Obviously this result is qualitative and other nonaccounted phenomena contribute to increasing attenuation in such a low frequency.

Although the uncertainty associated with the attenuation coefficient is significant, Eqs. (4) and (5) can be used to quantify the leak mass flow rate. First it is necessary to calculate the amplitude of the pressure wave at the leak location from the corresponding amplitudes measured at the inlet and outlet ends of the pipeline, denoted respectively by ΔP_{in} and ΔP_{out}. Thus, Eq. (5) can be written for both ends of the pipeline and used to produce an averaged estimation of ΔP_0, since ℓ has been previously determined

$$\Delta P_0 = \frac{\Delta P_{\text{in}} + \Delta P_{\text{out}}}{2 \exp(-\alpha \ell)} \tag{7}$$

The leak mass flow rate is then calculated by replacing Eq. (7) into the Joukowski Eq. (4) to calculate ΔU. Finally, a simple mass balance leads to

$$m_{\text{leak}} = \frac{\pi D^2}{8a} \cdot \frac{\Delta P_{\text{in}} + \Delta P_{\text{out}}}{\exp(-\alpha \ell)} \tag{8}$$

3 Leak Detection Based on Mass Balance Equations

A very important advantage of a mass balance LDS over the acoustic technology is its ability to detect leaks generated by a progressive structural failure due to corrosion or a slowly growing crack, for instance. Another important advantage is a direct, and therefore precise, assessment of the leak flow rate. On the other hand a mass balance LDS is strongly dependent on flow models, which limit their practical application to pipelines for transporting single-phase liquids.

The working principle is straightforward: If a leak occurs, the mass balance equation (accounting for the input and output mass flow rates and also the linepack variation rate) presents a systematic deviation. Although simple and certainly reliable, the main difficulty in implementing this principle in practice derives from the huge variations experienced by the linepack term. This effect implies a very long detection time and, therefore, a frequently unacceptable leaked mass until an alarm is declared.

In mathematical terms, a mass balance LDS is based on the following error signal denoted by $e(t)$ (see Ref. [2]):

$$e(t) = \int_{t-\Delta T^*}^{t} \left[\frac{dM}{d\tau} - (m_{\text{in}} - m_{\text{out}}) \right] d\tau \tag{9}$$

where ΔT^* is a carefully defined integration interval, $dM/d\tau$ represents the rate of change in the linepack, and m_{in} and m_{out} are the input and output mass flow rates, respectively,. Integration of $dM/d\tau$ in Eq. (9) produces the mass variation within ΔT^*, which varies in time due to the thermal and elastic expansion of the pipeline, in addition to the fluid's compressibility. The instantaneous amount of mass confined in the pipeline can be modeled by the following equations:

$$M(t) = \int_0^L \rho(x,t) \pi \frac{D(x,t)^2}{4} dx \tag{10}$$

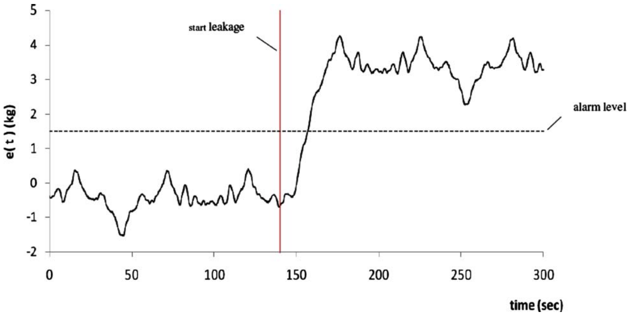

Fig. 2 Characteristic mass balance error signal according to Eq. (9) during a simulated leak test

$$D(t,x) = D_{\text{ref}} \left(1 + \frac{P(x,t) - P_{\text{ref}}}{2Ee^*} \cdot D_{\text{ref}} + \alpha_w [\theta(t,x) - \theta_{\text{ref}}] \right) \tag{11}$$

in which D_{ref}, P_{ref}, and θ_{ref} are reference diameter, pressure, and temperature, respectively, α_w is the pipe's material thermal expansion coefficient, E denotes the Young modulus, and e is the wall thickness. The need for instantaneous pressure and temperature profiles along the pipeline, which have to be calculated by solving the Navier–Stokes equations, becomes explicit in expressions (10) and (11). This is the Achilles heel of all mass balance LDS. In order to illustrate linepack fluctuations, consider a 30 km long natural gas pipeline operating at 100 bar. The internal diameter is 600 mm, the wall thickness is 50 mm, and the material is carbon steel. If the pipe experiences an unaccounted 10°C variation in temperature, the corresponding variation in volume is about 6.9 m^3 or approximately 518.7 kg of gas. If other error sources are considered, such as the intrinsic experimental errors in mass flow rates and modeling errors of pressure and temperature profiles, this fluctuation can increase even more, usually exceeding several tons. In fact, this is the order of magnitude of the alarm level in Eq. (9) associated with a mass balance LDS applied to a gas pipeline.

Figure 2 shows the error signal corresponding to the simulated leak test shown in Fig. 1. Despite the precision of the mass flow rate measurement, it is clear necessary to set a proper leak threshold above the normal fluctuation level in order to avoid false alarms. In this case, 1.5 kg would be a possible convenient choice. A longer integration time in Eq. (9) tends to smooth out the fluctuations but the response to a leak is slower. On the contrary, if ΔT^* is reduced in Eq. (9) the response to a leak is much faster, but the normal fluctuations increase, leading to a greater leak threshold. The ideal integration time is case dependent and must be carefully chosen to obtain a good tradeoff between stability and detection delay.

Once detected, the leak must be located and quantified. In a mass balance LDS, quantification of the leak is a very straightforward task exactly because it is based on the conservation of mass principle. However, due to the already mentioned fluctuations of the linepack, the leak mass flow rate (m_{leak}) cannot be stated as the instantaneous difference between the input and output flow rates of the pipe. Instead, it is preferable to calculate

$$m_{\text{leak}} = \frac{1}{\Delta T^*} \int_{\Delta T^*} (m_{\text{in}} - m_{\text{out}}) dt \tag{12}$$

that is, the average calculated over a sufficiently long integration interval ΔT^* for the fluctuations of the linepack and experimental errors have been filtered out.

Localization is accomplished by solving for steady state versions of the Navier–Stokes equations applied to the upstream and downstream sections of the pipe with respect to the leak spot.

Assuming that all transients due to the rupture have vanished and neglecting the convective terms, these equations can be written as

$$\begin{aligned} &\frac{\partial P}{\partial x}+\frac{\rho f}{D}\cdot\frac{U|U|}{2}=0, \quad 0\le x<\ell \\ &P(0)=P_{\text{in}} \quad \text{and} \quad P(\ell)=P_{\text{leak}} \end{aligned} \tag{13}$$

$$\begin{aligned} &\frac{\partial P}{\partial x}+\frac{\rho f}{D}\cdot\frac{U|U|}{2}=0, \quad L-\ell<x\le L \\ &P(L-\ell)=P_{\text{leak}}, \quad P(L)=P_{\text{out}} \end{aligned} \tag{14}$$

If the compressibility of the fluid is significant, the mass balance equation can be used together with a state equation in order to propagate the flow velocity from the pipe's ends to the leak location. Then, Eqs. (13) and (14) can be solved by some convenient discretisation method (finite differences, finite elements, etc.). If not, the following further simplifications can be made:

$$\frac{P_{\text{in}}-P_{\text{leak}}}{\ell}=\frac{\rho f_{\text{in}}}{D}\cdot\frac{U_{\text{in}}^2}{2} \tag{15}$$

$$\frac{P_{\text{leak}}-P_{\text{out}}}{L-\ell}=\frac{\rho f_{\text{out}}}{D}\cdot\frac{U_{\text{out}}^2}{2} \tag{16}$$

which solved for ℓ results

$$\ell=\frac{\dfrac{2D}{\rho f_{\text{out}}U_{\text{out}}^2}(P_{\text{in}}-P_{\text{out}})-1}{\dfrac{f_{\text{in}}U_{\text{in}}^2}{f_{\text{out}}U_{\text{out}}^2}-1} \tag{17}$$

Although quite simple, there are two issues associated with this expression. The first one concerns the calculus of the friction factor, for which there are precise models in single-phase flows. In the absence of a priori information about the flow regime, the friction factor can be modeled by Curchill's correlation, for instance. The second and most import issue shows the need for precise measurements of the variables, specially the flow rates used to determine the average velocities. If a small leak occurs, $U_{\text{in}}\to U_{\text{out}}$ and Eq. (17) becomes extremely unstable, particularly in the presence of experimental errors.

4 Statement of the Benchmark Problem

As already mentioned, acoustic and mass balance leak detection methods are the most frequently applied technologies and, most importantly, have complementary characteristics. Mass balance is capable of detecting a leak due to a slowly evolving structural failure of the pipe, while the acoustic method is not applicable to this situation. On the other hand, because on-line flow rate measurements in multiphase flows are subjected to large errors, mass balance technology is not applicable whereas the acoustic method is. Thus, a specific reference or benchmark problem in which both methods are applicable was defined in order to assess their performances: a pipeline for transporting liquids subjected to an abrupt loss of integrity through which a leak is created. Under these circumstances, the leak must be detected, located, and quantified. In practice, this information is necessary for an advised decision about which actions to take (sending a maintenance team to the leak location or shutting down the pipe immediately).

Depending on the characteristics of a particular situation, different parameters may be used to assess the performance of a leak detection technology, such as detection time, false alarm, and missed alarm probabilities, smallest detectable equivalent diameter, smallest detectable flow rate, localization precision, and leak assessment precision, among others. Currently there is no consensus on defining such parameters, neither on their relative importance. For instance, the smallest leak flow rate is likely to be the most relevant parameter in a sulfidric gas or ammonia pipeline while the false alarm probability should be the most important concern in a transnational natural gas pipeline. Several operation conditions affect the performance of an LDS, particularly the statistical or probabilistic ones. For example, false alarm rates are strongly influenced by transients such as starting up a pump or commuting discharge reservoirs. Another example is the amount of electric noise in the monitoring signals, which influences the sensitivity of the LDS. As these parameters are intrinsic to each application, we will not deal with them in this work. Instead, we will focus on the following aspects of a LDS.

The detection delay is probably one of the most important performance parameters to be considered in an LDS, together with the sensitivity to detect small leaks. In an acoustic-based LDS, this delay depends on the travel time from the leak spot to the pressure sensors at the pipeline extremities and, thus, is essentially determined by the acoustic propagation speed and the leak position. Roughly speaking, the longest detection delays are associated with leaks occurring at the inlet or outlet as the wave propagation path to the opposite pressure sensor corresponds to the whole pipeline length. The detection delay in a mass balance LDS is determined essentially by the leak flow rate because a certain amount of leak fluid must be achieved before a leak alarm is declared. In both cases the corresponding thresholds in Eqs. (1) and (9) have a strong influence on such performance parameter and, then, must be fixed according to a very conscious criterion. In this work the thresholds were systematically optimized to insure a minimum detection delay and zero false alarms.

Once the leak has been detected, it is important to base subsequent actions on supplementary information such as leak flow rate and location. For instance, provided that the fluid is not explosive or toxic and the leak flow rate is small enough, it would not be necessary to completely shut down the pipeline, if this implies important operation difficulties or financial losses. Decreasing the operating pressure and dispatching a maintenance team to the leak spot would, probably, be a much more reasonable decision than interrupting the transport or transfer operation. On the other hand, if the leak is significant and causes serious injuries and damages, shutting down the pipe is the only alternative. Thus, accurately assessing the leak flow rate is of great importance for a correct decision under the specific circumstances.

Acoustic and mass balance LDS assess the leak based on different principles, according to Eqs. (8) and (12), respectively. The first relies on the assumption that acoustic attenuation is known, which represents an important weakness of the acoustic method. The mass balance method, on the contrary, estimates the leak directly from flow rate measurements, of which the most important source (linepack) of error tend to be filtered out by choosing a sufficient integration interval in Eq. (12).

Likewise, the leak location is determined according to different strategies. The acoustic method relies on the time necessary for the leak waves to travel from the leak spot to the ends of the pipeline where the pressure sensors are installed. If the acoustic wave propagation speed and/or the flow velocity vary along the pipeline, Eq. (2) can be solved to determine the leak location. If not, a simplified version of this equation can be used, i.e., Eq. (3). Either way this is expected to be a precise and fast strategy, within which the most important source of error is associated with the determination of the arrival times of the acoustic pulses, particularly in the presence of background noise. The leak location is estimated in the mass balance method through Eq. (17), i.e., by solving for the steady state and simplified versions of the flow equations describing the pipeline altogether with the leak. As already mentioned, this corresponds to solve for an inverse problem, which is expected to be ill-conditioned. This characteristic is, in fact, recognizable in the denominator of Eq. (17), which may become unbounded when the leak is small ($U_{\text{in}}\cong U_{\text{out}}$) and/or due to experimental errors.

In conclusion, to assess these three performance characteristics,

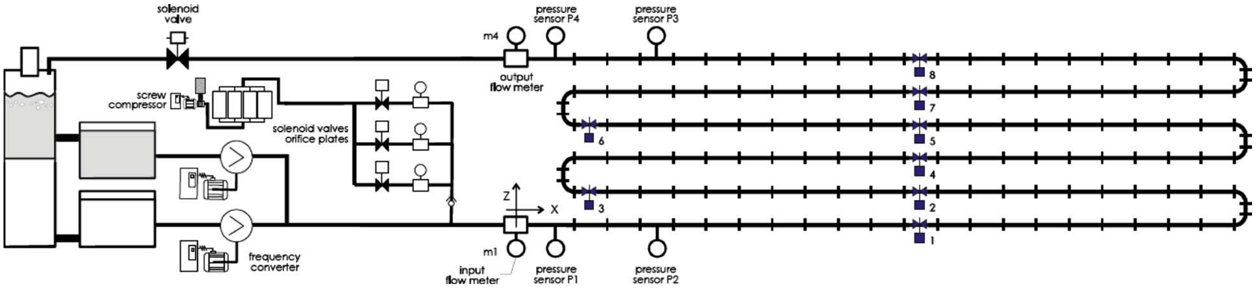

Fig. 3 Schematic representation of the experimental loop at the Industrial Multiphase Flow laboratory

i.e., detection delay and accuracies of the leak location and flow rate, in addition to the application conditions intrinsic to the benchmark problem, it is necessary to simulate benchmark leaks at previously known locations and flow rates. Furthermore, these benchmark leaks must be so that a variety of operating conditions are simulated. Thus, it is advisable to distribute these leaks along the pipeline, assuring different operating pressures and levels of background noise, and to calibrate them to produce a range of very small to very large leak flow rates. The experimental loop and the way these requirements were satisfied are described below.

5 Experimental Loop and Test Procedure

Experimental tests were performed at the pilot pipeline of the Industrial Multiphase Flow Laboratory at the University of São Paulo, the campus of São Carlos—SP. This circuit, as shown in Fig. 3, is capable of simulating several flow regimes occurring in oil and gas pipelines and works with compressed air, water, and mineral oil (Shell's vitrea 100). Water and oil are injected by 15 kW screw pumps controlled by frequency inverters. Compressed air is supplied by a 50 kW screw compressor and the corresponding flow rate is imposed by servo-valves controlled by orifice plates flowmeters. The test section is constituted by 50 mm internal diameter metallic tubes, with wall thickness $e=3$ mm, extending through approximately 1000 m between the exit of the water pump and the entrance of the separation reservoir. Four pressure sensors and two magnetic flowmeters are positioned ant the inlet and outlet sections of the pipeline. The inlet flowmeter is the reference for the x-z axis (x running along the pipe), that is $x=z=0$. In this coordinate system, the position of the outlet flowmeter is defined by $x=749.23$ m and $z=0.25$ m. The positions of the pressure sensors are given by the following coordinates: P_1 at $x=7.11$ m and $z=-0.10$ m, P_2 at $x=48.74$ m and $z=-0.59$ m, P_3 at $x=704.22$ m and $z=+0.95$ m, and P_4 at $x=745.15$ m and $z=+1.51$ m. Eight solenoid valves (coordinates given in Table 1) were used to simulate abrupt leaks at known positions and times. (Acoustic LDS is not applicable to progressive leaks.) A high speed video camera was used to determine the response time of these valves and the average value was 4 ms. The leak's diameter was defined with the help of 8 mm orifice plates placed between the solenoid valve and the "T" connection to the pipeline.

A National Instruments electronic hardware is responsible for acquiring all test or process signals (temperatures, pressures, flow rates, etc.), as well as for generating all command signals to pumps, solenoid valves, and so on. Specifically, a PXI1000B chassis equipped with an NI8176 controller module (1.26 GHz Pentium III processor) runs the experiment driver written in LABVIEW. The PXI chassis is equipped with NI6025E modules through which all input and output signals are analog to digital (A/D) converted. Sampling frequency was set to 120 Hz and, except for analogical anti-aliasing filters, and no preprocessing was applied to the test signals; they were stored as acquired.

Water at 27.6°C (ambient temperature) was used as the working fluid. The acoustic propagation speed was determined empirically by closing the exit servo-valve to produce water hammers. Measuring the transit times between pressure sensors 1 and 4 (apart by 738.04 m) we obtained an average acoustic speed of 1342 m/s.

The experimental matrix was generated by combining 11 different pumping powers to eight leak positions to generate one single test condition. The resulting steady state variables are given in Table 1 for no leak and leakage operations. These conditions were repeated three times to generate 264 experimental tests, which was sufficiently representative for the statistical analyses.

The experiment driver executed cyclically several operations in order to assure that each test was done precisely the same way. A typical experimental cycle is as follows:

1. Set the water pump frequency (0 or 10 or 20… 100% at random).
2. Wait for 10 s.
3. Start acquisition of test signals.
4. Wait for 10 s.
5. Open a solenoid valve (1 or 2… 8 at random).
6. Wait for 10 s.
7. Close the solenoid valve.
8. Wait for 20 s.
9. Stop acquisition of test signals.
10. Store acquired signals in an ASCII (American Standard Code for Information Interchange) file.

The signals obtained in one of these clycles are shown in Fig. 4.

6 Results and Discussion

Table 2 summarizes the statistical results concerning the average and the corresponding standard deviation of the detection delay, localization error, and leak flow rate error.

As expected, the acoustic method is faster than the mass balance method, but the average detection delays are misleading. For the acoustic method the detection delay is fundamentally determined by the time the rarefaction waves take to travel to the pressure sensors, which is essentially determined by the relative position of the leak. Thus, it is expected that leaks located near the inlet or outlet regions of the pipe are associated with greater detection times. Conversely, the smallest detection times are associated with leaks in the central section of the pipeline. This can be seen in Fig. 5(*a*), in which this "v" trend is clearly identifiable. It is clear that the maximum detection delay is slightly higher than the average value, as shown in Table 2, i.e., approximately 2.1 s. The determinant variable for the mass balance method is the leak flow rate because the detection is based on achieving a limiting error in the mass inventory defined by Eq. (9). The greater is the leak flow rate, the faster this limit is achieved and the smaller is the time to issue a leak alarm. This behavior is readily identifiable in Fig. 5(*b*), which also reveals that the detection time increases hyperbolically as the leak flow rate decreases. The main reason for this is the degradation of the signal to noise ratio of the flow rate

Table 1 Position of the leak simulation valves (relative to *x-z* coordinates indicated in Fig. 3) and operating variables at different pumping powers for steady state operations with and without leak

			Pumping power (%)										
Valve	Operation	Variable	0	10	20	30	40	50	60	70	80	90	100
Valve 1 $x=85.44$ m $z=3.71$ m	No leak	P_1 (bar)	1.04	1.11	1.29	1.58	1.97	2.47	3.06	3.76	4.54	5.44	6.43
		P_4 (bar)	0.68	0.75	0.89	1.14	1.47	1.90	2.41	3.02	3.69	4.48	5.35
		m_1 (l/min)	0.00	0.00	16.42	26.67	36.71	45.86	54.82	64.55	73.97	82.84	92.28
	Leakage	P_1 (bar)	1.03	1.10	1.28	1.55	1.94	2.43	3.01	3.69	4.46	5.34	6.31
		P_4 (bar)	0.67	0.74	0.87	1.11	1.43	1.85	2.35	2.94	3.60	4.36	5.21
		m_1 (l/min)	17.03	20.17	37.48	48.38	63.68	72.90	86.14	97.39	109.46	121.55	135.21
		m_4 (l/min)	0.00	0.36	15.38	25.99	36.14	45.99	55.62	64.79	74.03	83.02	92.47
Valve 2 $x=175.86$ m $z=-3.33$ m	No leak	P_1 (bar)	1.04	1.11	1.29	1.58	1.97	2.47	3.06	3.76	4.55	5.44	6.42
		P_4 (bar)	0.68	0.75	0.90	1.14	1.47	1.90	2.41	3.02	3.70	4.48	5.35
		m_1 (l/min)	0.00	0.03	16.86	26.75	36.24	46.72	54.79	64.48	73.82	83.00	91.90
	Leakage	P_1 (bar)	1.03	1.10	1.28	1.55	1.94	2.43	3.01	3.69	4.46	5.34	6.31
		P_4 (bar)	0.66	0.74	0.85	1.09	1.40	1.81	2.30	2.88	3.53	4.28	5.12
		m_1 (l/min)	17.60	18.55	37.77	49.81	63.55	75.42	87.84	98.65	112.27	122.08	131.03
		m_4 (l/min)	0.00	0.35	14.14	25.00	35.29	45.20	54.48	63.77	73.28	81.84	91.26
Valve 3 $x=254.24$ m $z=+0.36$ m	No leak	P_1 (bar)	1.04	1.11	1.29	1.58	1.97	2.47	3.06	3.76	4.55	5.44	6.41
		P_4 (bar)	0.69	0.75	0.90	1.13	1.47	1.90	2.41	3.01	3.70	4.48	5.34
		m_1 (l/min)	0.00	0.02	16.38	26.41	36.14	46.68	54.95	64.29	73.89	82.95	91.97
	Leakage	P_1 (bar)	1.04	1.11	1.27	1.56	1.94	2.43	3.01	3.69	4.46	5.33	6.29
		P_4 (bar)	0.65	0.73	0.85	1.07	1.39	1.78	2.26	2.82	3.47	4.20	5.00
		m_1 (l/min)	12.30	15.48	33.66	46.82	57.08	72.84	85.02	98.10	110.46	123.51	136.51
		m_4 (l/min)	0.00	0.25	13.09	24.35	34.76	44.22	53.70	63.22	72.12	81.05	90.38
Valve 4 $x=335.47$ m $z=2.96$ m	No leak	P_1 (bar)	1.04	1.11	1.29	1.58	1.97	2.47	3.06	3.76	4.54	5.44	6.42
		P_4 (bar)	0.69	0.75	0.90	1.14	1.47	1.90	2.41	3.01	3.70	4.48	5.35
		m_1 (l/min)	0.00	0.00	16.53	26.67	36.03	46.72	55.72	64.87	73.82	83.17	91.97
	Leakage	P_1 (bar)	1.03	1.11	1.28	1.56	1.94	2.43	3.02	3.70	4.47	5.35	6.32
		P_4 (bar)	0.65	0.73	0.83	1.06	1.37	1.81	2.24	2.80	3.44	4.16	4.98
		m_1 (l/min)	12.34	14.05	33.13	46.29	57.99	75.42	81.33	94.93	106.04	118.40	130.72
		m_4 (l/min)	0.00	0.20	12.18	23.66	33.88	45.20	53.25	62.55	70.96	80.85	89.88
Valve 5 $x=421.14$ m $z=-2.55$ m	No leak	P_1 (bar)	1.04	1.11	1.29	1.58	1.97	2.47	3.06	3.76	4.54	5.44	6.42
		P_4 (bar)	0.69	0.75	0.90	1.14	1.47	1.90	2.41	3.01	3.70	4.48	5.34
		m_1 (l/min)	0.00	0.00	16.46	26.59	36.14	45.61	55.44	64.88	73.34	82.88	92.37
	Leakage	P_1 (bar)	1.03	1.11	1.27	1.56	1.94	2.44	3.02	3.70	4.47	5.35	6.32
		P_4 (bar)	0.64	0.72	0.83	1.04	1.35	1.74	2.21	2.76	3.39	4.11	4.93
		m_1 (l/min)	10.74	13.01	30.96	43.68	57.03	67.90	80.78	92.88	104.74	115.82	126.51
		m_4 (l/min)	0.00	0.17	11.67	23.12	33.41	43.40	52.75	61.89	71.75	80.47	89.36
Valve 6 $x=499.42$ m $z=+1.17$ m	No leak	P_1 (bar)	1.04	1.11	1.29	1.58	1.97	2.47	3.06	3.76	4.55	5.44	6.41
		P_4 (bar)	0.68	0.75	0.90	1.13	1.47	1.90	2.41	3.01	3.70	4.48	5.34
		m_1 (l/min)	0.00	0.01	16.31	26.95	35.93	45.78	55.41	64.46	74.12	82.98	91.75
	Leakage	P_1 (bar)	1.04	1.11	1.28	1.56	1.95	2.44	3.02	3.71	4.48	5.36	6.32
		P_4 (bar)	0.64	0.72	0.83	1.04	1.35	1.73	2.19	2.73	3.35	4.06	4.84
		m_1 (l/min)	7.93	9.68	27.71	41.23	54.79	67.37	78.61	91.00	103.14	114.78	126.27
		m_4 (l/min)	0.00	0.13	11.30	23.05	33.11	42.97	52.36	61.61	70.46	79.40	88.19
Valve 7 $x=580.64$ m $z=-2.11$ m	No leak	P_1 (bar)	1.04	1.11	1.29	1.58	1.97	2.47	3.06	3.76	4.54	5.44	6.41
		P_4 (bar)	0.69	0.75	0.89	1.14	1.47	1.90	2.41	3.01	3.70	4.48	5.34
		m_1 (l/min)	0.00	0.00	16.01	26.39	35.96	46.39	55.19	64.79	73.82	82.87	92.16
	Leakage	P_1 (bar)	1.03	1.11	1.27	1.56	1.95	2.43	3.02	3.71	4.48	5.36	6.32
		P_4 (bar)	0.63	0.71	0.80	1.01	1.31	1.69	2.14	2.68	3.29	3.99	4.76
		m_1 (l/min)	9.76	11.11	28.97	42.68	54.18	67.52	78.86	91.30	102.48	114.35	126.45
		m_4 (l/min)	0.00	0.14	8.80	21.48	32.20	41.89	51.51	60.40	69.93	79.12	87.43
Valve 8 $x=66684$ m $z=-1.74$ m	No leak	P_1 (bar)	1.04	1.11	1.29	1.58	1.97	2.47	3.06	3.76	4.54	5.44	6.41
		P_4 (bar)	0.69	0.75	0.89	1.13	1.47	1.90	2.41	3.01	3.70	4.48	5.34
		m_1 (l/min)	0.00	0.04	15.88	26.96	36.61	45.74	55.43	64.56	73.64	83.10	91.92
	Leakage	P_1 (bar)	1.03	1.11	1.28	1.56	1.95	2.44	3.02	3.71	4.48	5.36	6.32
		P_4 (bar)	0.62	0.70	0.79	1.00	1.29	1.67	2.11	2.64	3.24	3.92	4.69
		m_1 (l/min)	8.16	10.50	27.01	42.21	54.34	65.78	79.48	90.53	102.55	113.79	125.43
		m_4 (l/min)	0.00	0.13	7.75	21.08	31.53	41.42	50.70	59.99	68.70	77.64	86.66

signals and, consequently, the need for a greater integration interval in Eq. (9). The maximum observed delay was approximately 11.3 s for the smallest leaks.

The results concerning the localization error confirm that the acoustic method is much more accurate than the mass balance method: The standard deviations are 0.30 m and 16.03 m, respectively. The average error is approximately zero in the first case, which indicates that no significant systematic error is associated with Eq. (3). (The 0.43 m value was probably due to an underestimation of the flow rate velocity.) However, the average error for the mass balance method is quite significant (21.96 m), probably due to the evaluation of the friction factors in Eq. (17). Figure 6

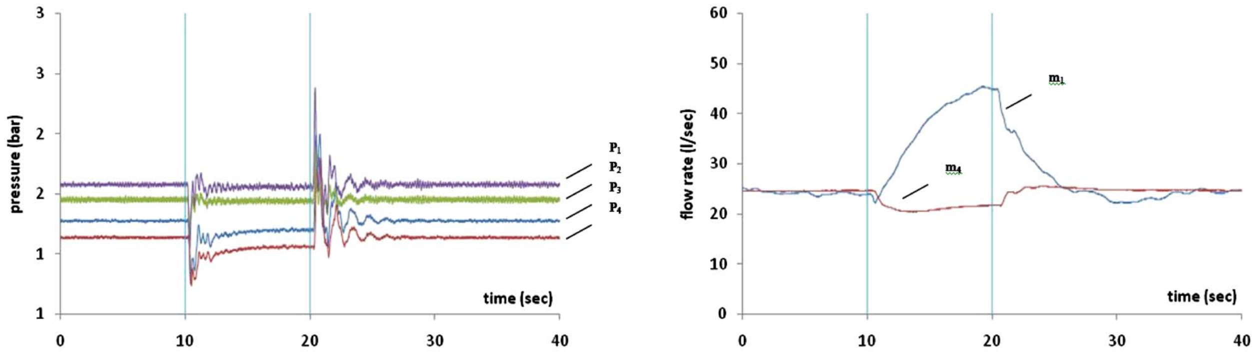

Fig. 4 Pressure and flow rate signals obtained during one experimental cycle (pumping power at 30% and operating valve number 3, as indicated by the vertical lines)

Table 2 Statistical characterization of both LDS

Performance parameter	Acoustic LDS	Mass balance LDS
Detection delay (s)	$\mu=1.88$ $\sigma=0.10$	$\mu=3.29$ $\sigma=1.96$
Localization error (m)	$\mu=0.43$ $\sigma=0.30$	$\mu=21.96$ $\sigma=16.03$
Leak flow rate error (l/min)	$\mu=3.21$ $\sigma=2.27$	$\mu=0.12$ $\sigma=0.14$

shows the corresponding histograms for these errors.

As already anticipated, the estimation of the leak flow rate was accomplished with great precision by the mass balance method: The average error is close to zero (0.12 l/min) and the standard deviation is also very small (0.14 l/min). Conversely the leak flow rate was poorly estimated by the acoustic method, i.e., with a great systematic error (3.21 l/min) and high data dispersion around the predicted value (2.27 l/min, almost 20% less accurate than the mass balance method). This deficiency can be attributed to two principal factors concerning Eq. (8), as follows: (1) intrinsic errors associated with the measurement of ΔP_{in} and ΔP_{out} (they are determined directly from the pressure by a signal processing procedure susceptible to the presence of noise), and (2) the attenuation coefficient α is poorly known (probably not constant during the tests due to dissolved gas, for instance). These arguments are consistent with the corresponding histograms of leak flow rate errors shown in Fig. 7.

7 Conclusions

In this work the acoustic and mass balance leak detection methods were compared with respect to a common reference situation, i.e., the same pressure and mass flow rate signals acquired at the pipe's extremities. More specifically, three performance parameters were compared: the detection delay (time length between the occurrence of the leak and emission of the corresponding alarm), and the errors of the leak localization and flow rate. These param-

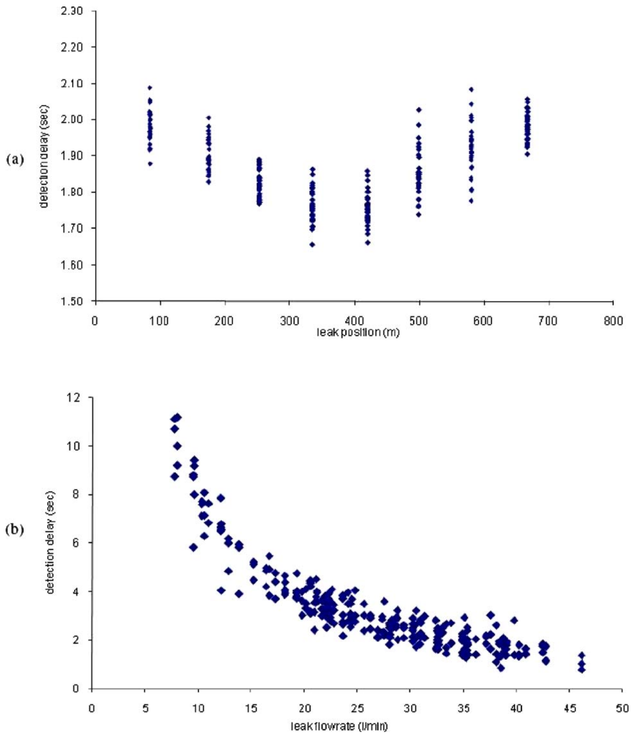

Fig. 5 Detection delay obtained in all tests for the acoustic: (*a*) and mass balance and (*b*) LDS's

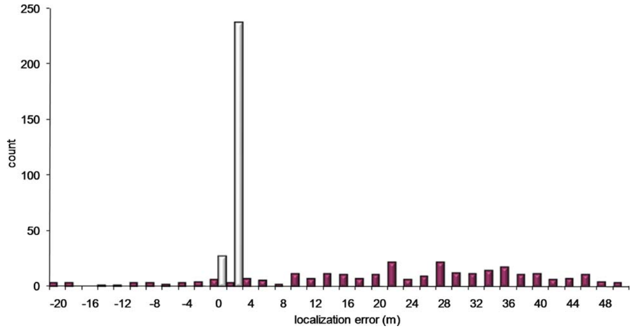

Fig. 6 Leak localization error histograms (■: mass balance, □: acoustic)

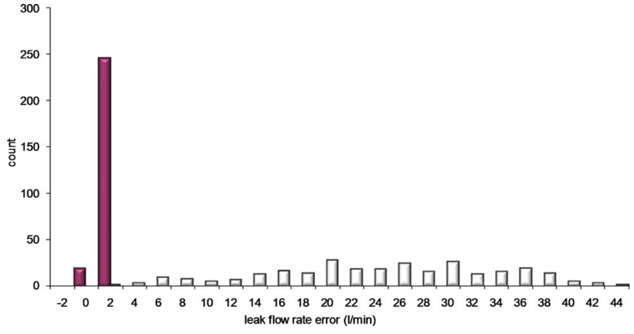

Fig. 7 Leak flow rate error histograms (■: mass balance, □: acoustic)

eters were statistically determined from 264 simulated leak experimental tests conducted in a 749 m test section transporting water. The main conclusion about the performance of each method is that they are complementary in nature, that is, a limitation of one corresponds exactly to a strong characteristic of the other.

First, regarding the detection delay, the acoustic method is generally superior because the information about the leak travels to the sensors at the extremities of the pipe at the speed of sound. In both methods this performance parameter is dependent on the leak position and also on some operating conditions. The graphs shown in Fig. 5 indicate that an alarm is declared in a minimum time if the leak occurs at the pipe's central region for the acoustic method, and that the detection delay of small leaks may increase unlimitedly for the mass balance approach.

Regarding the localization error, the performance of mass balance method is strongly affected by both the quality of flow models and the intrinsic ill-conditioned nature of the corresponding solution. In other words, since estimating the leak location implies solving for an inverse problem, any noise or other sources of errors are greatly amplified and tend to strongly corrupt the solution. This behavior is evident in Eq. (17), whose denominator becomes unstable for small leaks ($U_{\text{in}} \cong U_{\text{out}}$). Conversely, for the acoustic method, the leak is located based on the temporal difference between the arrival times of the corresponding characteristic pressure waves to the inlet and outlet pressure sensors. The main sources of error, according to Eq. (2), are uncertainties concerning the acoustic speed and flow average velocities along the pipe length, which is relevant only to gas and multiphase flows, which were not tested in this work. As expected, the performance of the mass balance method is inferior in comparison with the acoustic approach, regarding the localization error.

The strongest characteristic of the mass balance method is a very accurate quantification of the leak flow rate, as it is performed directly through Eq. (12), which closes the error Eq. (9) in an average sense. In contrast, the leak flow rate is poorly determined by the acoustic approach, as it is based on an acoustic attenuation equation given by Eq. (5). The underlying hypotheses are, in fact, very restrictive (one-dimensional propagation in a homogeneous medium, for example) and associated with large uncertainties. The principal one concerns the attenuation coefficient which, as elaborated in the text, is still largely unknown and deserves additional research.

Acknowledgment

The authors would like to acknowledge the financial support provided by FAPESP (Grant No. 03/13819-6) and CNPq (Grant No. 62.0012/99-4). The crucial collaboration of Eng. Jorge Nicolau dos Santos from NETeF/EESC/USP is also recognized.

Nomenclature

a = acoustic propagation velocity
D = pipe's diameter
D_{ref} = reference diameter
dM/dt = rate of change in the linepack
$e(t)$ = mass balance error signal
e^* = wall thickness
E = Young modulus
f = friction factor
m_{in} = inlet mass flow rate
m_{out} = outlet mass flow rate
m_{leak} = leaked mass
M = mass
P = local pressure
P_{ref} = reference pressure
P_0 = initial pressure
P_{in} = inlet pressure signal
P_{out} = outlet pressure signal
ΔP_0 = initial pressure pulse amplitude
$\Delta P(x)$ = amplitude of the pressure wave along the pipe
ΔP_{in} = inlet pressure wave amplitude
ΔP_{out} = outlet pressure wave amplitude
$r(t)$ = correlation signal
T = temporal support of the leak waveform
ΔT = delay between waveforms
ΔT^* = integration interval
U = local average flow velocity
ΔU = variation of the average flow velocity
ρ = liquid density
ρ_0 = reference density
$\psi(t)$ = leak waveform
ℓ = leak location
λ = wavelength
ω = wave frequency (Hz)
β, n = empirical constants
θ_{ref} = reference temperature
α_w = thermal expansion coefficient

References

[1] Papadakis, G. A., Porter, S., and Wettig, J., 1999, "EU Initiative on the Control of Major Accident Hazards Arising From Pipelines," J. Loss Prev. Process Ind., **12**(1), pp. 85–90.
[2] Stouffs, P., and Giot, M., 1993, "Pipeline Balance: Leak Detection Based on Mass Importance of the Packing Term," J. Loss Prev. Process Ind., **6**(5), pp. 307–312.
[3] Chuanhu G., Guizeng, W., and Hao, Y., 2008, "Analysis of the Smallest Detectable Leakage Flow Rate of Negative," Comput. Chem. Eng., **32**(8), pp. 1669–1680.
[4] Silk, M. G., and Carter, P., 1995, "A Review of Means of Pipeline Leak Detection Independent of Flow Measurement," Proceedings of the EC Project DE-PIRE DGXII Meeting, Harwell, UK.
[5] Liou, C. P., 1998, "Pipeline Leak Detection by Impulse Response Extraction," ASME Trans. J. Fluids Eng., **120**(4), pp. 833–838.
[6] Sattar, A. M. and Chaudhry, M. H., 2008, "Leak Detection in Pipelines by Frequency Response Method," J. Hydraul. Res., **46**(1), pp. 138–151.
[7] Siebert, H., 1981, "A Simple Method for Detecting and Locating Small Leaks in Gas Pipelines," Process Automation, **2**, pp. 90–95.
[8] Ellul, I., 1989, "Pipeline Leak Detection," Chem. Eng. (New York, NY), **461**, pp. 39–44.
[9] Selli, M. F., and Seleghim, P., Jr., 2007, "On-Line Identification of Horizontal Two-Phase Flow Regimes Through Gabor Transform and Neural Network Processing," Heat Transfer Eng., **28**, pp. 541–548.
[10] Belsito, S., Lombardi, P., Andreussi, P., and Banerjee, S., 1998, "Leak Detection in Liquefied Gas Pipelines by Artificial Neural Networks," AIChE J., **44**(12), pp. 2675–2688.
[11] Allen, R. L., and Mills, D. W., 2004, *Signal Analysis Time, Frequency, Scale, and Structure*, Wiley, New York.
[12] Szirtes, G., Póczos, B., and Lőrincz, A., 2005, "Neural Kalman Filter," Neurocomputing, **65–66**, pp.349–355.
[13] Botros, K. K., Geerligsa, J., Zhoub, J., and Gloverb, A., 2007, "Measurements of Flow Parameters and Decompression Wave Speed Following Rupture of Rich Gas Pipelines, and Comparison With GASDECOM," Int. J. Pressure Vessels Piping, **84**(6), pp. 358–367.
[14] Duck, F. A., Baker, A. C., and Starritt, H. C., 1998, *Ultrasound in Medicine*, Institute of Physics, University of Reading, Berkshire.

General Geometrical Model of Scroll Compression Chamber for Scroll Fluid Machine

Qiang Jianguo
School of Mechano-Electronic Engineering,
Lanzhou University of Technology,
287 Langongping Road,
730050 Lanzhou, China
e-mail: qiangjianguo@lut.cn

For a scroll fluid machine with an arbitrary number of scroll wraps on its individual scroll, the phase difference between adjacent scroll profiles on one scroll is defined as the characteristic angle of the scroll. Based on general profile theory, a scroll pitch line is defined as of A-type with which the outer profile of orbiting scroll and the inner profile of fixed scroll can be formed. Another scroll pitch line is defined as B-type with which the inner profile of orbiting scroll and the outer profile of fixed scroll can be formed. The scroll compression chambers corresponding to the pitch lines of A-type and that of B-type are defined as compression chambers of A-series and B-series, respectively. Then the general geometrical model of scroll compression chamber is set up. It can demonstrate the deforming, opening, and vanishing process of all scroll chambers. [DOI: 10.1115/1.4000647]

Keywords: scroll fluid machine, general profile, scroll compression chamber, general geometrical model

1 Introduction

The working principle of scroll fluid machine has been known since 1905 when it was invented by Leon Creux [1], a French engineer. For a scroll fluid machine, the meshing and geometry theories are its theoretical basis and, certainly, the most important study object. Zhenquan et al. [2,3], and Bush and Beagle [4] performed effective studies of meshing theory and profiles of the scroll fluid machine, Bush and co-workers [4,5] put forward a general profile geometry theory, Gagene and Nieter [6] simulated the working processes of a scroll compressor with a general profile. In the working process of a scroll fluid machine, its basic performance is determined by the geometrical characteristics of the scroll compression chamber. So it is very critical to establish a general geometrical model of compression chamber.

2 Characteristic Angle of Scroll

In the working process of scroll fluid machine, all compression chambers formed by one profile of an orbiting scroll (inner profile or outer one) and one profile of a fixed scroll (outer profile or inner one) can be called a set of compression chambers.

For a scroll fluid machine with z scroll wraps, as shown in Fig. 1, there are z identical scroll wraps with a phase difference of $2\pi/z$ on either orbiting or fixed scroll, respectively. In its working process, there is $2z$ sets of scroll compression chambers that are formed with a phase difference of π/z. Considering a phase difference of π/z between orbiting and fixed scrolls, the characteristic angle, θ_c, is defined for a scroll with z wraps as follows:

$$\theta_c = \frac{\pi}{z} \quad \text{for} \quad z = 1,2,3,\ldots \tag{1}$$

3 General Geometrical Model of Scroll Compression Chamber

3.1 Scroll Wrap With General Profile. As shown in Fig. 2, for a point on a continuous curve, assume that its normal angle φ is the positive angle between the x-axis and the normal to the curve at this point and has a property of superposition. Therefore, an arbitrary point on this curve can be expressed as a complex number by the normal component, R_n, and tangential component, R_t, of its radius-vector as follows:

$$\begin{gathered} P(\varphi) = R_n(\varphi)\exp(j\varphi) + R_t(\varphi)\exp\left[j\left(\varphi + \frac{\pi}{2}\right)\right] \\ R_t(\varphi) = \frac{dR_n(\varphi)}{d\varphi} \end{gathered} \tag{2}$$

According to the general profile theory, there are three types of general profile, they are

$$\begin{aligned} &R_n(\varphi) = c_0 + c_1(\varphi + c_2) \quad \text{for type-I of scroll profile} \\ &R_n(\varphi) = c_0 + c_1\cos(\varphi + c_2) \quad \text{for type-II of scroll profile} \\ &R_n(\varphi) = c_0 + c_1\varphi + c_2\varphi^2 + c_3\varphi^3 \quad \text{for type-III of scroll profile} \end{aligned} \tag{3}$$

As shown in Fig. 3, the inner and outer profiles of scroll wraps are formed by shifting their pitch lines by a distance of $R_{\mathrm{or}}/2$ in the normal direction of the pitch lines. The pitch line forming outer profile of orbiting scroll and inner profile of fixed scroll is defined as A-type pitch line and similarly, the pitch line forming inner profile of orbiting scroll and outer profile of fixed scroll is defined as the B-type one.

For a scroll fluid machine, A-type pitch line or B-type one may have z identical pitch lines in number. By using a subscript l ($l = a$ or b), the type of pitch line can be indicated, a subscript m (m=in or out) can be used to indicate the outer or inner profile of scroll wrap, a subscript u ($u=o$ or f) can be used to indicate the orbiting or fixed scroll, and a subscript i (i is positive integer and $1 \le i \le z$) is used to indicate the ordering number of pitch line. Taking the first pitch line ($i=1$) of A-type ($l=a$) as a reference and assuming $\varphi_{b,i,s} > \varphi_{a,i,s}$, then the relationship between the initial normal angles of A-type and B-type pitch lines is

$$\varphi_{b,i,s} = \varphi_{a,i,s} + \theta_c \tag{4}$$

The relationship between the phases of two pitch lines of identical type is

$$\varphi_{l,i,s} = \varphi_{l,1,s} + 2\theta_c(i-1) \quad \text{for} \quad i = 1,2,\ldots,z \tag{5}$$

The relationship between the normal components of radius-vector on two pitch lines of identical type can be expressed as

$$R_{n,l,1}(\varphi) = R_{n,l,i}[\varphi + 2\theta_c(i-1)] \quad \text{for} \quad \varphi_{l,1,s} \le \varphi \le \varphi_{l,1,e} \tag{6}$$

The pitch lines and scroll profiles can be expressed as

$$\left\{ \begin{aligned} P_{l,i} &= R_{n,l,i}(\varphi)\exp[\varphi + 2\theta_c(i-1)] \\ &\quad + R_{t,l,i}(\varphi)\exp\{j[\varphi + 2\theta_c(i-1)]\} \\ P_{l,i,m} &= P_{l,i} \pm \frac{R_{\mathrm{or}}}{2}\exp\{j[\varphi + 2\theta_c(i-1)]\} \end{aligned} \right. \quad \text{for } \varphi_{l,1,s} \le \varphi \le \varphi_{l,1,e} \tag{7}$$

where the positive sign "+" is used for m=in and negative sign "–" for m=out.

Effective turns of every scroll pitch line is the same as

$$n_{l,i} = \frac{\varphi_{l,i,e} - \varphi_{l,i,s}}{2\pi} = \frac{\varphi_{l,1,e} - \varphi_{l,1,s}}{2\pi} = n \tag{8}$$

Contributed by the Fluids Engineering Division of ASME for publication in the JOURNAL OF FLUIDS ENGINEERING. Manuscript received April 5, 2008; final manuscript received October 25, 2009; published online December 15, 2009. Assoc. Editor: Chunill Hah.

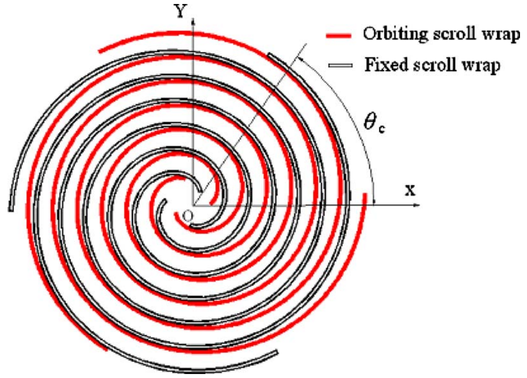

Fig. 1 Scroll wraps of multiwrap scroll

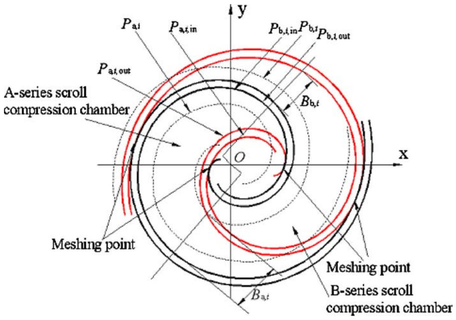

Fig. 4 Scroll compression chambers

3.2 General Geometrical Model of Scroll Compression Chamber. As shown in Fig. 4, every compression chamber is formed by moving the outer or inner profile of the orbiting scroll wrap in the direction of the profile normal at the meshing point up to the inner or outer profile of the fixed scroll wrap by a distance of R_{or}. The normal angle region of one scroll compression chamber is $[\psi_{l,i}, \psi_{l,i}+2\pi]$, where $\psi_{l,i}$ is the normal angle at the meshing point. The compression chamber formed by A-type pitch lines is defined as A-series scroll compression chamber, and the chamber formed by B-type pitch lines is defined as B-series scroll compression chamber. A-series or B-series scroll compression chamber may have z sets of compression chambers in number. Between two scroll compression chambers of different series, there is a phase difference of θ_c. On the other hand, between the scroll compression chambers of identical series but different set, there will be a phase difference of $2\theta_c$.

For an arbitrary scroll compression chamber, the distance between its opposed profiles along the normal of its pitch line is defined as its width and denoted by $B_{l,i}(\zeta_{l,i}, \psi_{l,i})$, where $\zeta_{l,i} \in [\psi_{l,i}, \psi_{l,i}+2\pi]$. The length of its pitch line is defined as its length and denoted by $L_{cl,i}(\psi_{l,i})$. The product of its width and height of scroll wrap is defined as its normal sectional area and denoted by $A_{nl,i}(\zeta_{l,i}, \psi_{l,i})$, that is

$$\begin{gathered} A_{nl,i}(\zeta_{l,i}, \psi_{l,i}) = HB_{l,i}(\zeta_{l,i}, \psi_{l,i}), \quad \varphi_{l,i,s} \le \psi_{l,i} \le \varphi_{l,i,e} - 2\pi \\ \psi_{l,i} \le \zeta_{l,i} \le \psi_{l,i} + 2\pi, \quad i = 1,2, \ldots ,z \end{gathered} \tag{9}$$

where H is the height of scroll wrap. The normal sectional area and length of a scroll compression chamber can be used to demonstrate its size and shape, and they reveal the nature of the orbiting movement.

For arbitrary $\psi_{l,i} \in [\varphi_{l,i,s}, \varphi_{l,i,s}-2\pi]$ and $\zeta_{l,i} \in [\psi_{l,i}, \psi_{l,i}+2\pi]$, the length of scroll compression chamber of A-series and B-series can be calculated by

$$L_{cl,i}(\psi_{l,i}) = \frac{L_{l,i,\text{in}}(\psi_{l,i}) + L_{l,i,\text{out}}(\psi_{l,i})}{2} \quad \text{for} \quad i = 1,2, \ldots ,z \tag{10}$$

In Eq. (10), $L_{l,i,\text{in}}(\psi_{l,i})$ and $L_{l,i,\text{out}}(\psi_{l,i})$ can be calculated as follows:

$$\begin{aligned} l_{l,i,m}(\psi_{l,i}) = \int_{\psi_{l,i}}^{\psi_{l,i}+2\pi} & R_{n,l,i}(\zeta_{l,i})\mathrm{d}\zeta_{l,i} \pm \pi R_{\text{or}} + R_{t,l,i}(\psi_{l,i} + 2\pi) \\ & - R_{t,l,i}(\psi_{l,i}) \end{aligned} \tag{11}$$

where the positive sign + is used for $m=\text{in}$ and negative sign − for $m=\text{out}$.

With the range of $0 \le \delta_{l,i}(\zeta_{l,i}, \psi_{l,i}) < \pi/4$, as shown in Fig. 5,

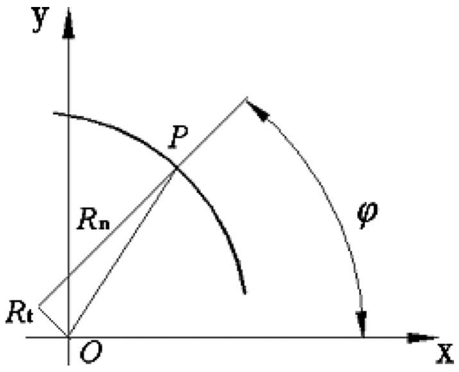

Fig. 2 Normal and tangential components of curve

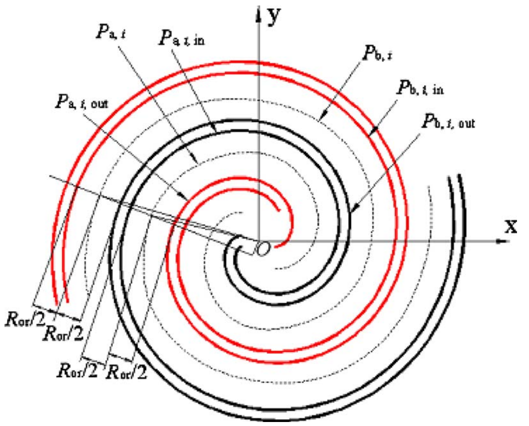

Fig. 3 Pitch lines and scroll profiles

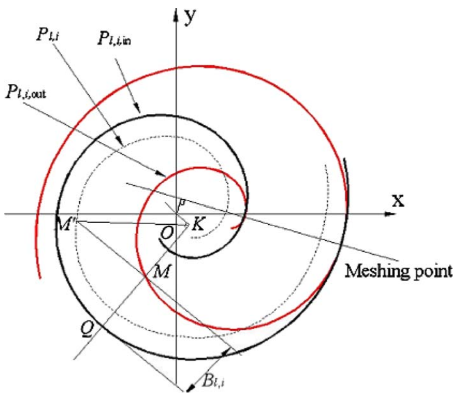

Fig. 5 Width of scroll compression chamber

there is $\delta_{l,i}(\zeta_{l,i},\psi_{l,i})=0$ for $\zeta_{l,i}=\psi_{l,i},\psi_{l,i}+\pi,\ldots,\psi_{l,i}+k\pi$, otherwise $\zeta_{l,i}$ and $\delta_{l,i}(\zeta_{l,i},\psi_{l,i})$ satisfy Eq. (12)

$$\frac{\sin[\zeta_{l,i}-\psi_{l,i}+\delta_{l,i}(\zeta_{l,i},\psi_{l,i})]}{\tan\delta_{l,i}(\zeta_{l,i},\psi_{l,i})}+\cos[\zeta_{l,i}-\psi_{l,i}+\delta_{l,i}(\zeta_{l,i},\psi_{l,i})] - \frac{\sin(\zeta_{l,i}-\psi_{l,i})}{\sin\delta_{l,i}(\zeta_{l,i},\psi_{l,i})}=0 \tag{12}$$

Then the width of scroll chamber $B_{l,i}(\zeta_{l,i},\psi_{l,i})$ can be calculated by using the following formula:

$$B_{l,i}(\zeta_{l,i},\psi_{l,i})=R_{n,l,i}(\zeta_{l,i},\psi_{l,i})+\frac{R_{\text{or}}}{2}-R_{\text{or}}\frac{\sin[\zeta_{l,i}-\psi_{l,i}+\delta_{l,i}(\zeta_{l,i},\psi_{l,i})]}{\sin\delta_{l,i}(\zeta_{l,i},\psi_{l,i})} \pm\sqrt{C_{l,i}^2(\zeta_{l,i},\psi_{l,i})+D_{l,i}^2(\zeta_{l,i},\psi_{l,i})-R_{t,l,i}^2(\zeta_{l,i})} \tag{13}$$

where $C_{l,i}(\zeta_{l,i},\psi_{l,i})=\sin(\zeta_{l,i}-\psi_{l,i})/\sin\delta_{l,i}(\zeta_{l,i},\psi_{l,i})+R_{n,l,i}[\zeta_{l,i}\pm\delta_{l,i}(\zeta_{l,i},\psi_{l,i})]$, and $D_{l,i}(\zeta_{l,i},\psi_{l,i})=R_{t,l,i}[\zeta_{l,i\pm}\delta_{l,i}(\zeta_{l,i},\psi_{l,i})]$, the positive sign + is used for $\zeta_{l,i}\in[\psi_{l,i},\psi_{l,i}+\pi]$ and otherwise the sign − is used. Obviously, $B_{l,i}(\zeta_{l,i},\psi_{l,i})=0$ for $\zeta_{l,i}=\psi_{l,i}$ and $\zeta_{l,i}=\psi_{l,i}+2\pi$, and $B_{l,i}(\zeta_{l,i},\psi_{l,i})=R_{\text{or}}$ for $\zeta_{l,i}=\psi_{l,i}+\pi$.

For an arbitrary scroll compression chamber changing from the instance of its formation to that of its vanishing, its living period $T_{l,i}$ is related to the effective turns of its pitch line in the following form:

$$T_{l,i}=\frac{\varphi_{l,i,e}-\varphi_{l,i,s}-2\pi}{\omega} \tag{14}$$

where ω is the angular speed of orbiting motion.

Thus, if the orbiting angle is an arbitrary $\theta(\psi_{l,i})\in[0,2\pi]$, then the orbiting angle $\theta(\psi_{l,i})$ and the number of living chambers $N_{l,i}(\psi_{l,i})$ can be expressed as

$$\begin{cases}\theta(\psi_{l,i})=\psi_{l,i}-2\pi\cdot\text{int}\left(\dfrac{\psi_{l,i}}{2\pi}\right)\\ N_{l,i}(\psi_{l,i})=\text{int}(n_{l,i}-1)+\text{sign}[n_{l,i}-\text{int}(n_{l,i})]+\text{int}\left[\dfrac{\theta(\psi_{l,i,s})}{\theta(\psi_{l,i})}\right]\end{cases} \quad \text{for} \quad \varphi_{l,i,s}\le\psi_{l,i}\le\varphi_{l,i,e}-2\pi, \quad i=1,2,\ldots z \tag{15}$$

Obviously, $\theta(\psi_{l,i})$ changes with a period of 2π. If $\psi_{l,i}=\varphi_{l,i,e}-2\pi$, then the suction process would be completed and a scroll chamber would be formed. With a subsequent reduction in $\psi_{l,i}$, the volume of the scroll compression chamber would gradually reduce and reach its minimum when $\psi_{l,i}=\varphi_{l,i,e}$. With further orbiting movement, the scroll compression chamber would be opened.

Taking the compression chamber composed of first scroll profile of A-type as a reference, the phase relationship between A-series and B-series scroll compression chambers is

$$\psi_{b,i}=\psi_{a,i}+\theta_c \quad \text{for} \quad i=1,2,\ldots,z \tag{16}$$

The phase relationship between two scroll compression chambers of the same series is

$$\psi_{l,i}=\varphi_{l,1}+2\theta_c(i-1) \quad \text{for} \quad i=1,2,\ldots,z \tag{17}$$

Therefore, the relationship between all living scroll compression chambers and the first one of A-series can be expressed as

$$\begin{cases}\theta=\theta(\psi_{a,1})=\psi_{a,1}-2\pi\cdot\text{int}\left(\dfrac{\psi_{a,1}}{2\pi}\right)\\ N_{l,i}(\theta)=\text{int}(n_{l,i}-1)+\text{sign}[n_{l,i}-\text{int}(n_{l,i})]+\text{int}\left\{\dfrac{\theta\left(\psi_{a,1,s}+2\theta_c(i-1)+\dfrac{\theta_c\pm\theta_c}{2}\right)}{\theta\left(\psi_{a,1}+2\theta_c(i-1)+\dfrac{\theta_c\pm\theta_c}{2}\right]}\right\}\end{cases} \quad \text{for} \quad \psi_{a,1,s}\le\psi_{a,1}\le\psi_{a,1,e}-2\pi, \quad i=1,2,\ldots,z \tag{18}$$

The relationship between normal sectional area and length of all scroll compression chambers can be expressed as

$$\begin{cases}A_{nl,i}(\zeta_{l,i},\psi_{l,i})=A_{na,1}\left[\zeta_{a,1}+\psi_{a,1}+2\theta_c(i-1)+\dfrac{\theta_c\pm\theta_c}{2},\psi_{a,1}+2\theta_c(i-1)+\dfrac{\theta_c\pm\theta_c}{2}\right]\\ L_{l,i}(\psi_{l,i})=L_{a,1}\left[\psi_{a,1}+2\theta_c(i-1)+\dfrac{\theta_c\pm\theta_c}{2}\right]\end{cases}$$
$$\text{for} \quad \varphi_{a,1,s}\le\psi_{a,1}\le\varphi_{a,1,e}-2\pi, \quad \psi_{a,1}\le\zeta_{a,1}\le\psi_{a,1}+2\pi, \quad i=1,2,\ldots,z \tag{19}$$

In Eqs. (18) and (19), the positive sign + is used for $l=b$ and negative sign − for $l=a$.

Summarizing the above analysis, it is recognized that the general geometrical model of scroll compression chamber is composed of combined Eqs. (7), (9), (10), (14), and (15), among which Eq. (7) characterizes its profile and orbiting movement, Eqs. (9) and (10) characterize its shape and deformation, Eq. (14) characterizes its living period, and finally Eq. (15) characterizes the number of scroll compression chambers in the working process. The relationship between an arbitrary scroll compression chamber and the first one of A-series can be expressed by Eqs. (18) and (19).

4 Conclusions

The general geometrical model of scroll compression chamber that covers all relevant and indispensable factors, such as the profiles, forms, deformation, living period, and the living numbers of scroll compression chambers, is established. By using it, the forming, deforming, and vanishing processes of the compression chamber can be described. The scroll pitch line can be classified into an A-type one, which forms the outer profile of orbiting scroll and the inner profile of fixed scroll, and the B-type one, which forms the inner profile of the orbiting scroll and the outer profile of the fixed scroll. Correspondingly, scroll compression chambers can be classified into an A-series and B-series, that A-series one relates to the A-type pitch lines and B-series one to B-type pitch lines. For a scroll fluid machine with z scroll wraps, either A-series or B-series scroll compression chambers have z sets, respectively. The phase difference between two different series of scroll compression chambers is equal to the characteristic angle. On the other hand, the phase difference between two adjacent scroll compression chambers with identical series but of different sets is equal to the characteristic angle doubled.

Acknowledgment

The author thanks Professor Liu Zhenquan for his helpful comments. This work is supported by the Doctor Foundation of the Education Department of China (Grant No. 2005731002), and the Doctor Foundation of the Lanzhou University of Technology (Grant No. BS02200902).

Nomenclature

c_0, c_1, c_2, c_3 = constant coefficients
n = effective turns of the scroll pitch line
R_n = normal component of the radius-vector, mm
R_{or} = radius of the orbiting circle, mm
R_t = tangential component of the radius-vector, mm
z = number of scroll wraps on the scroll
$\zeta, \psi, \delta, \gamma$ = angles, rad
θ = orbiting angle of the scroll, rad
θ_c = characteristic angle of the scroll wrap, rad

Subscripts

a = A-type pitch lines or A-series scroll compression chamber
b = B-type pitch lines or B-series scroll compression chamber
e = terminal location of curve
f = fixed scroll wrap
i = serial number (positive integer)
in = inner profile of scroll wrap
l = pitch line type
m = scroll profile type
o = orbiting scroll wrap
out = outer profile of scroll wrap
s = suction or starting location of curve
u = scroll wrap type

References

[1] Creux, L., 1905, "Rotary Engine," U.S. Patent No.801,182.
[2] Zhenquan, L., and Du Guirong, Q. Z., 1994, "The Conjugacy Analysis of Modified Part of Scroll Profiles," Proceedings of the International Compressor Engineering Conference, Purdue, pp. 479–484.
[3] Zhenquan, L., and Du Guirong, Y. S., 1992, "The Graphic Method of Modified Wrap of Scroll Compressor," Proceedings of the International Compressor Engineering Conference, Purdue, pp. 1099–1106.
[4] Bush, J. W., and Beagle, W. P., 1992, "Derivation of a General Relation Governing the Conjugacy of Scroll Profiles," Proceedings of the International Compressor Engineering Conference, Purdue, pp. 1079–1087.
[5] Bush, J. W., Beagle, W. P., and Housman, M. E., 1994, "Maximizing Scroll Compressor Displacements Using Generalized Wrap Geometry," Proceedings of the International Compressor Engineering Conference, Purdue, pp. 205–210.
[6] Gagene, D. P., and Nieter, J. J., 1994, "Simulating Scroll Compressor Using Generalized Conjugate Surface Approach," Proceedings of the International Compressor Engineering Conference, Purdue, pp. 553–558.

Single Phase Compressible Steady Flow in Pipes

David Hullender
e-mail: hullender@uta.edu

Robert Woods
e-mail: woods@uta.edu

Yi-Wei Huang
e-mail: yiwei0416@hotmail.com

University of Texas Arlington,
Arlington, TX 76019

In general, the computation of single phase subsonic mass velocity of gas flowing through a pipe requires a computerized iterative analysis. The equations for the friction factor for laminar and turbulent flow are used to obtain explicit equations for the subsonic mass velocity as a function of the pressures at the ends of a pipe. Explicit equations for mass velocity are presented. Included within the equations is a heat transfer ratio, which can vary between 0 for adiabatic flow conditions to 1 for isothermal flow conditions. The use of this heat transfer ratio also enables the formulation of an explicit equation for the gas temperature along the pipe for nonisothermal flow conditions. The explicit equations eliminate the need for an iterative solution. Laboratory data are used to support the accuracy of the model.

[DOI: 10.1115/1.4000742]

Keywords: compressible flow, adiabatic flow, isothermal flow, turbulent flow

1 Introduction

The compressible flow of fluid through circular pipes has been studied and documented for both adiabatic and isothermal flow conditions [1]. The density, temperature, and pressure all change as a gas flows through a pipe. In addition, there is a tendency for heat transfer to occur between the gas and the walls of the pipe as a result of a change in the gas temperature. Theoretically, the heat transfer coefficients could be small enough that there is no heat transfer (adiabatic conditions). The opposite extreme case is when there is sufficient heat transfer through the pipe walls to allow for the gas temperature to remain constant (isothermal conditions). Numerical algorithms for iteratively solving for mass velocity as a function of upstream temperature and pressure and downstream pressure have been formulated for personal computer calculations [2–4]. An iterative solution process utilizes an initial estimate of the friction factor [5,6] followed by converging calculations to obtain a solution for the mass velocity as a function of pressure and temperature. The objective of this paper is to formulate an explicit equation for the mass velocity by incorporating an equation for the friction factor thus avoiding the need for an iterative computer solution.

The formulation in this paper utilizes a normalized heat transfer ratio that can be between 0 for adiabatic and 1 for isothermal, thus, solutions for mass velocity as a function of the pressures at the ends of the pipe can be obtained for any level of heat transfer at or between either of these extreme cases. The formulation does neglect changes in viscosity associated with temperature and assumes subsonic gas velocities. Also, an explicit equation is derived and presented for the change in temperature as a function of the assumed level of heat transfer between isothermal and adiabatic flow conditions. This nonisothermal temperature formulation is beneficial if possible changes in the gas temperature are of interest; for instance, if there is only a small change in temperature associated with the extreme adiabatic condition, then the more simple isothermal solution for mass velocity may be justified.

As outlined in the paper, the procedure for handling the explicit equation for the mass velocity depends on the assumption of isothermal or nonisothermal flow conditions as well as if the flow is laminar or turbulent. Although single empirical equations exist for the friction factor that are valid for both laminar and turbulent flow conditions [7], simplified friction factor equations, unique to either laminar or turbulent flow, are used to allow explicit formulations for the mass velocity equation. Thus, an educated guess regarding laminar or turbulent flow is required; if wrong, then the other friction factor is used to get the solution. Laboratory data are included to support the accuracy of the model for a particular case study.

2 Model Formulation

A circular pipe with diameter D and length L is shown in Fig. 1; the positive direction of flow is from left to right. Also shown in Fig. 1 is the force balance terms on a small section of the pipe of length dx; flow resistance due to pipe couplings has been neglected.

The summation of the forces on the fluid in the small section of the pipe is equal to the mass M of the fluid times the acceleration $\dot{U}$ of the fluid. By substituting the equation for the drag force F_d and the equation for the mass M of the fluid results in the following well known equation:

$$dP + \rho U dU + f\frac{\rho U^2}{2D}dx = 0 \tag{1}$$

For steady compressible flow, the mass flow rate is constant but the decrease in density along the pipe results in a change in the fluid velocity U. The equation for the mass velocity G (mass flow rate per unit area) is given by

$$G = \rho U \tag{2}$$

Since the mass velocity G is constant, we can write

$$\rho dU + U d\rho = 0 \tag{3}$$

It will prove beneficial to use Eq. (2) and Eq. (3) to get

$$UdU = -\frac{G^2}{\rho^3}d\rho \tag{4}$$

The ideal gas equation is written in terms of the gas constant R and compressibility factor Z, i.e.,

$$T = \frac{P}{ZR\rho} \tag{5}$$

The final equation required in the compressible flow formulation is derived using conservation of energy. For steady flow and no shaft work, the energy equation simplifies to

$$q = AGdh + AGd\left(\frac{U^2}{2}\right) = AG(dh + UdU) = AG(c_p dT + UdU) \tag{6}$$

By denoting $q_{\max}$ as the heat transfer rate required to keep the temperature constant ($dT=0$), leads to

$$q_{\max} = AGUdU \tag{7}$$

A heat transfer ratio r is introduced and defined as follows:

Contributed by the Fluids Engineering Division of ASME for publication in the Journal of Fluids Engineering. Manuscript received November 3, 2009; final manuscript received November 23, 2009; published online January 12, 2010. Assoc. Editor: Zvi Rusak.

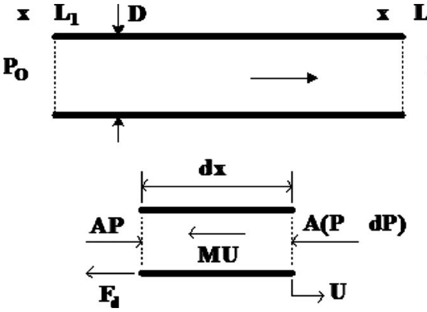

Fig. 1 Pipe and force balance on the fluid in a small section of the pipe

$$r = \frac{q}{q_{\max}} \tag{8}$$

where $0 \le r \le 1$, $r=1$ for isothermal conditions, and $r=0$ for adiabatic conditions. Thus,

$$dT = \frac{(r-1)UdU}{C_p} = \frac{(1-r)G^2}{C_p\rho^3}d\rho \tag{9}$$

Equations (1), (4), (5), and (9) and an equation for f represent five equations for the unknowns P, ρ, U, T, and f. These equations can be solved for any of these unknowns in terms of the mass velocity G.

The solution for the pressure P in terms of G begins by assuming the specific heat C_p is constant and integrating Eq. (9) to get an equation for the temperature of the gas, i.e.,

$$T = T_1 - \frac{(1-r)G^2}{2C_p}\left[\frac{1}{\rho^2} - \frac{1}{\rho_1^2}\right] \tag{10}$$

Using Eq. (5) for T in Eq. (10) gives

$$P = \left[RT_1 + \frac{(1-r)G^2RZ}{2C_p\rho_1^2}\right]\rho - \left[\frac{(1-r)G^2RZ}{2C_p}\right]\frac{1}{\rho} \tag{11}$$

By differentiating Eq. (11) assuming Z is constant gives

$$dP = \left[RT_1 + \frac{(1-r)G^2RZ}{2C_p\rho_1^2} + \frac{(1-r)G^2RZ}{2C_p\rho^2}\right]d\rho \tag{12}$$

By substituting dP from Eq. (12) into Eq. (1) and then integrating gives

$$\frac{fLG^2}{2D} = -G^2\left[\left(1 - \frac{(1-r)RZ}{2C_p}\right)\ln\left(\frac{\rho_1}{\rho_2}\right) - \frac{(1-r)RZ}{4C_p}\left(1 - \frac{\rho_2^2}{\rho_1^2}\right)\right] + \frac{RZT_1\rho_1^2}{2}\left(1 - \frac{\rho_2^2}{\rho_1^2}\right) \tag{13}$$

Equation (13) closely resembles the Peter Paige [1] equations depending on the value of r, which is between 0 and 1; 0 for adiabatic flow and 1 for isothermal flow.

In most cases, the overall objective is to compute G in terms of the pressures P_1, P_2, and T_1. By introducing the definition for C_p, collecting terms, and simplifying leads to

$$\left[a + \frac{fL}{2D}\right]G^2 - c = 0 \tag{14}$$

where

$$a = \ln\left(\frac{P_1T_2}{P_2T_1}\right) - \frac{(1-r)(k-1)Z}{4k}\left[1 + 2\ln\left(\frac{P_1T_2}{P_2T_1}\right) - \left(\frac{P_2T_1}{P_1T_2}\right)^2\right] \tag{15}$$

$$c = \frac{P_1^2}{2RZT_1}\left[1 - \left(\frac{P_2T_1}{P_1T_2}\right)^2\right] \tag{16}$$

An equation for f that is good for both turbulent and laminar flow conditions could be utilized in Eq. (14); however, an iterative solution for G and T_2 would be required. In order to obtain explicit solutions, the equation for f will depend on the assumption of laminar or turbulent flow. The value of T_2 will be determined by the heat transfer, which depends on the assumed value for r. Choosing $r=1$ produces isothermal conditions yielding $T_2=T_1$. Choosing $r<1$ yields nonisothermal conditions ($T_2 \neq T_1$); the value to use for T_2 in Eq. (15) and Eq. (16) is obtained by introducing Eq. (5) into Eq. (10), i.e.,

$$T_2 = -B + \sqrt{B^2 + P_2^2\left(\frac{T_1}{CG^2RZ^2} + \frac{T_1^2}{P_1^2}\right)} \tag{17}$$

where

$$B = \frac{P_2^2}{2CG^2RZ^2}, \quad C = \frac{(1-r)(k-1)}{2k} \tag{18}$$

A simple and reasonably accurate approach to solving Eq. (17) is to compute T_2 using the solution of Eq. (14) for G assuming isothermal conditions. Studies have revealed that this value of T_2 is reasonably accurate even for adiabatic conditions. Thus, for nonisothermal conditions, having a value for T_2 allows the use of Eq. (14) to solve for G. Note, choosing $r=0$ yields the maximum possible temperature change corresponding to adiabatic conditions; this change may be so small that the simpler isothermal solution for G defined by either Eq. (21) or Eq. (25) in the sections below is justified.

2.1 Compressible Laminar Flow.

For laminar flow, the friction factor expressed in terms of G is

$$f = \frac{64\mu}{DG} \tag{19}$$

The solution to Eq. (14) simplifies to

$$G = -\frac{16\mu L}{aD^2} + \sqrt{\left(\frac{16\mu L}{aD^2}\right)^2 + \frac{c}{a}} \tag{20}$$

If the flow is isothermal, Eq. (20) simplifies even further to

$$G = -\frac{16\mu L}{D^2\ln\left(\frac{P_1}{P_2}\right)} + \sqrt{\frac{256\mu^2L^2}{D^4\ln^2\left(\frac{P_1}{P_2}\right)} + \frac{P_1^2 - P_2^2}{2RZT_1\ln\left(\frac{P_1}{P_2}\right)}} \tag{21}$$

2.2 Compressible Turbulent Flow.

For turbulent flow in smooth pipes, an empirical equation for f in terms of G for Reynolds numbers up to about 80,000 [4] is

$$f \approx \frac{0.3164}{R_n^{0.25}} = \frac{0.3164\mu^{0.25}}{D^{0.25}G^{0.25}} \tag{22}$$

Thus for turbulent flow, equation Eq. (14) simplifies to

$$aG^2 + dG^{1.75} - c = 0 \tag{23}$$

where a and c are defined by Eq. (15) and Eq. (16), respectively, and

$$d = \frac{0.1582L\mu^{0.25}}{D^{1.25}} \tag{24}$$

The approximate solution to Eq. (23) is

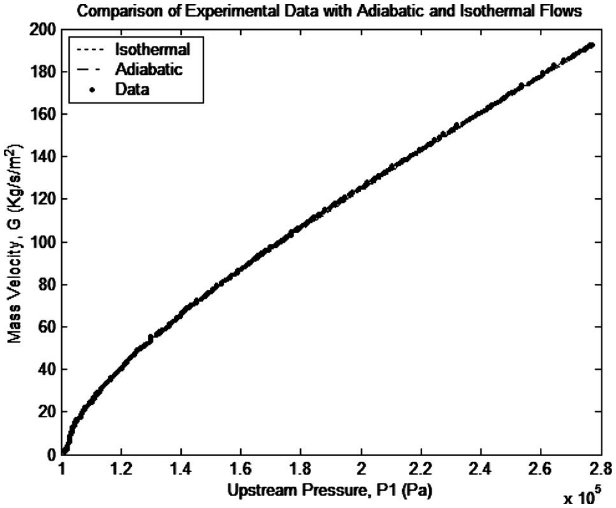

Fig. 2 Mass velocity for isothermal and adiabatic flow

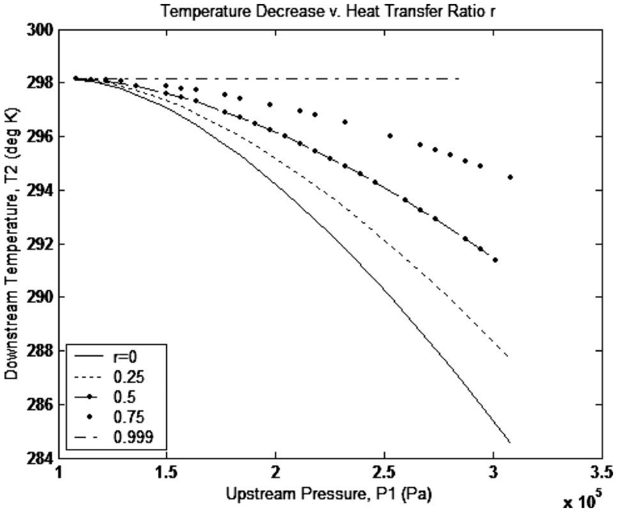

Fig. 3 Decrease in the downstream temperature as a function of heat transfer ratio *r*

$$G \approx \frac{aG_o^2 + 0.75dG_o^{1.75} + c}{2aG_o + 1.75dG_o^{0.75}} \tag{25}$$

where for the isothermal conditions G_o is computed using the following equation:

$$G_o = \left(\frac{c}{a+d}\right)^{0.57} \tag{26}$$

For nonisothermal conditions, G_o in Eq. (25) is the value of G found using Eq. (25) assuming isothermal conditions. For nonisothermal conditions, it is suggested, for confirmation, that a final value of T_2 be computed using Eq. (17) with the nonisothermal value for G obtained from Eq. (25).

It is of interest to note for constant G, the friction factor and Reynolds number are only functions of the viscosity μ, which is a function of temperature. As the gas flows through the pipe, the temperature will decrease (f and μ decrease) depending on the degree of heat transfer. Thus, if the flow starts out turbulent, it will remain turbulent even if the flow is nonisothermal. Thus, the suggested procedure for using the equations is to first calculate G using Eq. (21) and then calculate the Reynolds number to confirm that the flow is laminar. If not, then Eq. (25) is used to compute G. Theoretically, for nonisothermal conditions, the flow could start out laminar and end up turbulent. Knowing T_2 from Eq. (17) and μ as a function of temperature enables one to easily check for this possible transition.

2.3 Example Problem. Consider a smooth $L=6.096$ meter (20 ft) line with inside diameter of $D=0.0063246$ m (0.249 in.). The gas is air with an upstream temperature of $T_1=298.15$ K (77°F). The absolute viscosity of the air is $\mu=18.616 \times 10^{-6}$ Pa s. The gas constant for air is $R=286.8$ m^2/s^2 K. The ratio of specific heats is $k=1.4$. The downstream pressure is assumed atmospheric $P_2=101{,}325$ Pa (0 psig) and the upstream pressure varies from $P_1=108{,}220$ Pa (1 psig) to 308,168 Pa (30 psig). Note, for these pressures it can be shown that the compressibility factor Z is approximately 1, thus, in this case, air is essentially an ideal gas.

It is of interest to obtain plots of the mass velocity G as a function of P_1 for isothermal and for adiabatic conditions. The results are shown in Fig. 2. The flow is turbulent for the entire pressure range. As shown in Fig. 2, there is very little difference in the mass velocity as a function of pressure for isothermal and adiabatic conditions. Slight differences are observed at the higher pressures, which correspond to higher Reynolds numbers. A comparison of the theoretical formulation with laboratory data is also shown in Fig. 2. The laboratory test parameters correspond to the values in the example above. The results demonstrate the accuracy of the turbulent flow model for these pressure and flow conditions.

Plots of downstream temperature T_2 for various values of r are shown in Fig. 3. The plots confirm that the temperature does not change for $r=1$ and the maximum decrease in temperature occurs for $r=0$. It is of interest to note that the maximum temperature change is only 14 K, thus, the complexity associated with generating a nonisothermal solution may not be warranted depending on the specific design.

3 Summary and Conclusions

A new formulation for compressible steady flow has been introduced that includes empirical equations for the friction factor and a heat transfer ratio. Use of the heat transfer ratio enables one to obtain solutions for any level of heat transfer between isothermal and adiabatic flow conditions. The use of these equations provides simple and accurate explicit solutions to compressible flow variables as compared with implementing an iterative solution computer algorithm. An explicit solution for the downstream temperature is derived enabling one to evaluate the necessity of pursuing and analyzing the degree of heat transfer associated with nonisothermal flow conditions. The experimental data were used to confirm the accuracy of the turbulent flow model.

Nomenclature

A = pipe area equal to $\pi D^2/4$
a = constant defined by Eq. (15)
B = constant defined by Eq. (18)
C = constant defined by Eq. (18)
c = constant defined by Eq. (16)
C_p = constant pressure specific heat equal to $kR/(k-1)$
D = pipe diameter
d = constant defined by Eq. (24)
f = moody friction factor defined in terms of the Reynolds number in Eq. (19) and Eq. (22)
F_d = fluid drag force in small section of pipe equal to $f\rho U^2/2Ddx$
G = mass velocity, units of mass flow rate divided by area ρU
G_o = constant defined by Eq. (26)
h = enthalpy
k = ratio of specific heats

L = length of pipe equal to $L_2 - L_1$

L_1 = pipe length at upstream end typically taken to be zero

L_2 = pipe length at downstream end typically taken to be L

M = mass of fluid in small section of pipe equal to $\rho A dx$

P = absolute pressure

P_1 = absolute pressure at position L_1

P_2 = absolute pressure at position L_2

R = gas constant

r = heat transfer ratio defined to be $q/q_{\max}$

R_n = Reynolds number $\rho U d/\mu$ or Gd/μ; if $R_n > 3000$, then turbulent

q = heat transfer to the gas in the pipe

$q_{\max}$ = amount of heat transfer required to keep the gas temperature constant defined in Eq. (7)

T = gas absolute temperature

T_1 = gas absolute temperature at L_1

T_2 = gas absolute temperature at L_2

U = gas velocity

$\dot{U}$ = derivative of gas velocity with respect to time

x = position along pipe

Z = compressibility factor

μ = gas absolute viscosity

ρ = gas density

ρ_1 = gas density at L_1

ρ_2 = gas density at L_2

References

[1] Mulley, R., 2004, *Flow of Industrial Fluids—Theory and Equations, ISA—The Instrumentation, Systems, and Automation Society*, CRC, Boca Raton, FL, pp. 321–323.

[2] Cochran, T. W., 1966, "Calculate Pipeline Flow of Compressible Fluids," Chemical Engineering, **103**(2), pp. 115–122.

[3] Hörnell, K., and Lotstedt, P., 2004, "Adaptive Iteration to Steady State of Flow Problems," J. Sci. Comput., **20**(3), pp. 331–354.

[4] Abbaspour, M., Chapman, K. S., and Keshavarz, A., 2004, "Dynamic Modeling of Non-Isothermal Gas Pipeline Systems," *Proceedings of the International Pipeline Conference, IPC*, Vol. 3, pp. 2155–2163.

[5] Moody, L. F., 1944, "Friction Factors for Pipe Flow," Trans. ASME, **66**(8), pp. 671–684.

[6] Blasius, H., 1913, "Das Ahnlichkeits-Gesetz bei Reibungsvorgangen in Flussigkeiten," Forschungs-Arbeiten des Ver. Deutsch. Ing., **131**, pp. 1–12.

[7] Davis, R. L., and Campbell, B. T., 2007, "Quasi-One-Dimensional Unsteady-Flow Procedure for Real Fluids," AIAA J., **45**(10), pp. 2422–2428.